Spring 2024

GNSS Radio Propagation Through Trapped Atmospheric Lee Waves in the San Bernardino Valley, CA

Logan Grey
logan@greyemail.net

GNSS RADIO PROPAGATION THROUGH TRAPPED ATMOSPHERIC LEE WAVES IN THE SAN BERNARDINO VALLEY, CA

A Thesis

Presented to

The Graduate Faculty

Central Washington University

In Partial Fulfillment

of the Requirements for the Degree

Master of Science

Geological Sciences

---

by

Logan Mitchell Grey

May 2024

CENTRAL WASHINGTON UNIVERSITY

Graduate Studies

We hereby approve the thesis of

Logan Mitchell Grey

Candidate for the degree of Master of Science

APPROVED FOR THE GRADUATE FACULTY

_____ _____
Dr. Walter Szeliga, Committee Chair

_____ _____
Dr. Timothy Melbourne

_____ _____
Dr. Darci Snowden

_____ _____
Dean of Graduate Studies

ABSTRACT

GNSS RADIO PROPAGATION THROUGH TRAPPED ATMOSPHERIC LEE WAVES IN THE SAN BERNARDINO VALLEY, CA

by

Logan Mitchell Grey

May 2024

Atmospheric lee waves, also known as mountain waves, are a type of gravity wave that form as air that is forced over a mountain creates turbulence downstream. Trapped, or stationary, lee waves located directly over a Global Navigation Satellite System (GNSS) receiver on Earth's surface appear to lead to anomalies in the receiver's position estimate, usually skewed toward the neighboring mountain range. The exact mechanism by which trapped lee waves might cause these anomalies is not known, and so my research aims to understand this. GNSS station P612 located in the lee of the San Bernardino Mountains in southern California records positively-skewed north position time series data anomalies. Using 300 hPa upper-level air maps, I found that anomalous days tend to share an atmospheric configuration related to the jet stream forming a positively tilted trough which likely interacts with the topography of the San Bernardino Mountains to create trapped lee waves.

I use the Advanced Weather Research & Forecasting (WRF-ARW) Model V4.4 with one nested domain and initial and hourly boundary conditions from the NOAA HRRR 3 km model to simulate the atmospheres on anomalous days during boreal winter and spring of 2018-2019, where I model anomalous days which exhibit trapped lee wave events and the day prior for

comparison to a ‘normal’ atmosphere. I primarily use the Mellor-Yamada-Janjic (MYJ) planetary boundary layer (PBL) scheme and explore four other PBL schemes or damping parameters on two days with large anomalies, 22 January and 23 April 2019. I compared three diagnostics from the model output to three local weather stations to validate the model, and found the output acceptable. From vertical cross-section animations of the wave events, I found a weakly ($0 < R^2 < 0.3$) positive correlation to the duration and approximate downstream length of the trapped lee waves. I also ray traced through the output using the KARAT program, and compared the refractivity and delay output between days and parameters to understand the structure of the lee waves. I found the refractivity of a given trace can detect the presence of lee waves while the delay cannot.

DEDICATION

This thesis is dedicated to the late Daniel Genovese, one of the best grandfathers anyone could have asked for who always supported me and my academic endeavors.

ACKNOWLEDGEMENTS

This research was partially supported by the School of Graduate Studies and Research, Central Washington University, Ellensburg, Washington.

I would like to thank my advisor Dr. Walter Szeliga for his help on every step of this project and always teaching me something new every time we met, as well as Dr. Tim Melbourne and Dr. Darci Snowden for their valuable contributions to this project and their service as committee members. I would like to thank Dr. Robert Fovell of the University of Albany—SUNY for his help in the early stages of this project and his expertise in Santa Ana winds and Dr. Dale Durran of the University of Washington for his help and expertise in trapped lee waves.

I would like to thank my parents, grandparents, friends, and peers for all of their guidance and support throughout my undergraduate and graduate careers leading to this point.

TABLE OF CONTENTS

LIST OF TABLES

LIST OF FIGURES

CHAPTER I

INTRODUCTION

1.1 Trapped Atmospheric Lee Waves

Tropospheric lee waves, also known as mountain waves, are a type of atmospheric gravity wave that form as air that is forced over a mountain creates atmospheric turbulence downstream (Figure 1; Durran, 1990). Two types of lee waves are known to exist, those that propagate horizontally and those that propagate vertically, and the focus of this thesis is on the horizontal type, also known as trapped or stationary lee waves shown below in Figure 1. These waves can be extremely powerful and are a recognized aviation hazard that have led to numerous

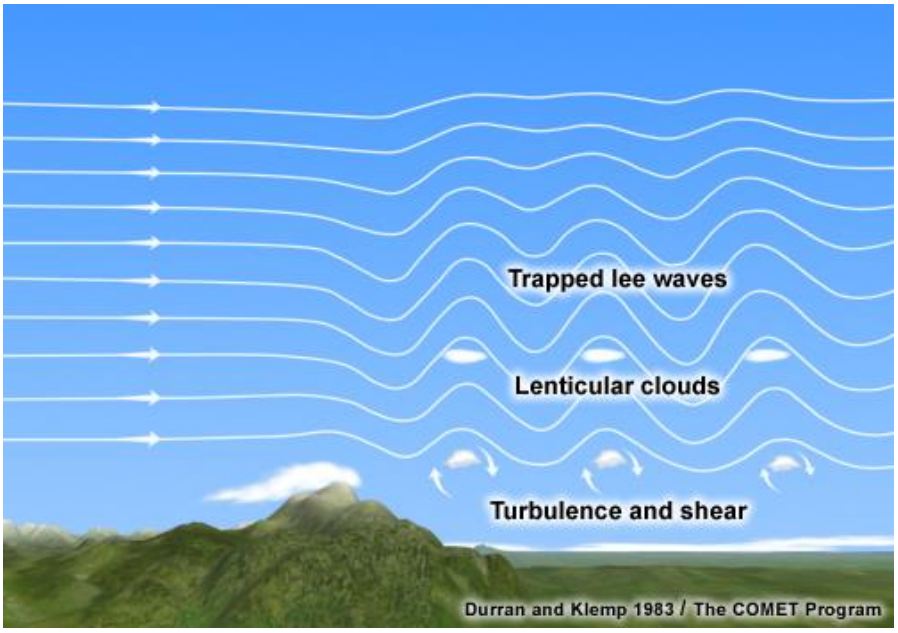

Figure 1. Vertical cross section of trapped lee waves formed from airflow over a peak also showing location of turbulent air. The direction of flow is indicated by the arrows. Image courtesy of the COMET Program.

plane crashes (Evans, 2013), but can be difficult to detect in the absence of lenticular or rotor clouds which are characteristic of the waves.

Trapped lee waves require three conditions to form: a very stable atmosphere near the mountain top, increasing wind speed with height, and strong cross-mountain winds (typically within 30° of the normal in either direction throughout most of the troposphere). The study area of the San Bernardino Basin has historically favorable atmospheric conditions with both onshore and offshore winds that interact with the steep topography of the San Bernardino Mountains to form lee waves.

1.2 GNSS Signals

Global Navigation Satellite Systems, or GNSS, are a series of satellite constellations orbiting the Earth to provide navigational data to users around the globe. The Global Positioning System, or GPS, is one such system that is owned and operated by the United States government (U.S. Space Force, 2021). GPS satellites actively transmit electromagnetic radiation at microwave radio frequencies shown in Figure 2, and receivers passively listen and receive

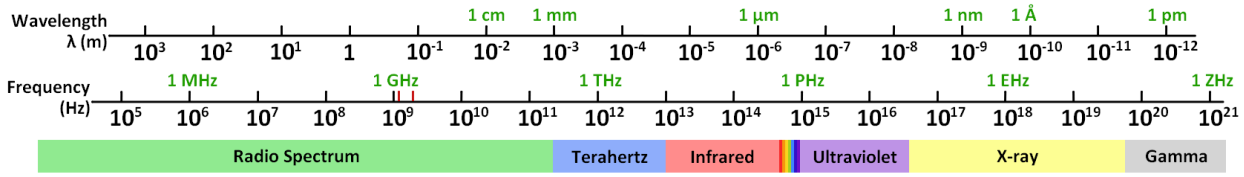

Figure 2. L1 and L2 GPS frequencies indicated by the red vertical lines. Figure modified from Wu (2012).

these radio signals. By multiplying the travel time of the radio wave from when the signal is emitted by the satellite to when it is received by the receiver by the speed of light, one can calculate the apparent distance between the two objects, or the pseudorange. This distance is shown in Figure 3 and is on the order of tens of thousands of kilometers (Sanz Subirana et al., 2013). The pseudorange estimate is skewed by the passage of the radio wave through the

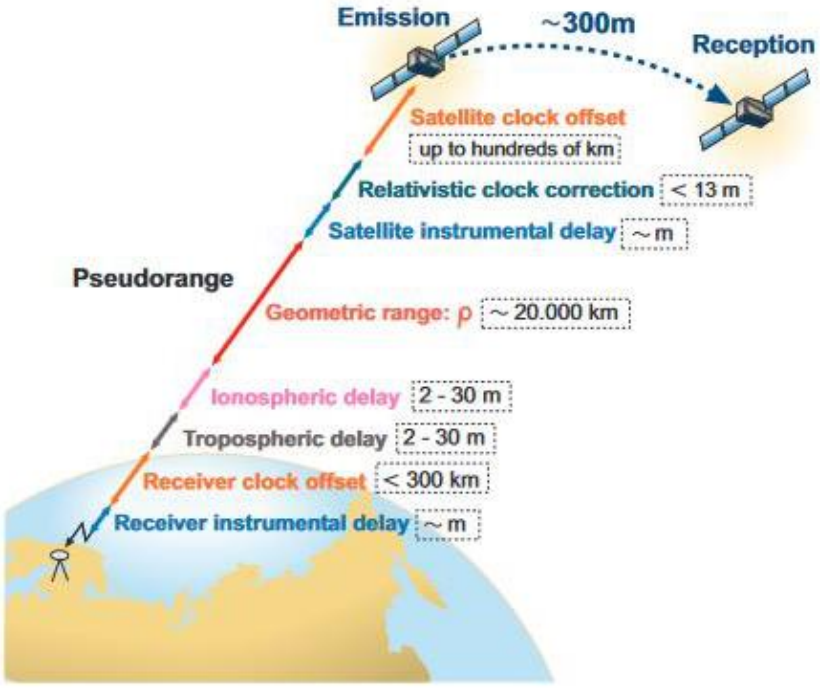

Figure 3. Components of the pseudorange measurement. Figure from Sanz Subirana et al. (2013).

different layers of the atmosphere, namely the ionosphere which is anything above 60 km and the greater troposphere which is anything below 60 km down to the surface, but for the purposes of this study, only the effects of the lower troposphere below 20 km are considered.

After corrections are applied, the receiver's position estimate from the pseudorange can be expressed as time series of east, north, and up components relative to a chosen reference coordinate. These time series can then be used to show how a receiver or a series of receivers has been moving within a given reference frame, such as the measurement of relative plate motions (Gordon & Stein, 1992).

1.3 North Position Estimate of Station P612

The San Bernardino Basin has excellent GNSS station coverage, and one particular GPS station named P612 (loc: 34.18738, -117.31552) shows many millimeter-centimeter-scale anomalies in the north position time series that are generally positively skewed north toward the San Bernardino Mountains (Figure 4). This time series is from the National Science Foundation's Geodetic Facility for the Advancement of Geoscience (GAGE) (Herring et al., 2016), however these outliers also appear in the time series from the University of Nevada-Reno (UNR) (Blewitt et al., 2018) (Figure 5) which indicates that these anomalies are not an issue of data processing.

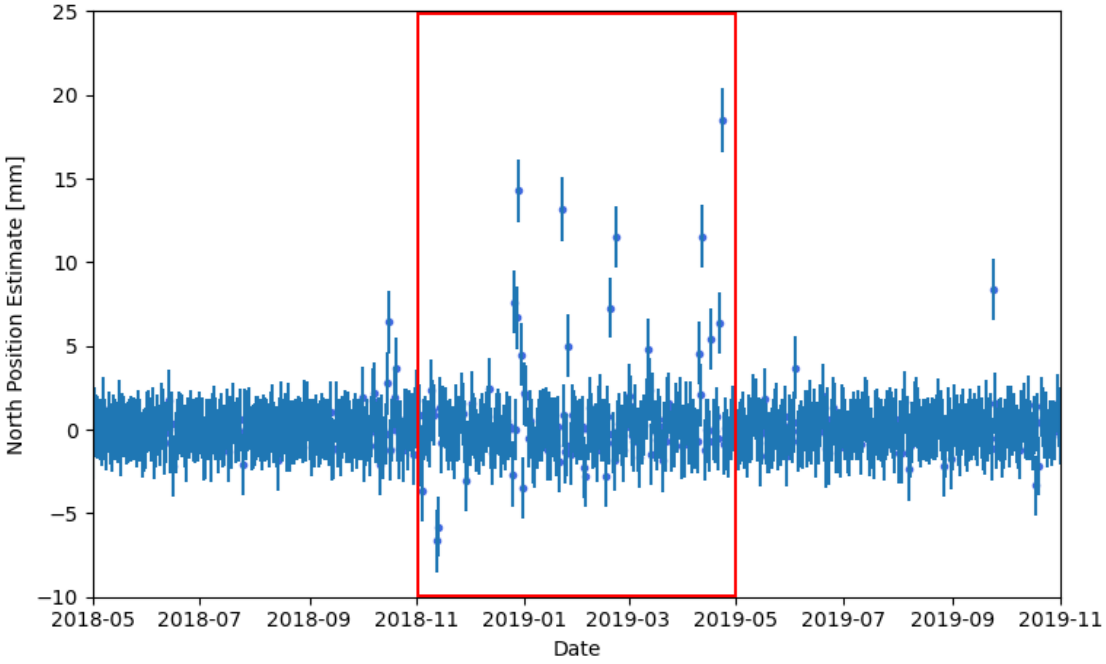

Figure 4. Detrended north position time series from 1 May 2018 to 1 November 2019 from GAGE. Vertical bars are one standard deviation. Note the seasonality of the position anomalies within the winter-spring seasons.

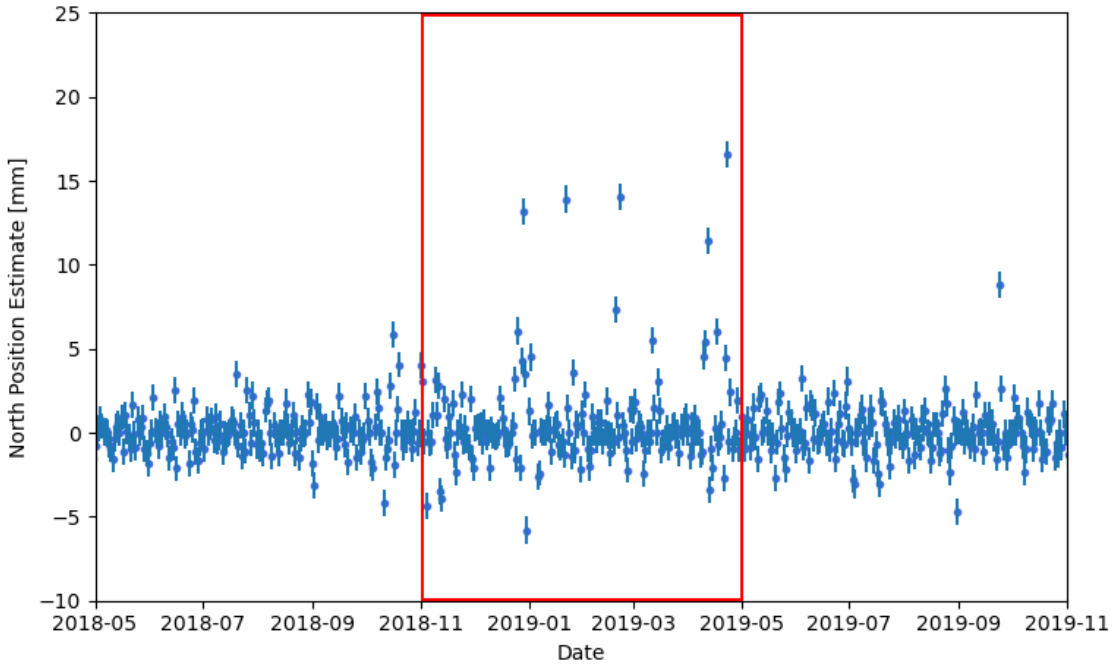

Figure 5. Detrended north position time series from 1 May 2018 to 1 November 2019 from UNR. Vertical bars are one standard deviation. Note the seasonality of the position anomalies within the winter-spring seasons.

This study encompasses mid-November 2018 to late-April 2019 as shown by the red outlined regions of Figures 4 and 5 as there is a necessary seasonal change in the overlying jet streams as these events tend to disappear once spring progresses into summer before the cycle begins anew in the fall. This particular timeframe was chosen due to an abundance of days with large position anomalies to better investigate the structure and effect on GNSS signals of trapped lee waves, and avoids possible post-seismic signals due to the 2019 Ridgecrest earthquake sequence. I will achieve this by characterizing the conditions necessary for lee wave formation in the San Bernardino Basin, running atmospheric models using these conditions, and then ray tracing GNSS signals through these models from P612 to orbiting satellites to examine the impact of the atmosphere and compare the traced delays to the recorded position estimates.

CHAPTER II

LITERATURE REVIEW

While the effect of the neutral atmosphere on slant and zenith total delays is well known (Herring et al., 1990; Tralli & Lichten, 1990), the basic observation of tropospheric phenomena such as the presence of trapped lee waves degrading GNSS positioning accuracy is relatively new and understudied (Shimada et al., 2002; Ichikawa et al., 2004; Seko et al., 2004; Materna, 2014). Recent modeling of GNSS position data by Masoumi et al. (2017) has reported a reduction in similar position outliers using improved estimates of tropospheric refractivity gradients. However, their work leads to improvements primarily for vertical outliers and appears to have little effect on outliers in horizontal position time series, which we see repeatedly, as shown in the north-skewed outliers of Figure 4.

CHAPTER III

GNSS RADIO PROPAGATION THROUGH TRAPPED ATMOSPHERIC LEE WAVES IN THE SAN BERNARDINO VALLEY, CA

Logan Grey, Walter Szeliga, Timothy Melbourne, Darci Snowden

To be submitted to *Journal of Geophysical Research: Atmospheres*

INTRODUCTION

3.1 Trapped Atmospheric Lee Waves

Tropospheric lee waves, also known as mountain waves, are a type of atmospheric gravity wave that form as air that is forced over a mountain creates atmospheric turbulence downstream (Figure 6; Durran, 1990). There exist two types of lee waves, horizontally and vertically propagating, and my focus is on the horizontal type, also known as trapped or stationary lee waves. These can be extremely powerful and are a recognized aviation hazard

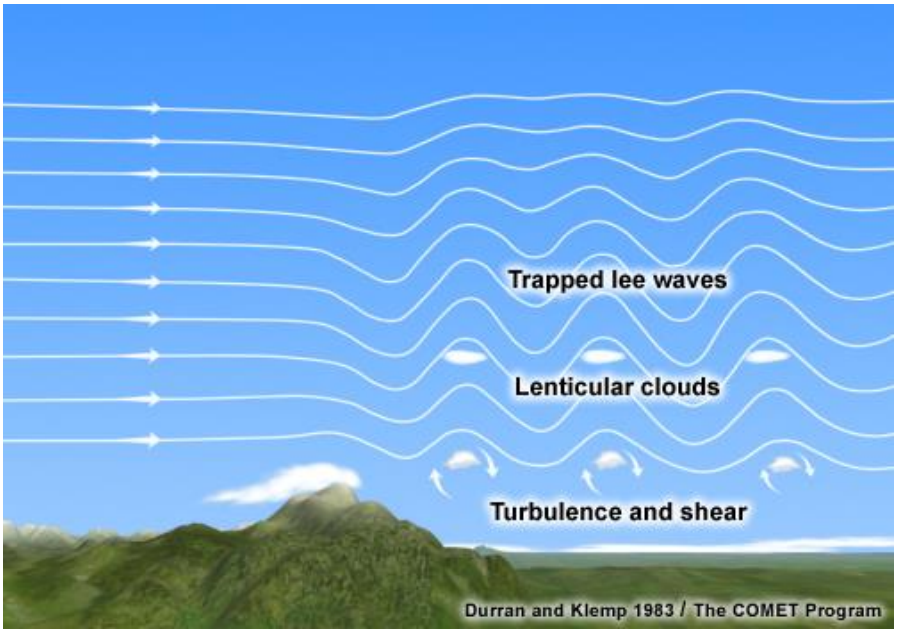

Figure 6. Vertical cross section of trapped lee waves formed from airflow over a peak also showing location of turbulent air. The direction of flow is indicated by the arrows. Image courtesy of the COMET Program.

that have led to numerous plane crashes (Evans, 2013), but are nonetheless difficult to detect in the absence of characteristic cloud formations such as lenticular or rotor clouds.

Trapped lee waves require three conditions to form: a very stable atmosphere near the mountain top, increasing wind speed with height, and strong cross-mountain winds (typically

within 30° of the normal in either direction throughout most of the troposphere). These criteria can be fulfilled by the presence of an overlying jet stream which can provide the necessary vertical wind speed gradient. A jet stream is a relatively narrow band or 'river' of strong wind located near the tropopause that is formed from the interaction between atmospheric circulation cells as well as the rotation of the Earth (Reiter, 1969; Stendel et al., 2021). I am interested in the branch of the jet stream which sometimes passes directly over the San Bernardino Mountains. The jet stream acts as a sort of 'cap' to the waves, preventing vertically transported energy from bleeding up higher in the atmosphere and allowing them to remain stable for long periods of time as this energy reflects off of the planetary boundary layer and sets up a wave train (Smith, 2001; Jiang et al., 2006; Hills & Durran, 2012). The San Bernardino Basin has historically favorable atmospheric conditions with both onshore and offshore winds that interact with the steep topography of the San Bernardino Mountains to form lee waves.

3.2 GNSS Signals

Global Navigation Satellite Systems, or GNSS, are a series of satellite constellations orbiting the Earth to provide navigational data to users around the globe. The Global Positioning System, or GPS, is one such system that is owned and operated by the United States government and is one of the four major navigational satellite constellations, the others being the European Union's Galileo, the Russian GLONASS, and the Chinese BeiDou (U.S. Space Force, 2021).

GPS satellites actively transmit electromagnetic radiation at microwave radio frequencies (L1 = 1575.42 MHz and L2 = 1227.6 MHz, Figure 7) and receivers passively listen and receive

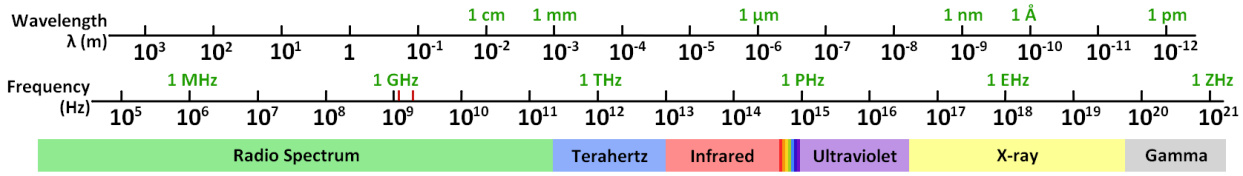

Figure 7. L1 and L2 GPS frequencies indicated by the red vertical lines. Figure modified from Wu (2012).

the radio signals at the antenna phase center (APC). By multiplying the travel time from signal transmission to reception by the speed of light, one can calculate the apparent distance between the two objects, or the pseudorange. This distance is shown in Figure 8 and is on the order of

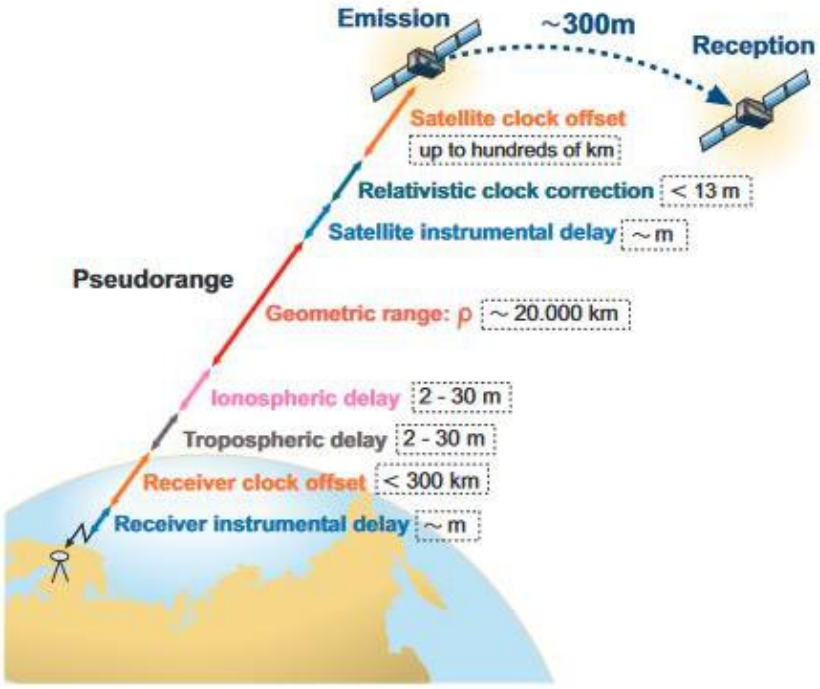

Figure 8. Components of the pseudorange measurement. Figure from Sanz Subirana et al. (2013).

tens of thousands of kilometers, largely due to the geometric range, which is the Euclidean distance between the satellite, at an altitude of 20,200 km, and receiver antenna APC coordinates (Sanz Subirana et al., 2013). The pseudorange estimate is skewed by passage through the

different layers of the atmosphere, namely the ionosphere above 60 km and the greater troposphere below 60 km to the surface, but for the purposes of this study, only the effects of the lower troposphere are considered.

At least four satellites are required to obtain all desired spatial and temporal positioning information for the ground antenna. After corrections are applied, the ground antenna position can be expressed as time series of east, north, and up relative to a reference coordinate. Time series of these east, north, and up positions can then be used to show how a receiver or a series of receivers has been moving within a given reference frame, such as the measurement of relative plate motions (Gordon & Stein, 1992). For Continuous GPS (CGPS) stations such as those in this study, these time series typically report the position as the average position across the 24-hour UTC day. GPS time series contain many other geophysically interesting signals which may only become apparent after least-squares fitting to remove the signal due to long-term plate motion.

3.3 North Position Estimate of Station P612

The San Bernardino Basin has excellent GNSS station coverage, and one particular GPS station named P612 (loc: 34.18738, -117.31552) shows many millimeter-centimeter-scale anomalies in the north position time series that are generally positively skewed north toward the San Bernardino Mountains (Figure 9). This time series is from the National Science Foundation's Geodetic Facility for the Advancement of Geoscience (GAGE) (Herring et al., 2016), however these outliers also appear in the time series from the University of Nevada-Reno (UNR) (Blewitt et al., 2018) (Figure 10) which indicates that these anomalies are not an issue of data processing.

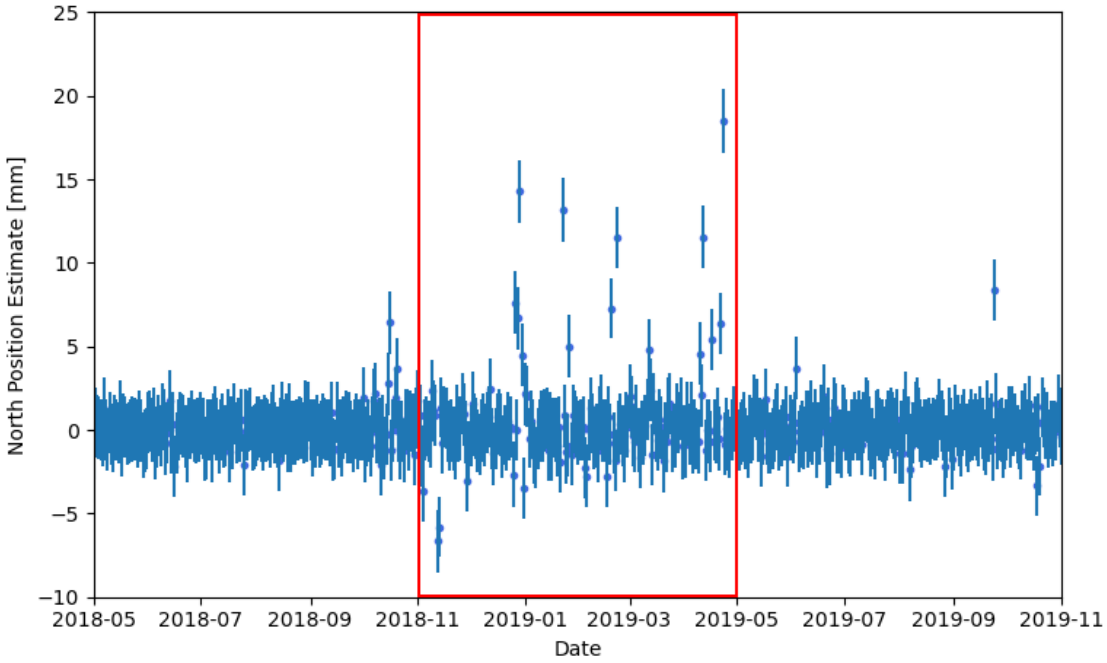

Figure 9. Detrended north position time series from 1 May 2018 to 1 November 2019 from GAGE. Vertical bars are one standard deviation. Note the seasonality of the position anomalies within the winter-spring seasons.

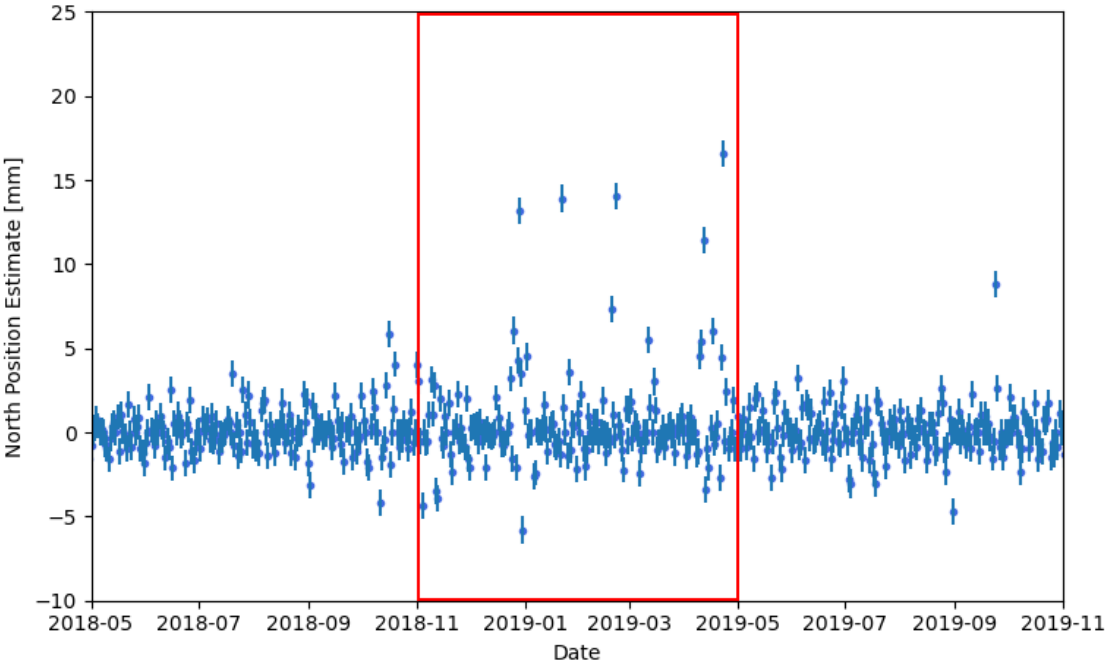

Figure 10. Detrended north position time series from 1 May 2018 to 1 November 2019 from UNR. Vertical bars are one standard deviation. Note the seasonality of the position anomalies within the winter-spring seasons.

This study encompasses mid-November 2018 to late-April 2019 as shown by the red outlined regions of Figures 9 and 10 as there is a necessary seasonal change in the overlying jet streams as these events tend to disappear once spring progresses into summer before the cycle begins anew in the fall. I focus on a selection of north and south-directed position outliers classified as data points 5 median absolute deviations away from the mean, as well as a few additional boundary or intermediate days. This serves to constrain the number of anomalous days to analyze. This particular timeframe was chosen due to an abundance of days with large position anomalies, and avoids possible post-seismic signals due to the 2019 Ridgecrest earthquake sequence.

While the effect of the neutral atmosphere on slant and zenith total delays is well known (Herring et al., 1990; Tralli & Lichten, 1990), the basic observation of tropospheric phenomena such as the presence of trapped lee waves degrading GNSS positioning accuracy is relatively new and understudied (Shimada et al., 2002; Ichikawa et al., 2004; Seko et al., 2004; Materna, 2014). Recent modeling of GNSS position data by Masoumi et al. (2017) has reported a reduction in similar position outliers using improved estimates of tropospheric refractivity gradients. However, their work leads to improvements primarily for vertical outliers and appears to have little effect on outliers in horizontal position time series, which we see repeatedly, as shown in the north-skewed outliers of Figure 9.

This research aims to better understand the structure and effect on GNSS signals of trapped atmospheric lee waves by completion of the following objectives.

1. Characterize the conditions necessary for lee wave formation in the San Bernardino Basin of southern California from GNSS data and recorded weather data of vertical wind and

temperature profiles and the topography of the San Bernardino Mountains in the direction of air flow.

2. Run atmospheric models using these conditions in the San Bernardino Basin on days favorable for lee wave formation that both show and do not show the position outliers to create atmospheres that a signal will be ray traced through from receiver to satellite.
3. Ray trace GNSS signals through these models to examine the relationship between potential sources of bias such as changes in the dry air component of refractivity and the perturbation to the GNSS position, and compare the traced delays to the recorded position estimates.

CHAPTER IV

METHODS

4.1 Atmospheric Configurations

To identify common atmospheric configurations during times of position outliers, I have used a self-organizing map (SOM) to produce a grid of these weather types based on upper-level atmospheric pressure level maps. Originally developed by Teuvo Kohonen in the 1980's, SOMs are a type of neural network which receives a multidimensional dataset as input and outputs a grid of nodes, or descriptive models, organized in such a way that proximal nodes are similar and distal nodes are different (Kohonen, 1982, 1998; Schauer et al., 2021). My work follows the methods of Schauer et al. (2021) to create similar map patterns, using the 300 hPa level instead of 500 hPa as it better reflects the location of the jet stream. The SOM is then run using daily 300 hPa level maps between 2010 and 2020 from the NCEP-NCAR Reanalysis 1 (Kalnay et al., 1996).

To determine the optimal number of nodes to use, Schauer et al. noted that they saw improvements as they increased from 9 nodes to 20 nodes and began receiving diminishing returns on further increases past 20. Symmetric grids were chosen for ease of analysis and were generated with a width of 3, 4, and 5 nodes. Initial results with the 3x3 grid showed incorrect mapping of upper-level data to nodes, likely due to an insufficiently diverse basis of nodes, while a 5x5 grid resulted in too diverse of a basis where differences between nearby nodes became more subtle and configurations on anomalous days were divided between multiple similar types. As a result, I chose a 4x4 grid to constrain the configurations while still maintaining a sufficient quantity of types. From this setup, I was able to create a 'heat map' and identify the most

commonly observed 300 hPa configurations, and consequently jet stream locations, during winter 2018-2019.

The 16 most common configurations overall, and of these, the most common configurations when one observes the north-skewed position outliers are shown in Figure 11. The most common atmospheric configuration for the outliers (WT=11) consists of a positively tilted trough over the center of North America. This configuration is the most conducive to producing a north-south directed jet stream over southern California (National Weather Service, 2023) which is favorable for lee wave formation.

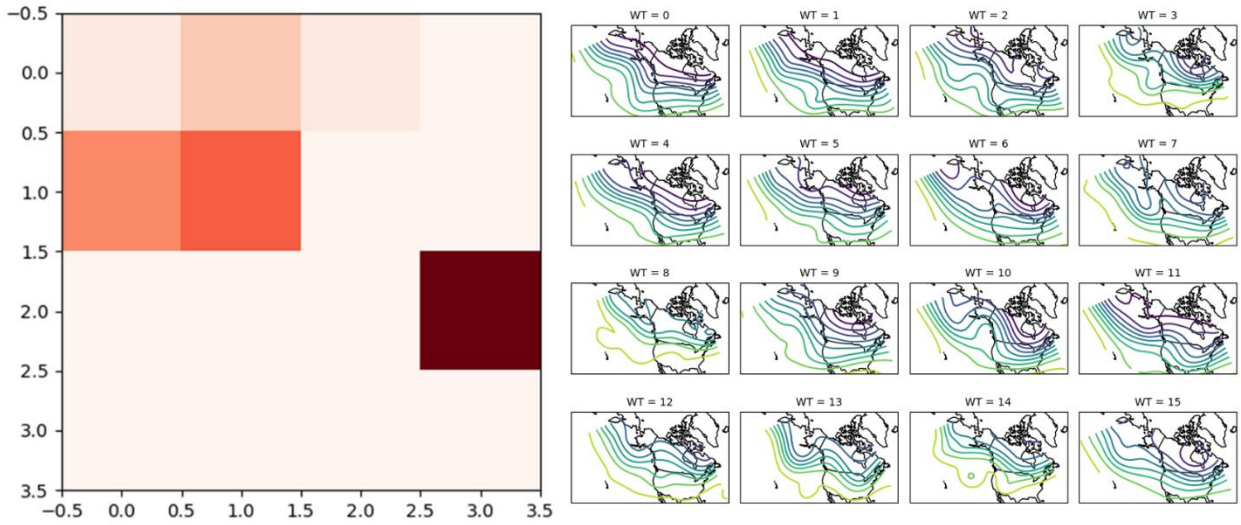

Figure 11. Grid of weather types found during the winter seasons from 2010-2020 and the most common types on anomalous days.

To further investigate the conditions of the troposphere that are required for lee waves to form such as the stability of the air being forced over the mountain range, I analyze the atmospheric soundings at GPS station P577 on the windward side of the San Bernardino Mountains (loc: 34.30461, -117.31892) using Skew-T diagrams. Skew-T diagrams, also known as Skew-T log-P, are a way to visualize such soundings above a particular location. Figure 12b

shows the Skew-T plot for 22 January at the time of maximum wave amplitude, plotted using the Skew-T function from MetPy (May et al., 2022) and output from the WRF Model.

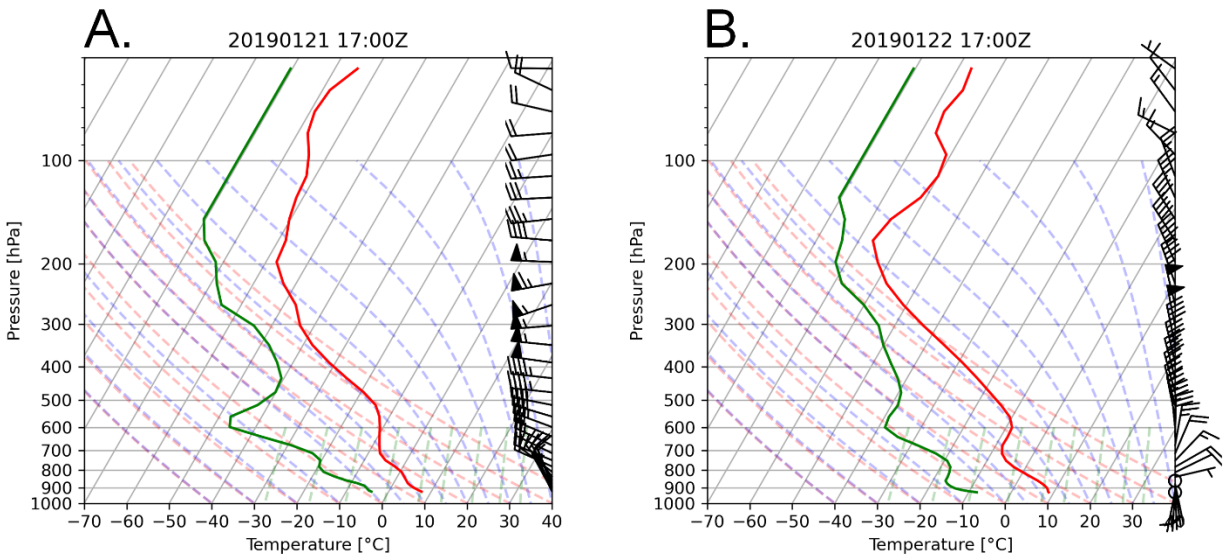

Figure 12. Skew-T plot for 21 (a) and 22 (b) January 2019 at 17:00 UTC at P577 upwind of the San Bernardino Mountains.

The gray diagonal lines are the isotherms, meaning lines of equal temperature. These lines are tilted, or skewed, 45°, hence the name Skew-T. The gray horizontal lines represent the isobars, meaning lines of equal pressure. The pressure axis is logarithmic, hence the name log-P. The dashed red lines represent the dry adiabatic lapse rate or the dry adiabats, meaning the rate of cooling of 10°C/km for a rising unsaturated parcel of air (University of Washington Department of Atmospheric Sciences [ATMS], 2005). The dashed blue lines represent the moist adiabatic lapse rate or the moist adiabats meaning the rate of cooling for a rising saturated parcel of air. This value can vary depending on the moisture content of the air but is approximately 6°C/km (ATMS, 2005; National Weather Service, n.d.b). The dashed green lines represent the saturation mixing ratio lines or the lines of equal mixing ratio, meaning the mass of water vapor

divided by the mass of dry air [g/kg] (National Weather Service, n.d.b). The solid red and green lines represent the actual measured temperature and dew point temperature respectively [°C]. The barbs on the right side of the plot give the wind speed [m s-1] and direction, angled towards the direction of the incident wind.

For this study, I am most interested in the steepness of the temperature compared to the dry adiabats as a measure of atmospheric stability and the magnitude and direction of the wind. Figure 12b shows a stable atmosphere, cross-mountain winds, and an increase in wind speed with height, which are required for the formation of trapped lee waves and accurate simulations of these parameters are the main focus of the atmospheric modeling.

Other assessments of the atmospheric stability are given by the Brunt-Väisälä frequency or the Scorer parameter. The Brunt-Väisälä frequency N, or buoyancy frequency, in meteorology is the frequency at which a parcel of air will oscillate when displaced vertically (American Meteorological Society, 2014) defined as:

$$N \stackrel{\text{def}}{=} \sqrt{\frac{g}{\theta_0}\frac{d\bar{\theta}}{dz}} \tag{1}$$

where g is the acceleration due to gravity, $\bar{\theta}$(z) is the potential temperature, or the temperature a parcel of air would have if it was brought to a standard pressure of 1000 hPa adiabatically, and θ_0 is a constant reference value of the potential temperature at the surface. When $N^2 > 0$, the atmosphere is said to be statically stable, when $N^2 = 0$ it is statically neutral, and in statically unstable air the frequency is undefined (American Meteorological Society, 2014; Zwatz-Meise, n.d.).

The Scorer parameter l^2(z) (Eq. 2), originally derived in Scorer (1949), is used to describe how air currents flow over mountains and the resulting type of lee wave that will form.

If the parameter increases with an increase in altitude, gravity waves are not thought to develop at all. If the parameter is approximately constant with increasing altitude, the vertically propagating wave type is generated. For the case of trapped lee wave formation which I am interested in, it is necessary that l^2(z) decreases with increasing altitude (Scorer, 1949; Zang et al., 2007). l^2(z) is given by:

$$l^2(z) = \frac{N^2}{U^2} - \frac{\left(\frac{\partial^2 U}{\partial z^2}\right)}{U} \tag{2}$$

where U = U(z) > 0 is the vertical profile of the horizontal wind, and N = N(z) is the Brunt-Väisälä frequency and is allowed to be negative. In a simple 2-layer model, there are two main conditions for lee waves to form (Scorer, 1949; Durran, 2013). The first condition is that the Scorer parameter decreases from the lower layer below a critical value κ^2 into the upper layer:

$$l_L^2 > \kappa^2 > l_U^2 \tag{3}$$

where l_L^2 is the Scorer parameter in the lower layer and l_U^2 is the Scorer parameter in the upper layer and κ^2 is the wavenumber of the topography of the mountain range given by:

$$\kappa^2 = \left(\frac{2\pi}{L_x}\right)^2 = \frac{4\pi^2}{L_x^2} \tag{4}$$

where L_x is the horizontal wavelength of the mountain range. While the San Bernardino Mountains are not a perfect sinusoid, for the purpose of this study it is an acceptable approximation which gives L_x as ~16.4 km leading to a κ^2 value of 0.1468. This value is shown in the stability plots in Appendix A also located at P577 by a vertical orange line. The second condition is that the difference of the Scorer parameters between the lower and upper layers exceeds another critical value k^2:

$$l_L^2 - l_U^2 > k^2 \tag{5}$$

where k^2 is given by:

$$k^2 = \frac{\pi^2}{4H^2} \tag{6}$$

where H is the depth of the lower layer. This depth often corresponds with the height above ground level of a mid-tropospheric temperature inversion (e.g. the 700 hPa level in Figure 12b).

4.2 The WRF Model

To simulate the atmosphere above the San Bernardino Valley, I use the Advanced Weather Research & Forecasting (WRF-ARW) Model V4.4 (Skamarock et al., 2021), a numerical weather prediction model developed by the National Center of Atmospheric Research (NCAR) during periods with similar synoptic conditions where we both do and do not see GNSS position outliers. The use of the WRF Model is justified by previous success in modeling similar trapped lee wave events (Eckermann et al., 2006; Feltz et al., 2008; Mahalov et al., 2011; Hills & Durran, 2012; Mateus et al., 2013; Kinoshita et al., 2017; Li & Chen, 2017; Udina et al., 2017; Soufflet et al., 2019; Metz et al., 2020).

I run the WRF Model with one nested domain up to 20 km altitude. Above this point, I use the International Standard Atmosphere (ISA) 1976 (U.S. Government Printing Office, 1962) to save computational resources as this project focuses only on the troposphere. As the name implies, a nested domain is a region located within a larger parent domain. This nesting allows for higher-resolution processing without needing to run the entire parent domain at the same high-resolution to save on time and processing resources (Wang et al., 2021). In my study, this means covering a large region of southern California with a coarser 3 km scale parent domain, to match the input and boundary condition data resolution, and a finer 1 km scale nested domain that encompasses the stations of interest within the San Bernardino Valley.

As input for this model, I use the NOAA High-Resolution Rapid Refresh (HRRR) 3 km model analysis products (Dowell et al., 2022) as the hourly boundary and initial conditions, and I automatically retrieve this data from an Amazon Web Services (AWS) repository (https://registry.opendata.aws/noaa-hrrr-pds/) using a shell script. Within the AWS explorer, I choose the files containing 'f00' which is the 0th hour forecasted time, or the initial analysis product, for that hour. The HRRR is run hourly with forecasts for every hour up to the 18th hour and additionally up to the 36th hour for hours 00, 06, 12, and 18, of which these additional hours are unnecessary for this study.

Here I provide the basic steps to run the locally-compiled WRF Model. More detailed information about running the WRF Model with tutorials for setting up basic model runs and more advanced Case Studies, as well as tools to visualize the output is available online (Wang et al., 2021). Before any model steps are started, first download the input data from an external data source such as the NOAA AWS repository for HRRR data.

The first three steps constitute the WRF Preprocessing System (WPS). Geogrid.exe reads the namelist.wps file to obtain information about the grids for the model domain(s) including size, parent:nest resolution ratio, and map projection, and then maps terrestrial datasets such as soil type and albedo to the grid. Ungrib.exe takes the required meteorological data input, in this case output from the HRRR model in the Gridded Binary Second Edition (GRIB2) format, and repacks it into an intermediate file format more easily readable by subsequent programs with a prefix specified in namelist.wps. Metgrid.exe maps the unpacked GRIB2 data horizontally onto the model domain with the output to then be used as input for the WRF Model. Ungrib and geogrid can be run in either order as these two steps are independent from one another but metgrid must be run after both ungrib and geogrid have completed.

The next two steps are the actual WRF Model. Real.exe reads the namelist.input file for variables such as domain sizes, model start and end times, urban physics (through the variable sf_surface_physics), and planetary boundary layer (PBL) physics (through the variable bl_pbl_physics) and vertically maps the input data onto the model. Finally, wrf.exe generates the forecast using the items produced from the previous steps, running for anywhere from 17-36 hours to complete based on the domain size and model parameters used for a 24-hour forecast. Any changes made to land surface models, temporal values, or input data require real to be re-run while other changes just require wrf to be re-run. However, real executes very quickly so both can be run sequentially without much loss of time. The base namelist.input and namelist.wps settings used for 22 January and 23 April are included in Appendices B and C for parties interested in varying my chosen parameters further.

The largest change I had made in running the model is in varying the urban physics models used. I initially started with the single-layer Urban Canopy Model (UCM), but I opted to try the multi-layer building environment parameterization (BEP) model to account for some nighttime temperature and wind speed discrepancies between the model output and local weather station data. This switch led to a positive or neutral effect on the output depending on the severity of the discrepancy and so all previously UCM and future runs used BEP as a result of this.

In addition to the normal runs with my default parameters for every day pair, 21-22 January and 22-23 April were additionally re-run with varied physics parameters. While the results of this would not impact my overall methods, I wanted to observe how the simulations would differ and if one setup matched surface observations better than the default. These sometimes required changing other parameters such as surface layer physics but as many

parameters were kept to default as possible. These are the two day pairs with the largest anomalies within our time period, though it should be noted that the position estimate for 22 April is not near-zero like 21 January, but still has a sizeable jump in position estimate to 23 April. Late into the study it was discovered that 21 April was never run despite being a good candidate for an atmospherically calm day comparison for 22 April, and it was then run only with the base parameters due to time constraints.

The planetary boundary layer is the lowest layer of the atmosphere where the surface directly influences airflow, and above this point, the atmosphere no longer experiences surface drag and becomes the free atmosphere (Holton & Hakim, 2012). Hu et al. (2010) describes the use of PBL schemes within the WRF Model as a way to "parameterize the unresolved turbulent vertical fluxes of heat, momentum, and constituents such as moisture within the planetary boundary layer and throughout the atmosphere" (p. 1832). The WRF Model can use one of two types of PBL schemes, diagnostic non-local and turbulent kinetic energy (TKE) prediction (Wang et al., 2021). The default PBL scheme (bl_pbl_physics) for the contiguous United States (CONUS) suite I use is the turbulent kinetic energy Mellor-Yamada-Janjic (MYJ) option, however I wanted to see how different planetary boundary layer models might change the development of the lee waves. As I use the BEP urban physics model, I am limited to only compatible schemes which are Yonsei University (YSU), Mellor-Yamada-Janjic (MYJ), Bougeault-Lacarrère (BouLac), and testing revealed the SMS-3DTKE model was compatible with BEP.

MYJ is an eta operational (assumes a step-like mountain) one-dimensional TKE scheme that is useful for severe storm forecasting (Mesinger, 1993; Janjić, 1994; Wang et al., 2021). BouLac is described by the WRF Users Guide as a TKE-prediction option designed for use with

the BEP urban physics model, and the authors claim their method allows for successful predictions of clear-air turbulence from air flow over steep topography (Bougeault & Lacarrere, 1989; Wang et al., 2021). SMS-3DTKE is a new TKE scheme added in V4.2 of the WRF Model that is "self-adaptive" (Wang et al., 2021, p. 7) to the sub-kilometer grid size gray-zone between where large-eddy simulations (LES) and PBL schemes would be used (Figure 13) (Zhang et al., 2018; Wang et al., 2021). As our 1 km model scale is very near to this zone, it might also be a good choice. YSU is a diagnostic non-local scheme that includes an explicit treatment of the entrainment of air that occurs at the top of the PBL (Hong et al., 2006; Wang et al., 2021). This scheme was not used as it fell into a different class of PBL schemes and I wanted a more direct comparison between each varied parameter.

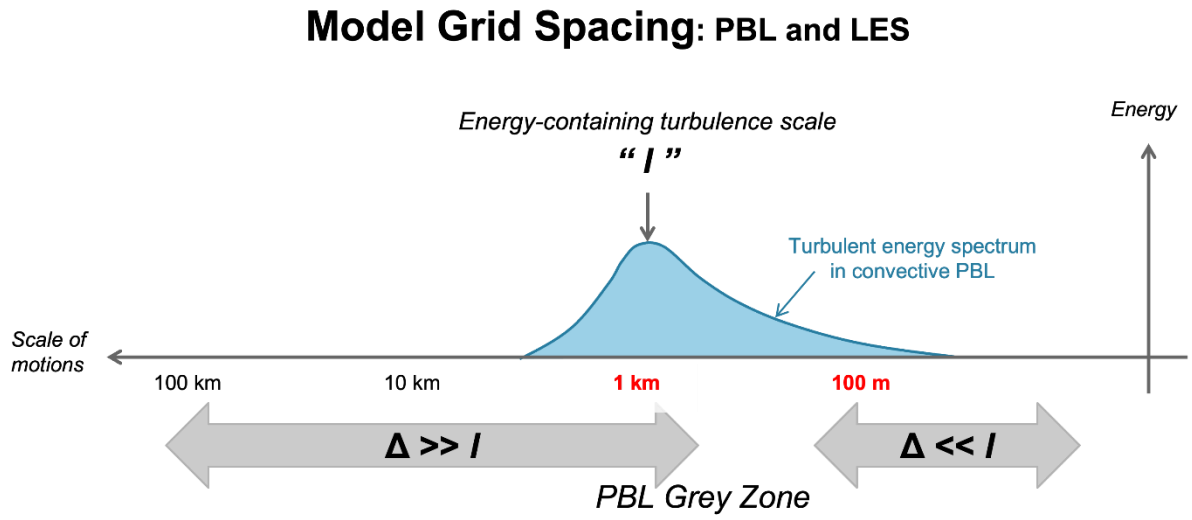

Figure 13. Diagram of the WRF Model grid spacing showing the two regions of resolutions where PBL schemes are used (Δ >> I) and LES schemes are used (Δ << I). Figure from Wang et al. (2021).

In addition to the planetary boundary layer models, I also varied the variable zdamp. Zdamp is the depth in meters from the top of the model over which the specified wave damping method is applied, which in this study is Rayleigh damping by setting the variable damp_opt = 3

(Klemp et al., 2008). This option is default set to 5 km and literature searches showed that most authors indeed keep this value. The model height reaches 20 km, and so I chose a ±1 km difference as this would be 5% of the range in either direction and was deemed sufficient for testing. As future model runs had modified the namelist of my original run, the other settings are left the same as the original MYJ run for these two. Other schemes I wanted to try but could not were MYNN2, UW, Shin-Hong, or the LES PBL settings, as these options were either incompatible with the BEP model or I could not get the model to work due to a mismatch with the dx ~ dz ratio so I stopped after these additional four due to time constraints on model processing.

The domain size was increased to allow for ray tracing to lower elevations for station P612 and traces farther east and west outside of the original domain without rerunning the same model parameters (Figure 14). 22-23 April was the first day pair to use the expanded domain and all of the varied schemes for those days use the expanded domain as well. 21-22 January with the MYJ scheme used both the base and expanded domains as it was run later than the other January runs after I had decided on which additional input parameters to use. I do not compare differences resulting from the change in domain size as the additional processing time was better spent running other days or schemes rather than looking for slight differences in the ray tracing through functionally the same atmosphere.

While I am primarily interested in what the atmosphere is doing on an anomalous day, the adjacent, atmospherically calm day is also of interest as a point of comparison to differences in the atmosphere as it should have changed drastically from the development of the lee wave across a 24-hour period. It is also easy to compare ray tracing data from the adjacent day as the GPS satellites only vary in their position in the sky by 00:03:56.4 (one sidereal day = one mean

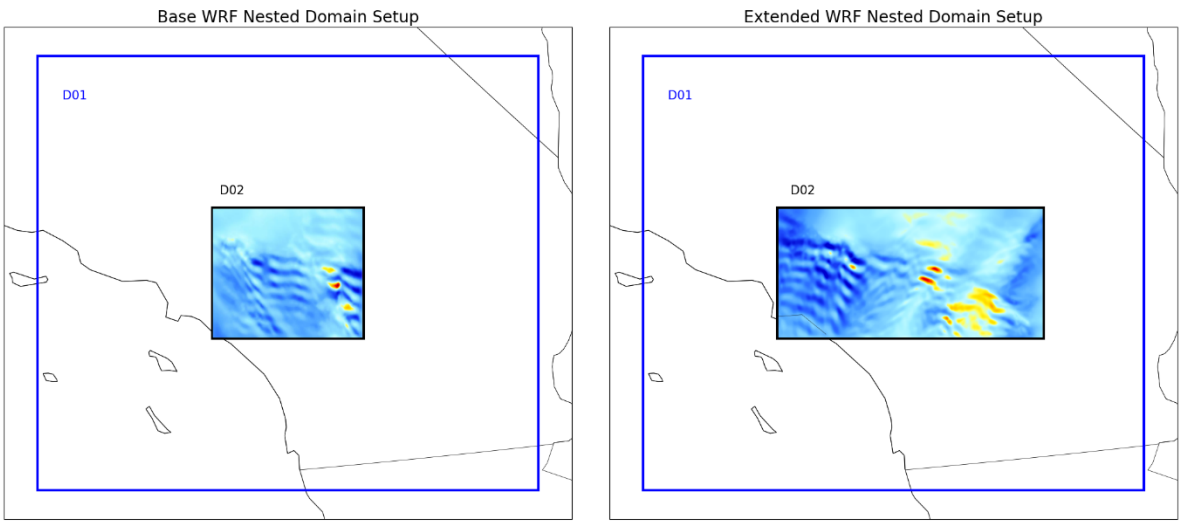

Figure 14. Base (left) and expanded (right) domain sizes used in the WRF Model.

solar day - 00:03:56.4) (Sanz Subirana et al., 2013) and thus sample approximately the same path through the atmosphere and therefore through where the lee wave should be at the same time of day.

I set the restart output timing (through the variable restart_interval) to 1440 for 1440 minutes (exactly 24 hours later) for the first day and the restart flag (through the variable restart) to true for the subsequent day in order to utilize the restart run capabilities of the WRF Model. This allows the next adjacent day of interest I am modeling to start where the prior day's run had ended to avoid needing to reinitialize the model and lose the structure of the atmosphere for the first timesteps of the next day. For example, Figure 15 shows the transition between days with and without restart runs on 22-23 April, which shows the clear need for a restart when the structure at the start of a day could be useful. The model uses UTC time instead of local as it was the most straightforward method to keep track of the HRRR input data. Depending on the date, local time lags UTC by 7 (during Daylight Saving) or 8 hours. This offset became important

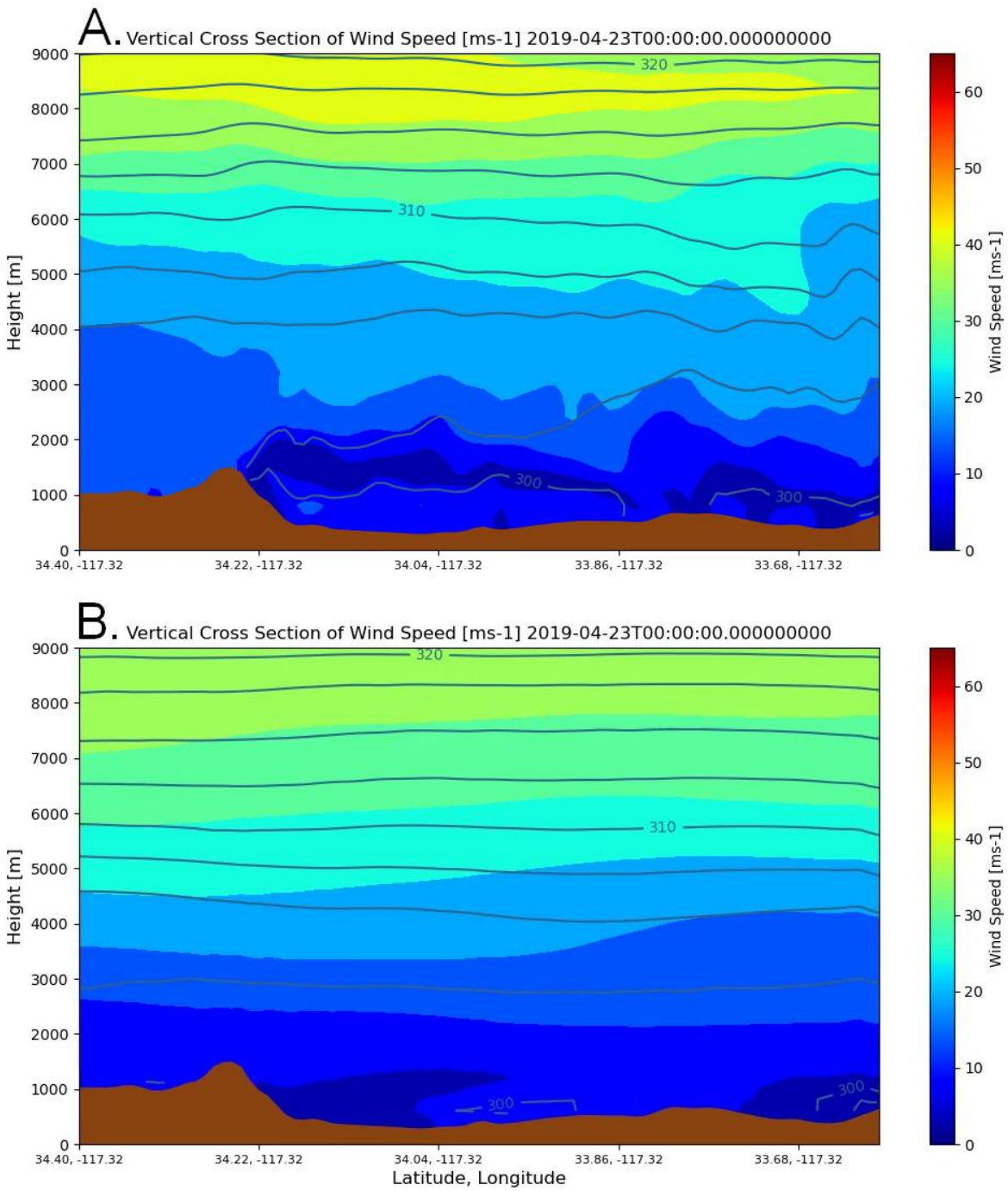

Figure 15. Model run with restart (a) and without restart (b) for 22-23 April 2019.

when compiling weather station data or while looking at when lee waves form due to diurnal heating.

One issue I encountered throughout this project was primarily a combination of the long run time of the model and correctly setting the namelist variables to be compatible with each other. As previously mentioned, the model required between 17 and 36 hours of computing time, less for the normal domain and more for the expanded domain, so models must be run well in advance to get desired output. The metgrid.exe, real.exe, and wrf.exe steps either output errors directly to the console or to a separate log file and show that a setting was incorrect, after which I could change it and rerun real.exe to reinitialize the model and then start wrf.exe where it would then run correctly. While not a persistent problem, maintaining adequate storage space on the computing node drives was something to always keep track of. The HRRR input data used is large at 8-9GB per 24 hour day on average, and output files are smaller but still sizable at ~2.5GB per day for the normal domain and ~5.5GB for the expanded.

With my input parameters, the WRF Model outputs one netCDF file for every two hours of model time for each domain after each run. The first domain is labeled as d01 with two coarse, one hour timesteps, and the second domain is d02 with four finer, 30 minute timesteps. This is based on a combination of the variable history_interval set to 60 and 30 minutes and the variable frames_per_outfile to 2 and 4 for d01 and d02 respectively in namelist.input. The resulting dataframes are four-dimensional, containing values along x, y, z, and time axes, more specifically west-east, south-north, bottom-top, and time.

Initial examination of the WRF output was performed using NASA's Panoply software (Version 5.3.3; Schmunk, 2024) with detailed investigation of the derived values performed using wrf-python (Ladwig, 2017). WRF-python (Ladwig, 2017) is a Python module developed at UCAR/NCAR to handle the reading and processing of wrfout files which I utilized to create vertical cross-section animations to show the progression of the model, as well as to retrieve

certain variables to compare with observations recorded by local weather stations. The primary functions used were getvar and vertcross which allowed extraction and plotting respectively of the variables of interest such as height (“z”), potential temperature (“theta”), or horizontal windspeed in the correct coordinate system (“uvmet_wspd_wdir”) with the initial plotting code utilizing it for my runs modified from the tutorials on the wrf-python documentation by Dr. Szeliga. With this, I produced plots up to 9 km as that is the average height of the 300 hPa pressure level (Nigam & DeWeaver, 2003), though 20 km plots were also made for some days to investigate what occurs up to the top of the non-ISA atmosphere within the model.

Using the vertcross function and wave contours from potential temperature values, I have looked at the following quantities in the model output shown in Table 1: wave duration, amplitude, wavelength, number of stable peaks, and the approximate potential temperature at 6 km.

To analyze a specific layer of a lee wave represented by a potential temperature contour, the Lomb–Scargle periodogram, an “algorithm for detecting and characterizing periodicity in unevenly sampled time-series" (VanderPlas, 2018), can be a useful tool. From the dominant frequency of a Lomb-Scargle periodogram performed on the detrended 312.5K potential temperature contour (Astropy Collaboration et al. 2013, 2018, 2022), the maximum amplitude and wavelength from the reciprocal of the spatial frequency of the wave were calculated. Note that this contour does not necessarily fall at 6 km on every day, however this was the average contour at 6 km across all runs so this is used to greatly simplify processing.

I define a stable peak to be a wave that I am reasonably certain persists for at least two hours (four frames of 30 minute timesteps) with a similar shape across the entire time period. This does not necessarily occur at the same time as the maximum amplitude as a large peak may

Date	Primary varied parameters	GAGE estimate [mm]	UNR estimate [mm]	Wave start (UTC)	Wave end (UTC)	Duration [hours]	Max amplitude time (UTC)	Max amplitude [m]	Max wavelength @ max amplitude time [km]	Max stable peaks	θ contour @ 6 km [K]	Katabatic winds
2018-11-11†		0.86	2.783	11:00	-	13	18:00	142.5	16	2	317.5	Y
2018-11-12†		-6.66	-3.454	-	-	24	18:00	201.5	13.5	2	315	Y
2018-12-25		-2.68	-1.581								310	
2018-12-26		7.63	6.038	0:00	-	24	7:00	45	10	3	310	Y
2018-12-27		0	-2.106	-	6:00	6	3:30	N/A	N/A	1	307.5	Y
2018-12-28		6.71	4.284	17:00	-	7	21:30	102	21.5	5	302.5	Y
2018-12-29		14.28	13.189	-	-	24	14:30	44.5	14	5	310	Y
2018-12-30†		4.47	3.5	-	18:00	18	9:30	123.5	20	3	315	
2018-12-31		-3.48	-5.802	18:30	-	5.5	23:30	172	14	1	312.5	Y
2019-01-01		2.16	1.298	-	-	24	22:30	76.5	14	3	312.5	Y
2019-01-21		-1.88	-1.277								312.5	Y
2019-01-21	BouLac	" "	" "								312.5	Y
2019-01-21	SMS-3DTKE	" "	" "								312.5	Y
2019-01-21	zdamp = 4km	" "	" "								312.5	Y
2019-01-21	zdamp = 6km	" "	" "								312.5	Y
2019-01-22†		13.17	13.915	3:30	-	20.5	17:00	167.5	12.5	7	317.5	Y
2019-01-22†	BouLac	" "	" "	3:30	-	20.5	17:00	273.5	15.5	6	317.5	Y
2019-01-22†	SMS-3DTKE	" "	" "	3:30	-	20.5	17:00	268	12.5	7	317.5	Y
2019-01-22†	zdamp = 4km	" "	" "	3:30	-	20.5	17:00	171.5	12.5	7	317.5	Y
2019-01-22†	zdamp = 6km	" "	" "	3:30	-	20.5	17:00	168.5	12	7	317.5	Y
2019-01-25		-0.91	-1.411	19:00	-	5	23:30	67.5	12	1	315	Y
2019-01-26†		5.02	3.569	-	-	24	14:00	786	11.5	3	320	Y
2019-02-18		-0.26	-0.514								307.5	
2019-02-19		7.29	7.327	4:30	22:00	17.5	8:00	74.5	19	3	305	
2019-02-20		-0.77	1.054								307.5	
2019-02-21		-1.85	-0.22								295	
2019-02-22		11.53	14.025	3:30	-	18.5	12:00	N/A	N/A	2	310	Y
2019-03-11		1.26	0								305	Y
2019-03-12		4.77	5.502	14:30	21:30	7	17:00	185	15	2	307.5	
2019-04-11		2.06	5.375	4:00	16:00	12	11:00	N/A	N/A	2	310	Y
2019-04-12		11.55	11.423	7:30	23:00	15.5	17:00	150	12.5	2	317.5	
2019-04-16		-0.66	0.266								312.5	
2019-04-17		5.44	6.007	8:30	-	15.5	17:00	118	12	3	317.5	
2019-04-21		-0.51	-2.711								315	

2019-04-22		6.38	4.465	5:30	21:30	16	14:30	312.5	11	3	310	Y
2019-04-22	BouLac	“ “	“ “	5:00	23:00	18	14:30	313	12	3	310	Y
2019-04-22	SMS-3DTKE	“ “	“ “	5:00	22:00	17	14:30	315.5	10	4	310	Y
2019-04-22	zdamp = 4km	“ “	“ “	5:30	20:30	15	14:30	307	11	3	310	Y
2019-04-22	zdamp = 6km	“ “	“ “	5:30	20:30	15	14:00	315.5	10.5	3	310	Y
2019-04-23		18.51	16.596	6:00	-	18	14:00	158.8	14	2	315	
2019-04-23	BouLac	“ “	“ “	6:30	23:00	16.5	17:00	175	15	2	315	
2019-04-23	SMS-3DTKE	“ “	“ “	6:30	23:00	16.5	14:00	83	13	2	315	
2019-04-23	zdamp = 4km	“ “	“ “	6:00	-	18	14:00	152	14	2	315	
2019-04-23	zdamp = 6km	“ “	“ “	6:00	-	18	14:00	153.5	14	2	315	

Table 1. Results from analysis of vertcross windspeed/potential temperature contour animations. Dashes for times indicate the wave continued into the next day. Amplitudes and wavelengths are rounded to the nearest half-kilometer. † = Lomb-Scargle fitting of dominant amplitude and wavelength.

evolve into a longer train of smaller amplitude. I also check if any katabatic winds (i.e. Santa Ana winds) are present on the lee side of the San Bernardino Mountains based on the wind speed gradient near the surface.

While it is used mainly for storm prediction, the 0-6 km or surface to 6 km bulk shear is one measure of wind shear used by meteorologists which may be useful for these anomalous days with the fast north-south-directed jet stream (National Weather Service, 2015), and 6 km is generally located above or at the top of the trapped lee waves at the 500 hPa level. The start of the wave is the frame of the animation when the wave begins to collapse into the main wave, and the end is the last time it was visible using a similar designation to Figure 9a in Li & Chen (2017).

4.3 Ray Tracing

4.3.1 Index of Refraction of the Atmosphere

As the GPS signals will be traveling through a non-vacuum, the waves will interact with the atmosphere. This interaction as the waves travel through the atmosphere is governed by Snell's law of refraction:

$$n_1 * \sin\theta_1 = n_2 * \sin\theta_2 \tag{7}$$

where θ_1 and θ_2 are the incident and transmitting angles across the medium boundary [°] and n_1 and n_2 are the indices of refraction (or refractive indices) defined as the ratio of the speed of light in a vacuum to the speed of light in a given medium such as Earth's atmosphere (Hecht, 2017):

$$n \stackrel{\text{def}}{=} \frac{c}{v} \tag{8}$$

where c is the speed of light in a vacuum.

The index of refraction within the troposphere has a value > 1. This indicates how much a light wave, in our case, radio waves transmitted at L1 = 1575.42 MHz and L2 = 1227.6 MHz (see Figure 7), bends (refracts) which leads to the curvature of the signal path. An example path a light ray might take is shown in Figure 16 where the GPS signal takes a curved path. As observed here, the signal bends away from the normal as it travels through the different layers and the medium becomes less optically dense (Hecht, 2017).

Refractivity (N) is used instead of the index of refraction (n) as values for air in realistic conditions are on the order of 10^{-4} (Hecht, 2017; Kinoshita et al., 2017) and differences between the values can be two orders of magnitude smaller (10^{-6}) that comparisons of two indices would be difficult.

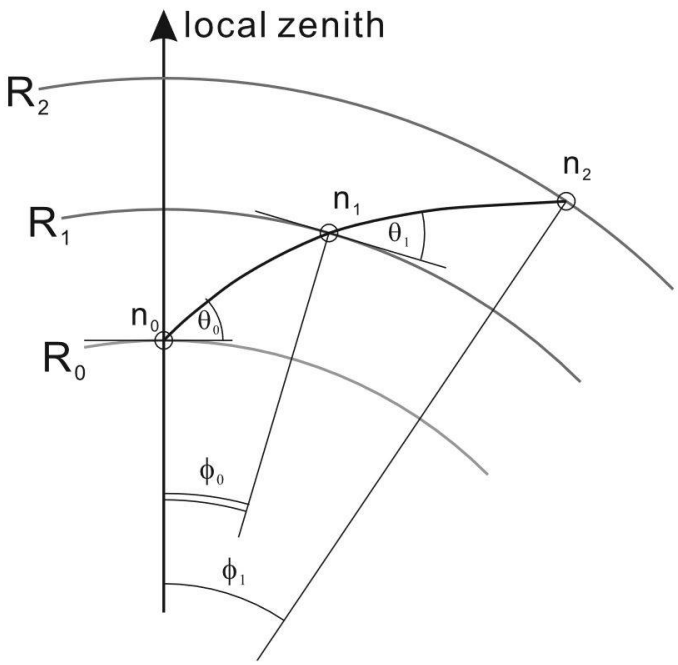

Figure 16. Curved ray path using the Thayer approach. Figure from Hobiger et al. (2008).

An equation for the refractivity of a given layer of air is given by Equation 1 in Thayer (1974):

$$(\mathrm{n}-1)*10^6 = \mathrm{N} = 77.6\left(\frac{\mathrm{P_a}}{\mathrm{T}}\mathrm{Z_a^{-1}}\right) + 64.8\left(\frac{\mathrm{e}}{\mathrm{T}}\right)\mathrm{Z_w^{-1}} + 3.776*10^5\left(\frac{\mathrm{e}}{\mathrm{T^2}}\right)*\mathrm{Z_w^{-1}} \quad (9)$$

where n = index of refraction, N = refractivity, P_a = partial pressure of dry air [hPa], T = absolute temperature [K], e = partial pressure of water vapor [hPa], and Z_a^{-1} and Z_w^{-1} are the inverse compressibility factors for dry air and water vapor given by

$$Z_a^{-1} = 1 + P_a * \left[57.90*10^{-8}*\left(1+\frac{0.52}{T}\right) - 9.4611*10^{-4}*\frac{T_c}{T^2}\right] \quad (10)$$

$$Z_w^{-1} = 1 + 1650*\frac{e}{T^3}*(1 - 0.01317*T_c + 1.75*10^{-4}*T_c^2 + 1.44*10^{-6}*T_c^3) \quad (11)$$

where T_c = absolute temperature in degrees Celsius. At T = 273.15K, P_a = 989 hPa, and e = 23 hPa, the hydrostatic, or dry component constitutes approximately 70% of the value and the non-hydrostatic, or wet component is the remaining 30%. While a minority component, the non-hydrostatic component is the most variable.

4.3.2 Satellite Selection Criteria

Using the WRF output, I ray trace radio signals to several satellites through the simulated atmospheres on adjacent days with similar GPS constellation positions that do and do not show the position outliers in Figure 9 to see how the ray paths from a receiver to different satellites each sample the lee wave. I use the Kashima Ray-tracing Tools (KARAT) software package from Hobiger et al. (2008) for ray tracing and SP3 Ephemeris files from NASA's Archive of Space Geodesy Data for the estimation of GPS satellite positions (https://cddis.nasa.gov/Data_and_Derived_Products/GNSS/orbit_products.html). The index of

refraction for each atmospheric layer along the ray path is calculated from the refractivity equation given in Thayer (1974).

I set the program to trace to all possible satellites, however there are a few required conditions to ensure the tracing is meaningful. The first condition I check for is time. Not all satellites are visible to the station, and therefore the ray tracer, after the lee wave has developed. Note, some chosen satellites have a break between subsequent traces as the satellite's orbit briefly dips below the horizon relative to the station. I chose satellites based on whether they were visible during the time of maximum lee wave amplitude. As I will discuss below, I attempted to choose satellites with the most observations that were centered within at least 2 hours on either side around the maximum lee wave amplitude time, if possible, to see how it changes before and after the maximum, but sometimes this was at the end of the UTC day, and I was limited in the options I had. For example, 30-31 December only had two satellites that met all of my criteria at end of the day so I had to use both of those.

The second condition to ensure a meaningful trace is the azimuth at a given time. Not all traced paths are directed south of the station and mountain range through the lee wave within a <124° cone centered around due south. The ray tracing cone was set to <124° (non-inclusive) to ensure that the ray path does not pass through the lee waves perpendicular to the direction of airflow and reasonably crosses the peaks and troughs of the wave, and as seen in Figure 17, the traces should still meaningfully pass

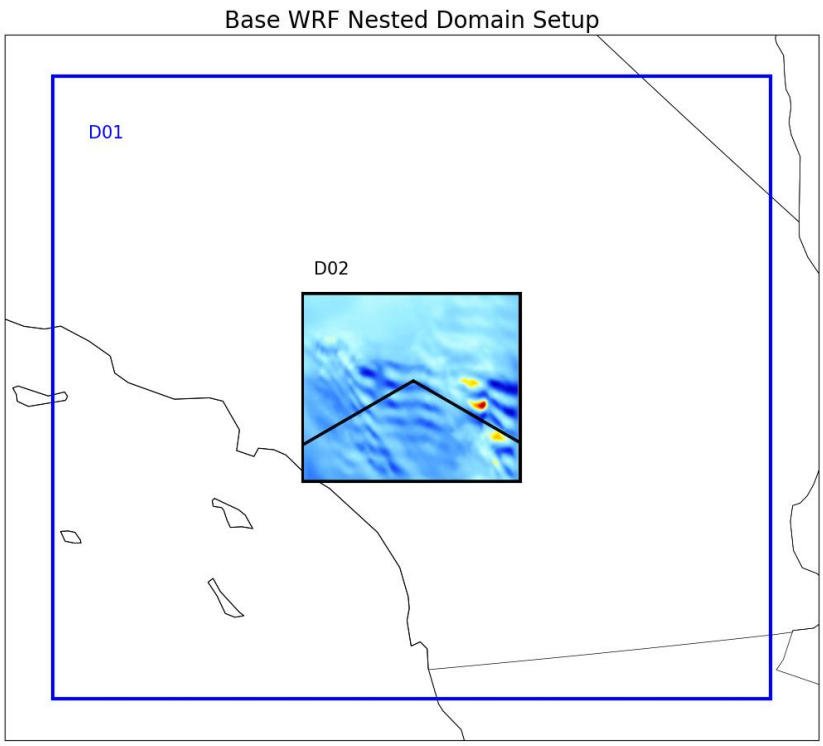

Figure 17. Approximate ray tracing cone (black lines) overlain on the base domain.

through the waves at these angles. I used the same cone for all days regardless of the domain size, and while the waves themselves should not necessarily be wider on days that use the expanded domain, this wider cone should help to see more of the waves if they are present towards the sides of the domain.

The third condition I checked to ensure a meaningful trace is calculated delay. As this is the main output from the program, rays laterally exiting the WRF domain below the top of the model resulted in a calculated delay of 0 m and were excluded. These rays are also flagged as incomplete by KARAT in the output file, so for redundancy I checked for both as it did not drastically impact computation time.

The last condition I checked was the number of usable data points. While many of the satellites may meet all of the above criteria, I only used satellites which produced a ray tracing

file within the specified time window containing at least 20 observations. This allowed me to see the progression of the satellite as it crossed the sky and was traced through different sections of the wave at different elevation angles and azimuths and I could better see if a large delay was the result of interaction with the lee wave or an overall longer path through an atmosphere.

One condition I did not explicitly filter for was the elevation angle of the trace. Some satellites traced down to the lowest possible angles and others traced closer to the zenith and I wanted a mix of angles to sample more sections of the lee waves as a lower angle would theoretically travel through more of the lee wave compared to a higher angle which might only go through the largest peak closest to the San Bernardino Mountains.

This selection results in only a few satellites that meet all of these conditions that are useful for comparing traced refractivity and delay values. Of the available satellites, the two with the largest number of observations with at least 20 observations at the time of selection before any adjustments were made were chosen, though many ended up containing significantly more. If the maximum amplitude time is within two observations of the start or end of the potential output ray tracing file, that satellite was excluded in case I needed to temporally shift the observations to account for differences in the sidereal day and would end up missing this time in the delay calculation.

4.3.3 Ray Tracing Output

To compare the delays of the day pairs, I take the ray traced files for each of the acceptable satellites for the anomalous day and subtract away the traced delay from the ray traced files of the previous, non-anomalous day, adjusted for the sidereal offset of the GPS constellation, around the time of maximum amplitude. To better match the evolution of the lee

waves between days, I chose to adjust the output by time and not elevation angle, final elevation, or azimuth. I had to choose one since they will not necessarily all align and settled on time as I care more about the structure of the lee wave and not necessarily what part it goes through, especially since the comparison should be to a non-anomalous day with a calm atmosphere. Values are shifted in increments of 0.08 hours (00:04:48) as that is the smallest unit of time in the ray tracer output and is as close to the difference in sidereal days as I could reasonably get. Files were either not shifted at all or by one observation, however some required two or very rarely three shifts to align the two days. For 21-22 January and 22-23 April, each scheme uses the time for the MYJ run (17:00 and 14:00 UTC respectively) for all of the ray tracing analyses.

Originally only day pairs consisting of a non-anomalous to an anomalous day (e.g. 21-22 January) were chosen as I wanted to be consistent and also to reduce the number of days to process. However, since I eventually ran all of the modeled days through the ray tracer on the chance I would investigate something like this, I decided it would be interesting to investigate if I would see negative delay differences from anomalous to non-anomalous days (e.g. 26-27 December). Perhaps future work could redo this with the following boundary day as another similar comparison to fully capture the anomalies such as 24-23 April or 23-22 February.

The KARAT software has an option to trace using the normal Thayer approach with the full atmosphere which I used for every modeled day, and a “Thayersymm” approach which follows the same methods as the normal version but assumes an azimuthally-symmetric atmosphere by using the refractivity values directly above the station to the top of the model at the specified coordinates. This symmetric version was not used as it is not a realistic representation of what the ray paths would travel through and may not even encounter a lee wave

if it is not directly overhead, however it is an interesting thought experiment that may have uses in other studies.

CHAPTER V

RESULTS

5.1 Validation of the WRF Model

Having successfully recreated the trapped lee wave events with the WRF Model, I validate my output with comparisons to observations of select relevant parameters from three ground-based meteorological stations within my model domain (APRSWXNET, 2023). Station F0494 is located on the CSU San Bernardino campus (loc: 34.18383, -117.32200), AU239 is located in Rialto, CA (loc: 34.08017, -117.37967), and F1895 is located in Apple Valley Narrows, CA (loc: 34.53300, -117.28000). These are shown in relation to P612 in Figure 18.

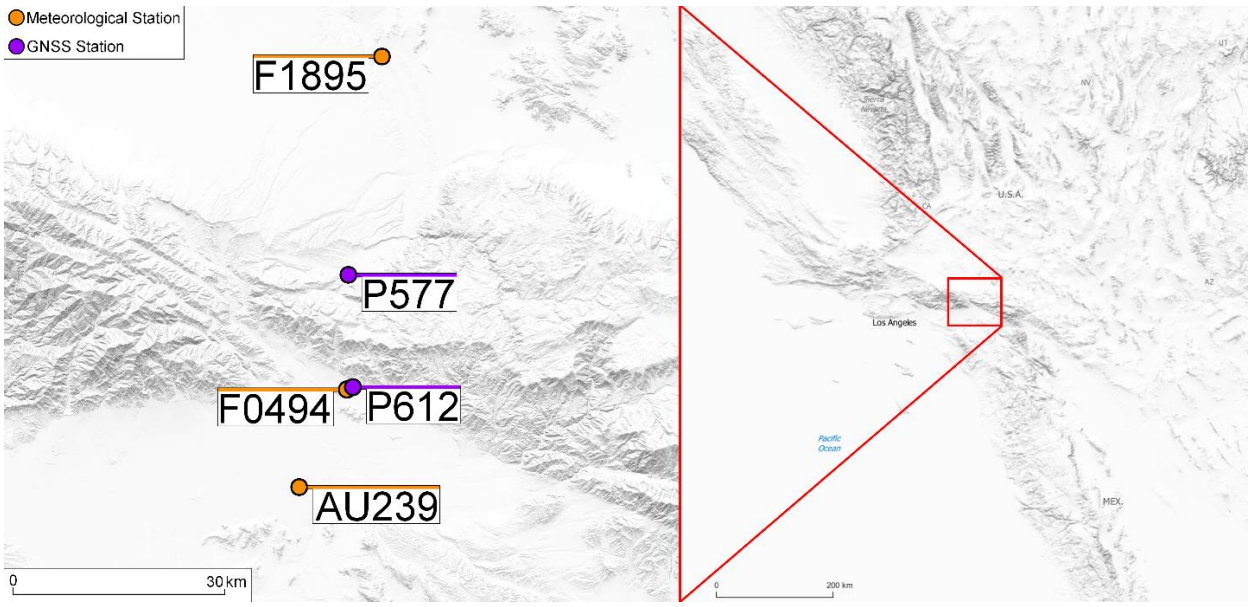

Figure 18. Shaded relief map showing the GNSS and local weather stations in relation to the San Bernardino Mountains and southern California. Modified from U.S. Geological Survey (2021).

Here I consider the changes in wind speed and maximum wind gusts [m s-1], temperature [K], and sea level pressure (SLP) [hPa] as measured by the weather stations to the most similar WRF diagnostics available through the getvar() function in the wrf-python package. These

diagnostics are 10m Wind Speeds [m s-1], 2m Temperature [K], and Sea Level Pressure [hPa] at the closest grid point to the station coordinates within the output of the WRF Model. While a similar 10m or lower pressure may have been available in the WRF output, the meteorological stations provide sea level pressure observations directly, so this was used for ease of comparison. For the two pairs of 21-22 January and 22-23 April, I also compare wind speed, 2m temp, and SLP of the different schemes compared to the 'truth' of the MYJ run versus the observed data. The comparison for 21-22 January is shown below in Figures 19 (F0494), 20 (AU239), and 21 (F1895). Timesteps for station F0494 were 10 minutes starting on 11 April and 15 minutes for all previous days through 12 March which indicates a switch to higher-resolution data sometime between the two dates. AU239 was the least consistent, with steps generally being 5 minutes but occasionally 10 or 15 minutes. F1895 always has approximately 15 minute steps, though the actual steps may be ±1-3 minutes. All other plots of these are included in Appendix D.

I used a simple 1-5 scale to visually assess the quality of model output based on how closely it matches the actual station value as well as the shape of the particular curve, where 5 is the closest possible match such as the SLP on 18-22 February at AU239, 3 is an average fit with something missing, usually either following the curve but with different values or similar values but not always matching the curve, and 1 is the worst possible match such as SLP on 22-23 April at F1895 where the shape and values are both incorrect. The model at AU239 was the best fitting, followed distantly by F0494 and F1895 in that order which were roughly equal. For 21-22 January and 22-23 April only the MYJ run was considered as the other schemes will be discussed later.

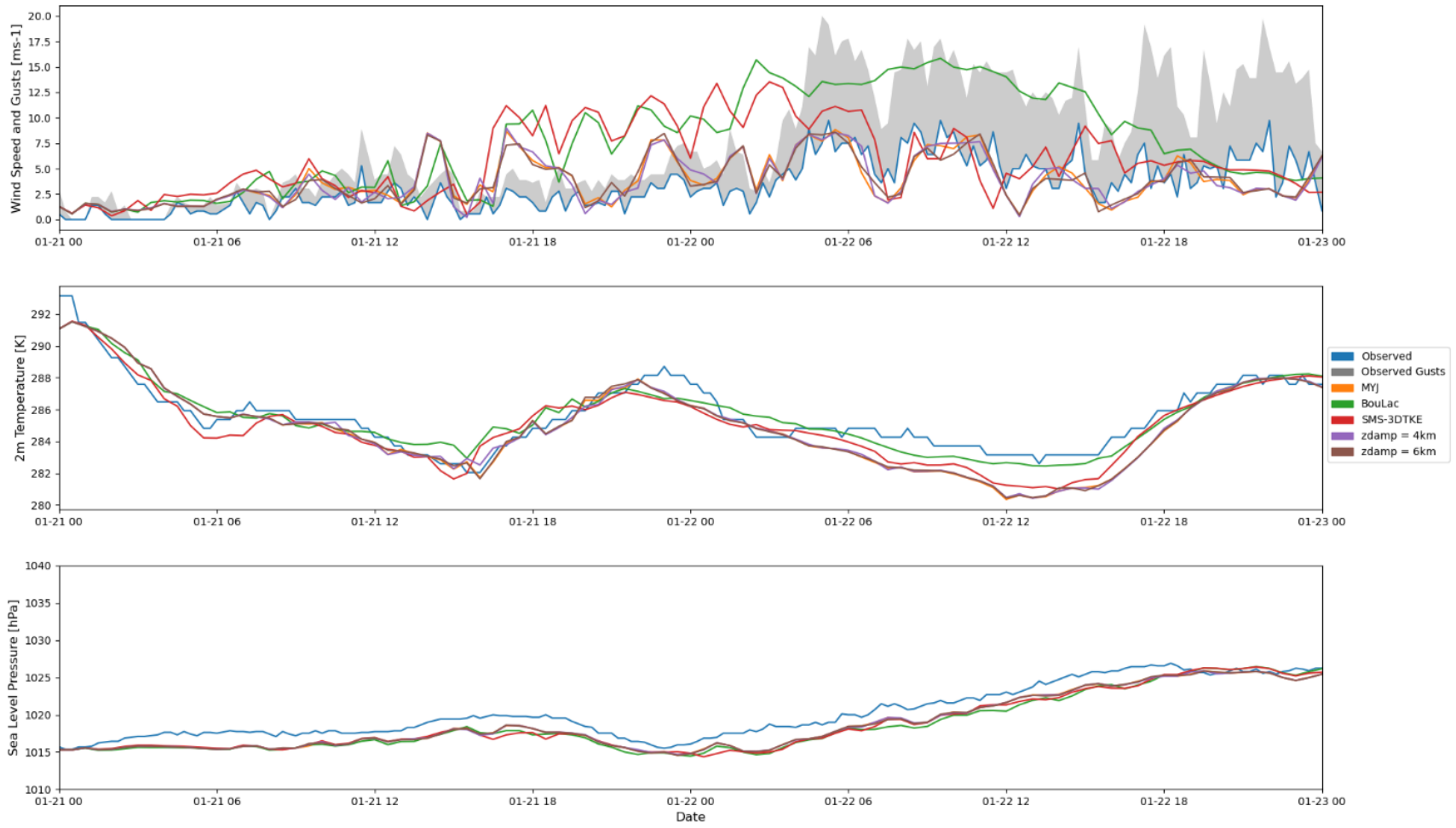

Figure 19. WRF Model comparisons to weather station F0494 on 21-22 January 2019. Winds from WRF output are 10m Wind Speed.

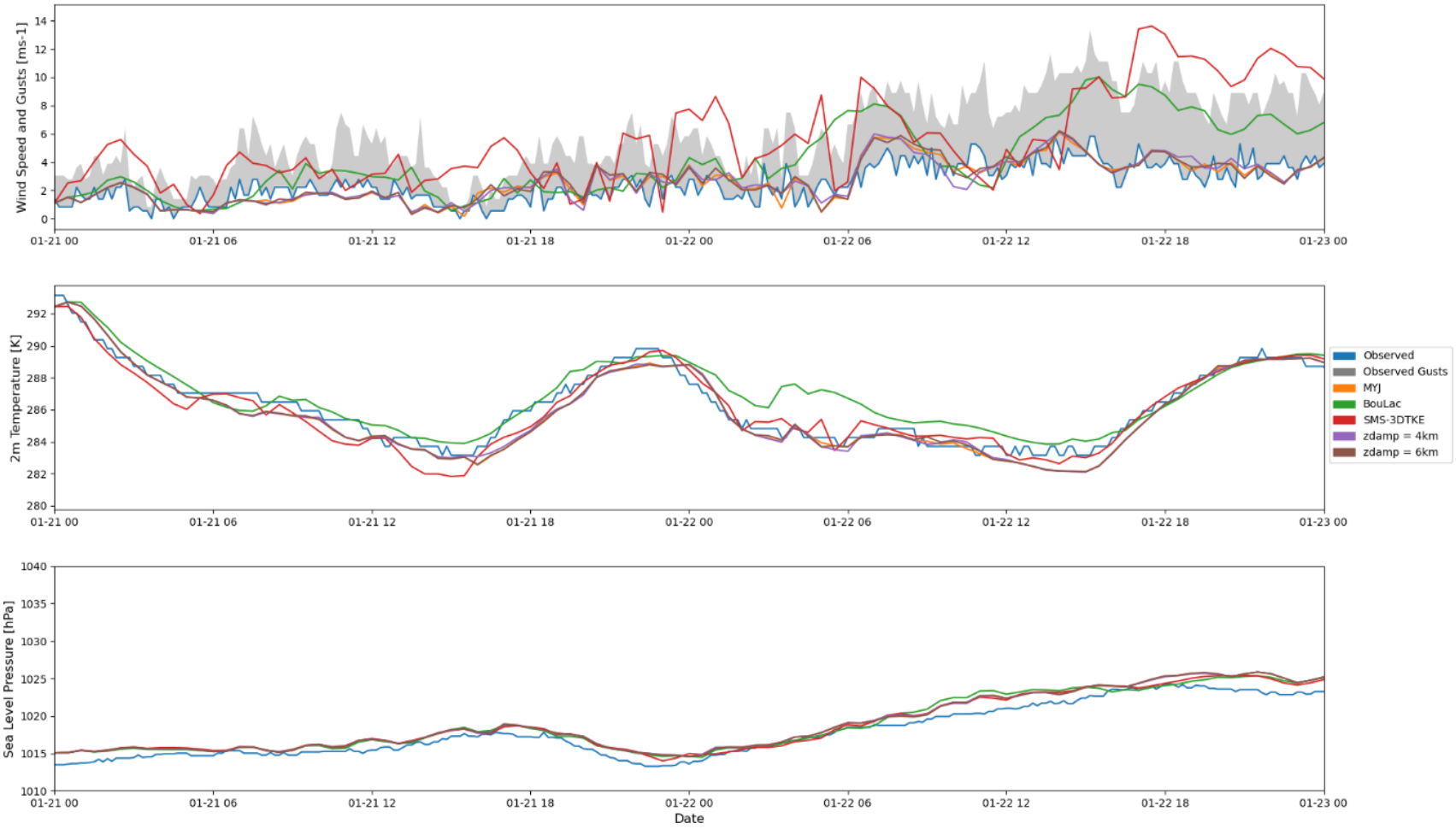

Figure 20. WRF Model comparisons to weather station AU239 on 21-22 January 2019. Winds from WRF output are 10m Wind Speed.

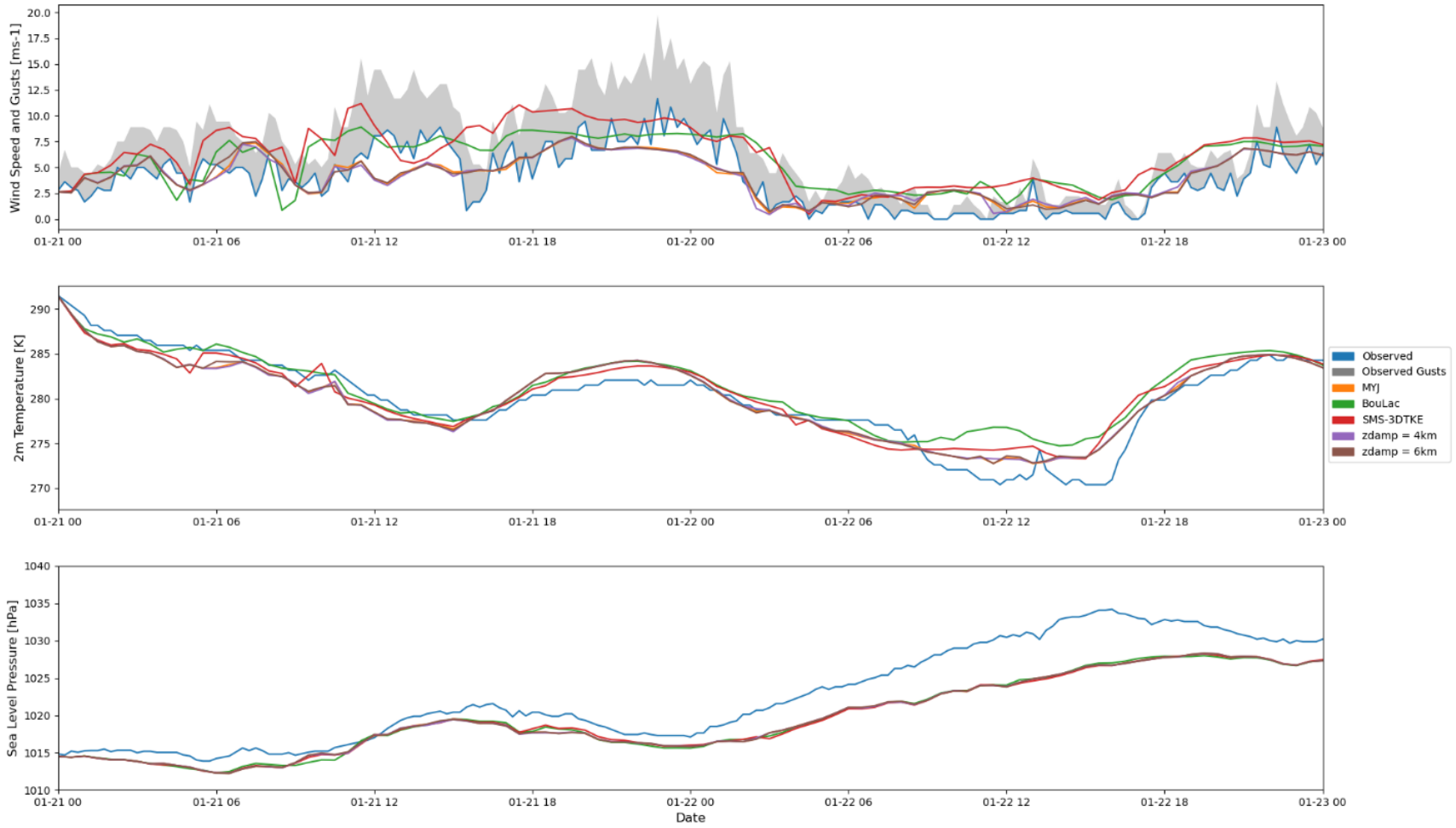

Figure 21. WRF Model comparisons to weather station F1895 on 21-22 January 2019. Winds from WRF output are 10m Wind Speed.

Across all days and stations, 2m Temperature fit the best followed by SLP and then 10m Wind Speed. 25-26 January was the worst matching day pair by a considerable amount while 18-22 February was the best followed by 25 December - 1 January. It should be noted that these latter two time periods do have the benefit of more than two days so any inaccuracies on a particular day are averaged out compared to other day pairs.

At F0494, the model wind speed matches the worst of the three stations, overestimating it or not matching the shape of the curve on multiple days such as 21 January (Figure 19, orange line) or 16-17 April (Figure D7). There is a slight underestimation of 2m Temperature, but still many points where the curves match or are very close, and the model underestimated the SLP on almost every day. At AU239, wind speed fit the best however the score was lowered by severe overestimations for short durations, usually during an increase of the wind speed. If it does not match, it tends to overestimate 2m Temperature more than it underestimates it but still the best of the three stations. The model also has a very good match to SLP, usually slightly overestimating it. At F1895, model wind speed was the middle of the three locations with a mix of good and bad fits. The model usually appeared to match the shape of the 2m Temperature and SLP but not always match the magnitude from over and underestimations respectively, though still matched the 2m Temperature station values at certain times such as 11-12 November (Figure D19) or 25 December - 1 January (Figure D20). The model appears to be more smoothed as it does not record as strongly the highs or lows of either diagnostic, even when accounting for the difference in timestep between the model and station (30 versus 15 minutes).

5.2 Vertcross Animation Analysis

Table 1 shows the results from visual analysis of the wave characteristics from the vertcross animations such as Figure 22.

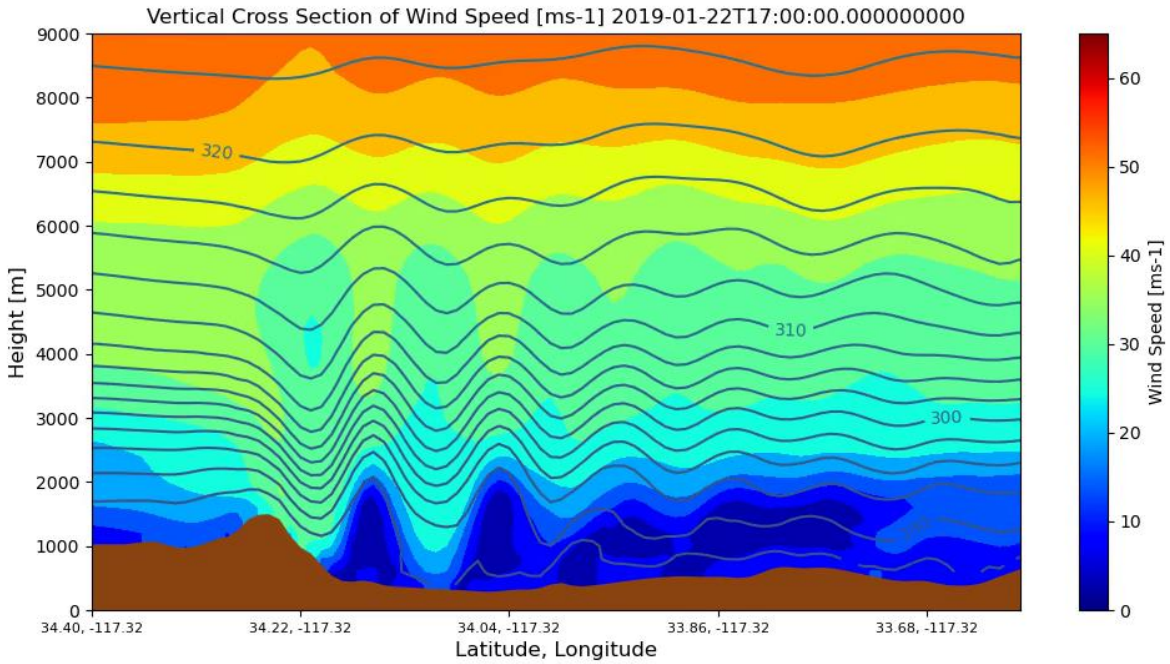

Figure 22. Vertcross animation for 22 January 2019 at 17:00 UTC.

The wave start times tended to be early in the UTC day, corresponding to late local time of 7-8 hours behind depending on exact date and often after sunset, and the end times tended to be late in the UTC day or continued into the next day. While lee waves on several days persisted into the next day, taking just the modeled days into account, the average duration was just under 20 hours, the median was 18 hours, the longest was 49 hours long from 28-30 December, and the shortest is a mere 7 hours on 12 March.

As previously defined, potential temperature is the temperature a parcel of air would have if it was adiabatically, meaning without gain or loss of heat, brought to a standard pressure of 1000 hPa. In other terms, potential temperature is a conserved value under adiabatic conditions such as the synoptic conditions observed during the days of position anomalies (Holton &

Hakim, 2012). Air parcels under these conditions tend to "move toward a region with the same density" along surfaces of constant potential temperature (National Weather Service, n.d.a, p. 1), and therefore the potential temperature contours represent the actual airflow within the model. The average potential temperature contour at 6 km was 312.35K but ranged from as low as 295K to as high as 320K as shown in Table 1. Although this temperature should vary seasonally, there does not immediately appear to be a correlation between the day of year and the temperature of the 6 km contour, however this is a very small sample size for this kind of analysis and I am additionally missing points for many non-anomalous days in mid-January, early February, late March, and early April. As the average is close to the 312.5K contour which is usually plotted for each day with exceptions for particularly cold days, the 312.5K contour is used for wavelength and amplitude analysis.

For a majority of the runs, the Lomb-Scargle fitting unfortunately did not capture the finer structure of the contour. In these cases, the wavelength (spatial frequency) was below the minimum threshold and set to 0.01 / km, the wavelength appeared reasonable but did not match the actual contour, or the amplitude was incorrect as a result of these. I then manually estimated the amplitude and wavelength of the dominant peak directly above P612 from the 312.5K contour. The days that are not manually estimated are marked by a dagger in Table 1. If neither the amplitude nor wavelength could be reasonably estimated due to waves showing constructive interference or the contour was significantly higher than the wave and did not show the dominant peak, it is replaced by N/A. 22 January is the best example of a well-fit sine wave (Figure 23a), matching both the expected amplitude and wavelength very well, while 19 February is a very poor-fitting day (Figure 23b).

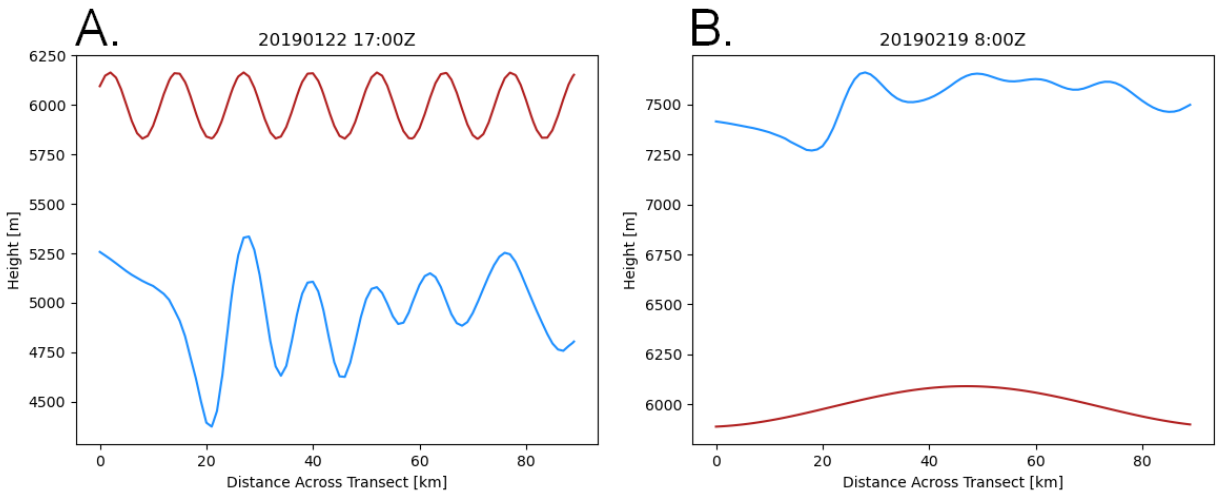

Figure 23. Modeled 312.5K contour (blue) and sine wave output from the Lomb-Scargle periodogram performed on the detrended 312.5K contour (red) for 22 January (a) and 19 February (b) 2019.

The average number of stable peaks based on my criteria was approximately 3. Longer trains could potentially have continued outside of the domain but are not visible in the animations as it reached the end of the domain. The stable peak count was generally low as the waves became perturbed and dissipated farther downwind as distance from the wave-generating mountaintop increased. The most common number of peaks on unique days (as varied schemes tended to have the same number of peaks) were 2 and 3 peaks with 7 occurrences, followed by 1, 5, and 7 peaks with 3, 2, and 1 occurrences respectively, while 4 or 6 peak trains were not present.

Comparing each of the measured values to both GAGE and UNR position estimates for unique days, there is a weakly ($0 < R^2 < 0.3$) positive linear correlation between both number of stable peaks and duration and the position estimate while there is found to be no correlation between amplitude or wavelength and the position estimate as shown in Figures 24-27. This is true even after removing the outlier in Figure 26 which corresponds to 26 January. The last column of Table 1 lists that katabatic winds were found to be present on both anomalous and

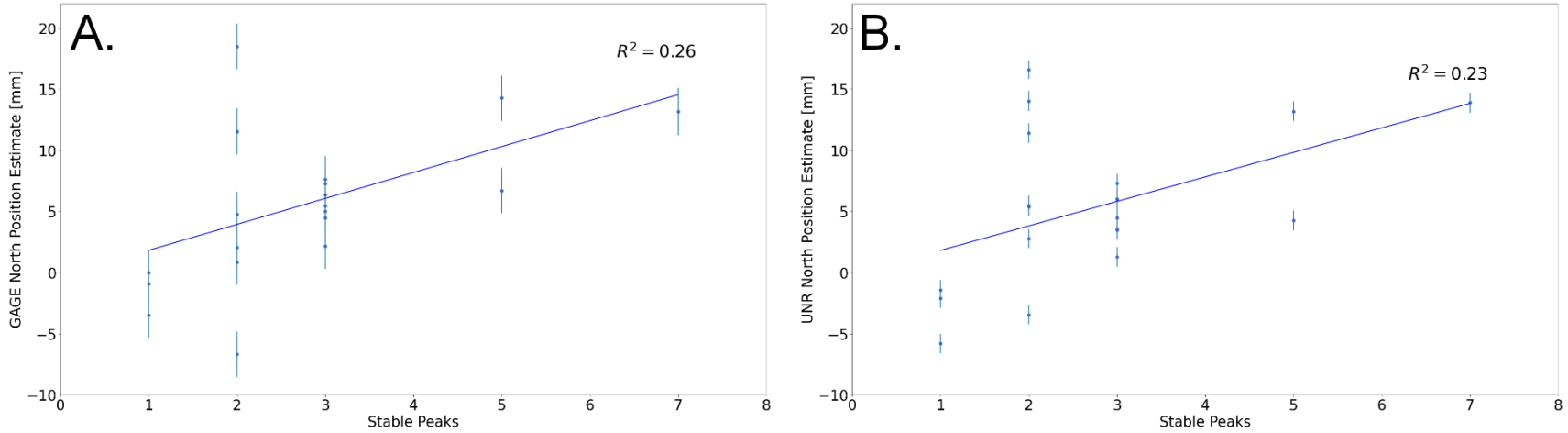

Figure 24. GAGE (a) and UNR (b) north position estimate versus number of stable peaks from vertcross analysis.

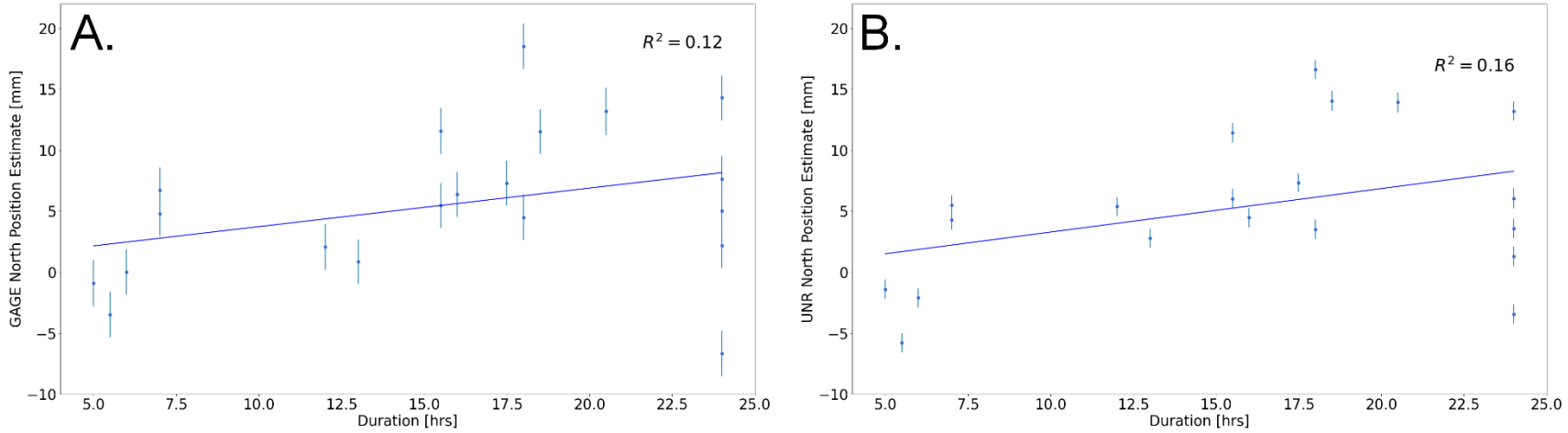

Figure 25. GAGE (a) and UNR (b) north position estimate versus duration of the wave from vertcross analysis.

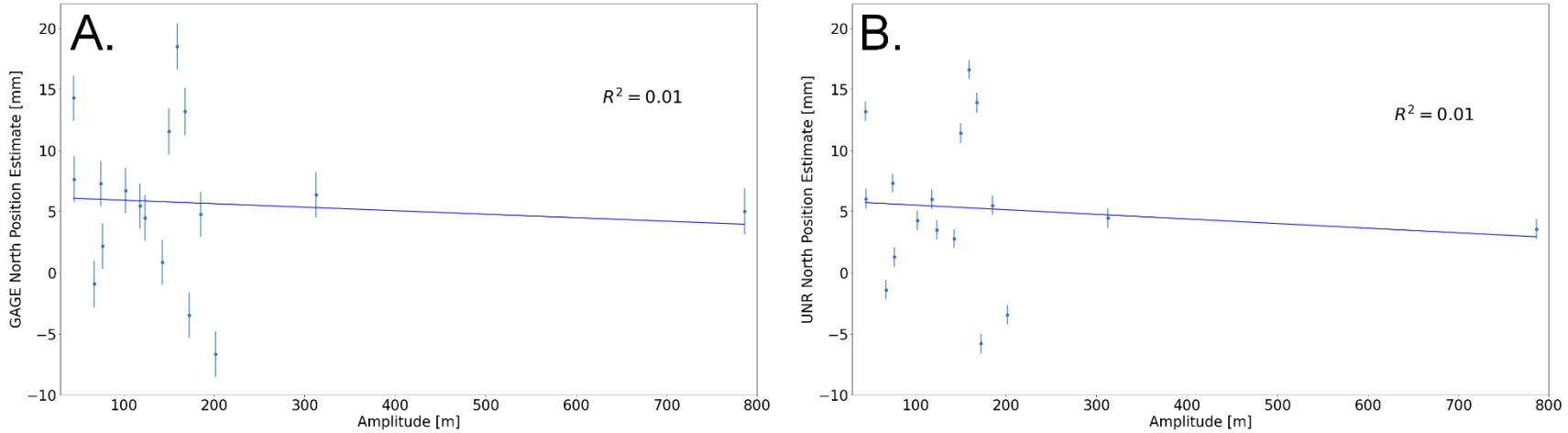

Figure 26. GAGE (a) and UNR (b) north position estimate versus maximum amplitude from vertcross analysis.

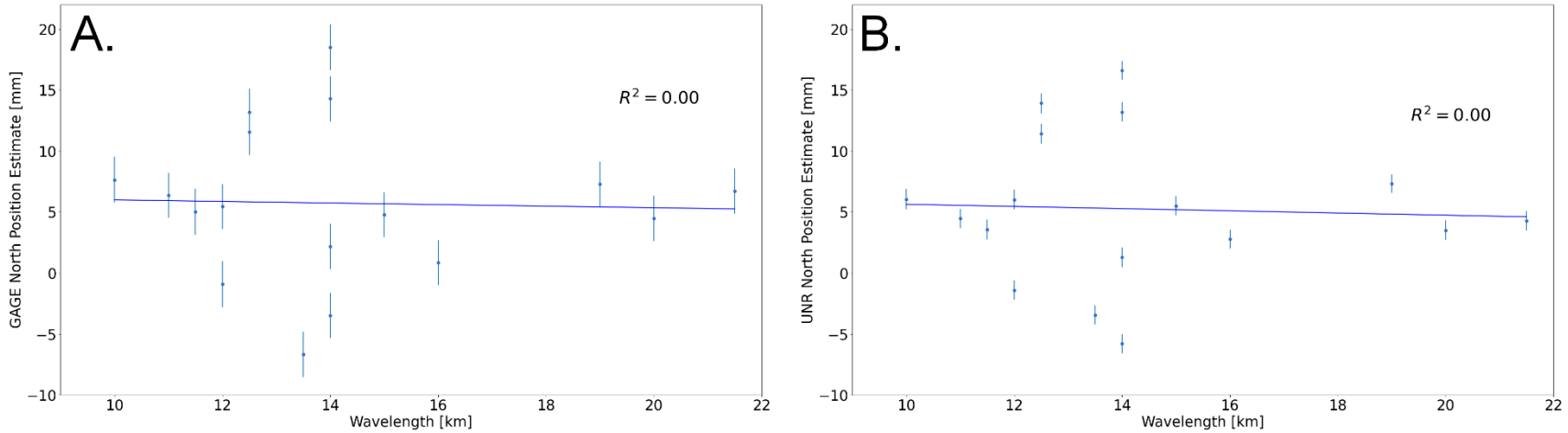

Figure 27. GAGE (a) and UNR (b) north position estimate versus wavelength from vertcross analysis.

non-anomalous days and do not show a correlation to either the presence or absence of an anomaly or to the magnitudes of the anomalies.

5.3 Stability Parameters

The Brunt-Väisälä and Scorer parameter plots for 21-22 January are presented here in Figure 28, and the plots for other modeled days are included in Appendices E and A for Skew-T and the combined Brunt-Väisälä and Scorer parameter plots respectively. As previously shown in Figure 12b, 22 January shows the three required conditions of increased wind speed with height at least up to 300 hPa, cross mountain winds, and a stable atmosphere with a temperature inversion from 700 to 600 hPa. The Brunt-Väisälä frequency is also positive for nearly all of the heights and the Scorer parameter crosses the critical value around 4.5 km near the top of the main lee wave body. Conversely, 21 January in Figure 12a shows a similar temperature profile but with winds parallel to the San Bernardino Mountains, and an equally positive Brunt-Väisälä frequency plot but the Scorer parameter remains above the critical value even while seeing a decrease with height before a larger spike at 8-9 km. Note that all three plots are done at the time of maximum amplitude which is at least a few to several hours into the wave duration. The plots do show though that a lee wave is capable of existing as these are calculated for P577 upwind of the San Bernardino Mountains.

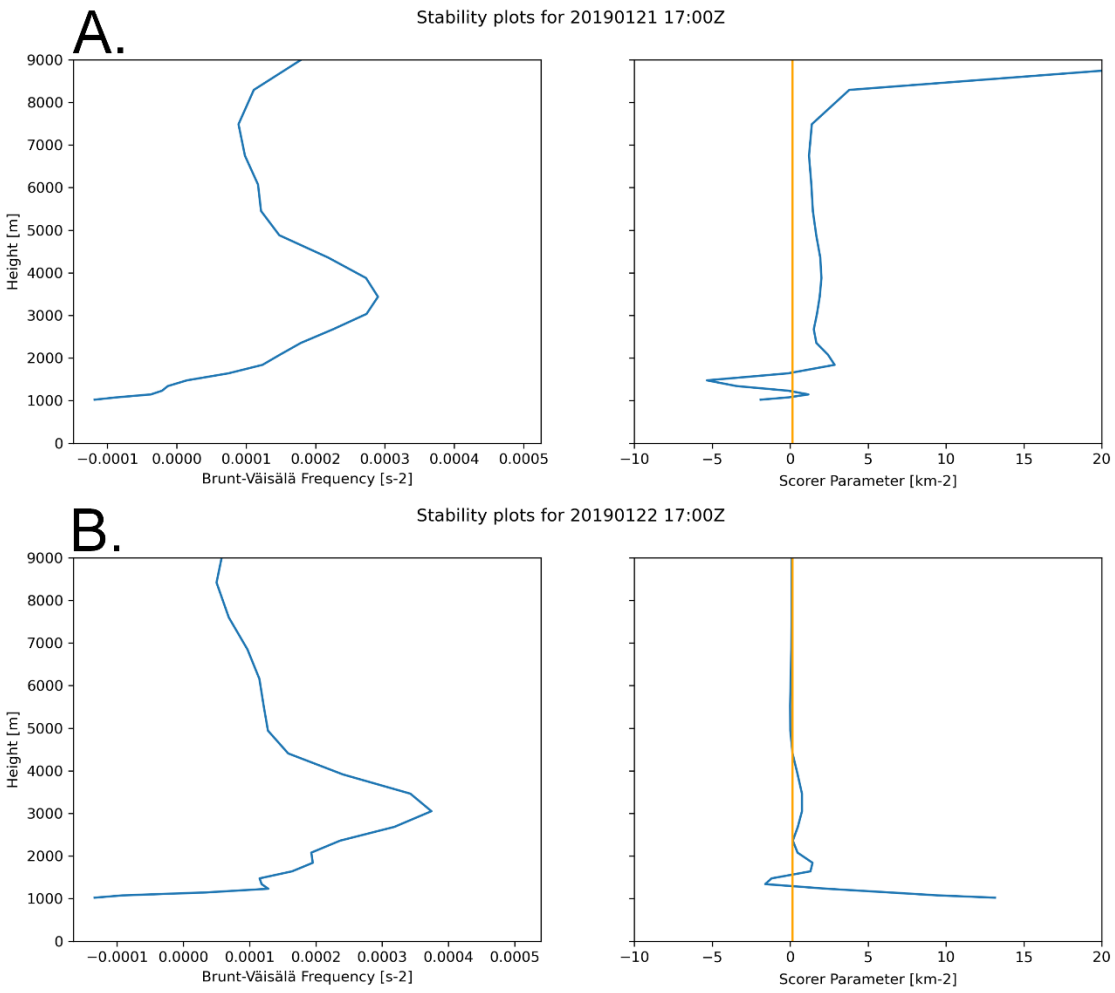

Figure 28. Brunt-Väisälä frequency (left) and Scorer parameter (right) plots for 21 (a) and 22 (b) January 2019. The κ^2 value of 0.1468 is shown in the Scorer parameter plots by the vertical orange line.

5.4 Refractivity

The most distinct feature when comparing the refractivities of each day pair is the formation of an 'envelope' where the two plotted refractivities cross twice for a significant distance along the ray path. For this analysis, I am excluding the beginning of the plot at the lowest heights and only counting from the first apparent intersection onwards as the lower values are typically below the body of the lee wave. This intersection does not need to cause a change in which day is larger, only that the two days meet. For example in each subplot of Figure 29, on

21-22 January there is an envelope forming at 1.5 km up to 4 km and before and after that the refractivities are very similar up to 9 km. Figure 30 is a zoomed-in version of Figure 29, showing the lower 4 km of the atmosphere to better highlight this.

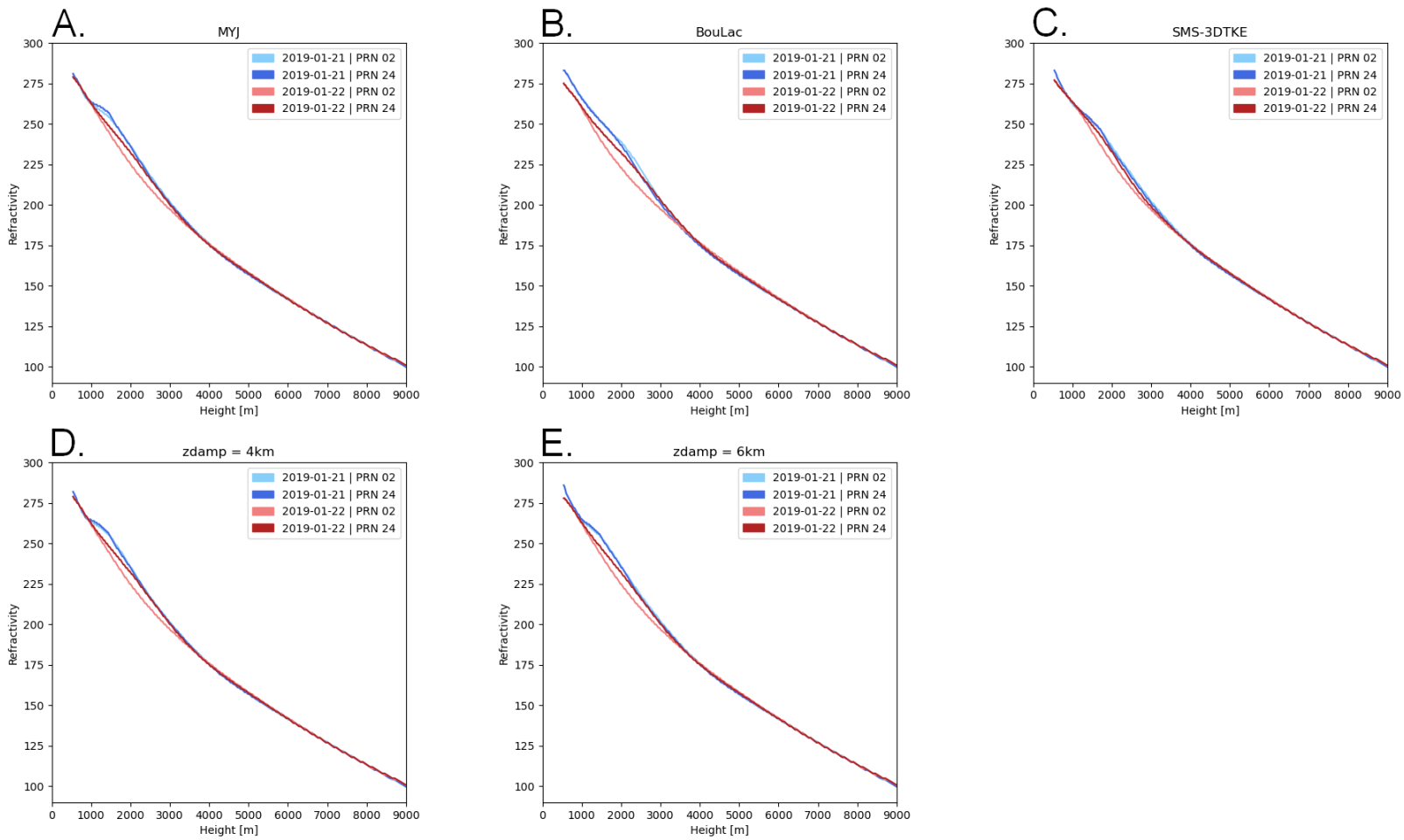

Figure 29. Refractivities for 21-22 January 2019 across the different schemes (a-e) up to 9 km.

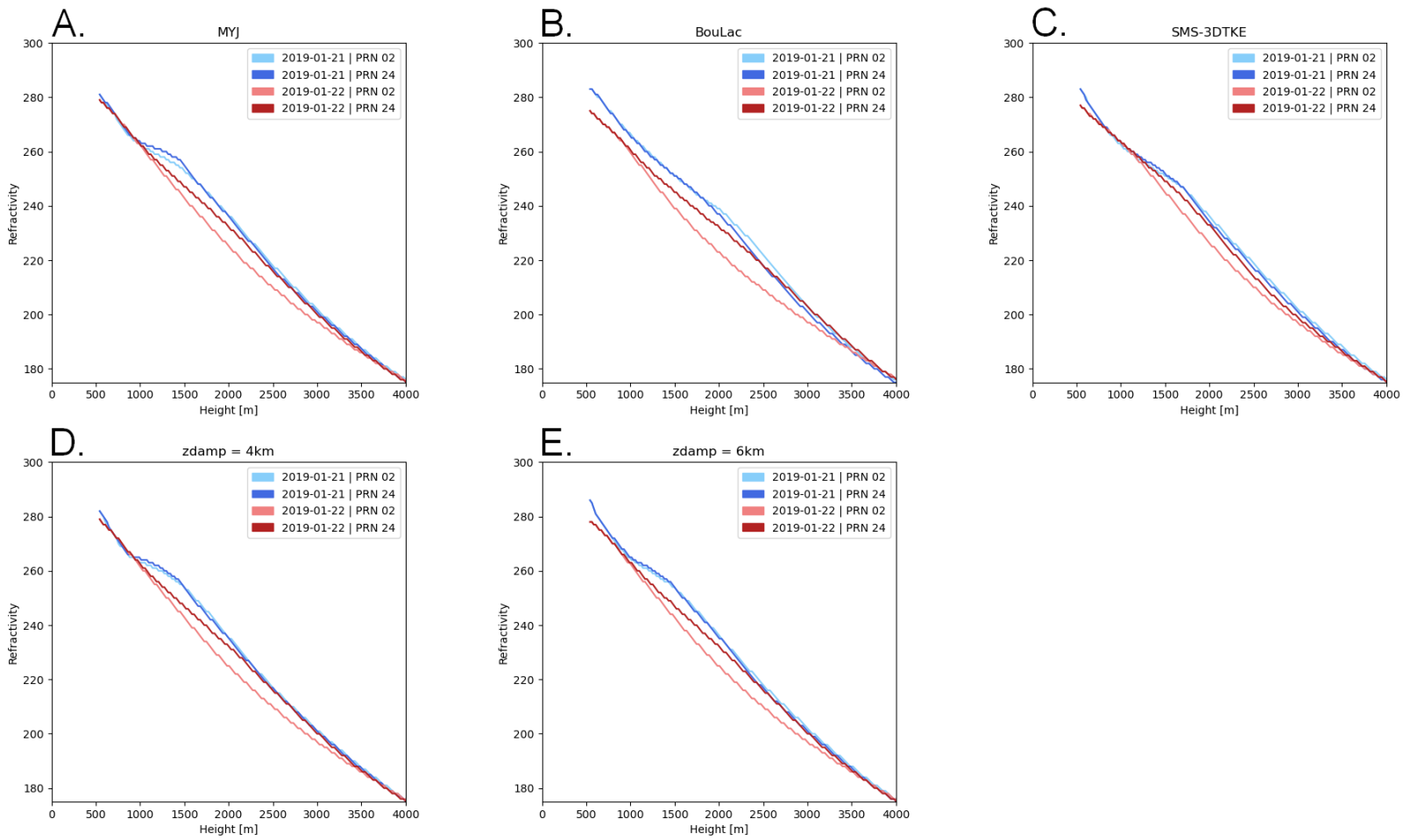

Figure 30. The same as Figure 29 but up to 4 km instead.

A similar envelope appears on most days, though it is not always the same second day that is larger. Some days also have multiple envelopes that close such as 22-23 April in Figure 31. Figure 32 is another zoomed-in version of Figure 31 up to 6 km height. For up to 9 km, it is not always the same setup of Day 1 (blue) larger than Day 2 (red) and sometimes with the multiple envelope days both occur. Envelopes are also not always the same size or even shape as other days (30-31 December versus 26-27 December). Across all of the modeled day pairs, 10 pairs feature a larger Day 1 while 9 pairs feature a larger Day 2 for the lowest envelope where the main body of the lee wave is, usually at 1.5-4 km so it does not appear that one day was more common at lower heights. A specific breakdown of these are given in Tables 2 and 3. The refractivities for each day up to 20 km is additionally plotted in the second panel of each figure and as separate figures for 21-22 January and 22-23 April in Appendix F but are not discussed here.

Pair difference	Expected larger Day	# with larger Day 1	# with larger Day 2
Positive – Zero	2	4	4
Positive – Negative	2	3	0
Positive – Positive	None (2 for 22-23 April)	1	2 (2 for 22-23 April)
Negative – Zero	1	0	1
Negative – Positive	1	1	1
Zero – Positive	1	1	0
Zero – Zero	None	0	1
Total		10	9

Table 2. Expected and actual number of day pairs with the lower refractivity envelope showing a larger value for the first (Day 1) or second (Day 2) day. X – Y means the first day (Y) subtracted from the second day (X). For example, the pair 21-22 January is a Positive – Zero day as 22 January is a large positive anomaly and 21 January is a 'zero' day. An exception is made for 22-23 April as even though both days are positive, there is still a significant increase in positive estimate on 23 April.

Day pair	Envelope types	Lower larger Day	Other observations
11-12 November	Single	2	Very slight envelope, potentially two other very small envelopes at lower heights
25-26 December	Double	2	Slight Day 1 extending past 9 km
26-27 December	Double	1	Day 2 extending past 9 km
27-28 December	Triple	1	Day 1 then Day 2 then beginning of third envelope before 9 km with Day 1
28-29 December	Double	1	Day 2 extends past 9 km
29-30 December	Double	2	Day 2 again extends out past 9 km
30-31 December	Double	2	Slight Day 1
31-01 December-January	Double	1	Very slight Day 2
21-22 January	Single	1	Same for all schemes but vary in envelope sizes. PRN 02 shows the largest separation
25-26 January	Single	2	Not a true envelope but still separation
18-19 February	Double	1	Day 1 then Day 2
19-20 February	Double	1	Day 2 extends out past 9 km
20-21 February	Double	2	Day 1 extends out past 9 km
21-22 February	Double	2	Day 1 extends out past 9 km
11-12 March	Single	1	
11-12 April	Single	1	Only extends past 9 km, bottom of model almost has an envelope with a larger Day 2
16-17 April	Single	1	
21-22 April	Single	2	
22-23 April	Double	2	Same for all schemes and with similar envelope sizes

Table 3. Number of refractivity envelopes and the Day with larger values for the lower envelope observed below 9 km. Double and Triple include envelopes which begin below 9 km but continue to higher altitudes as shown in the second plot of each figure in Appendix F.

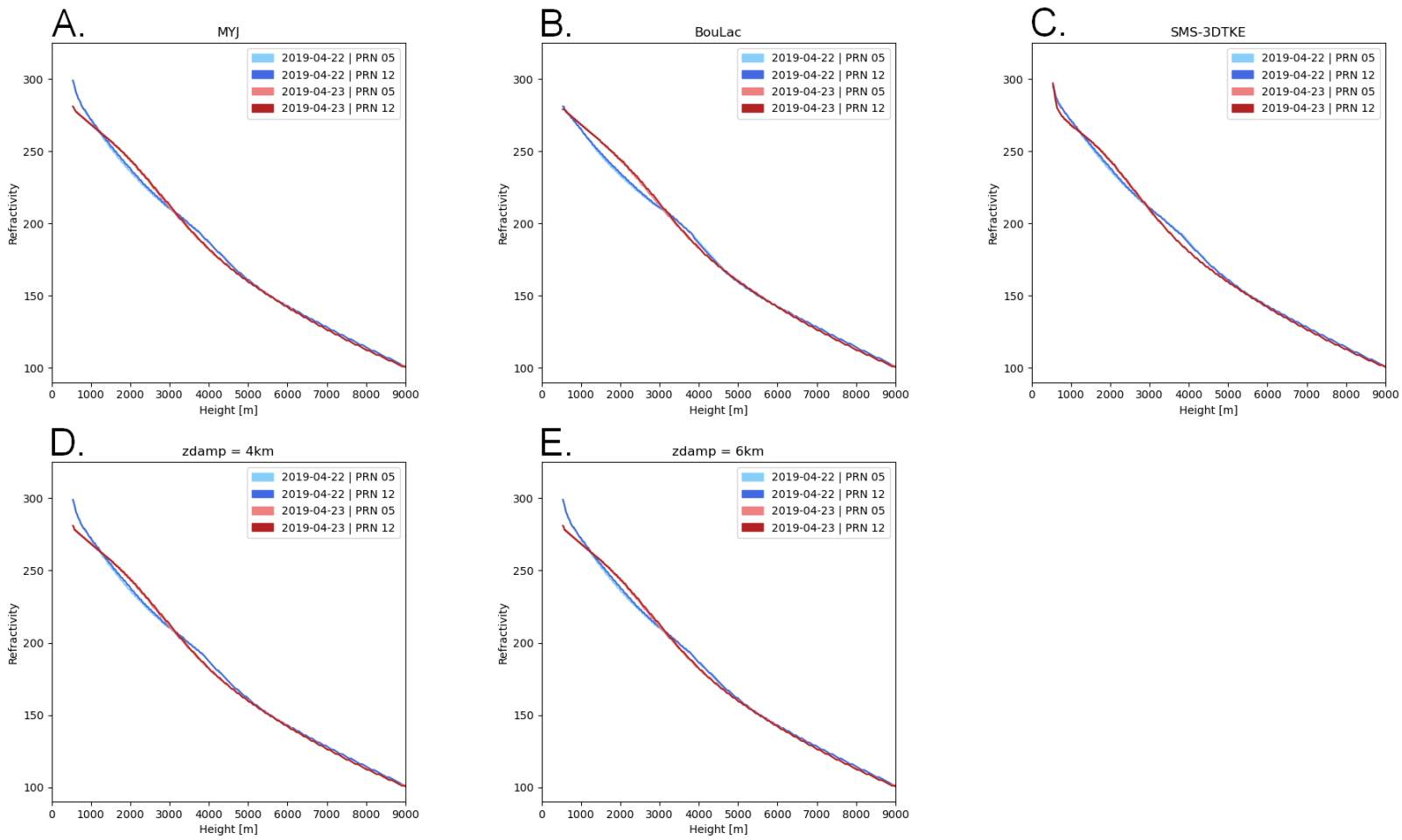

Figure 31. Refractivities for 22-23 April 2019 across the different schemes (a-e) up to 9 km.

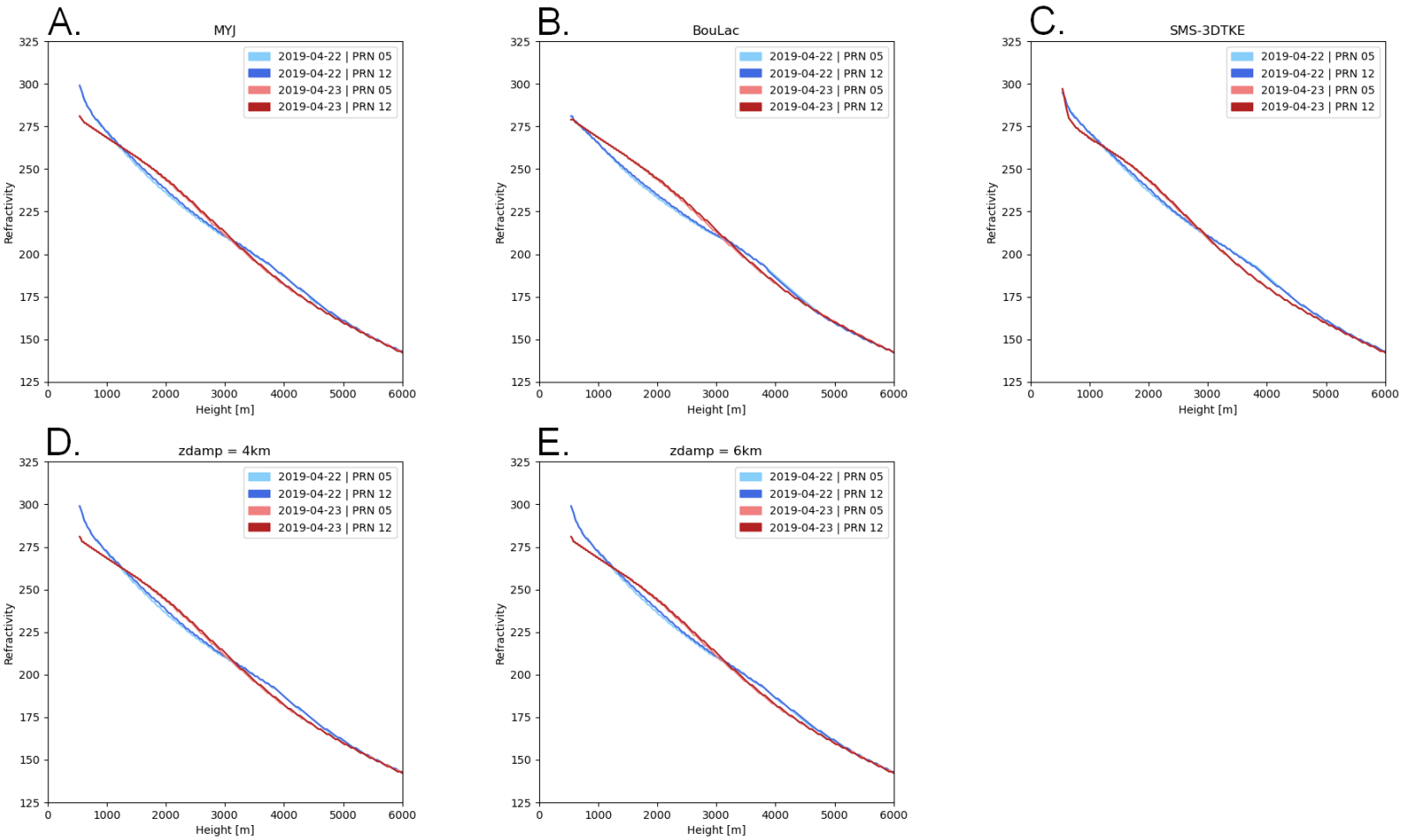

Figure 32. The same as Figure 31 but up to 6 km instead.

As another way to visualize the structure of the lee waves, Kinoshita et al. (2017) calculated what they called the perturbation refractivity $N' = N(x, y, z) - \overline{N}(z)$ as the difference from the horizontally averaged refractivity at a given altitude along with vertical wind velocity contours (see Figure 6 of Kinoshita et al., 2017). To compute the same perturbation refractivity (Figures 33 and 34), I used their equations and values for N and k_1, k_2, k_3 which do not include the inverse compressibility factors for dry and wet air (Z). Z is typically included to correct for the non-ideal gas behavior of air (Thayer, 1974), however for a more direct comparison to Kinoshita et al. (2017), the additional factors are not included for this particular analysis. To achieve this, I calculated the refractivity at each grid point from the WRF output, then averaged them over the x-y plane at each altitude level after adjusting for variations in pressure from topography and subtracted the averaged value from the individual points. The authors had additionally plotted vertical wind velocity contours on their plot. From this, one can observe the lee wave from the change in sign of the vertical wind speed which matches where the refractivity oscillates with the peaks and troughs of the wave. The same waves can be observed as in Figure 22 including the buildup of the wave train as the lobes of the perturbation refractivity and alternating vertical wind regions are created.

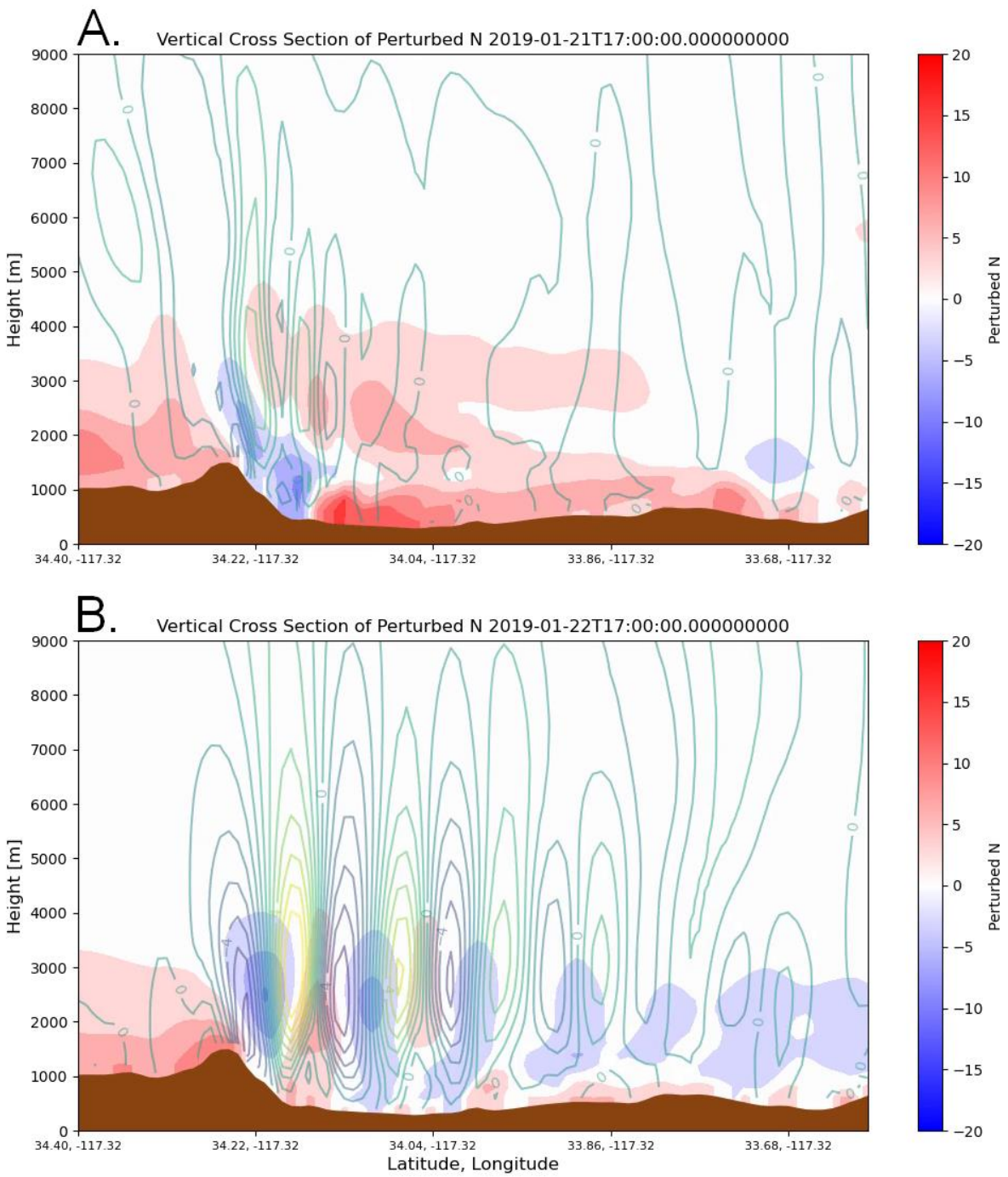

Figure 33. Vertcross animation of perturbation refractivity (Perturbed N) for 21 (a) and 22 (b) January 2019 at 17:00 UTC. Colors show refractivity values (red is positive and blue is negative) and contours show vertical wind speeds (yellow-green contours are positive and purple-blue are negative).

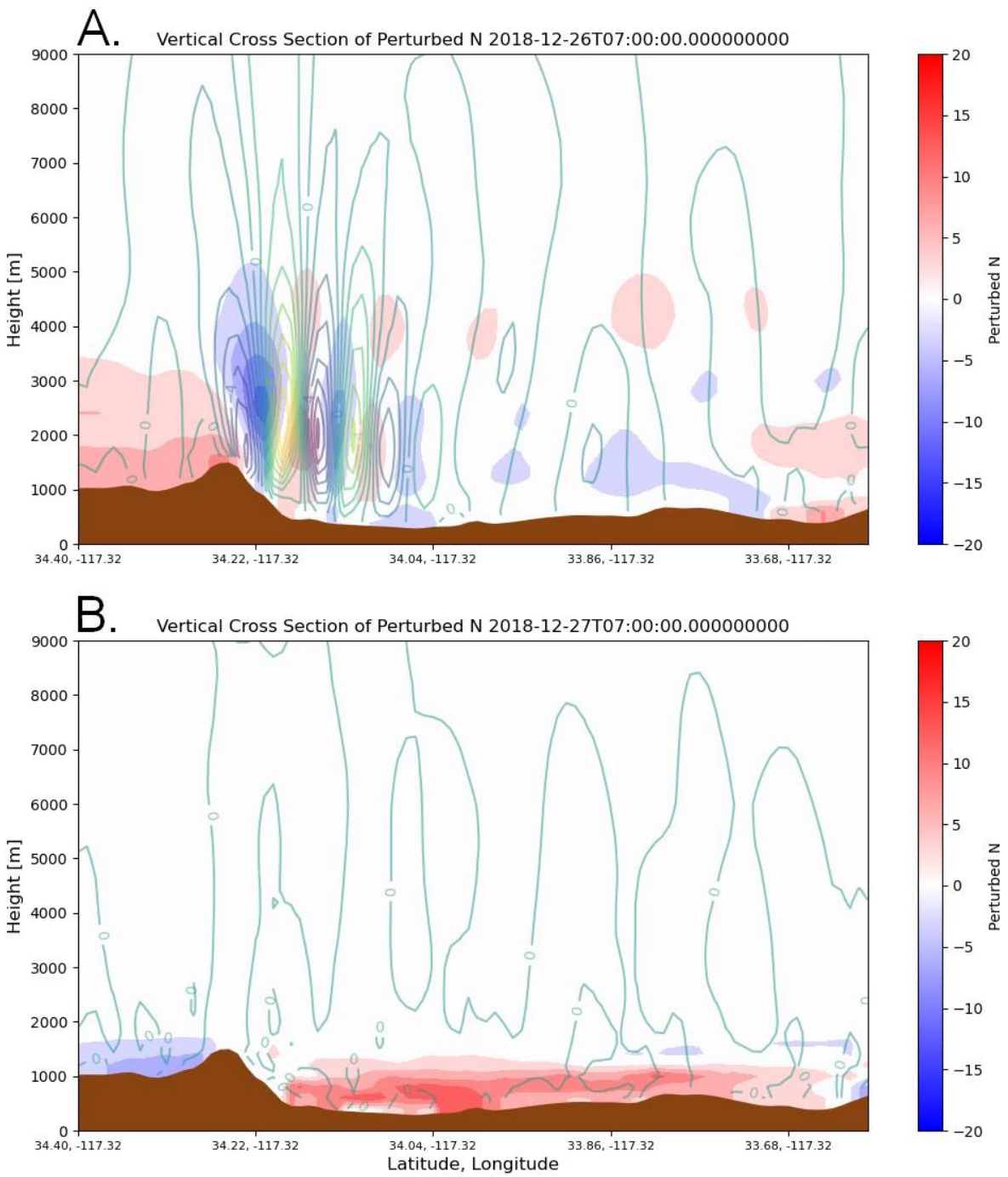

Figure 34. Vertcross animation of perturbation refractivity (Perturbed N) for 26 (a) and 27 (b) December 2018 at 7:00 UTC. Colors show refractivity values (red is positive and blue is negative) and contours show vertical wind speeds (yellow-green contours are positive and purple-blue are negative).

5.5 Delay Estimate

I then investigate whether the ray tracer would be able to estimate a positive delay relative to the previous adjacent non-anomalous day similar to the positive position outliers recorded in the GAGE or UNR time series of P612 and later extended that idea to see if a negative delay could be estimated when comparing to the subsequent adjacent non-anomalous day if available. The titles on figures indicate the order of which day was subtracted from which, for example in Appendix G for 11-12 November, the title of the plot is 20181112-11, meaning 12 November 2018 minus 11 November 2018. This is true even for 31 December to 1 January where the title of the plot is more explicit due to the change in year.

I divide the actual traced delay differences into three categories based on the GAGE position estimates for a given day pair: Expected Positive, Expected Negative, and Expected Zero. These are provided in Table 4 with the related plots provided in Appendix G. The most interesting result is that the majority of the day pairs do not appear to match these expectations at least by sign, however, with 25-26 January and 31 December - 1 January being the only two days to have the differences for both satellite traces correspond to the same expectations from the difference in position estimates between adjacent days. 25-26 December, 29-30 December, 19-20 February, and 16-17 April are the pairs which are opposite for both satellites, and every other day is some combination of one matching satellite, one opposite satellite, or one zero satellite. Note that the ray tracing for SMS-3DTKE on 21 January was roughly an hour shorter compared to the other schemes for an unknown reason so those missing hours were removed from 22 January for lack of comparison, but I believe this would lead to a similar result as the other 5 schemes.

Day pair	PRN expected (+, -, 0)	PRN actual (+, -, 0)	Other observations
11-12 November	Both negative	07 positive, 17 positive-negative	
25-26 December	Both positive	Both negative	Large decrease in 31
26-27 December	Both negative	18 positive-zero, 31 negative	
27-28 December	Both positive	05 negative, 12 positive-zero	Large decrease in 05
28-29 December	Both small positive	07 positive, 17 zero	Positive at end of 17
29-30 December	Both small negative	Both positive	
30-31 December	Both negative	Both positive-negative	
31-01 December-January	Both positive	Both positive	
21-22 January	Both positive	02 zero-positive-zero, 24 positive	
25-26 January	Both positive	Both positive	
18-19 February	Both positive	03 zero, 23 positive	
19-20 February	Both negative	Both positive	
20-21 February	Both zero	19 negative, 30 slight positive-negative	
21-22 February	Both positive	19 negative, 30 positive-negative	
11-12 March	Both positive	05 positive-negative, 12 positive	
11-12 April	Both positive	15 zero-negative, 25 positive	
16-17 April	Both positive	Both negative	
21-22 April	Both positive	05 positive-negative, 12 positive	
22-23 April	Both positive	05 zero-negative, 12 positive	

Table 4. Expected and actual delay difference (positive, negative, zero, or a combination) per satellite for each day pair based on the difference in position estimate from the GAGE time series (Table 1).

Having modeled 21-22 January and 22-23 April with five different physics schemes or variable damping parameters, here I highlight some differences between the runs for the different aspects of this study. In general the evolution, structure, and decay of the lee waves from the vertcross animations are similar to each other.

The waves last a similar amount of time, only differing by 1.5 hours at most from MYJ, though the difference between schemes could be in opposite directions as is the case with BouLac which differs from both zdamp runs by 2.5 hours. While every other scheme had the same maximum amplitude times for 22 and 23 April, BouLac was later by three hours on 23 April, peaking at 17:00 UTC instead of 14:00 despite appearing to have a similar wave buildup to the other runs. BouLac and SMS-3DTKE had a greater maximum amplitude of the lee waves on 22 January while SMS-3DTKE had the smallest amplitude by a factor of nearly two on 23 April. The wavelengths were within a kilometer of each other with the exception of BouLac on 22 January which was three kilometers greater than any other scheme. The number of stable peaks tended to be the same as MYJ or one lower or higher as with BouLac on 22 January or SMS-3DTKE on 22 April respectively.

Zdamp = 4km is the closest to MYJ for 21-22 January and 22-23 April refractivities, while SMS-3DTKE was typically the most different. There is an underestimation of the delay for PRN 24 using the SMS-3DTKE scheme for 21-22 January and an overestimation for the BouLac scheme for 22-23 April by a factor of two for both satellites. The BouLac scheme also is greater than the other varied parameters on the individual 22 and 23 April MYJ comparisons by around an order of magnitude for both satellites.

MYJ appeared to be the closest to the observed values at each weather station for each of the three diagnostics while BouLac and SMS-3DTKE were the furthest, especially for 10m Wind

Speed and 2m Temperature. The Skew-T plots for 21 January did not vary significantly across schemes, only seeing slight shifts in dewpoint and ambient temperatures and wind direction at lower elevations. For 22 January, both zdamp = 4km and 6km are similar to MYJ while BouLac shows a somewhat flatter but still stable ambient temperature profile. For both 22 and 23 April, all of the Skew-T plots were nearly identical with very slight differences occurring only at the bottom and top of the model.

The Brunt-Väisälä frequencies for 21 January were generally similar in profile and magnitude across runs. The Scorer parameters from approximately 2-8 km were similar with slight changes in profile in this range. 22 January is similar with the Brunt-Väisälä frequency profiles not varying much again with the exception of a small decrease and increase for MYJ, and the Scorer parameters all behaving similarly above 2.5 km. As with the Skew-T plots for 22 and 23 April, all of the schemes for these days have similar profiles for the Brunt-Väisälä frequency at all heights and for the Scorer parameter above 2.5 km.

CHAPTER VI

DISCUSSION

6.1 Weather Station Comparisons

As the lowest level for wind speed was 10m compared to 2m Temperature, this may lead to an overestimation of the wind speed at each of the station locations. This is still two orders of magnitude smaller than the planetary boundary layer height (1.5-2 km on 22 Jan @ 16:30-18:00). The diagnostic height is far from being truly decoupled from the surface but still experiences reduced friction from a height increase (Fang et al., 2020). The WRF Model also cannot output gusts separately as the weather stations do, which could potentially offer another explanation for why the WRF winds can be so much faster throughout the day. Instead, the WRF Model reports only the instantaneous wind speed for a given timestep at the location and not an average over the 30-minute period and so it does not allow for a separation of gusts and regular speeds. While unfortunate for this analysis, it may be beneficial for a reduction in output file size by not storing the additional wind data.

The 2m Temperature was the best fitting diagnostic for all three stations so I do not have strong critiques of this. The main discrepancies tend to occur at night, and due to the desert climate of the San Bernardino Basin and the urbanization of CSU San Bernardino, these temperature differences as well as the wind speed differences are more likely related to how the WRF Model handles low-level winds and the interaction with buildings. For similar urban areas, Barlage et al. (2016) concluded that the BEP scheme is more realistic than UCM as it better captures effects such as building drag on the evolution of the planetary boundary layer which is one reason for the switch to BEP.

I do not know for sure why some days underestimated the sea level pressure. Varga & Breuer (2020) found that WRF-derived mean SLP is "underestimated in the months dominated by large-scale processes" (p. 2859) which should include the times of enhanced jet stream activity over the San Bernardino Basin, though the authors did not include the magnitude of this underestimation.

While not a large factor in the differences to the observed data, a limitation of a grid point-based weather model is that it can only use integer values for the grid points and so the actual location from geographical coordinates may be different by as much as 0.005° of latitude and longitude for each station for both the base and expanded domains as I had to round the grid point up or down by a maximum of 0.45.

6.2 Vertcross Animation Correlations

Here I discuss the potential correlations to the magnitude of the anomaly with the diagnostics in Table 1, namely the maximum amplitude and wavelength, the number of stable peaks, and duration of the wave.

There being no correlation to the maximum amplitude of the wave appears reasonable as this amplitude was taken from the dominant peak which was located almost directly above P612. Over approximately 2-2.5 hours, the elevation angle changes by about 40° to or from the higher angles (>80°) depending on the exact satellite path for every day and satellite that traces to those high angles. This is enough to change the trace from crossing through the dominant peak to well into the second peak or vice versa. As this is a relatively small window of time spent within the dominant peak, the particular magnitude of the dominant amplitude may be getting averaged out in the GPS processing with the other time spent tracing through the subsequent waves which

appear to all be the same or smaller (Figure 35). There not being a correlation with wavelength also makes sense as the waves should all have similar if not the same wavelengths as they all form from air forced over the same topography (Scorer, 1949).

The weakly positive ($0 < R^2 < 0.3$) correlation to the number of stable peaks is interesting. My first hypothesis is that a larger number of peaks with a similar wavelength necessarily means a longer wave train and therefore a larger area of the sky that contains the lee wave. This could have a non-negligible effect on satellites transmitting at lower elevation angles that would either encounter several peaks this way or one peak farther from the San Bernardino Mountains. The other weakly positive correlation to wave duration is the most plausible because as previously stated, GPS processing is done as an average of a 24 UTC hour window, so longer

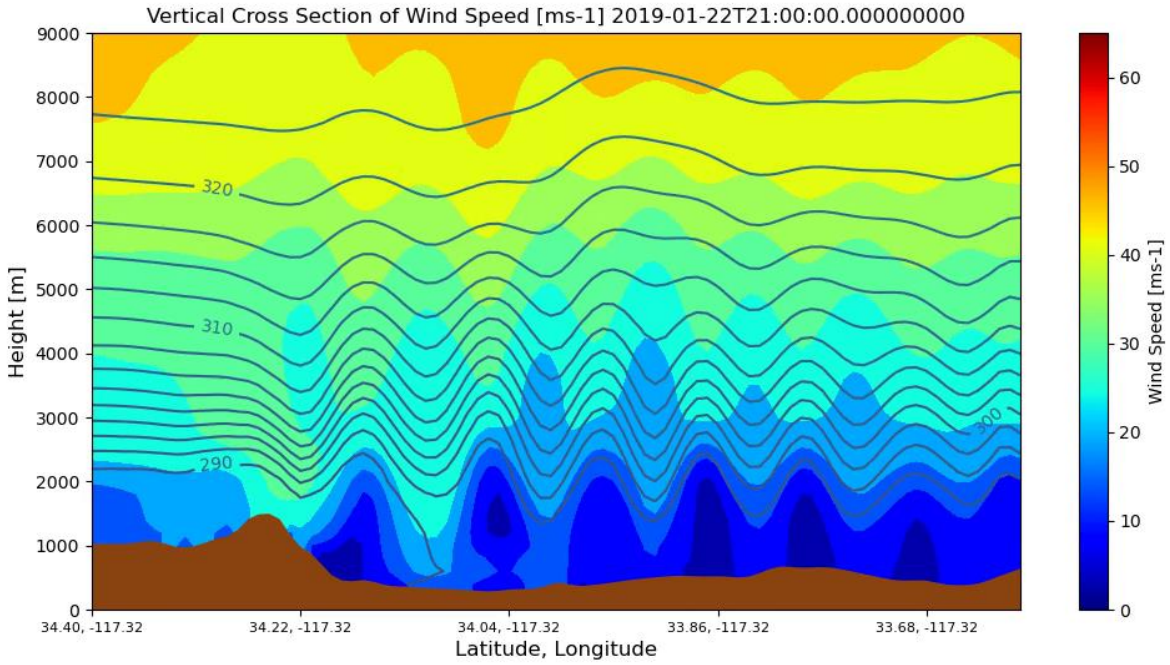

Figure 35. Vertcross animation for 22 January 2019 at 21:00 UTC showing the decrease in amplitude of successive peaks when the wave is fully developed.

duration waves are present for more of the 24-hour day which may lead to a larger anomaly. Taking a closer look at 28-30 December, the largest anomaly of this three day period is on 29 December with a lee wave present for the full 24 hours. This is followed by 30 December with an 18 hour lee wave continued from the previous day but with only a slightly larger (0.7 mm GAGE, 2.3 mm UNR) position estimate than 28 December which only saw the lee wave form in the last seven hours of the day. The wave on 30 December had a smaller amplitude and fewer stable peaks, so while amplitude may not factor into this, the length of the wave train may be negatively affecting the estimate while the duration is positively affecting it. Interestingly enough, one of the 24 hour days, 12 November, is also one of the few negative anomalies using the GAGE time series I modeled, the others being 27 and 31 December which both have short-duration lee waves from ending early and starting late in the day respectively.

6.3 Stability Parameters

For 21 January, the simplest explanation for the discrepancy between the stability and absence of lee waves is that the winds are flowing near-parallel to the San Bernardino Mountains as shown in the Skew-T in Figure 12a. While the atmosphere may be stable, the wind direction is not correct for lee wave formation which is reflected in the Scorer parameter and so none form. The first term of the Scorer parameter (N^2/U^2) typically dominates over the second term (Eq. 2) (American Meteorological Society, 2012), and as the Brunt-Väisälä frequency is similar in magnitude between days and is only dependent on potential temperature, variations in the numerator can be neglected. The denominator (and the second term) depends on the wind speed in a particular direction of flow, in this case perpendicular to the San Bernardino Mountains at an azimuth of 180°. This means the perpendicular component of the wind on 21 January is much

smaller than 22 January as shown in the Skew-T plots, leading to a larger Scorer parameter even if the wind speed may be larger on 21 January. This scenario also occurs for similar day pairs such as 25-26 December.

6.4 Refractivity and Delay Estimate

The refractivity envelopes shown in Appendix F likely form because of the differences in the atmosphere from the lee wave. It is not always the same day, the second in an anomalous day pair, that is larger, however, as listed in Table 2. Shimada et al. (2002), Ichikawa et al. (2004), and Seko et al. (2004) implicate increased water vapor concentration as the cause of increased zenith and slant wet delays. While it is true that the wet component of refractivity is the most variable, seeing different anomalous pairs with both a larger refractivity for the first and second day at the same altitudes might mean something else is occurring.

If these anomalies were solely due to increased refractivities from water vapor within the lee wave, then we would expect the anomalous day to have a greater refractivity for every anomalous day pair. This does not appear to be true at least for this study period as there is an equal amount of pairs with a larger Day 2 versus Day 1 for Positive – Zero pairs, and three additional times with a larger Day 1 for positive – negative pairs. One might think this could be due to a combination of differences in ray tracing paths and lee wave structure as shown in Figure 33 where the refractivity may be greater at certain points and less at others, and the path to the particular satellite does not always cross through the regions of high refractivity. This could cause the delay differences to not agree as shown in Table 4 and Appendix G, but the refractivities for both satellites at the same time do generally agree. If the path differences are

then insignificant, then there should be no difference in the delay differences between the two satellites that trace through different sections of the wave, but that is also not true.

It is important to note that the first day traces slightly behind the second day as the timesteps in the ephemeris files are 15 minutes compared to the smaller 00:04:48 difference from the adjustments made to the delay comparisons and the 00:03:56.4 offset from the difference to a sidereal day, so it had to be kept at the same time for both days. The vertcross animations are also within a 2-D cross-section of the study area so it is possible that there are differences in the perturbation refractivity at other longitudes where the satellites trace at an azimuth not directly south which could help explain these discrepancies.

As noted in Table 3, the refractivity envelope on some days extends beyond 9 km. As this study focused on the lower troposphere, I did not deeply investigate why this occurs. My initial thought was that the proximity to the lower bound of the jet stream may cause some dry pressure differences from the fast-moving winds or carry additional water vapor over the basin. However, both Figures 33 and 34 do not show any large refractivity differences on a singular day, and if there was a contrast in refractivities for the whole atmosphere, there would be a longer envelope. Additionally, there is again not a consistent larger day at these higher altitudes for a day with a 9 km envelope (Figure 34) and a day without (Figure 33).

Brief waves should probably result in a smaller delay and temporally longer waves should probably result in a larger delay from the weakly positive correlation above. I attempted to find satellites at the peak amplitude time which for most days was at least a few hours into the existence of the lee wave. Then, using a smaller window of usually 3-4 hours, should remove the impact of duration to better analyze the lee wave structure. As noted above and in Table 4, the actual delay differences rarely matched with about half matching at least one satellite. The

discrepancies between satellites at the same time showing different delays must then be due to differences in azimuth or elevation angle that changes what section and how much of the lee wave the ray travels through as that is the only notable difference from the ray tracer.

Looking at the satellite paths from several days, azimuth does not seem to have an impact on whether a delay is positive or negative which appears reasonable since the wave should be relatively symmetric about due south if the winds flow close to that direction. However, seeing an increase in elevation angle may lead to a more positive delay and a decrease leading to a more negative delay. This makes some sense for the actual positive delays as the traces through lower elevation angles travel through thicker and more of the atmosphere before exiting the domain, but for actual negative delays, it is confusing that there is then no increase in delay as it reaches the lower angles and they instead tend to continue to decrease. This also seems to disregard the lee wave as some expected positive days have negative delays and vice versa. It is curious that the ray tracer is able to pick up on the presence of the lee wave as shown in the refractivity plots with the two satellites agreeing even when the traces go along different paths, but is not able to have both agree on the delay differences. Perhaps analyzing the traces on a particular day pair that sees multiple lee wave events over several years would be a better choice to instead observe more seasonal trends, but overall I do not think that there are any meaningful conclusions that can be drawn from the delay comparisons in this study.

6.5 PBL Scheme Differences

Looking now at some of the differences between the MYJ scheme and the other four parameters, it is unsurprising that the zdamp runs for all four days were the most similar to the default setup since those runs still use the MYJ scheme but with a slightly higher or lower

damping layer. The differences in vertcross waves, delay, and surface observations for both BouLac and SMS-3DTKE are most likely due to the difference in PBL scheme type. Hope et al. (2024) found that the SMS-3DTKE scheme encounters some issues recreating wind speeds, PBL heights, and occasional underestimation of water vapor concentrations compared to another TKE scheme (MYNN) which was not used in this study. Interestingly, Cohen et al. (2015) summarized that the BouLac scheme shared similar disadvantages to the often better performing MYJ scheme. It is a little surprising that MYJ is usually much better or at least closer to the diagnostic non-local schemes than to the other two TKE schemes for many of the investigated diagnostics. Perhaps this is because its development for severe storms leads to a better modeling of jet stream activity and the wide lee waves that spans much of the nested domain. Barlage et al. compared MYJ and BouLac and additionally concluded that the MYJ scheme is the better PBL scheme for urban areas even with a positive ~2°C temperature bias.

CHAPTER VII

CONCLUSION

This thesis investigated the occurrence and cause of north-skewed GNSS position anomalies in the lee of the San Bernardino Mountains in southern California. Using the WRF Model to simulate the atmosphere on these anomalous days, I found that trapped lee waves were present on all of the positively-skewed days and two of the negatively-skewed days 12 November and 31 December. The model and the different planetary boundary layer schemes generally do a good job of recreating the trapped lee waves within the San Bernardino Basin and key diagnostics of 10m Wind Speed, 2m Temperature, and Sea Level Pressure at three local weather stations. I found these anomalies to be weakly ($0 < R^2 < 0.3$) positively correlated with the duration and approximate downstream length of trapped lee waves.

I was able to observe the presence and rough structure of lee waves from differences in refractivity between days if the refractivity on the previous day was also estimated. Unfortunately, I cannot conclude anything from the delay estimate from the ray tracer as positive traced delays appeared to result from increasing elevation angle of the ray path to the satellite, regardless of the position anomaly magnitude. For others interested in a similar study, I recommend the use of the MYJ PBL scheme when using the default CONUS suite as it most closely matched local surface observations. I would not presently recommend using the BouLac scheme for modeling other trapped lee wave events, at least within this study area.

The first avenue for future work in this area I think should be prioritized is modeling more days and years to see if the lee waves are still correlated to anomalies outside of the 2018-2019 winter and early spring seasons. Next, I would suggest investigating the same refractivity

and delay difference estimates at other times during the lee wave, not only at the time of maximum amplitude as wave amplitude was not correlated to the position estimate. This would include times such as when the maximum number of stable peaks are present, at the start and end of the wave, and any other notable times as there were too many days to try and accomplish all of this for this study. I would also suggest investigating the apparent jet stream-related refractivity structures as initial vertcross animations of 21-22 January up to 20 km likely show the jet stream at similar altitudes of 8-13 km. I would also propose incorporating satellite imagery from satellites such as MODIS following Materna (2014) to additionally confirm the modeled lee wave events if conditions are favorable for cloud formation. Lastly, I would suggest investigating other stations outside of southern California that record similar anomalous position estimates to contribute to a better understanding of how trapped lee waves affect GNSS signals in mountainous regions.

DATA AVAILABILITY STATEMENT

The NOAA High-Resolution Rapid Refresh (HRRR) Model analysis products used for each run can be accessed through the AWS archive located at https://registry.opendata.aws/noaa-hrrr-pds/. The SP3 Ephemeris files used for ray tracing can be accessed through the directory located at https://cddis.nasa.gov/Data_and_Derived_Products/GNSS/orbit_products.html.

REFERENCES

American Meteorological Society. (2012). Scorer parameter. Glossary of Meteorology. Retrieved from https://glossary.ametsoc.org/wiki/Scorer_parameter

American Meteorological Society. (2014). Brunt–Väisälä frequency. Glossary of Meteorology. Retrieved from https://glossary.ametsoc.org/wiki/Brunt-v%C3%A4is%C3%A4l%C3%A4_frequency

APRSWXNET. (2019). Synoptic Data Viewer [Data service]. Retrieved from https://viewer.synopticdata.com/table/null/basic-weather/now

Astropy Collaboration et al. (2013). Astropy: A community Python package for astronomy. Astrophysical Journal, 558, A33. https://doi.org/10.1051/0004-6361/201322068

Astropy Collaboration et al. (2018). The Astropy Project: Building an Open-science Project and Status of the v2.0 Core Package. Astrophysical Journal, 156(3), 123. https://doi.org/10.3847/1538-3881/aabc4f

Astropy Collaboration et al. (2022). The Astropy Project: Sustaining and Growing a Community-oriented Open-source Project and the Latest Major Release (v5.0) of the Core Package. Astrophysical Journal, 935(2), 167. https://doi.org/10.3847/1538-4357/ac7c74

Barlage, M., Miao, S., & Chen, F. (2016). Impact of physics parameterizations on high-resolution weather prediction over two Chinese megacities. J. Geophys. Res. Atmos., 121, 4487–4498, https://doi.org/10.1002/2015JD024450

Blewitt, G., Hammond, W. C., & Kreemer, C. (2018). Harnessing the GPS Data Explosion for Interdisciplinary Science. Eos, 99. https://doi.org/10.7283/T5222RQD

Bougeault, P., & Lacarrere, P. (1989). Parameterization of Orography-Induced Turbulence in a Mesobeta--Scale Model. Monthly Weather Review, 117(8), 1872-1890. https://doi.org/10.1175/1520-0493(1989)117<1872:POOITI>2.0.CO;2

Cohen, A. E., Cavallo, S. M., Coniglio, M. C., & Brooks, H. E. (2015). A Review of Planetary Boundary Layer Parameterization Schemes and Their Sensitivity in Simulating Southeastern U.S. Cold Season Severe Weather Environments. Weather and Forecasting, 30(3), 591-612. https://doi.org/10.1175/WAF-D-14-00105.1

Dowell, D. C., Alexander, C. R., James, E. P., Weygandt, S. S., Benjamin, S. G., Manikin, G. S., Blake, B. T., Brown, J. M., Olson, J. B., Hu, M., Smirnova, T. G., Ladwig, T., Kenyon, J. S., Ahmadov, R., Turner, D. D., Duda, J. D., and Alcott, T. I. (2022). The High-Resolution Rapid Refresh (HRRR): An Hourly Updating Convection- Allowing Forecast Model. Part I: Motivation and System Description. Weather and Forecasting, 37, 8, 1371-1395, https://doi.org/10.1175/WAF-D-21-0151.1

Durran, D. R. & Blumen, W., eds (1990). Mountain Waves and Downslope Winds. Atmospheric Processes over Complex Terrain. Meteorological Monographs, 23, 59-81. https://doi.org/10.1007/978-1-935704-25-6_4

Eckermann, S. D., Broutman, D., Ma, J., & Lindeman, J. (2006). Fourier-Ray Modeling of Short-Wavelength Trapped Lee Waves Observed in Infrared Satellite Imagery near Jan Mayen. Monthly Weather Review, 134(10), 2830-2848. https://doi.org/10.1175/MWR3218.1

Evans, J. K. (2013). An Examination of Aviation Accidents Associated with Turbulence, Wind Shear and Thunderstorm. (NTRS No. 20130013459). Retrieved from https://ntrs.nasa.gov/citations/20130013459

Fang, P., Jiang, W., Tang, J., Lei, X., & Tan, J. (2020). Variations in Friction Velocity with Wind Speed and Height for Moderate-to-Strong Onshore Winds Based on Measurements from a Coastal Tower. Journal of Applied Meteorology and Climatology, 59(4), 637-650. https://doi.org/10.1175/JAMC-D-18-0327.1

Feltz, W. F., Bedka, K. M., Otkin, J. A., Greenwald, T., & Ackerman, S. A. (2009). Understanding Satellite-Observed Mountain-Wave Signatures Using High-Resolution Numerical Model Data. Weather and Forecasting, 24(1), 76-86. https://doi.org/10.1175/2008WAF2222127.1

Gordon, G. R., Stein, S. (1992). Global Tectonics and Space Geodesy. Science, 256, 333-342. https://doi.org/10.1126/science.256.5055.333

Hecht, E. (2017). Optics (5th ed.). London, England: Pearson Higher Education

Herring, T., Davis, J. L., & Shapiro, I. I. (1990). Geodesy by radio interferometry: The application of Kalman filtering to the analysis of very long baseline interferometry data. J. Geophys.Res., 95(B8), 12561-12581. https://doi.org/10.1029/JB095iB08p12561

Herring, T., Melbourne, T. I., Murray, M., Floyd, M., Szeliga, W., King, R. W., Phillips, D., Puskas, C., Santillan, V. M., & Wang, L. (2016). Plate Boundary Observatory and Related Networks: GPS Data Analysis Methods and Geodetic Products. *Rev. Geophys.,* 54(4), 759–808

Hills, M. O. G., & Durran, D. R. (2012). Nonstationary Trapped Lee Waves Generated by the Passage of an Isolated Jet. Journal of the Atmospheric Sciences, 69(10), 3040-3059. https://doi.org/10.1175/JAS-D-12-047.1

Hobiger, T., Ichikawa, R., Koyama, Y., & Kondo, T. (2008). Fast and accurate ray- tracing algorithms for real-time space geodetic applications using numerical weather models. J. Geophys. Res., 113(D20302), 1-14. https://doi.org/10.1029/2008JD010503

Holton, J. R., Hakim, G. J. (2012). An Introduction to Dynamic Meteorology (Fifth Edition). Amsterdam-London-New York: Elsevier Publishing Co.

Hong, S., Noh, Y., & Dudhia, J. (2006). A New Vertical Diffusion Package with an Explicit Treatment of Entrainment Processes. Monthly Weather Review, 134(9), 2318-2341. https://doi.org/10.1175/MWR3199.1

Hope, A. P., Lopez-Coto, I., Hajny, K., Tomlin, J. M., Kaeser, R., Stirm, B., Karion, A., & Shepson, P. B. (2024). Analyzing "Gray Zone" Turbulent Kinetic Energy Predictions in the Boundary Layer from Three WRF PBL Schemes over New York City and Comparison with Aircraft Measurements. Journal of Applied Meteorology and Climatology, 63(1), 125-142. https://doi.org/10.1175/JAMC-D-22-0181.1

Hu, X., Nielsen-Gammon, J. W., & Zhang, F. (2010). Evaluation of Three Planetary Boundary Layer Schemes in the WRF Model. Journal of Applied Meteorology and Climatology, 49(9), 1831-1844. https://doi.org/10.1175/2010JAMC2432.1

Ichikawa, R., Seko, H., & Bevis, M. G. (2004). An evaluation of geodetic positioning error simulated using a mesoscale nonhydrostatic model. Proc. of SPIE, 5661, 37-45. https://doi.org/10.1117/12.578647

Janjić, Z. I. (1994). The Step-Mountain Eta Coordinate Model: Further Developments of the Convection, Viscous Sublayer, and Turbulence Closure Schemes. Monthly Weather Review, 122(5), 927-945. https://doi.org/10.1175/1520-0493(1994)122<0927:TSMECM>2.0.CO;2

Jiang, Q., Doyle, J. D., & Smith, R. B. (2006). Interaction between Trapped Waves and Boundary Layers. J. Atmos. Sci., 63, 617–633. https://doi.org/10.1175/JAS3640.1

Kalnay et al. (1996). The NCEP/NCAR 40-year reanalysis project, Bull. Amer. Meteor. Soc., 77, 437-470. Retrieved from https://psl.noaa.gov/data/gridded/data.ncep.reanalysis.html

Kinoshita, Y., Morishita, Y. & Hirabayashi, Y. (2017). Detections and simulations of tropospheric water vapor fluctuations due to trapped lee waves by ALOS-2/PALSAR-2 ScanSAR interferometry. Earth Planets Space, 69, 104. https://doi.org/10.1186/s40623-017-0690-7

Klemp, J. B., Dudhia, J., & Hassiotis, A. D. (2008). An Upper Gravity-Wave Absorbing Layer for NWP Applications. Monthly Weather Review, 136(10), 3987-4004. https://doi.org/10.1175/2008MWR2596.1

Kohonen, T. (1982). Self-organized formation of topologically correct feature maps. Biol. Cybern., 43, 59-69. https://doi.org/10.1007/BF00337288

Kohonen, T. (1998). The self-organizing map. Neurocomputing, 21(1-3), 1-6. https://doi.org/10.1016/S0925-2312(98)00030-7

Ladwig, W. (2017). wrf-python (Version 1.3.4.1): A collection of diagnostic and interpolation routines for use with output from the Weather Research and Forecasting (WRF-ARW) Model [Computer Software]. GitHub. https://doi.org/10.5065/D6W094P1

Li, L., & Chen, Y. (2017). Numerical Simulations of Two Trapped Mountain Lee Waves Downstream of Oahu. Journal of Applied Meteorology and Climatology, 56(5), 1305-1324. https://doi.org/10.1175/JAMC-D-15-0341.1

Mahalov, A., Moustaoui, M., & Grubišić, V. (2011). A numerical study of mountain waves in the upper troposphere and lower stratosphere. Atmos. Chem. Phys., 11, 5123–5139. https://doi.org/10.5194/acp-11-5123-2011

Masoumi S., McClusky S., Koulali A., & Tregoning, P. (2017). A directional mode of tropospheric horizontal gradients in Global Positioning System and its application for particular weather scenarios. J Geophys Res Atmos, 122, 4401–4425. https://doi.org/10.1002/2016JD026184

Materna, K. (2014). Analysis of atmospheric delays and asymmetric positioning errors in the global positioning system (Bachelor's thesis). Retrieved from DSpace@MIT. (http://hdl.handle.net/1721.1/90657). Location: Massachusetts Inst. of Technol., Cambridge, Mass.

Mateus, P., Nico, G., Tome, R., Catalao, J., & Miranda, P. M. A. (2013). Experimental Study on the Atmospheric Delay Based on GPS, SAR Interferometry, and Numerical Weather Model Data. IEEE Transactions on Geoscience and Remote Sensing, 51(1), 6-11. https://doi.org/10.1109/TGRS.2012.2200901

May, R. M., Goebbert, K. H., Thielen, J. E., Leeman, J. R., Camron, M. D., Bruick, Z., Bruning, E. C., Manser, R. P., Arms, S. C., & Marsh, P. T. (2022). MetPy: A Meteorological Python Library for Data Analysis and Visualization. Bulletin of the American Meteorological Society, 103(10), 2273-2284. https://doi.org/10.1175/BAMS-D-21-0125.1

Mesinger, F. (1993). *Forecasting Upper Tropospheric Turbulence within the Framework of the Mellor-Yamada 2.5 Closure*. Retrieved from https://www2.mmm.ucar.edu/wrf/users/physics/phys_refs/PBL/MYJ_part2.pdf

Metz, J. J., Durran, D. R., & Blossey, P. N. (2020). Unusual Trapped Mountain Lee Waves with Deep Vertical Penetration and Significant Stratospheric Amplitude. Journal of the Atmospheric Sciences, 77(2), 633–646. https://doi.org/10.1175/JAS-D-19-0093.1

National Weather Service. (n.d.a). *Skew-T Parameters*. Skew-T Parameters and Indices. Retrieved from https://www.weather.gov/source/zhu/ZHU_Training_Page/convective_parameters/skewt/skewtinfo.html

National Weather Service. (n.d.b). *Isentropic Lifting*. Isentropic Analysis. Retrieved from https://www.weather.gov/source/zhu/ZHU_Training_Page/clouds/Isentropic_Analysis/ISENTROPIC_LIFTING.htm

National Weather Service. (2015). *Week 2: What is Wind Shear?* Severe Weather Topics. Retrieved from https://www.weather.gov/ilx/swop-springtopics

National Weather Service. (2023). *Basic Wave Patterns*. JetStream - An Online School for Weather. Retrieved from https://www.noaa.gov/jetstream/upper-air-charts/basic-wave-patterns

Nigam, S., & DeWeaver, E. (2015). DYNAMICAL METEOROLOGY | Stationary Waves (Orographic and Thermally Forced). Encyclopedia of Atmospheric Sciences (Second Edition), 431-445. http://dx.doi.org/10.1016/B978-0-12-382225-3.00381-9

Reiter, E. (1969). Tropospheric Circulation and Jet Streams. In D. F. Rex (Ed.), World Survey of Climatology, Climate of the Free Atmosphere (Vol. 4, 85-202). Amsterdam-London-New York: Elsevier Publishing Co.

Sanz Subirana, J., Juan Zornoza, J. M., & Hernández-Pajares M. (2013). GNSS Data Processing, Vol. I: Fundamentals and Algorithms. Prais, France: European Space Agency. Retrieved from https://www.esa.int/About_Us/ESA_Publications/ESA_TM-23_GNSS_DATA_PROCESSING

Schauer, A. R., Hendrikx, J., Birkeland, K. W., & Mock, C. J. (2021). Synoptic atmospheric circulation patterns associated with deep persistent slab avalanches in the western United States. Nat. Hazards Earth Syst. Sci., 21, 757–774. https://doi.org/10.5194/nhess-21-757-2021

Schmunk, R. B. (2024). Panoply Data Viewer [Computer Software]. New York, NY: NASA Goddard Institute for Space Studies. Retrieved from https://www.giss.nasa.gov/tools/panoply/

Seko, H., Nakamura, H., & Shimada, S. (2004). An evaluation of atmospheric models for GPS data retrieval by output from a numerical weather model. Journal of the Meteorological Society of Japan, 82, 339-350. https://doi.org/10.2151/JMSJ.2004.339

Shimada, S., Seko, H., Nakamura, H., Aonashi, K., & Herring, T. A. (2002). The impact of atmospheric mountain lee waves on systematic geodetic errors observed using the Global Positioning System. Earth, Planets and Space, 54(4), 425-430. https://doi.org/10.1186/BF03352433

Skamarock, W. C., Klemp, J. B., Dudhia, J., Gill, D. O., Liu, Z., Berner, J., Wang, W., Powers, J. G., Duda, M. G., Barker, D. M., & Huang, X.-yu. (2021). A Description of the Advanced Research WRF Model Version 4.3 (No. NCAR/TN-556+STR). Retrieved from http://dx.doi.org/10.5065/1dfh-6p97

Soufflet, C., Lott, F., & Damiens, F. (2019). Trapped mountain waves with a critical level just below the surface. Quarterly Journal of the Royal Meteorological Society, 145(721), 1503–1514. https://doi.org/10.1002/qj.3507

Stendel, M., Francis, J., White, R., Williams, P. D., & Woollings, T. (2021). The jet stream and climate change. In Letcher, T (Ed.), Climate Change, (pp. 327-357). Amsterdam-London-New York: Elsevier Publishing Co. https://doi.org/10.1016/B978-0-12-821575-3.00015-3

Thayer, G. D. (1974). An improved equation for the radio refractive index of air. Radio Sci., 9(10), 803–807. https://doi.org/10.1029/RS009i010p00803

Tralli, D. M. & Lichten, S. M. (1990). Stochastic estimation of tropospheric path delays in global positioning system geodetic measurements. Bull. Geod., 64, 127-159. https://doi.org/10.1007/BF02520642

Udina, M., Soler, M. R., & Sol, O. (2017). A Modeling Study of a Trapped Lee-Wave Event over the Pyrenees. Monthly Weather Review, 145(1), 75–96. https://doi.org/10.1175/MWR-D-16-0031.1

University of Washington Department of Atmospheric Sciences. (2005). Soundings in depth. Forecast Graphics Descriptions. Retrieved from https://a.atmos.washington.edu/wrfrt/descript/pages/soundings_in_depth.html

U.S. Geological Survey. (2021). USGS Shaded Relief. Sioux Falls, SD: USGS Earth Resources Observation & Science (EROS) Center. Accessed 1 April 2024 at https://basemap.nationalmap.gov/arcgis/rest/services/USGSShadedReliefOnly/MapServer

U.S. Government Printing Office. (1962). U.S. Standard Atmosphere. Washington, D.C. Retrieved from https://en.wikipedia.org/wiki/International_Standard_Atmosphere

U.S. Space Force. (2021). *The Global Positioning System*. GPS.gov: GPS Overview. Retrieved from https://www.gps.gov/systems/gps/

VanderPlas, J. T. (2018). Understanding the Lomb–Scargle Periodogram. ApJS 236(16), 1-28. https://doi.org/10.3847/1538-4365/aab766

Varga, Á. J., & Breuer, H. (2020). Sensitivity of simulated temperature, precipitation, and global radiation to different WRF configurations over the Carpathian Basin for regional climate applications. Clim Dyn, 55, 2849–2866. https://doi.org/10.1007/s00382-020-05416-x

Wang, W., Bruyère, C., Duda, M., Dudhia, D., Gill, D. Kavulich, M., Werner, K., Chen, M., Lin, H.-Chuan, Michalakes, J., Rizvi, S., Zhang, X., Berner, J., Munoz-Esparza, D., Reen, B., Ha, S., & Fossell, K. (2021). *WRF Users Guide documentation*. Mesoscale & Microscale Meteorology. Retrieved from https://www2.mmm.ucar.edu/wrf/users/wrf_users_guide/build/html/index.html

Wu, T. (2012). A Brief Review of the Impact of Precision Measurement Technology on Scientific Advances. (Technical Report TR-REV-2012, pp. 1-15) http://dx.doi.org/10.13140/RG.2.2.35113.21604

Zang, Z. l., Zhang, M., & Huang, H. (2007). Influence of the Scorer Parameter Profile on the Wavelength of Trapped Lee Waves. J Hydrodyn, 19, 165–172. https://doi.org/10.1016/S1001-6058(07)60044-4

Zhang, X., Bao, J. W., Chen, B., & Grell, E. D. (2018). A three-dimensional scale-adaptive turbulent kinetic energy scheme in the WRF-ARW model. Mon. Wea. Rev., 146, 2023–2045. https://doi.org/10.1175/MWR-D-17-0356.1

Zwatz-Meise, V. (n.d.). LEE CLOUDINESS - METEOROLOGICAL PHYSICAL BACKGROUND. MANUAL OF SYNOPTIC SATELLITE METEOROLOGY. Retrieved from https://rammb.cira.colostate.edu/wmovl/vrl/tutorials/satmanu-eumetsat/satmanu/cms/leecl/backgr.htm

APPENDICES

Appendix A – Stability Plots

Figures A1-A26. Brunt-Väisälä and Scorer parameter plots for Day 1 (a) and Day 2 (b) at the specified UTC time at P577 upwind of the San Bernardino Mountains.

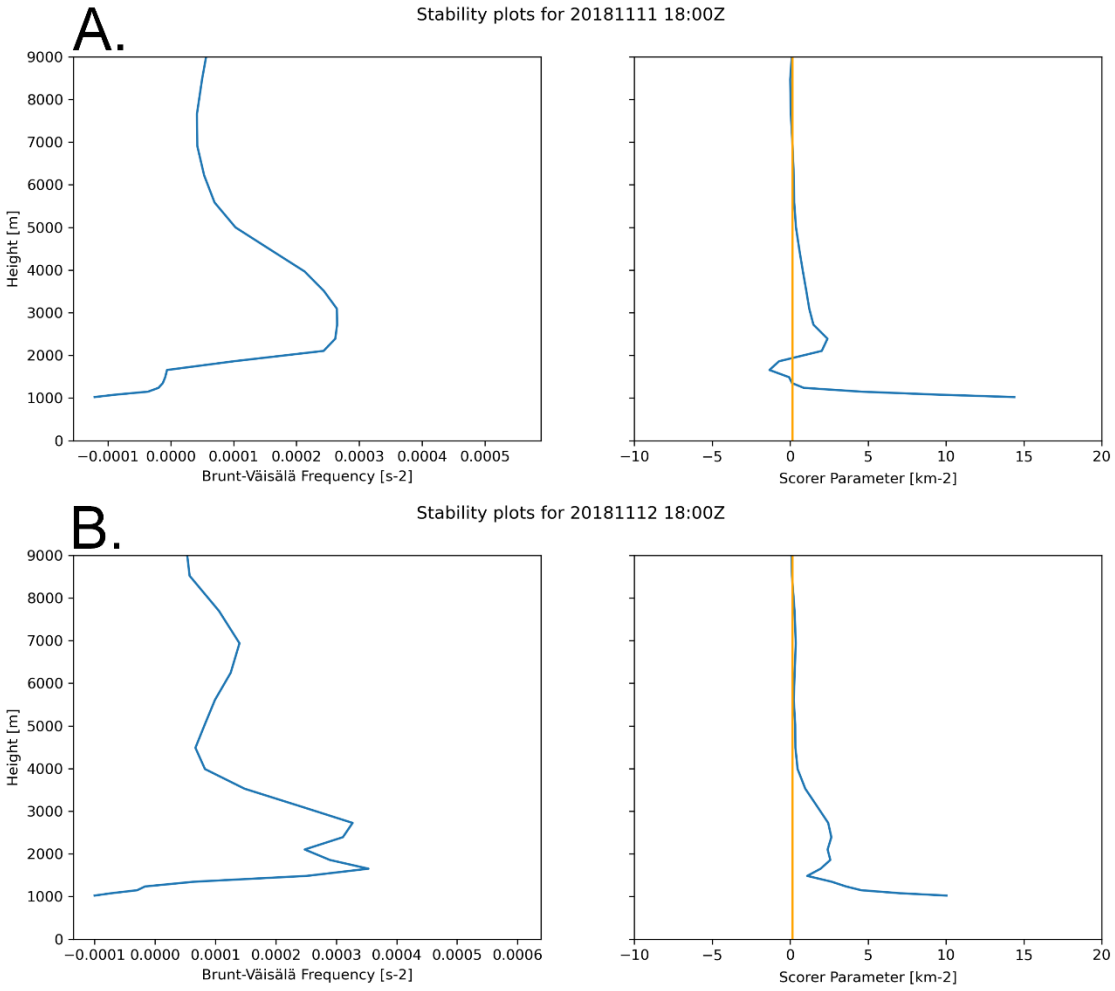

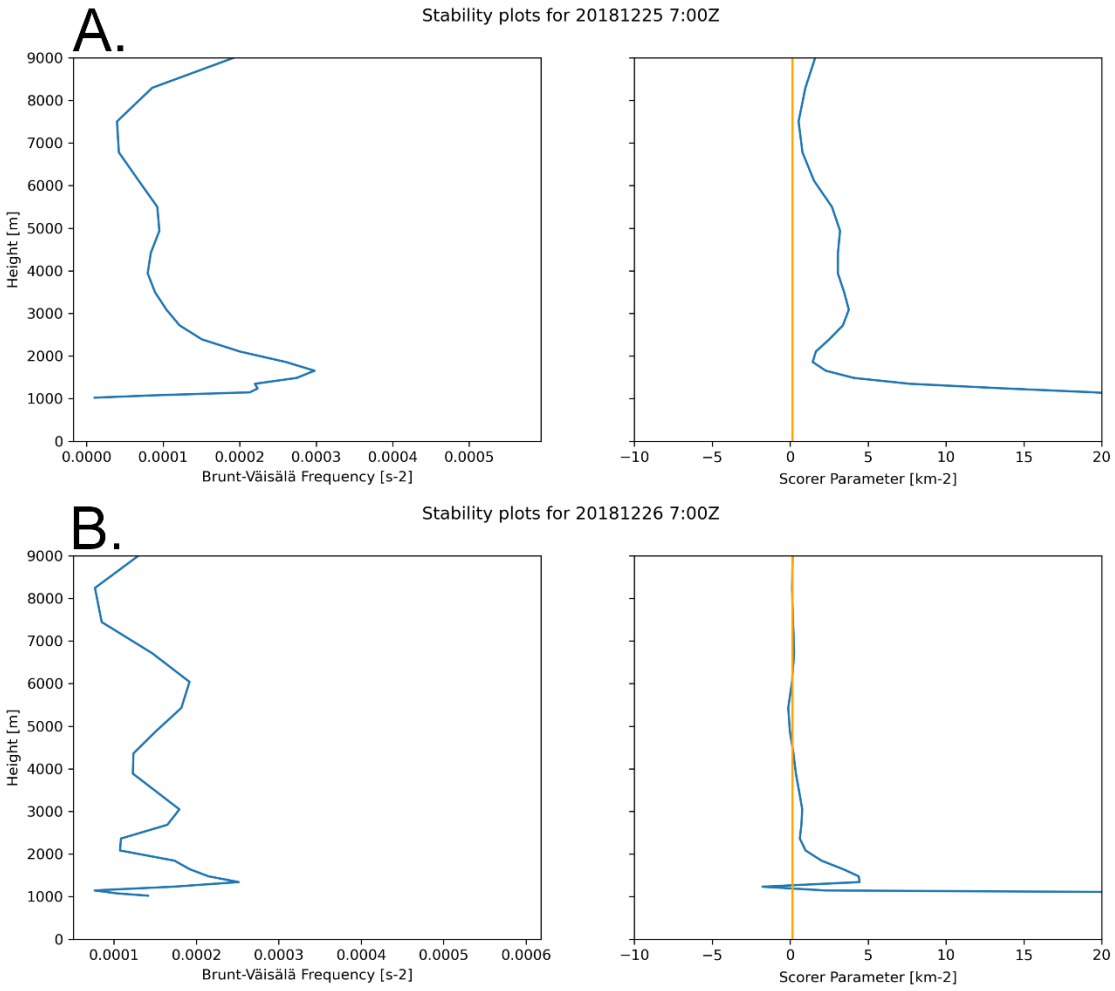
A.
Stability plots for 20181225 7:00Z
Height [m]
Brunt-Väisälä Frequency [s-2]
Scorer Parameter [km-2]
B.
Stability plots for 20181226 7:00Z
Height [m]
Brunt-Väisälä Frequency [s-2]
Scorer Parameter [km-2]

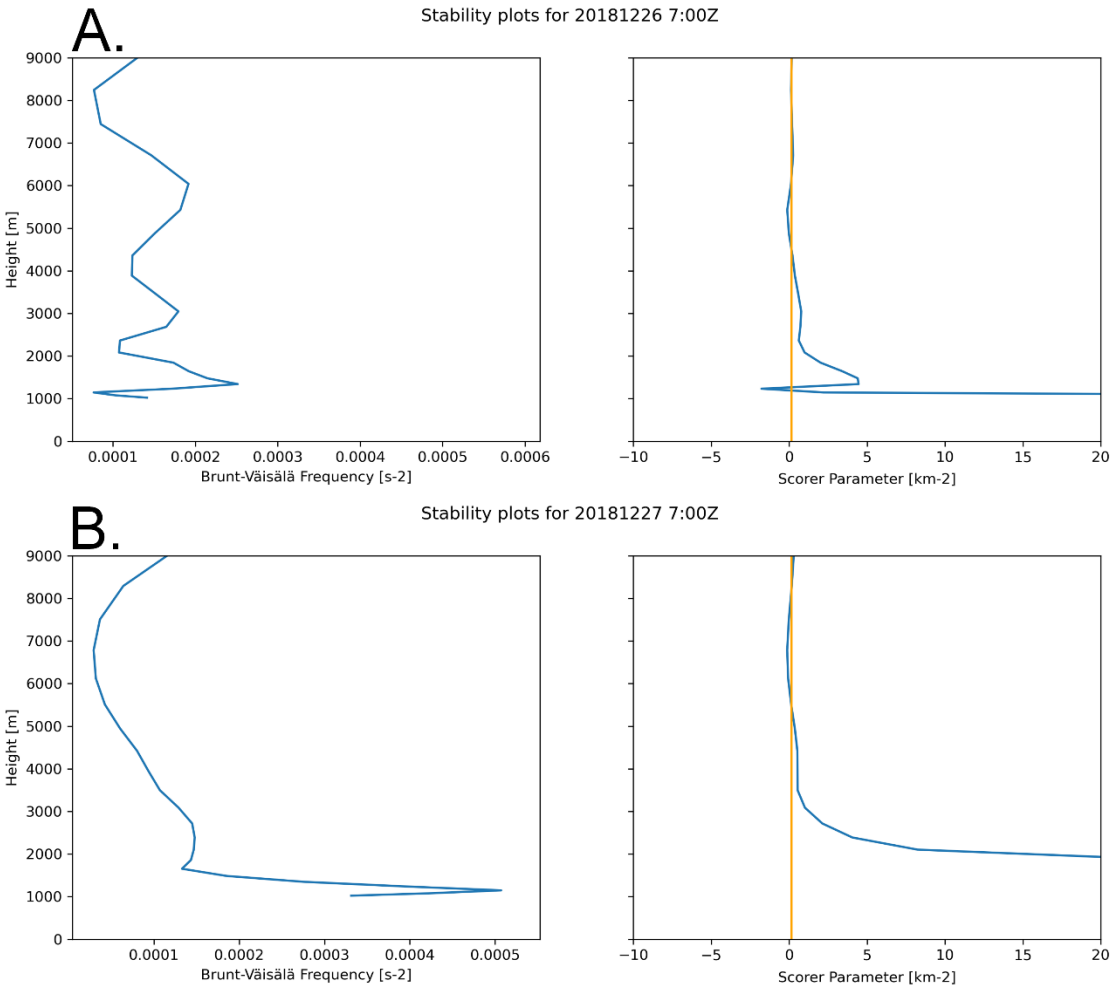
A.
Stability plots for 20181226 7:00Z
Height [m]
Brunt-Väisälä Frequency [s-2]
Scorer Parameter [km-2]
B.
Stability plots for 20181227 7:00Z
Height [m]
Brunt-Väisälä Frequency [s-2]
Scorer Parameter [km-2]

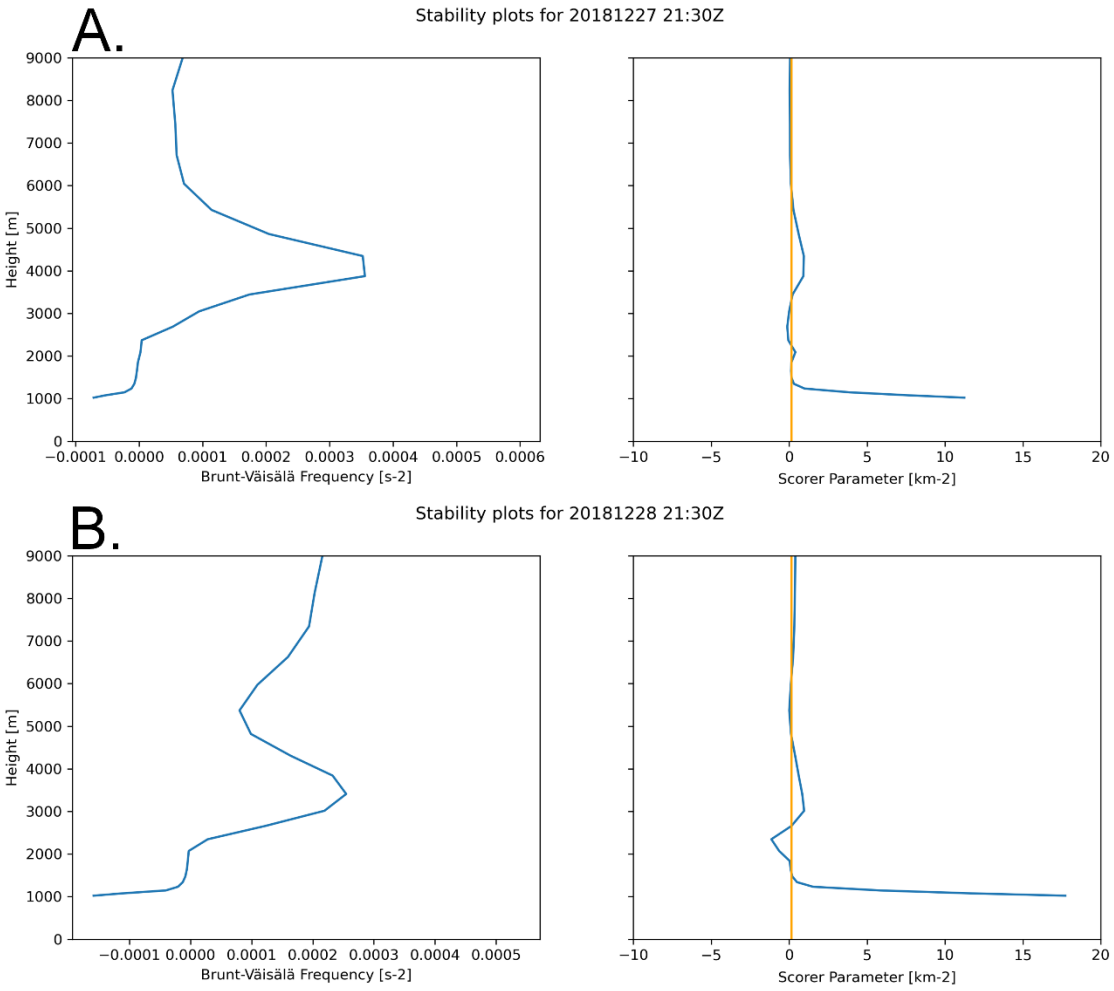
A.
Stability plots for 20181227 21:30Z
Height [m]
Brunt-Väisälä Frequency [s-2]
Scorer Parameter [km-2]
B.
Stability plots for 20181228 21:30Z
Height [m]
Brunt-Väisälä Frequency [s-2]
Scorer Parameter [km-2]

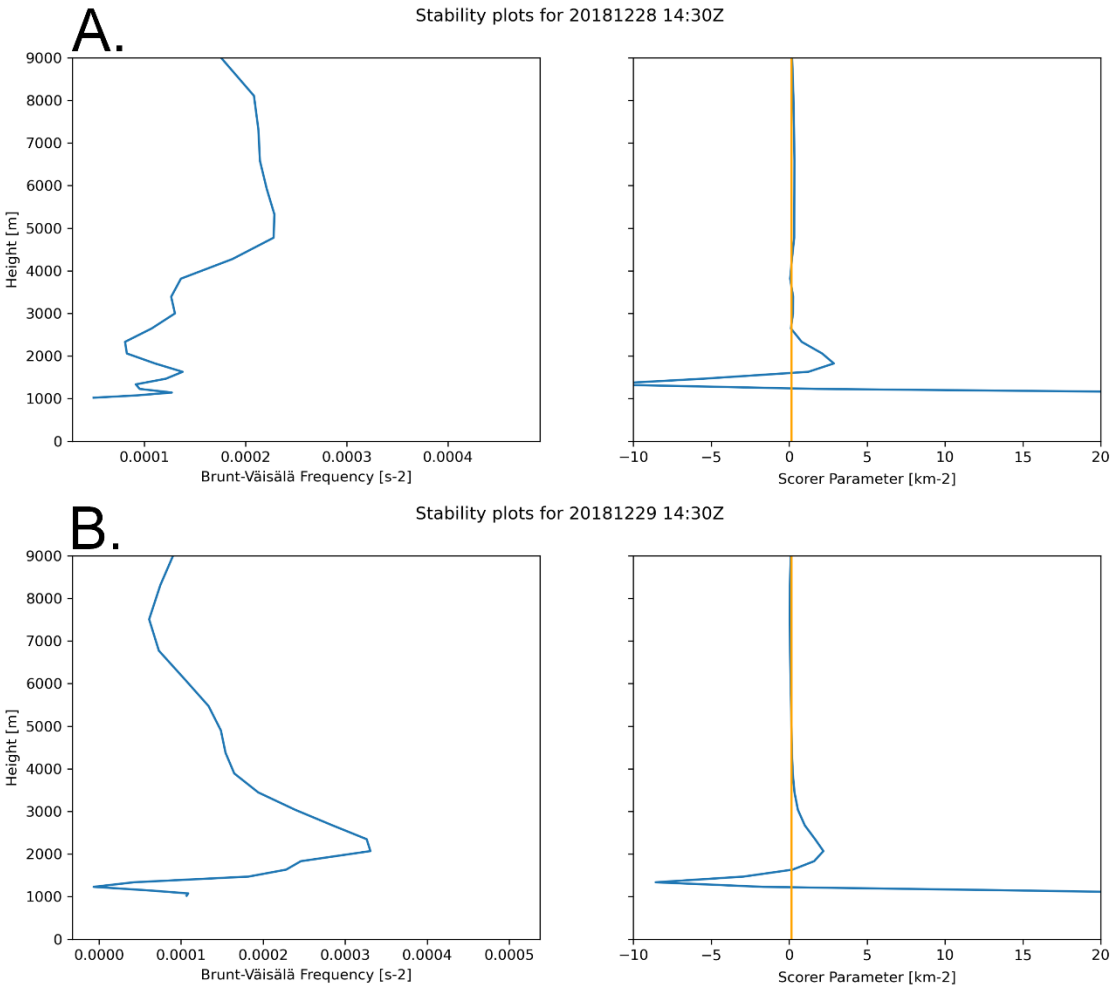
A.
Stability plots for 20181228 14:30Z
Height [m]
Brunt-Väisälä Frequency [s-2]
Scorer Parameter [km-2]
B.
Stability plots for 20181229 14:30Z
Height [m]
Brunt-Väisälä Frequency [s-2]
Scorer Parameter [km-2]

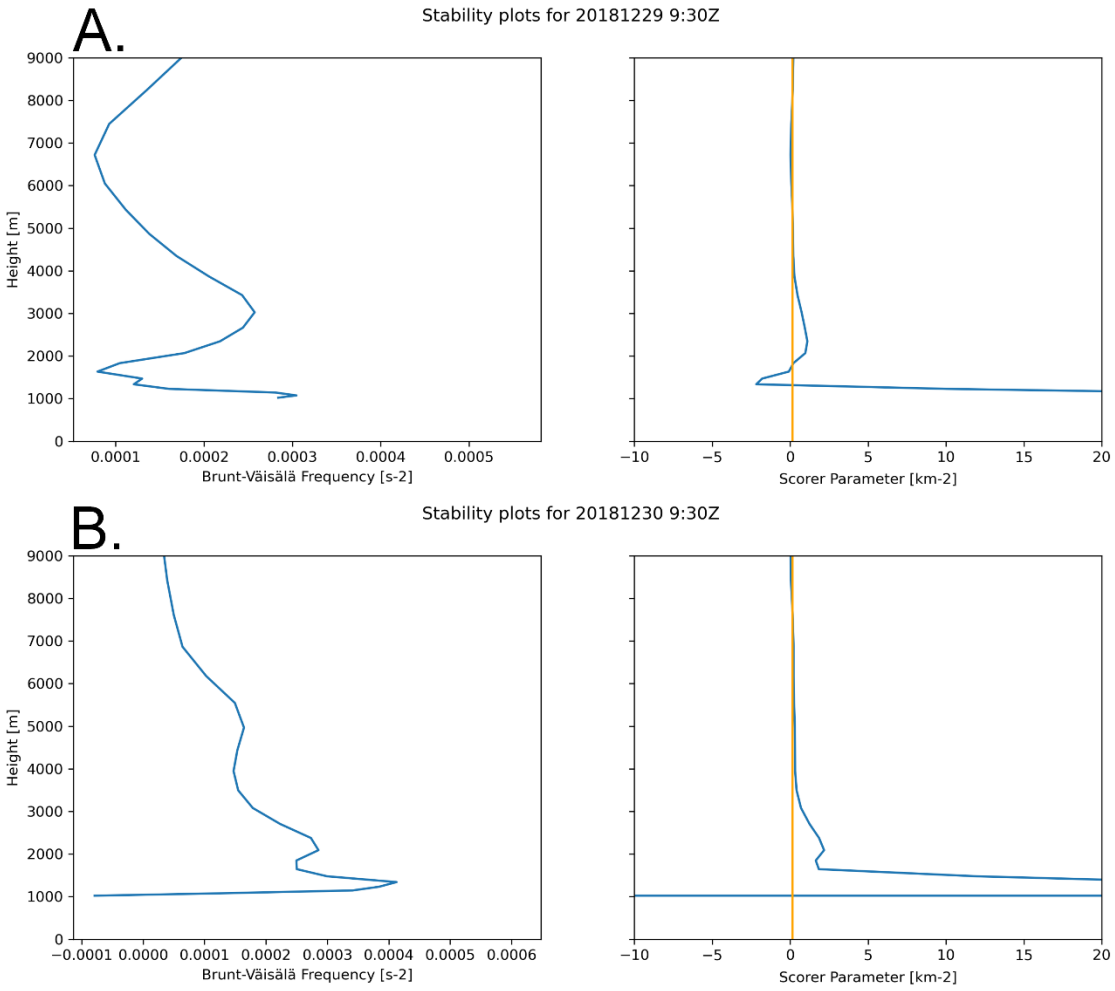
A.
Stability plots for 20181229 9:30Z
Height [m]
Brunt-Väisälä Frequency [s-2]
Scorer Parameter [km-2]
B.
Stability plots for 20181230 9:30Z
Height [m]
Brunt-Väisälä Frequency [s-2]
Scorer Parameter [km-2]

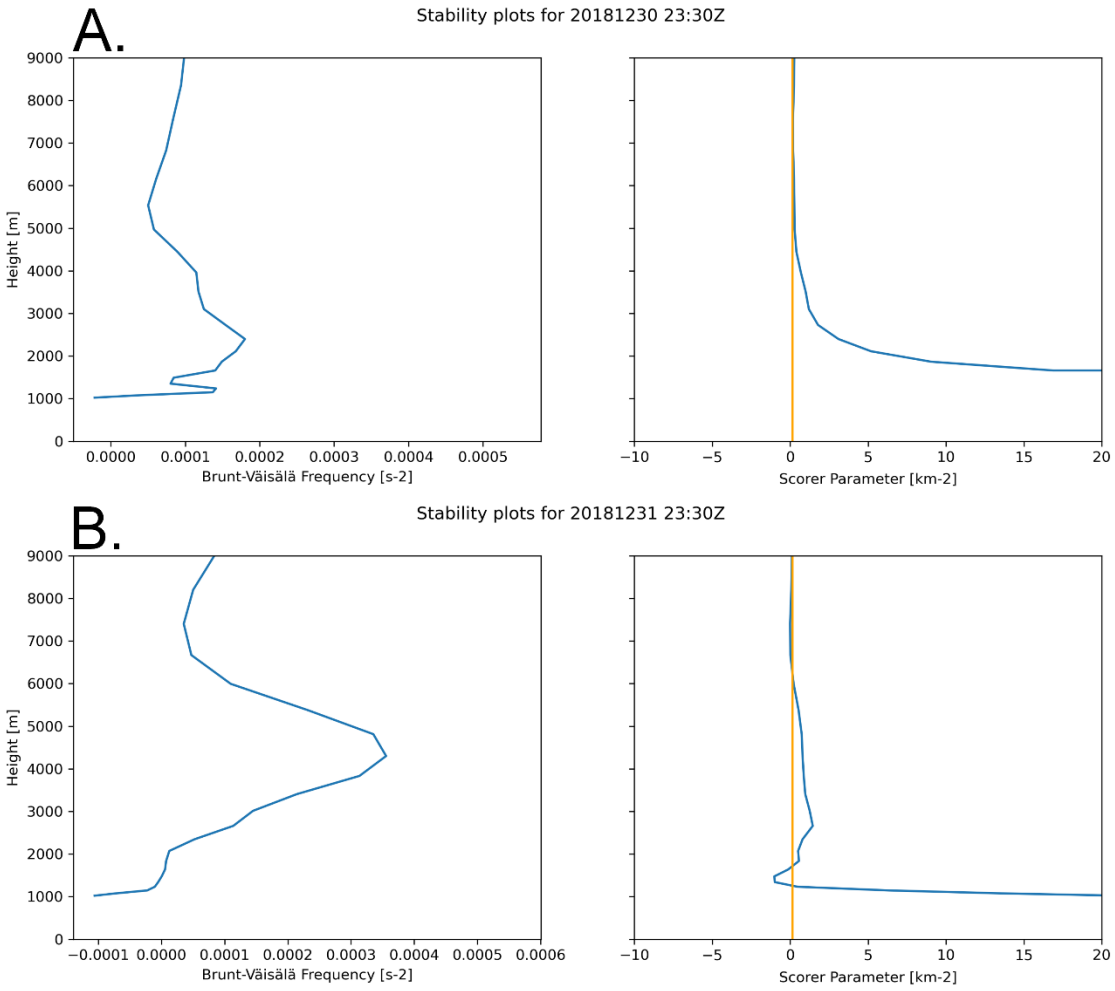
A.
Stability plots for 20181230 23:30Z
Height [m]
Brunt-Väisälä Frequency [s-2]
Scorer Parameter [km-2]
B.
Stability plots for 20181231 23:30Z
Height [m]
Brunt-Väisälä Frequency [s-2]
Scorer Parameter [km-2]

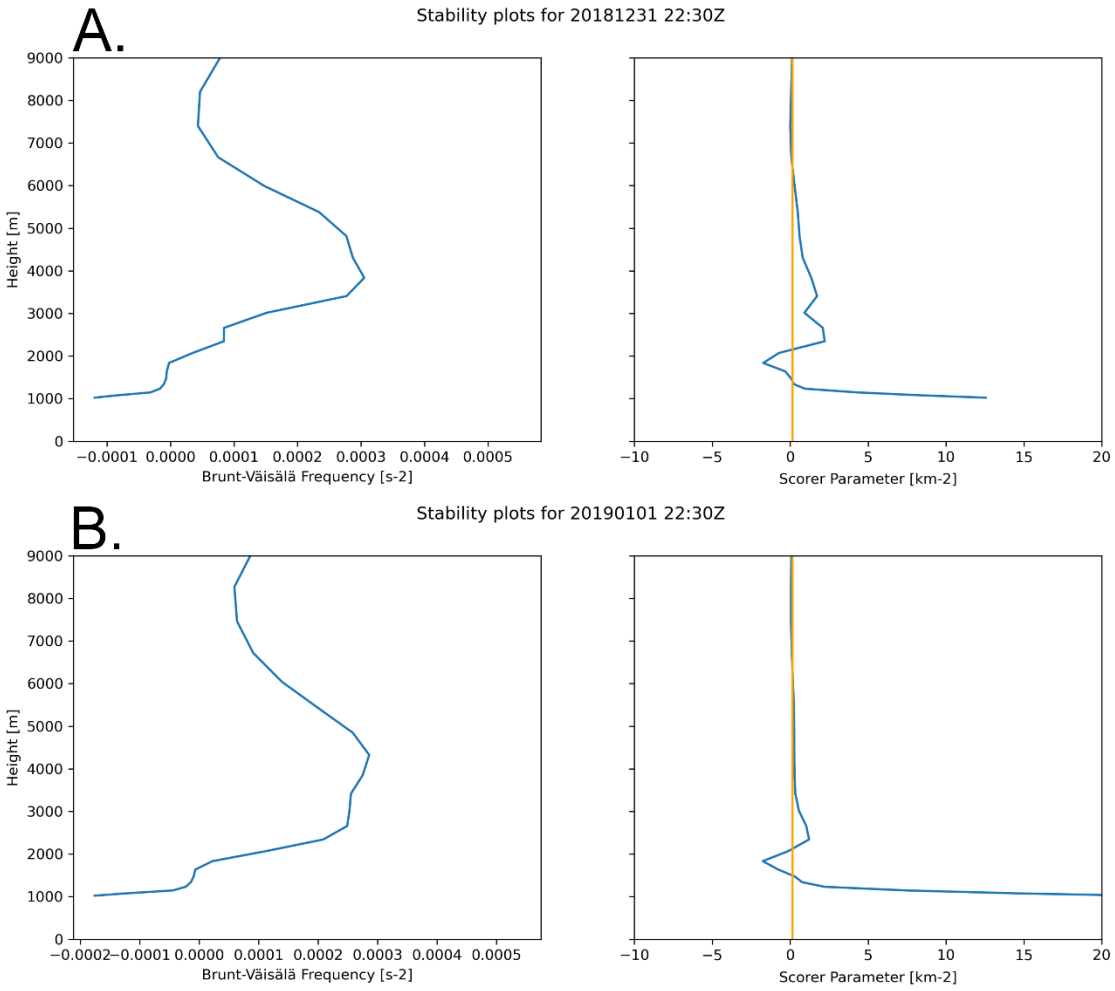
A.
Stability plots for 20181231 22:30Z
Height [m]
Brunt-Väisälä Frequency [s-2]
Scorer Parameter [km-2]
B.
Stability plots for 20190101 22:30Z
Height [m]
Brunt-Väisälä Frequency [s-2]
Scorer Parameter [km-2]

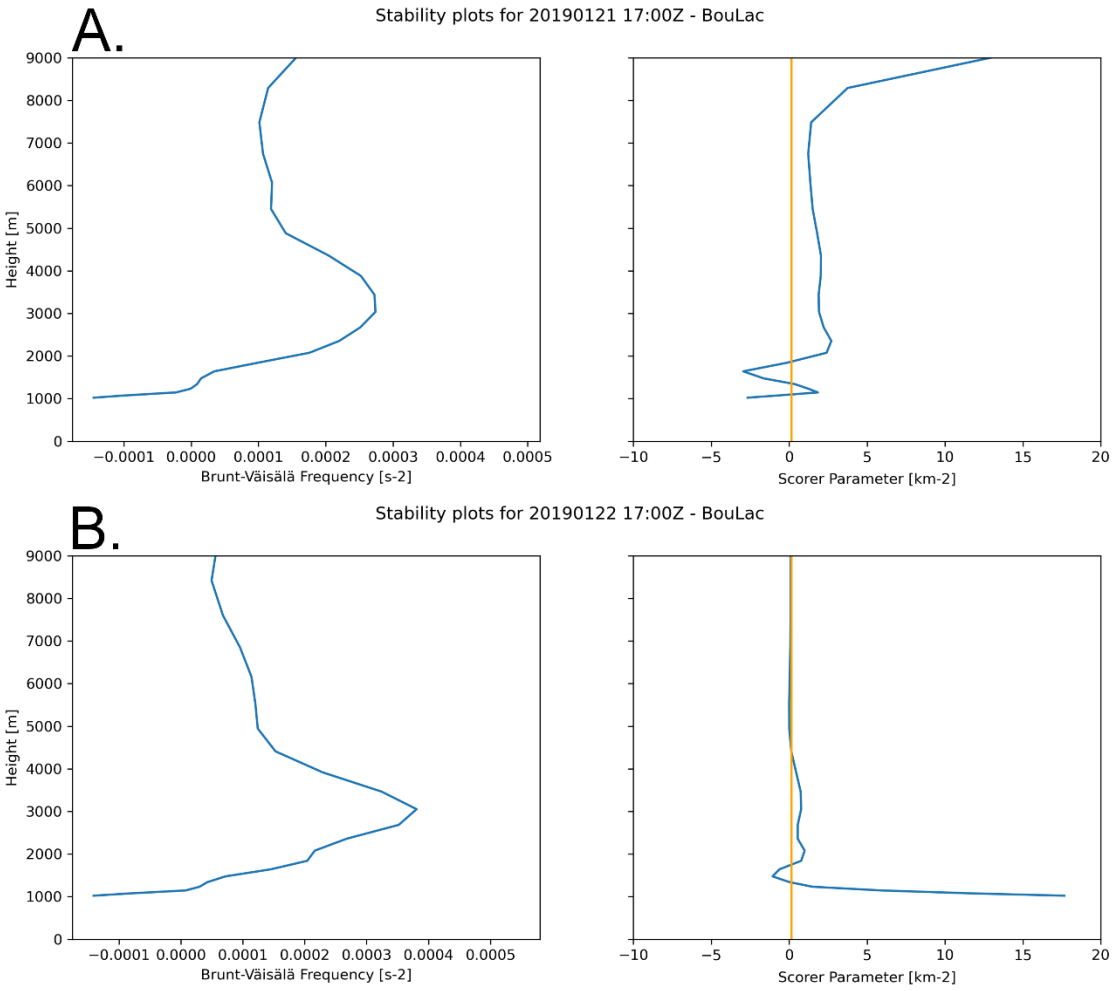
A.
Stability plots for 20190121 17:00Z - BouLac
Height [m]
Brunt-Väisälä Frequency [s-2]
Scorer Parameter [km-2]
B.
Stability plots for 20190122 17:00Z - BouLac
Height [m]
Brunt-Väisälä Frequency [s-2]
Scorer Parameter [km-2]

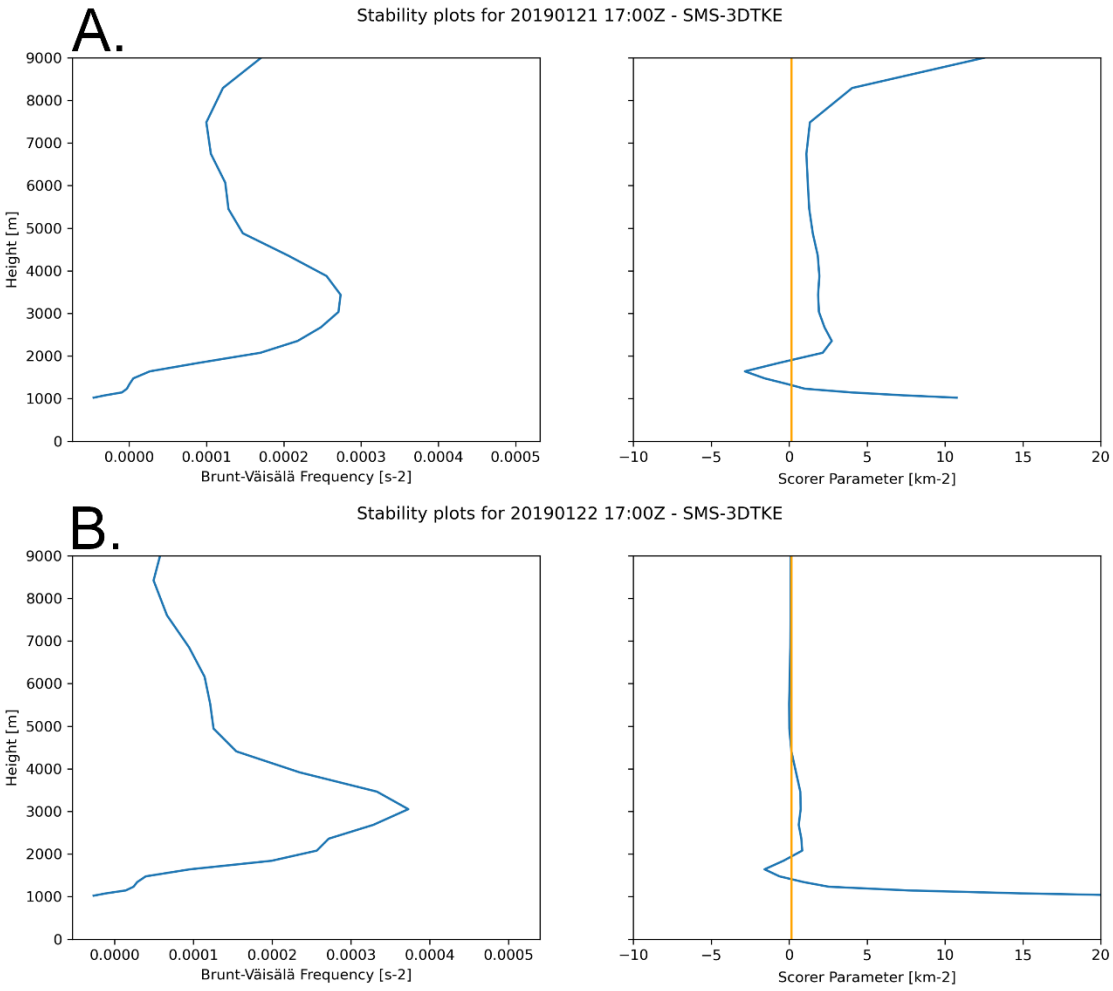
A.
Stability plots for 20190121 17:00Z - SMS-3DTKE
Height [m]
Brunt-Väisälä Frequency [s-2]
Scorer Parameter [km-2]
B.
Stability plots for 20190122 17:00Z - SMS-3DTKE
Height [m]
Brunt-Väisälä Frequency [s-2]
Scorer Parameter [km-2]

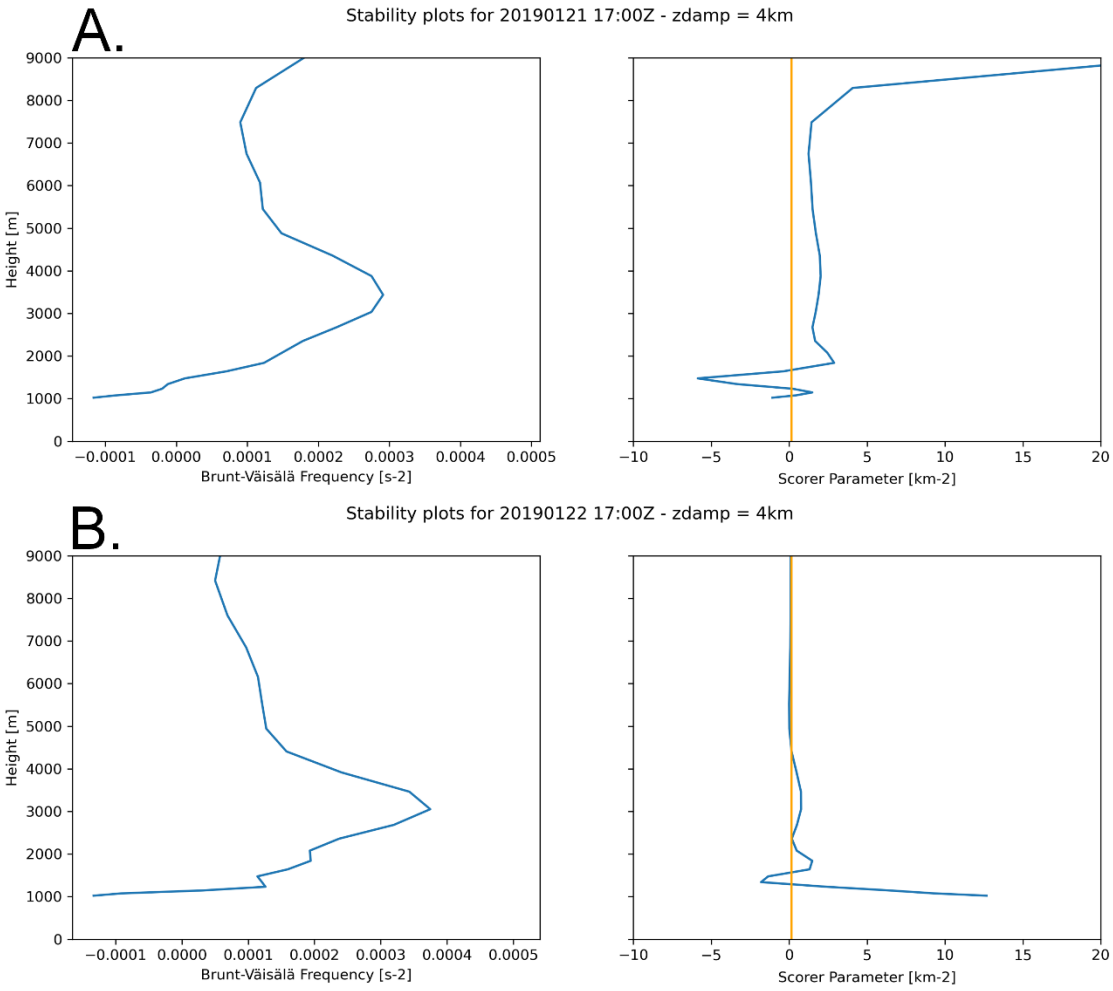
A.
Stability plots for 20190121 17:00Z - zdamp = 4km
Height [m]
Brunt-Väisälä Frequency [s-2]
Scorer Parameter [km-2]
B.
Stability plots for 20190122 17:00Z - zdamp = 4km
Height [m]
Brunt-Väisälä Frequency [s-2]
Scorer Parameter [km-2]

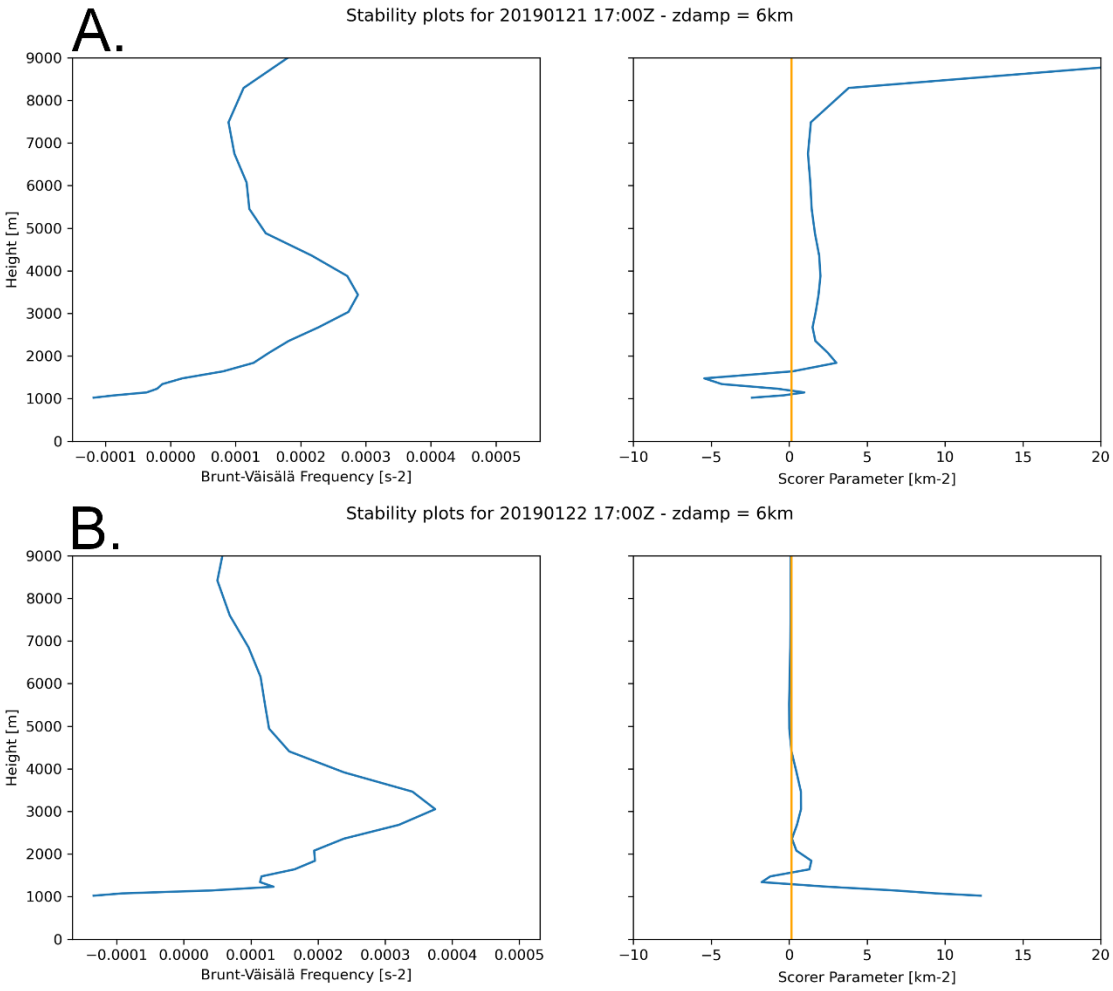
A.
Stability plots for 20190121 17:00Z - zdamp = 6km
Height [m]
Brunt-Väisälä Frequency [s-2]
Scorer Parameter [km-2]
B.
Stability plots for 20190122 17:00Z - zdamp = 6km
Height [m]
Brunt-Väisälä Frequency [s-2]
Scorer Parameter [km-2]

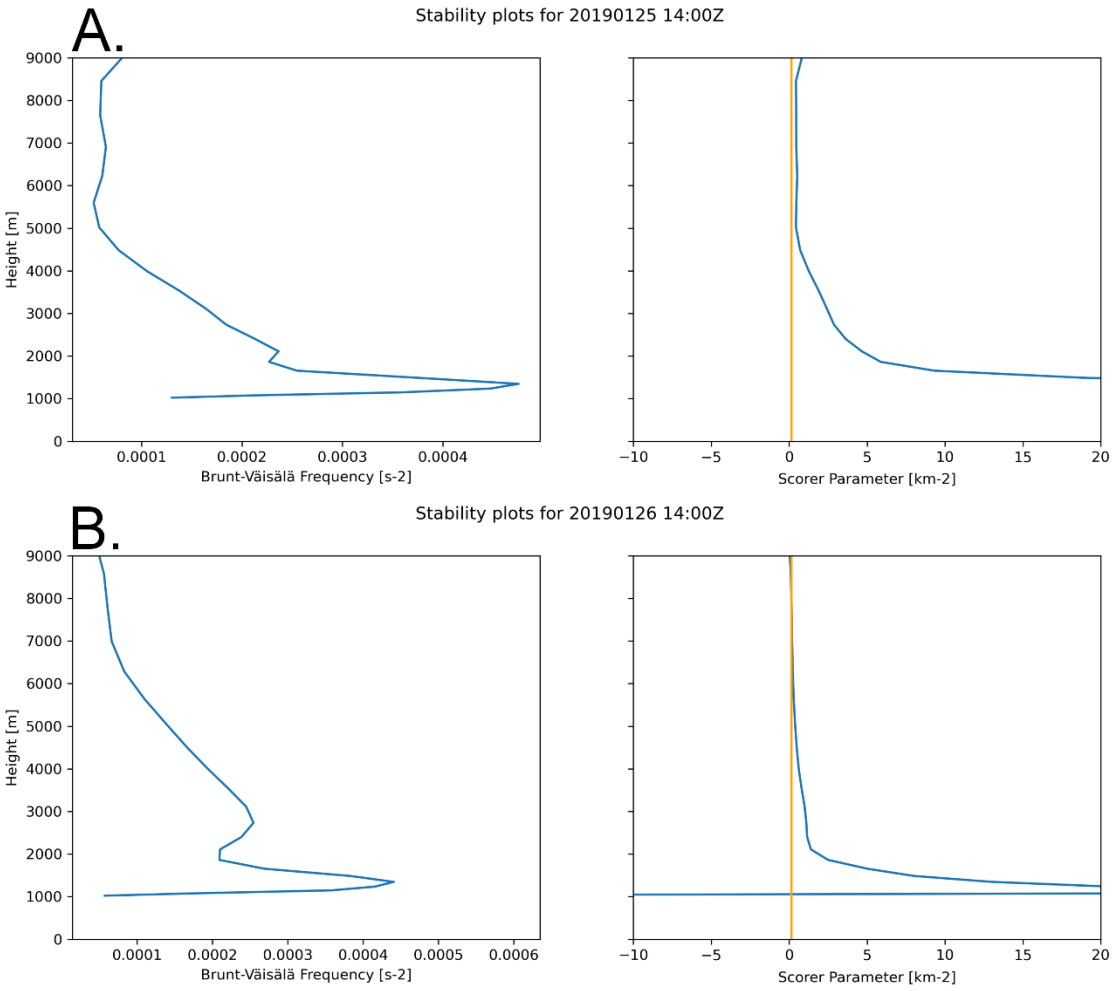
A.
Stability plots for 20190125 14:00Z
Height [m]
Brunt-Väisälä Frequency [s-2]
Scorer Parameter [km-2]
B.
Stability plots for 20190126 14:00Z
Height [m]
Brunt-Väisälä Frequency [s-2]
Scorer Parameter [km-2]

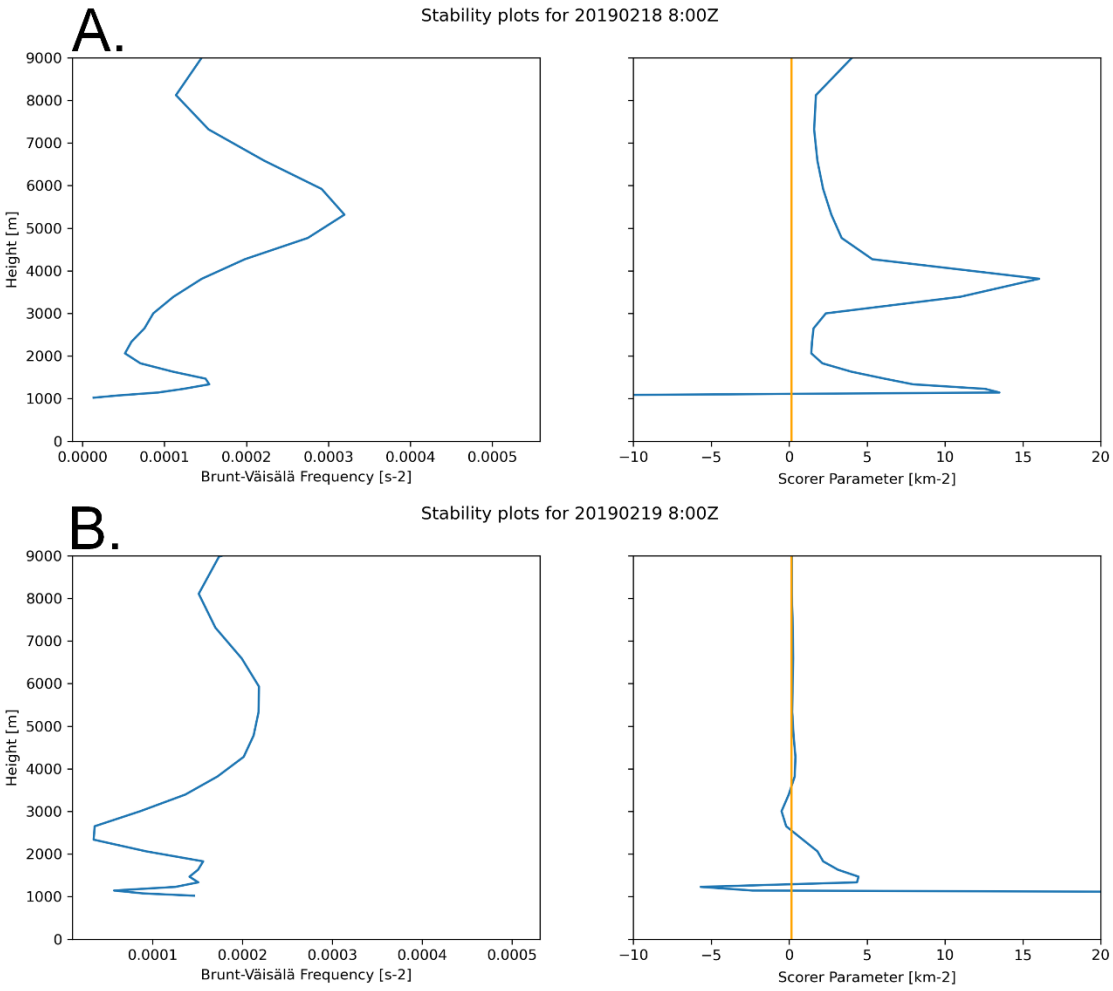
A.
Stability plots for 20190218 8:00Z
Height [m]
Brunt-Väisälä Frequency [s-2]
Scorer Parameter [km-2]
B.
Stability plots for 20190219 8:00Z
Height [m]
Brunt-Väisälä Frequency [s-2]
Scorer Parameter [km-2]

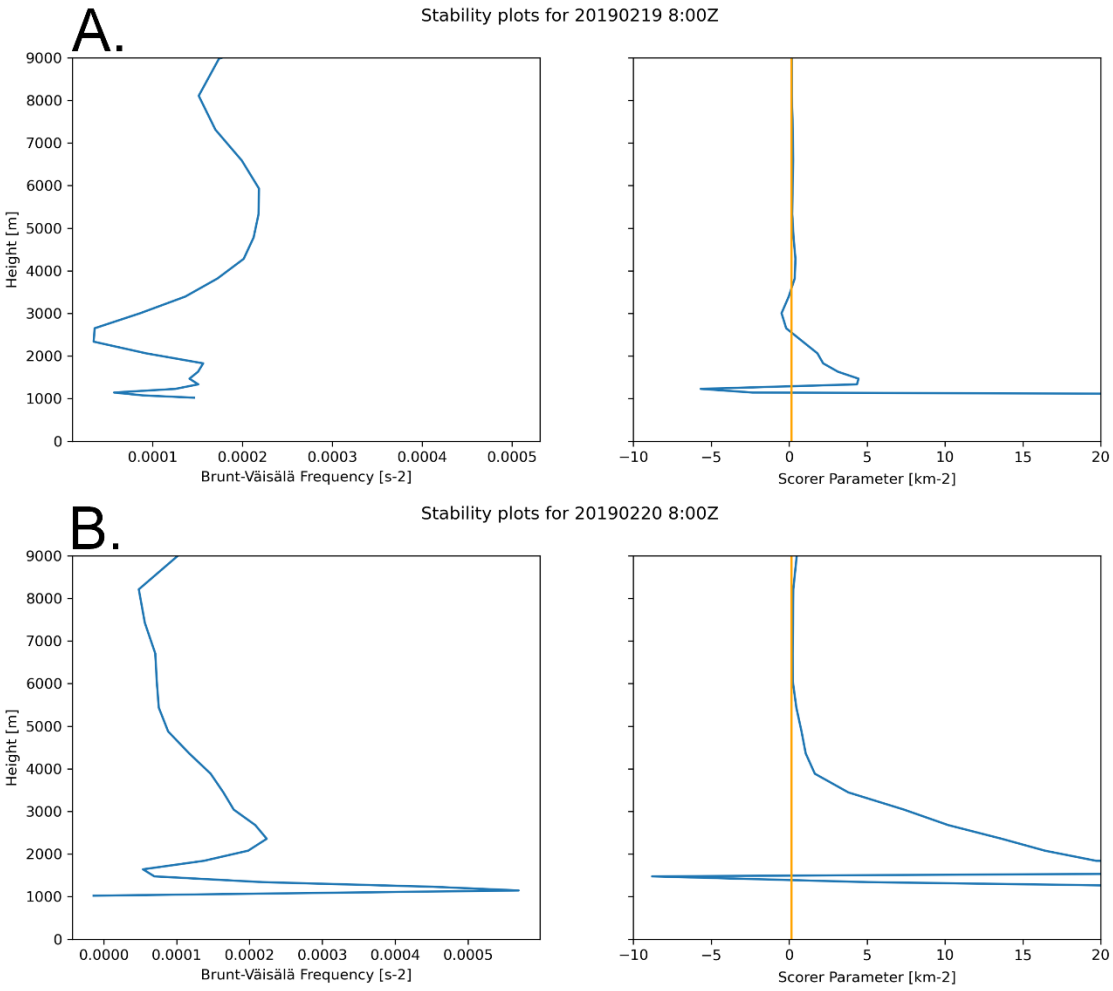
A.
Stability plots for 20190219 8:00Z
Height [m]
Brunt-Väisälä Frequency [s-2]
Scorer Parameter [km-2]
B.
Stability plots for 20190220 8:00Z
Height [m]
Brunt-Väisälä Frequency [s-2]
Scorer Parameter [km-2]

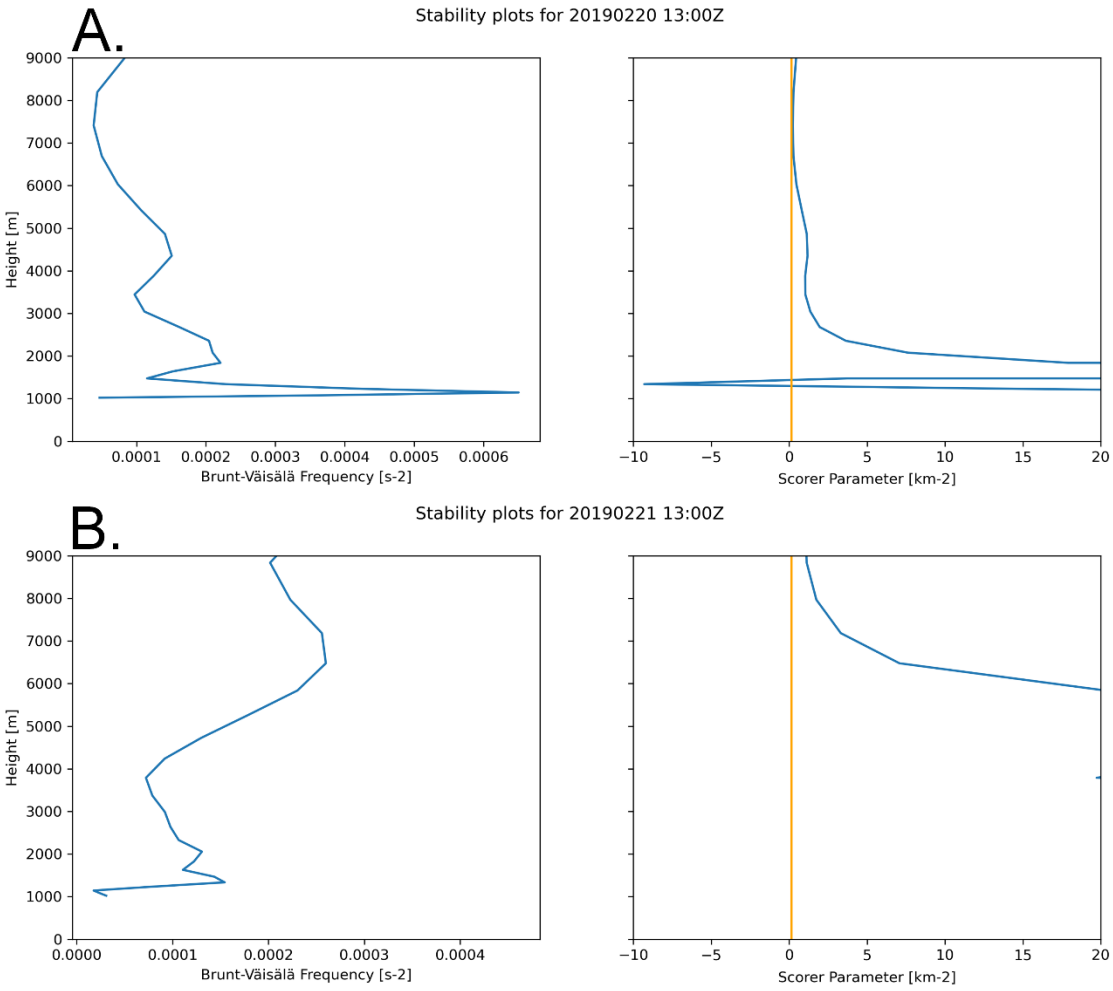
A.
Stability plots for 20190220 13:00Z
Height [m]
Brunt-Väisälä Frequency [s-2]
Scorer Parameter [km-2]
B.
Stability plots for 20190221 13:00Z
Height [m]
Brunt-Väisälä Frequency [s-2]
Scorer Parameter [km-2]

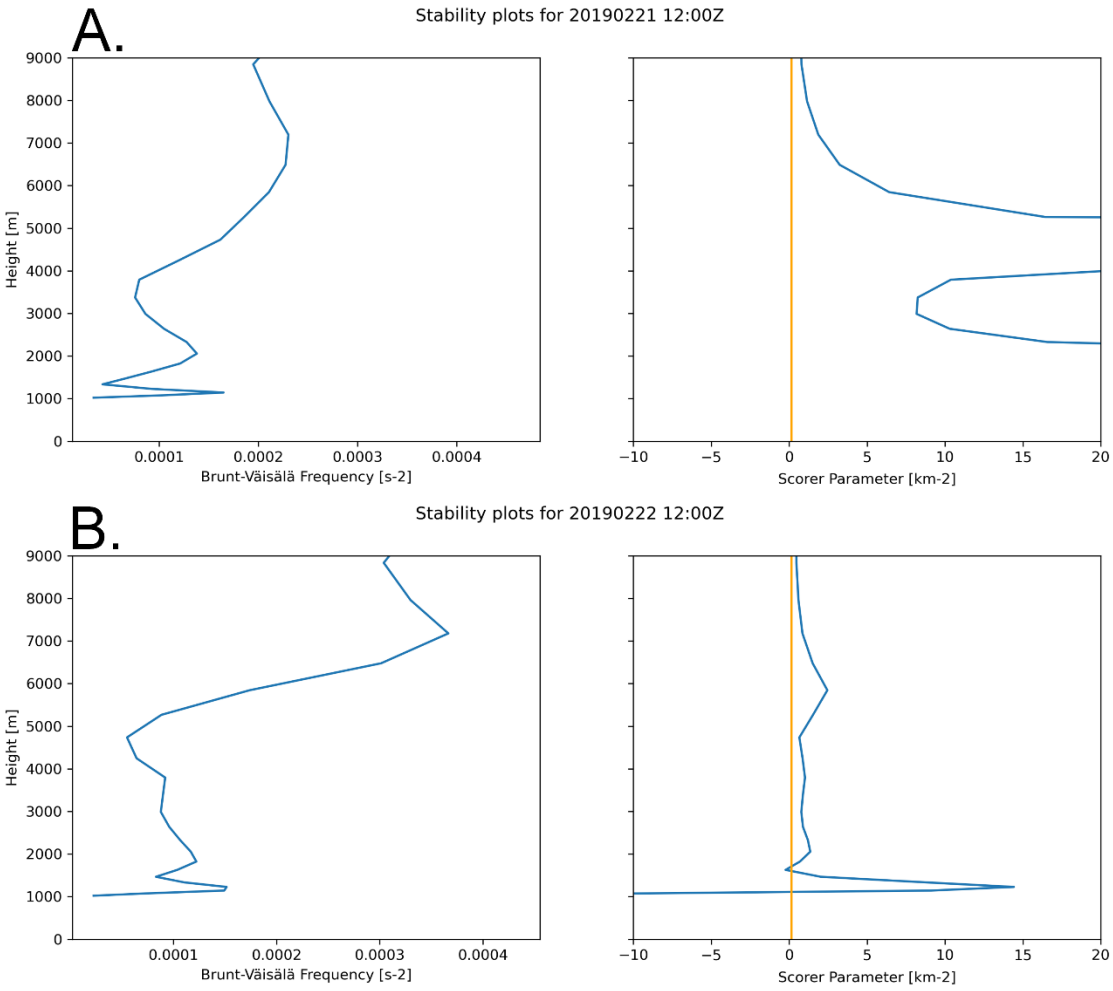
A.
Stability plots for 20190221 12:00Z
Height [m]
Brunt-Väisälä Frequency [s-2]
Scorer Parameter [km-2]
B.
Stability plots for 20190222 12:00Z
Height [m]
Brunt-Väisälä Frequency [s-2]
Scorer Parameter [km-2]

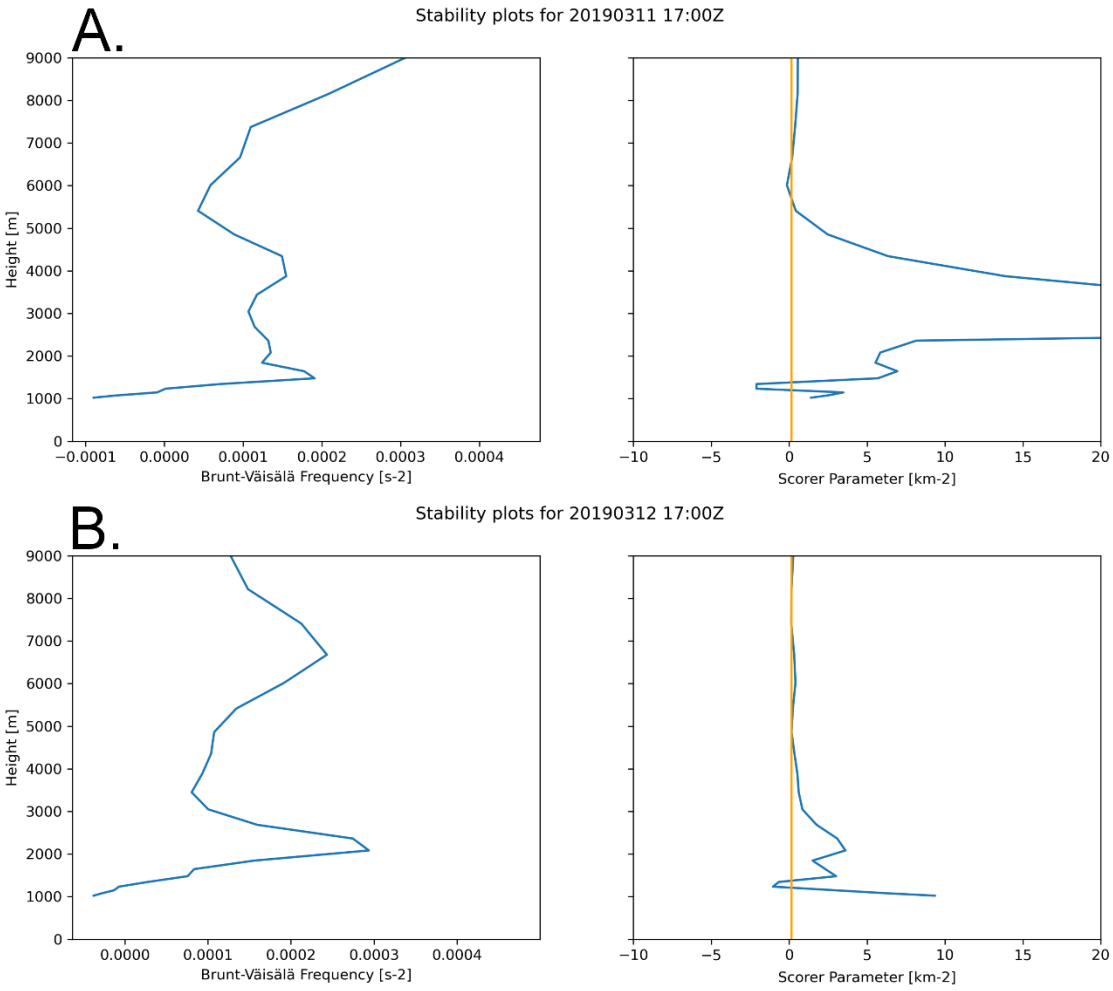
A.
Stability plots for 20190311 17:00Z
Height [m]
Brunt-Väisälä Frequency [s-2]
Scorer Parameter [km-2]
B.
Stability plots for 20190312 17:00Z
Height [m]
Brunt-Väisälä Frequency [s-2]
Scorer Parameter [km-2]

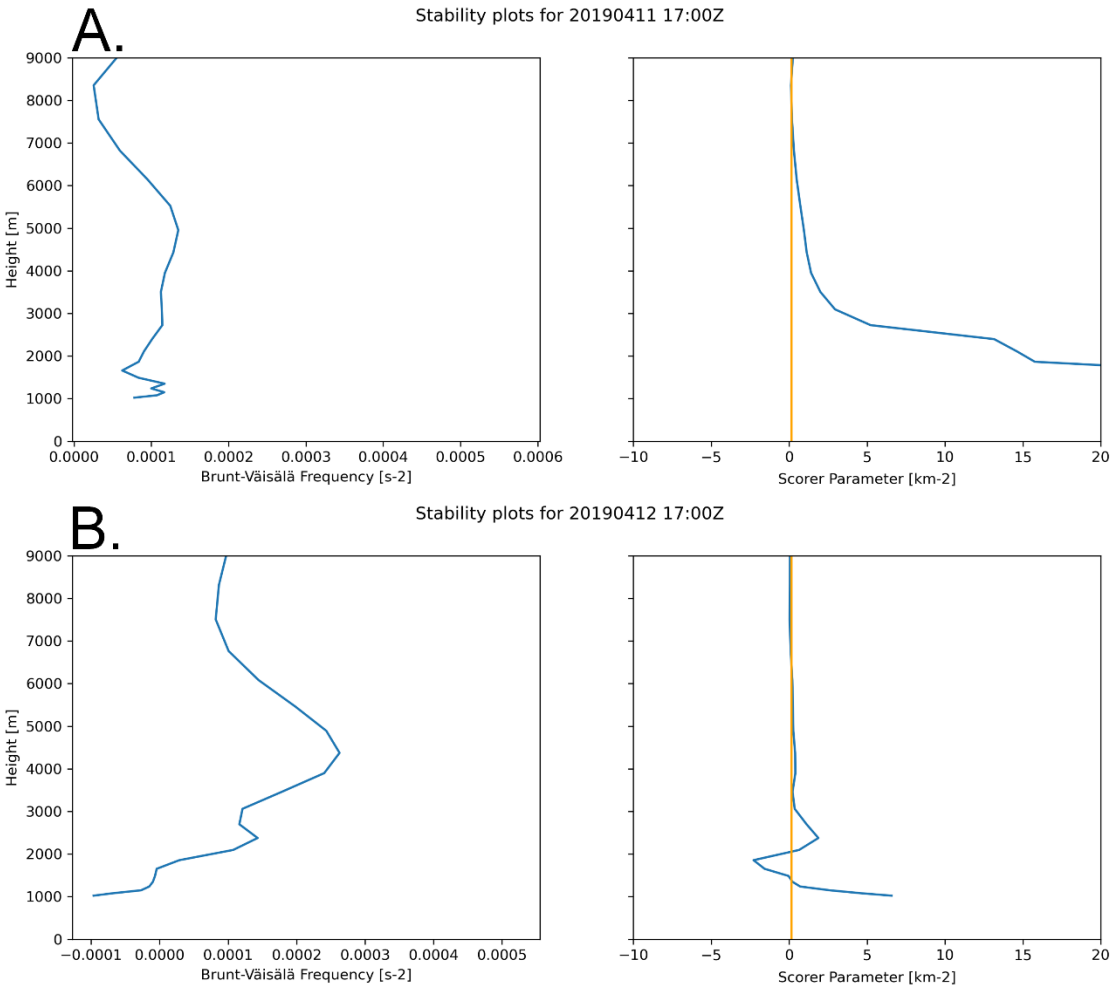
A.
Stability plots for 20190411 17:00Z
Height [m]
Brunt-Väisälä Frequency [s-2]
Scorer Parameter [km-2]
B.
Stability plots for 20190412 17:00Z
Height [m]
Brunt-Väisälä Frequency [s-2]
Scorer Parameter [km-2]

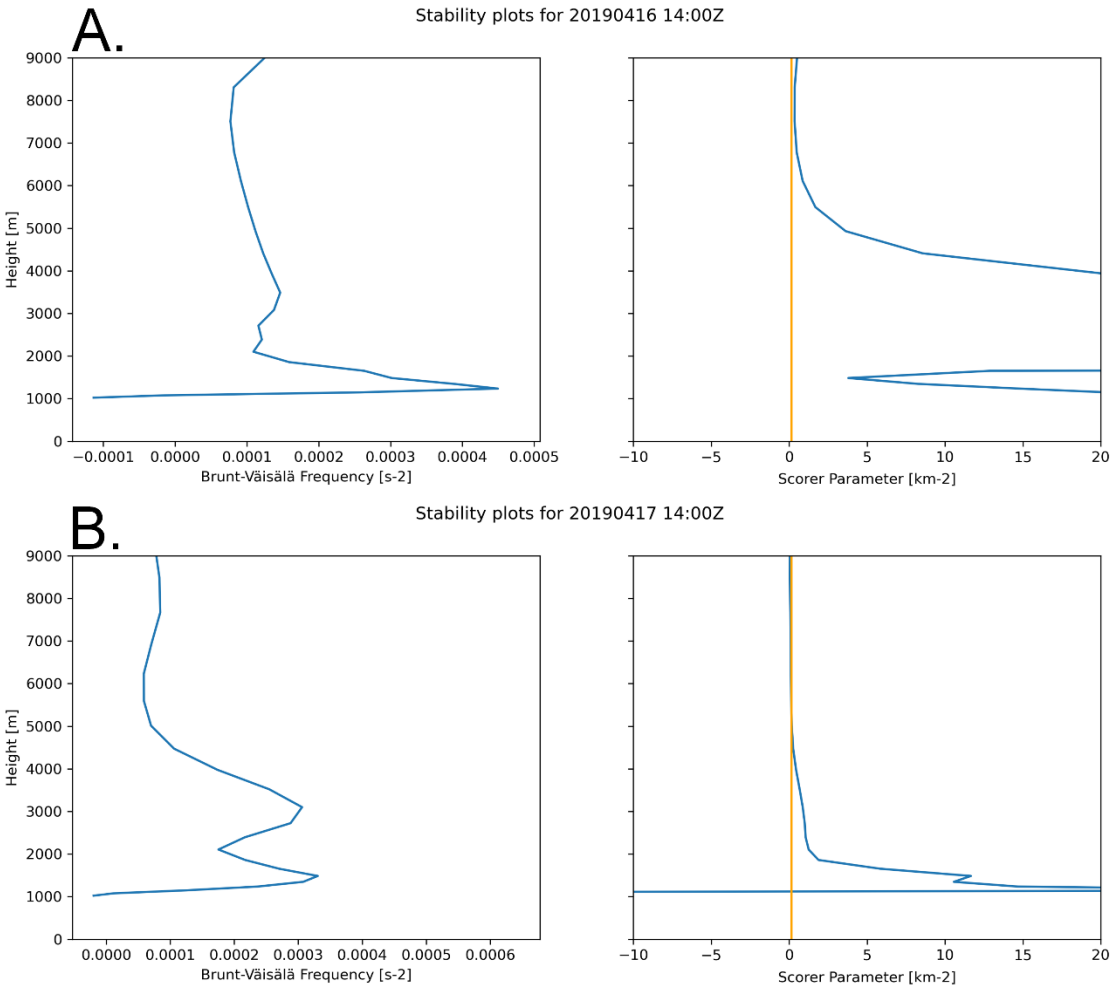
A.
Stability plots for 20190416 14:00Z
Height [m]
Brunt-Väisälä Frequency [s-2]
Scorer Parameter [km-2]
B.
Stability plots for 20190417 14:00Z
Height [m]
Brunt-Väisälä Frequency [s-2]
Scorer Parameter [km-2]

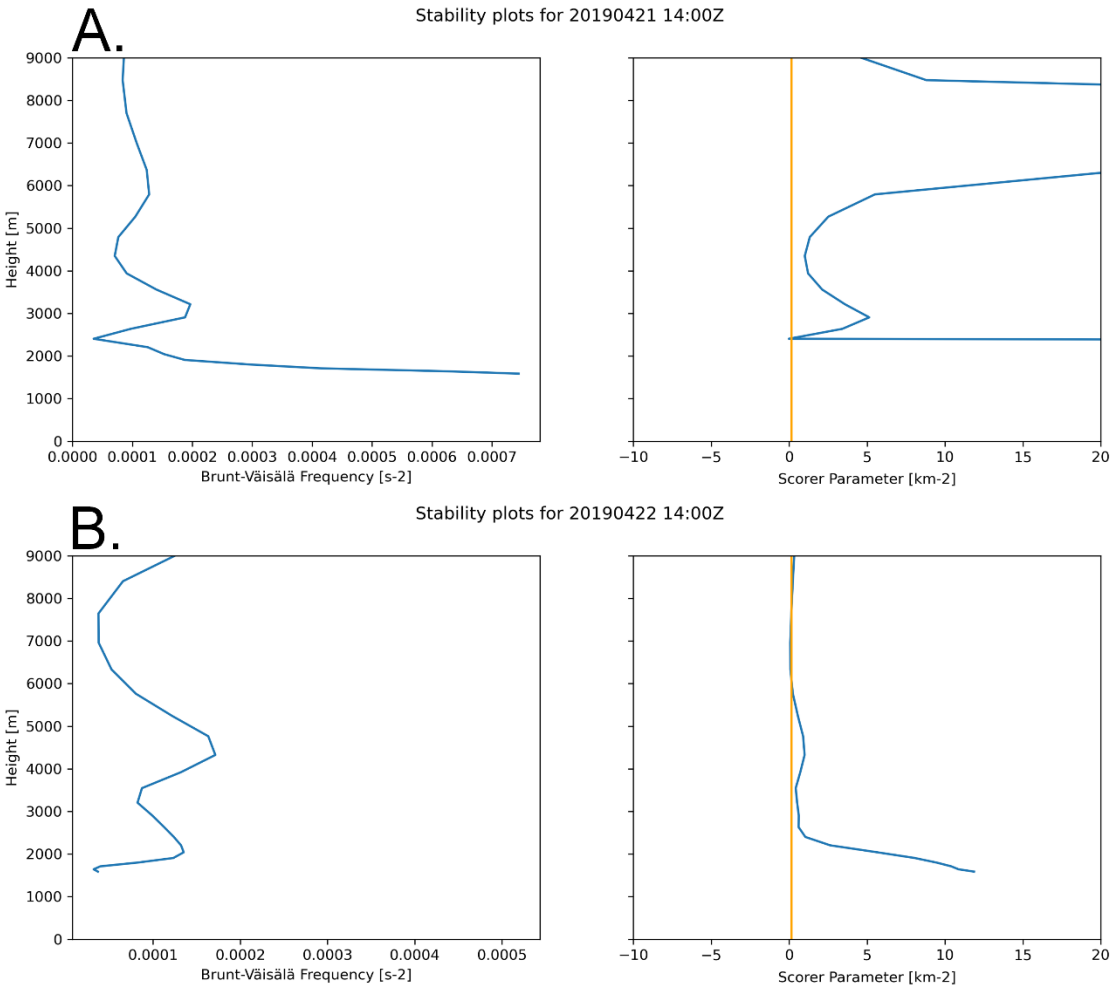
A.
Stability plots for 20190421 14:00Z
Height [m]
Brunt-Väisälä Frequency [s-2]
Scorer Parameter [km-2]
B.
Stability plots for 20190422 14:00Z
Height [m]
Brunt-Väisälä Frequency [s-2]
Scorer Parameter [km-2]

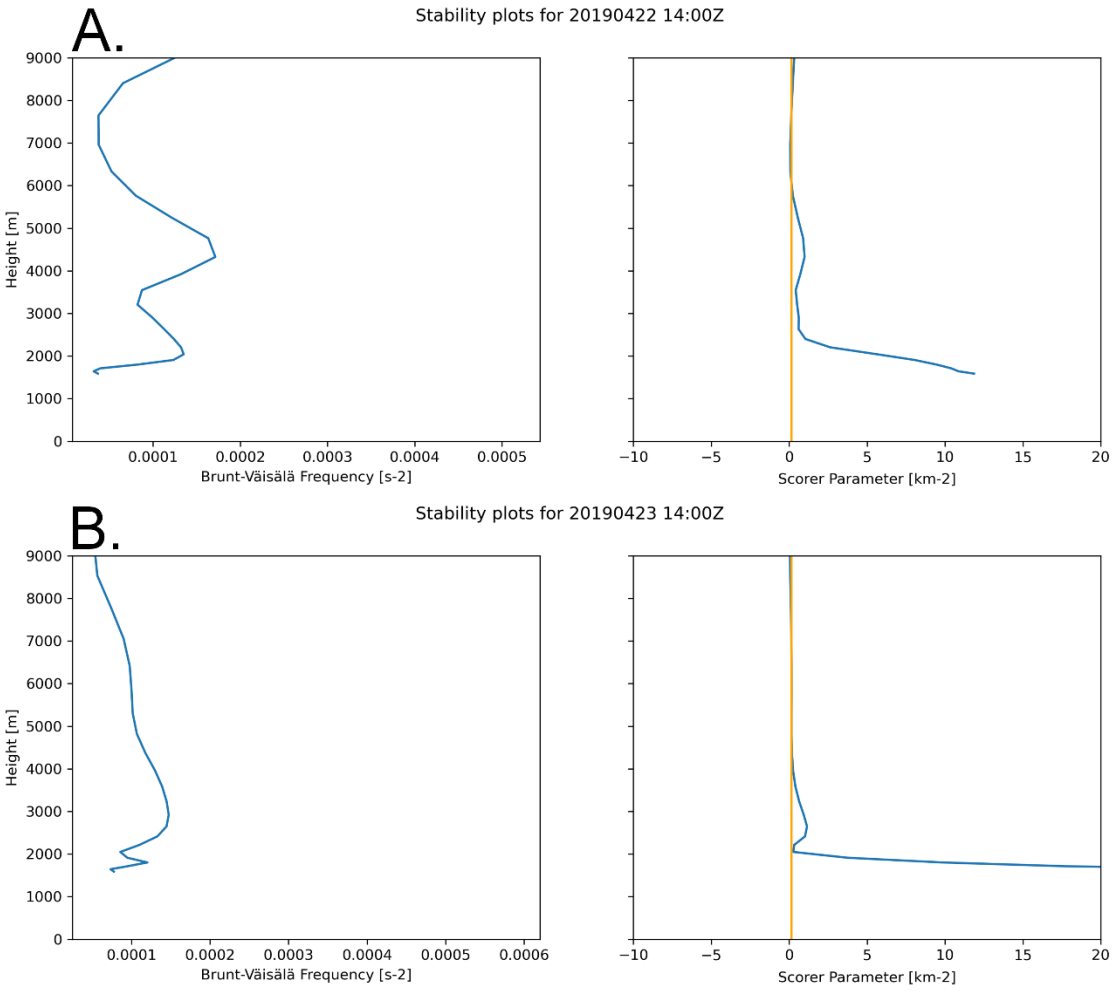
A.
Stability plots for 20190422 14:00Z
Height [m]
Brunt-Väisälä Frequency [s-2]
Scorer Parameter [km-2]
B.
Stability plots for 20190423 14:00Z
Height [m]
Brunt-Väisälä Frequency [s-2]
Scorer Parameter [km-2]

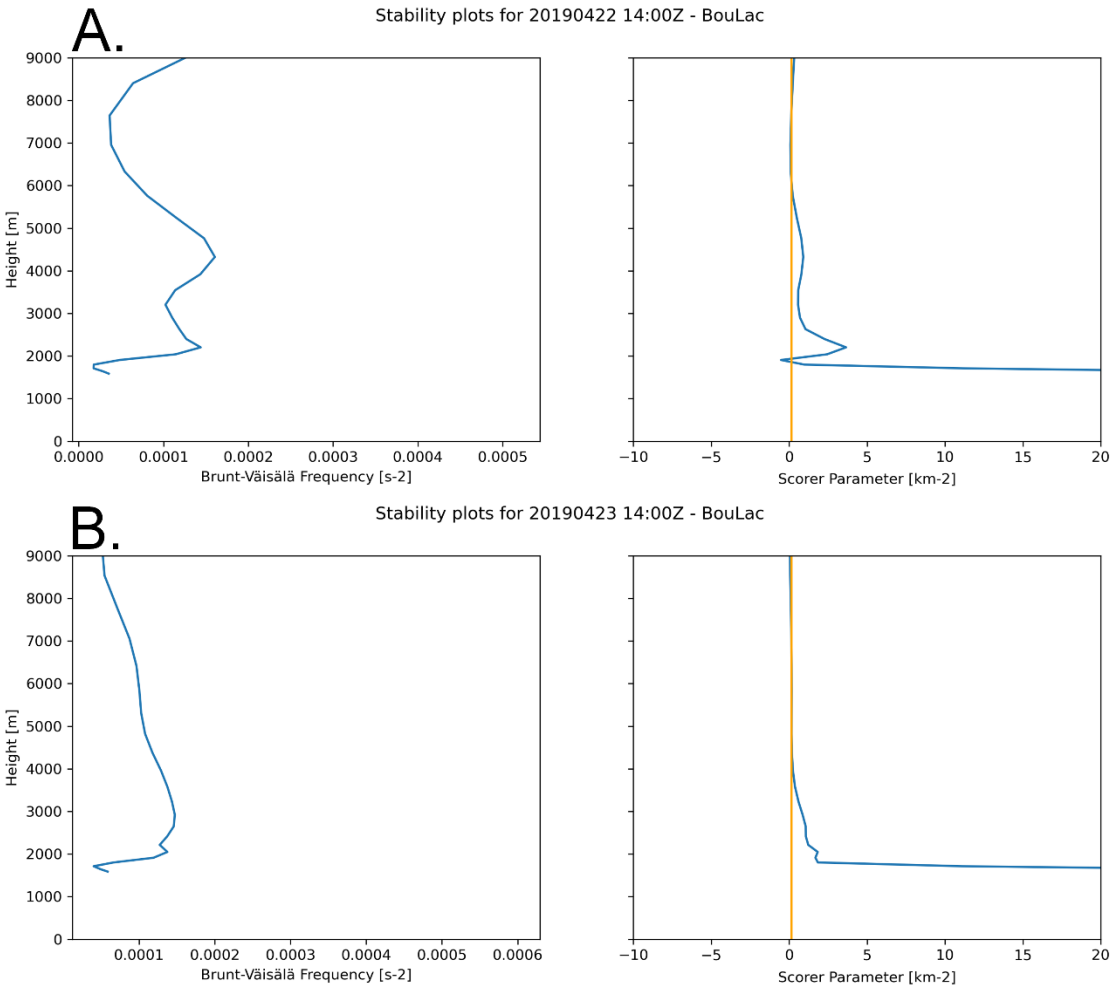
A.
Stability plots for 20190422 14:00Z - BouLac
Height [m]
Brunt-Väisälä Frequency [s-2]
Scorer Parameter [km-2]
B.
Stability plots for 20190423 14:00Z - BouLac
Height [m]
Brunt-Väisälä Frequency [s-2]
Scorer Parameter [km-2]

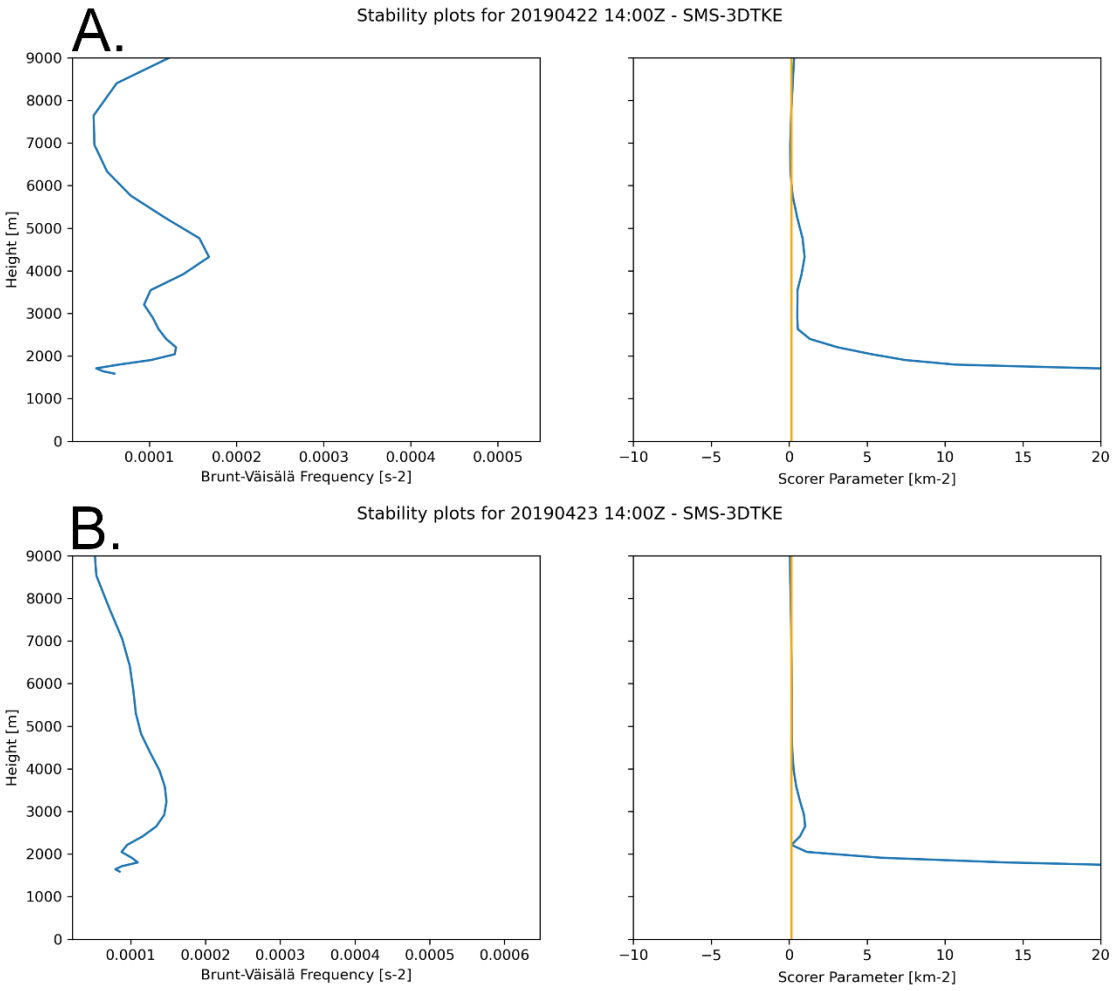
A.
Stability plots for 20190422 14:00Z - SMS-3DTKE
Height [m]
Brunt-Väisälä Frequency [s-2]
Scorer Parameter [km-2]
B.
Stability plots for 20190423 14:00Z - SMS-3DTKE
Height [m]
Brunt-Väisälä Frequency [s-2]
Scorer Parameter [km-2]

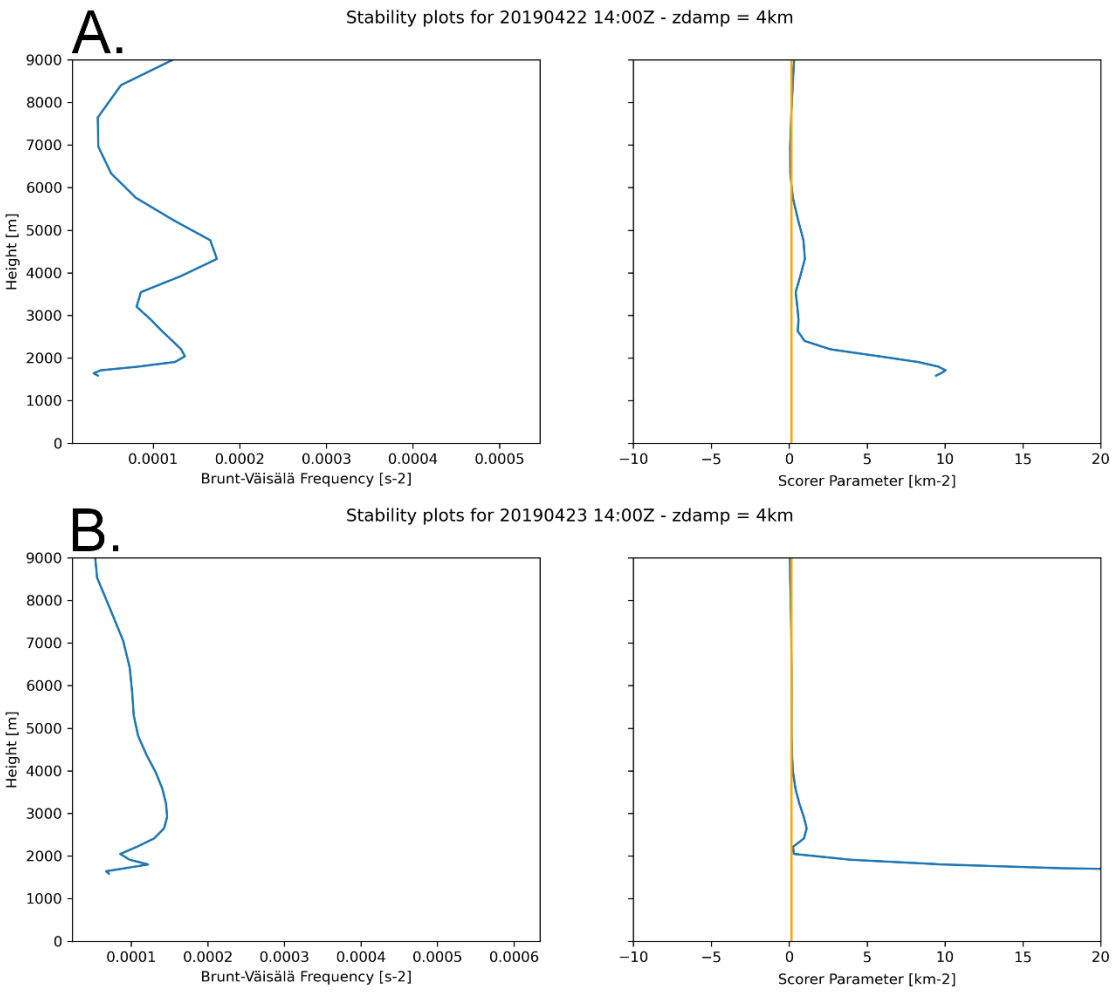
A.
Stability plots for 20190422 14:00Z - zdamp = 4km
Height [m]
Brunt-Väisälä Frequency [s-2]
Scorer Parameter [km-2]
B.
Stability plots for 20190423 14:00Z - zdamp = 4km
Height [m]
Brunt-Väisälä Frequency [s-2]
Scorer Parameter [km-2]

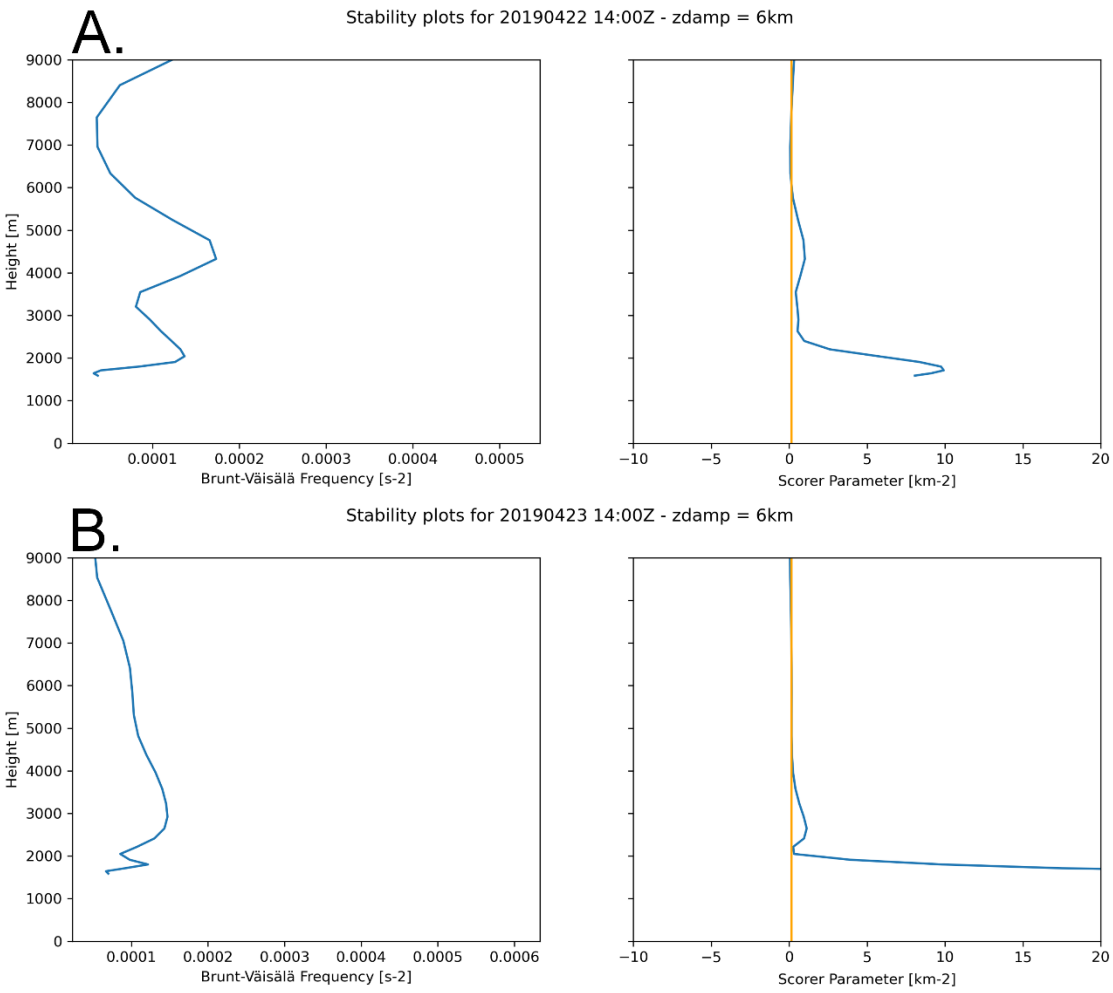
A.
Stability plots for 20190422 14:00Z - zdamp = 6km
Height [m]
Brunt-Väisälä Frequency [s-2]
Scorer Parameter [km-2]
B.
Stability plots for 20190423 14:00Z - zdamp = 6km
Height [m]
Brunt-Väisälä Frequency [s-2]
Scorer Parameter [km-2]

Appendix B – WRF Model namelist.input Settings

B1. WRF namelist.input settings for 22 January 2019. A setting of '-1' means the default values for the suite were used.

```
&time_control
 run_days                  = 0,
 run_hours                 = 24,
 run_minutes               = 0,
 run_seconds               = 0,
 start_year                = 2019, 2019,
 start_month               = 01,   01,
 start_day                 = 22,   22,
 start_hour                = 00,   00,
 end_year                  = 2019, 2019,
 end_month                 = 01,   01,
 end_day                   = 23,   23,
 end_hour                  = 00,   00,
 interval_seconds          = 3600,
 input_from_file           = .true.,.true.,
 history_interval          = 60,  30,
 frames_per_outfile        = 2, 4,
 restart                   = .true.,
 restart_interval          = 1440,
 io_form_history           = 2,
 io_form_restart           = 2,
 io_form_input             = 2,
 io_form_boundary          = 2,
 debug_level               = 0,
 /

&domains
time_step              = 12,
time_step_fract_num    = 0,
time_step_fract_den    = 1,
max_dom                = 2,
e_we                   = 150,    136,
e_sn                   = 130,    118,
e_vert                 = 35,     35,
p_top_requested        = 5000,
num_metgrid_levels     = 41,
num_metgrid_soil_levels = 9,
dx                     = 3000,   1000,
dy                     = 3000,   1000,
grid_id                = 1,      2,
parent_id              = 1,      1,
i_parent_start         = 1,      53,
```

```
j_parent_start          = 1,       46,
parent_grid_ratio       = 1,        3,
parent_time_step_ratio  = 1,        3,
feedback                = 0,
smooth_option           = 0,
nproc_x                 = -1,
nproc_y                 = -1,
/

 &physics
 physics_suite                  = 'CONUS'
 mp_physics                     = -1,    -1,
 cu_physics                     = -1,    -1,
 ra_lw_physics                  = -1,    -1,
 ra_sw_physics                  = -1,    -1,
 bl_pbl_physics                 = -1,    -1,
 sf_sfclay_physics              = -1,    -1,
 sf_surface_physics             = -1,    -1,
 sf_urban_physics               = 2,     2,
 /

 &fdda
 /

 &dynamics
 hybrid_opt                     = 2,
 w_damping                      = 0,
 diff_opt                       = 2,      2,
 km_opt                         = 4,      4,
 diff_6th_opt                   = 0,      0,
 diff_6th_factor                = 0.12,   0.12,
 base_temp                      = 290.
 damp_opt                       = 3,
 zdamp                          = 5000.,  5000.,
 dampcoef                       = 0.2,    0.2,
 khdif                          = 0,      0,
 kvdif                          = 0,      0,
 non_hydrostatic                = .true., .true.,
 moist_adv_opt                  = 1,      1,
 scalar_adv_opt                 = 1,      1,
 /

 &bdy_control
 spec_bdy_width                 = 5,
 spec_zone                      = 1,
 relax_zone                     = 4,
```

```
specified                       = .true.,   .false.,
nested                                  = .false.,  .true.,
/

&grib2
/

&namelist_quilt
nio_tasks_per_group = 0,
nio_groups = 0,
/
```

B2. WRF namelist.input settings for 23 April 2019. A setting of '-1' means the default values for the suite were used.

```
&time_control
run_days                 = 0,
run_hours                = 24,
run_minutes              = 0,
run_seconds              = 0,
start_year               = 2019,     2019,
start_month              = 04,       04,
start_day                = 23,       23,
start_hour               = 00,       00,
start_minute             = 00,       00,
start_second             = 00,       00,
end_year                 = 2019,     2019,
end_month                = 04,       04,
end_day                  = 24,       24,
end_hour                 = 00,       00,
end_minute               = 00,       00,
end_second               = 00,       00,
interval_seconds         = 3600,
input_from_file          = .true.,   .true.,
history_interval         = 60,       30,
frames_per_outfile       = 2, 4
restart                  = .false.,
restart_interval         = 1440,
io_form_history          = 2,
io_form_restart          = 2,
io_form_input            = 2,
io_form_boundary         = 2,
debug_level              = 0,
/

&domains
```

```
time_step                = 12,
time_step_fract_num      = 0,
time_step_fract_den      = 1,
max_dom                  = 2,
e_we                     = 150,     238,
e_sn                     = 130,     118,
e_vert                   = 35,      35,
p_top_requested          = 5000,
num_metgrid_levels       = 41,
num_metgrid_soil_levels  = 9,
dx                       = 3000,    1000,
dy                       = 3000,    1000,
grid_id                  = 1,       2,
parent_id                = 1,       1,
i_parent_start           = 1,       41,
j_parent_start           = 1,       46,
parent_grid_ratio        = 1,       3,
parent_time_step_ratio   = 1,       3,
feedback                 = 0,
smooth_option            = 0,
nproc_x                  = -1,
nproc_y                  = -1,
/

 &physics
 physics_suite                    = 'CONUS'
 mp_physics                       = -1,    -1,
 cu_physics                       = -1,    -1,
 ra_lw_physics                    = -1,    -1,
 ra_sw_physics                    = -1,    -1,
 bl_pbl_physics                   = -1,    -1,
 sf_sfclay_physics                = -1,    -1,
 sf_surface_physics               = -1,    -1,
 sf_urban_physics                 = 2,     2,
 /

&fdda
/

&dynamics
hybrid_opt              = 2,
w_damping               = 0,
diff_opt                = 2,       2,
km_opt                  = 4,       4,
diff_6th_opt            = 0,       0,
diff_6th_factor         = 0.12,    0.12,
```

```
base_temp               = 290.,
damp_opt                = 0,
zdamp                   = 5000.,    5000.,
dampcoef                = 0.2,      0.2,
khdif                   = 0,        0,
kvdif                   = 0,        0,
non_hydrostatic         = .true.,   .true.,
moist_adv_opt           = 1,        1,
scalar_adv_opt          = 1,        1,
/

&bdy_control
spec_bdy_width          = 5,
spec_zone               = 1,
relax_zone              = 4,
specified               = .true.,  .false.,
nested                  = .false.,   .true.,
/

&grib2
/

&namelist_quilt
nio_tasks_per_group      = 0,
nio_groups               = 0,
/
```

Appendix C – WRF Model namelist.wps Settings
C1. WRF namelist.wps settings for 22 January 2019

```
&share
 wrf_core = 'ARW',
 max_dom = 2,
 start_date = '2019-01-22_00:00:00', '2019-01-22_00:00:00',
 end_date   = '2019-01-23_00:00:00', '2019-01-23_00:00:00',
 interval_seconds = 3600,
 io_form_geogrid = 2,
 opt_output_from_geogrid_path = '/---/',
 debug_level = 0,
/

&geogrid
 parent_id         = 1,1,
 parent_grid_ratio = 1,3,
 i_parent_start    = 1,53,
 j_parent_start    = 1,46,
 e_we          = 150,136,
 e_sn          = 130,118,
 geog_data_res = 'default','default',
 dx = 3000,
 dy = 3000,
 map_proj =  'lambert',
 ref_lat   = 34.1,
 ref_lon   = -117.24,
 truelat1  = 34.1,
 truelat2  = 34.1,
 stand_lon = -117.24,
 geog_data_path = '/---/WPS_GEOG',
 opt_geogrid_tbl_path = '/---/',
 ref_x = 75.0,
 ref_y = 65.0,
/

&ungrib
 out_format = 'WPS',
 prefix = 'FILE',
/

&metgrid
 fg_name = 'FILE',
 io_form_metgrid = 2,
 opt_output_from_metgrid_path = '/---/',
 opt_metgrid_tbl_path = '/---/',
```

```
/

&mod_levs
 press_pa = 201300 , 200100 , 100000 ,
            95000 ,  90000 ,
            85000 ,  80000 ,
            75000 ,  70000 ,
            65000 ,  60000 ,
            55000 ,  50000 ,
            45000 ,  40000 ,
            35000 ,  30000 ,
            25000 ,  20000 ,
            15000 ,  10000 ,
             5000 ,   1000
 /
```

C2. WRF namelist.wps settings for 23 April 2019

```
&share
 wrf_core = 'ARW',
 max_dom = 2,
 start_date = '2019-04-23_00:00:00', '2019-04-23_00:00:00',
 end_date   = '2019-04-24_00:00:00', '2019-04-24_00:00:00',
 interval_seconds = 3600,
 io_form_geogrid = 2,
 opt_output_from_geogrid_path = '/---/',
 debug_level = 0,
/

&geogrid
 parent_id         = 1,1,
 parent_grid_ratio = 1,3,
 i_parent_start    = 1,41,
 j_parent_start    = 1,46,
 e_we          = 150,238,
 e_sn          = 130,118,
 geog_data_res = 'default','default',
 dx = 3000,
 dy = 3000,
 map_proj =  'lambert',
 ref_lat   = 34.1,
 ref_lon   = -117.24,
 truelat1  = 34.1,
 truelat2  = 34.1,
 stand_lon = -117.24,
 geog_data_path = '/---/WPS_GEOG',
```

```
 opt_geogrid_tbl_path = '/---/',
 ref_x = 75.0,
 ref_y = 65.0,
/

&ungrib
 out_format = 'WPS',
 prefix = 'FILE',
/

&metgrid
 fg_name = 'FILE',
 io_form_metgrid = 2,
 opt_output_from_metgrid_path = '/---/',
 opt_metgrid_tbl_path = '/---/',
/

&mod_levs
 press_pa = 201300 , 200100 , 100000 ,
            95000 ,  90000 ,
            85000 ,  80000 ,
            75000 ,  70000 ,
            65000 ,  60000 ,
            55000 ,  50000 ,
            45000 ,  40000 ,
            35000 ,  30000 ,
            25000 ,  20000 ,
            15000 ,  10000 ,
             5000 ,   1000
 /


&domain_wizard
 grib_data_path = '/---/',
 grib_vtable = 'Vtable.HRRR.wrfprs',
 dwiz_name    =test
 dwiz_desc    =
 dwiz_user_rect_x1 =325
 dwiz_user_rect_y1 =284
 dwiz_user_rect_x2 =382
 dwiz_user_rect_y2 =345
 dwiz_show_political =true
 dwiz_center_over_gmt =true
 dwiz_latlon_space_in_deg =10
 dwiz_latlon_linecolor =-8355712
 dwiz_map_scale_pct =12.5
```

```
 dwiz_map_vert_scrollbar_pos =0
 dwiz_map_horiz_scrollbar_pos =0
 dwiz_gridpt_dist_km =3.0
 dwiz_mpi_command =
 dwiz_tcvitals =null
 dwiz_bigmap =Y
/
```

Appendix D – Weather Station Comparisons

Figures D1-D9. WRF Model comparisons to weather station F0494.

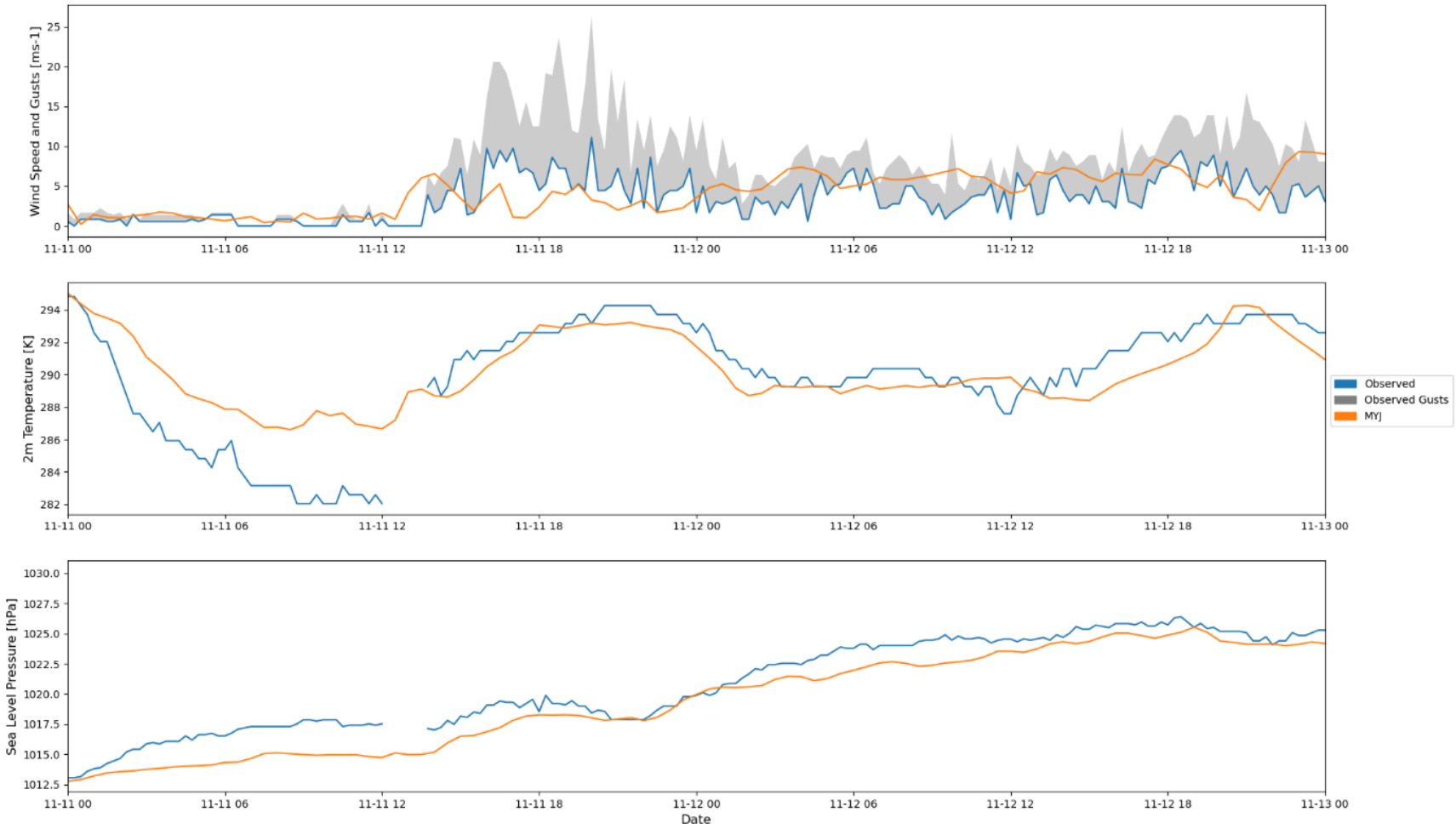

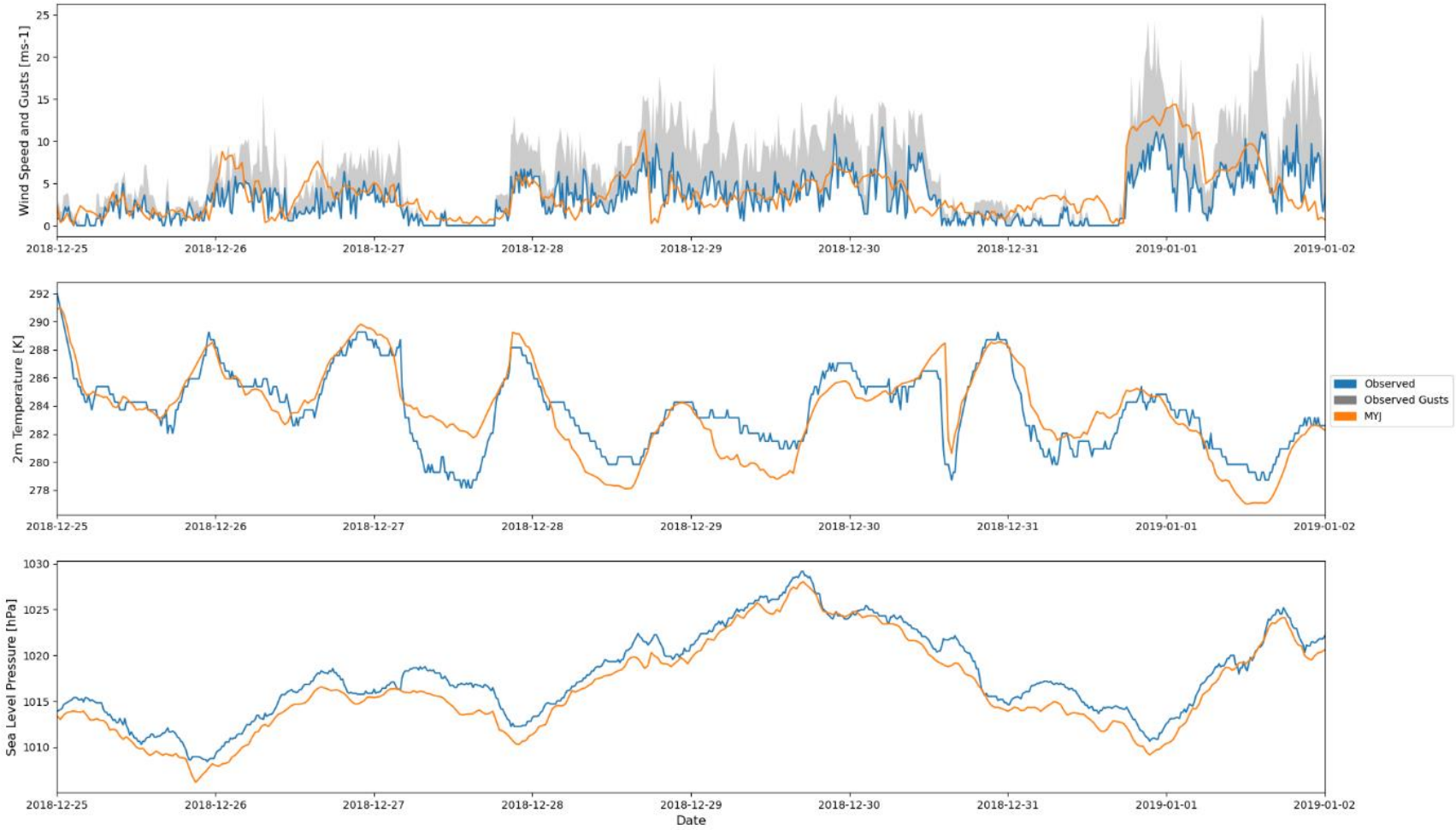
Wind Speed and Gusts [ms-1]
2m Temperature [K]
Sea Level Pressure [hPa]
Date
2018-12-25
2018-12-26
2018-12-27
2018-12-28
2018-12-29
2018-12-30
2018-12-31
2019-01-01
2019-01-02
Observed
Observed Gusts
MYJ

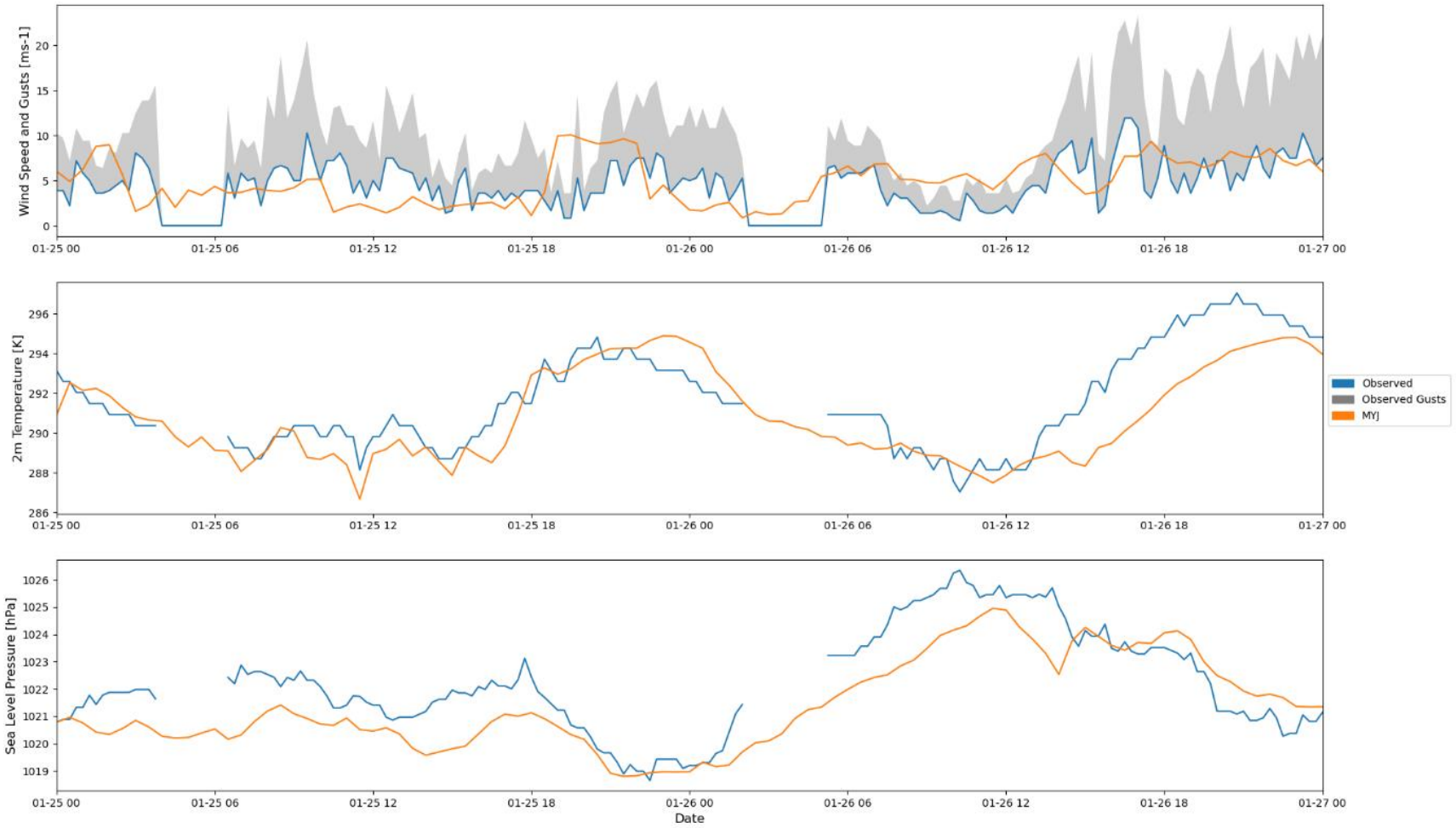
Wind Speed and Gusts [ms-1]
2m Temperature [K]
Sea Level Pressure [hPa]
Date
01-25 00
01-25 06
01-25 12
01-25 18
01-26 00
01-26 06
01-26 12
01-26 18
01-27 00
Observed
Observed Gusts
MYJ

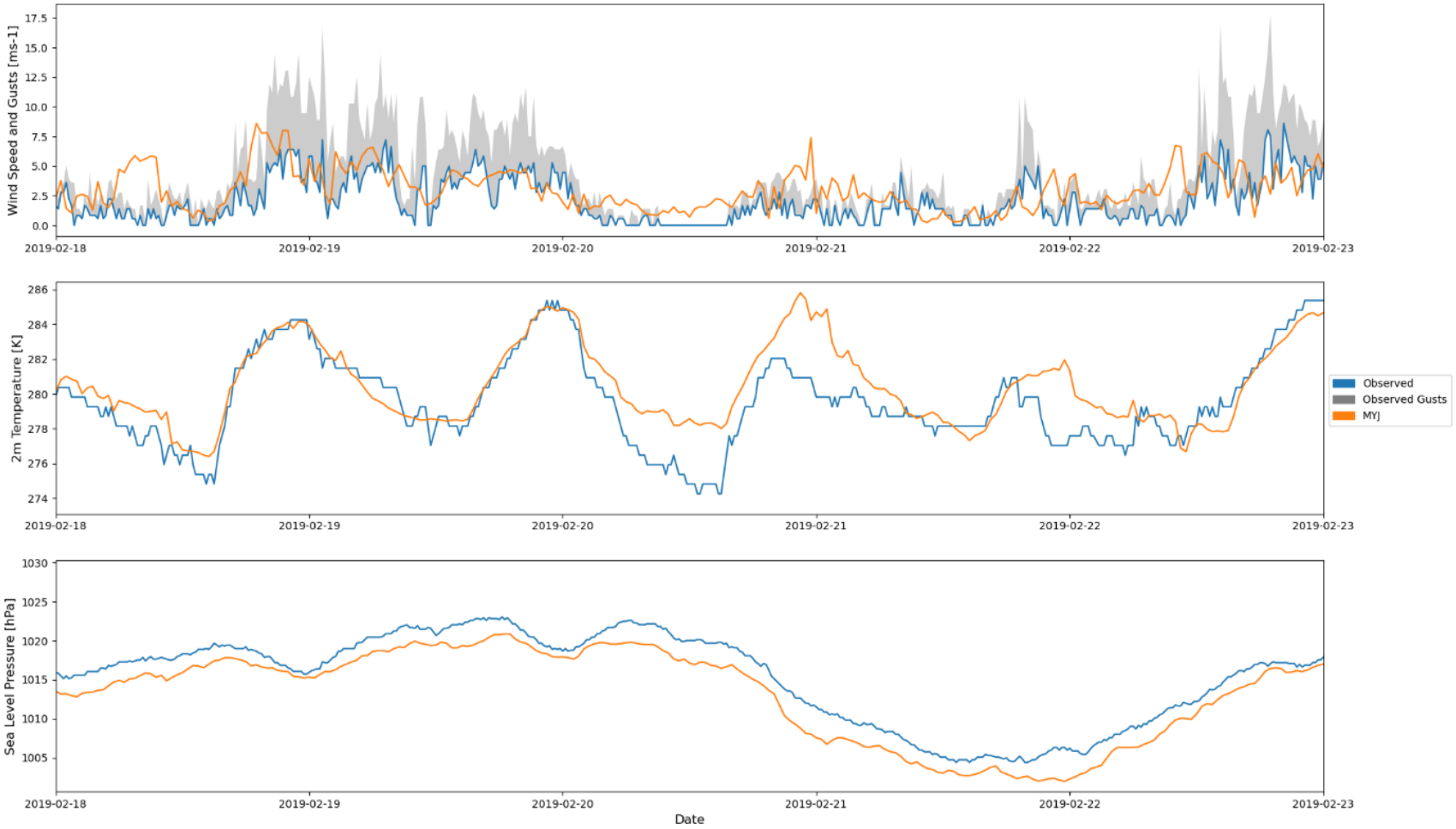
Wind Speed and Gusts [ms-1]
17.5
15.0
12.5
10.0
7.5
5.0
2.5
0.0
2019-02-18
2019-02-19
2019-02-20
2019-02-21
2019-02-22
2019-02-23
2m Temperature [K]
286
284
282
280
278
276
274
Observed
Observed Gusts
MYJ
Sea Level Pressure [hPa]
1030
1025
1020
1015
1010
1005
Date

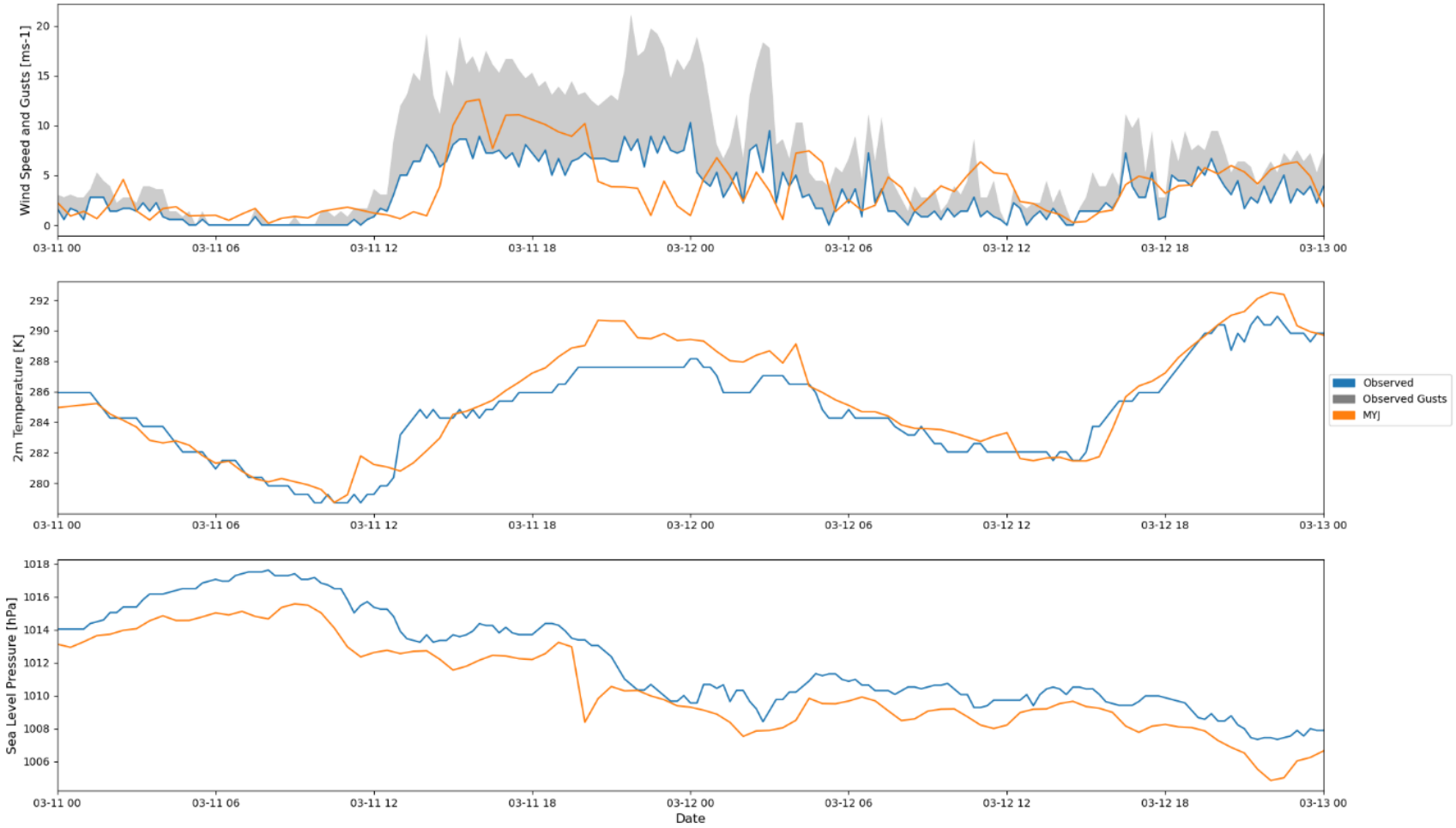
Wind Speed and Gusts [ms-1]
2m Temperature [K]
Sea Level Pressure [hPa]
Date
03-11 00
03-11 06
03-11 12
03-11 18
03-12 00
03-12 06
03-12 12
03-12 18
03-13 00
Observed
Observed Gusts
MYJ

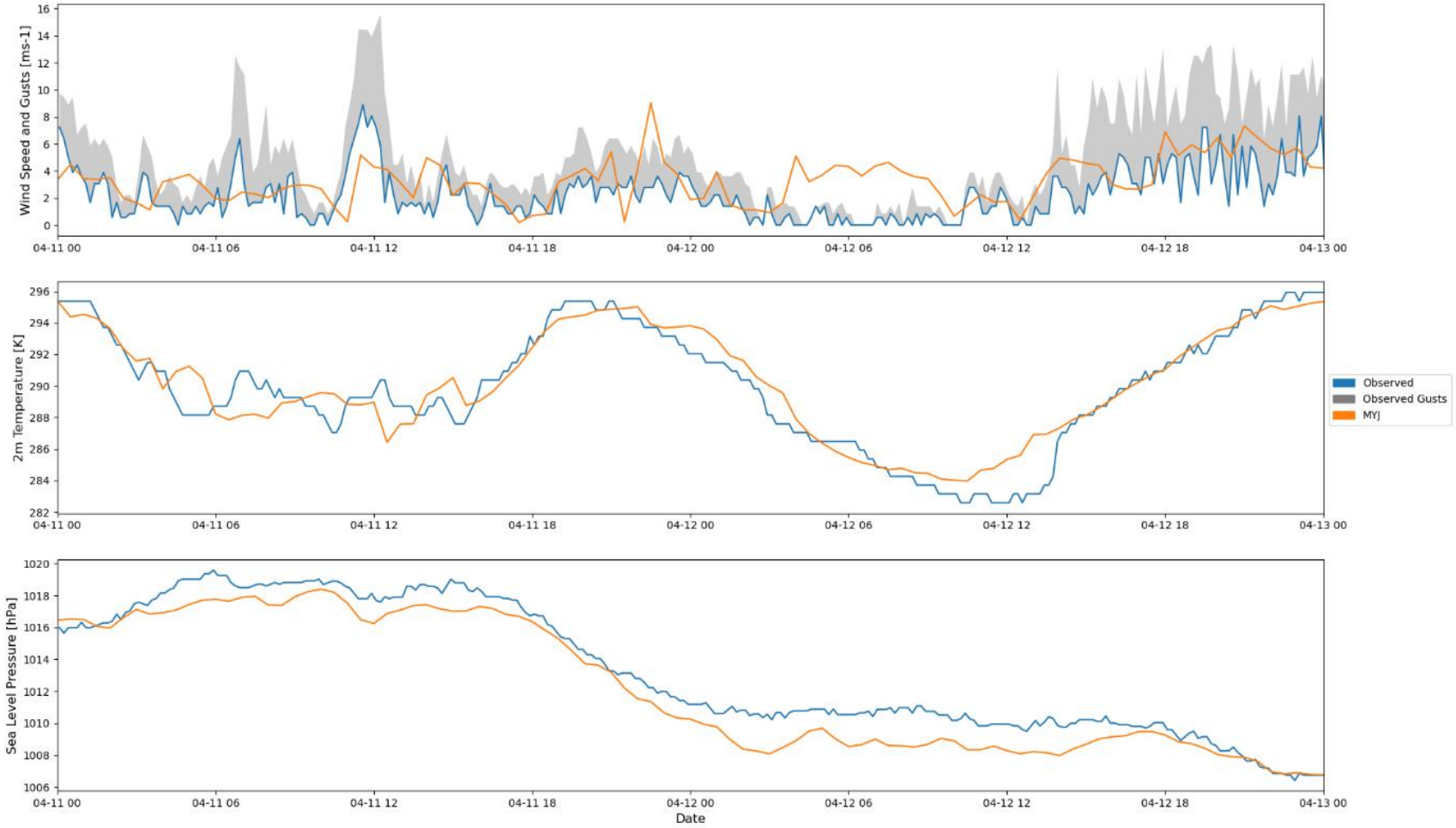
Wind Speed and Gusts [ms-1]
2m Temperature [K]
Sea Level Pressure [hPa]
Date
04-11 00
04-11 06
04-11 12
04-11 18
04-12 00
04-12 06
04-12 12
04-12 18
04-13 00
Observed
Observed Gusts
MYJ

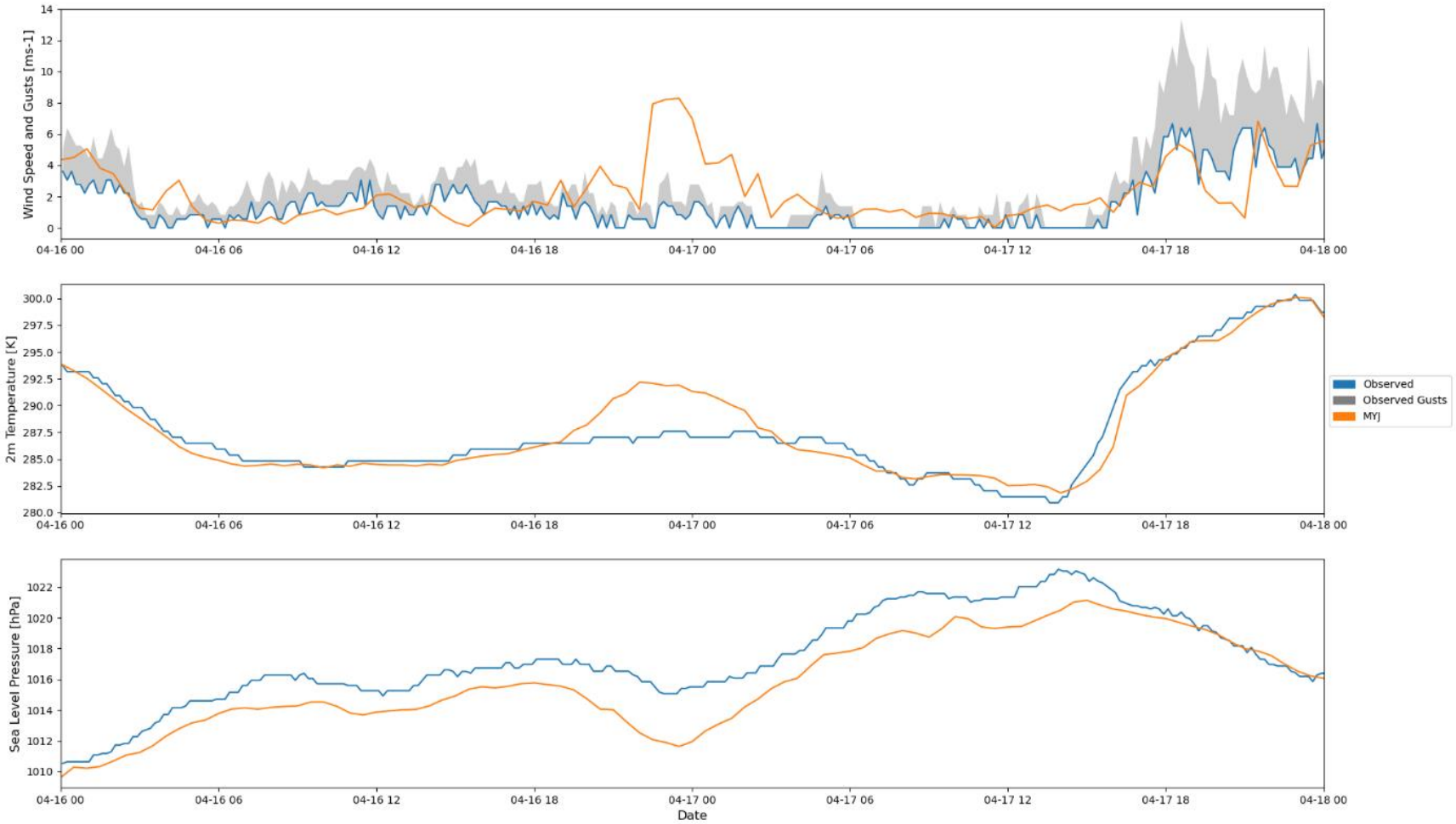
Wind Speed and Gusts [ms-1]
2m Temperature [K]
Sea Level Pressure [hPa]
Date
04-16 00
04-16 06
04-16 12
04-16 18
04-17 00
04-17 06
04-17 12
04-17 18
04-18 00
Observed
Observed Gusts
MYJ

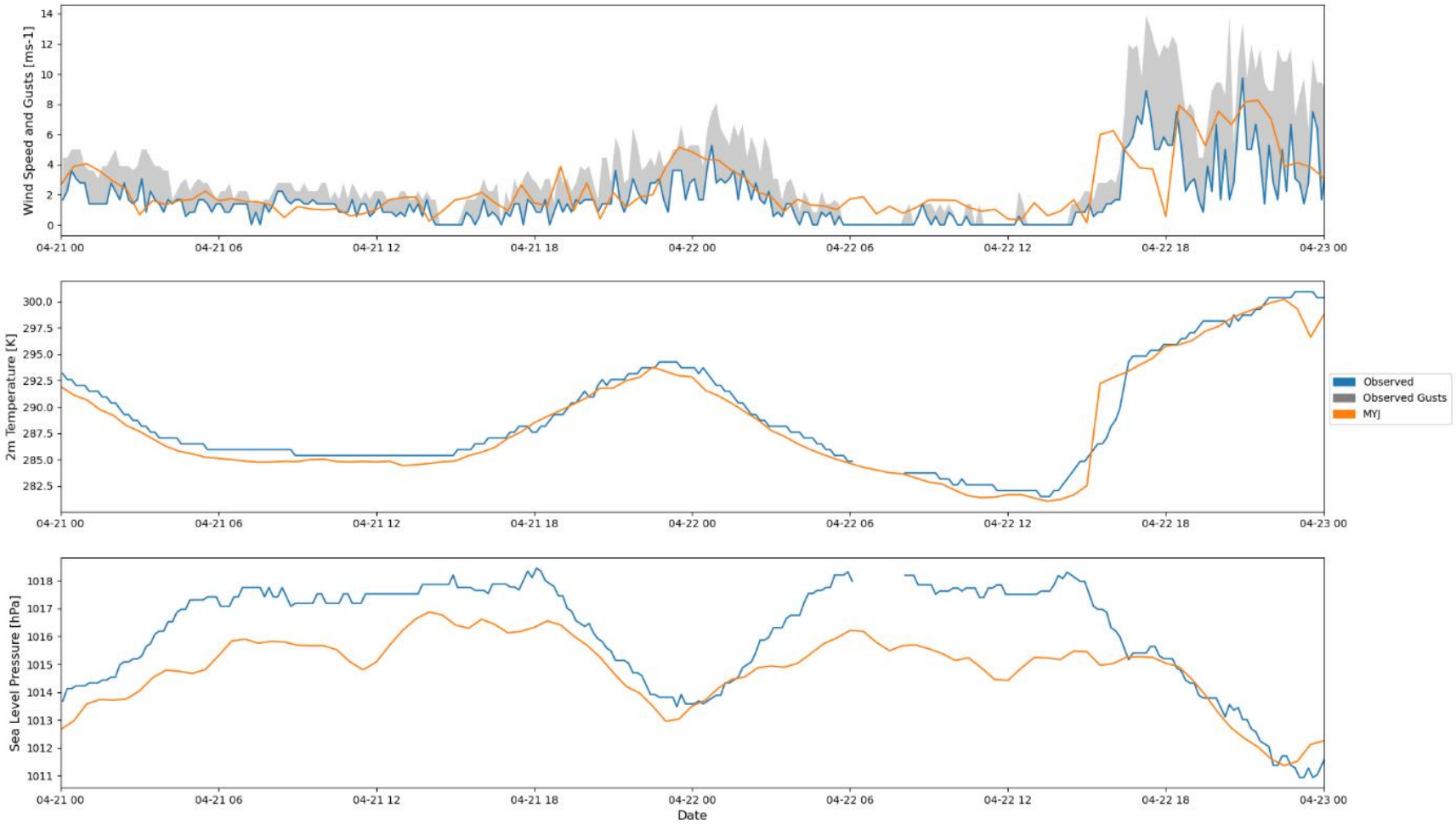
Wind Speed and Gusts [ms-1]
2m Temperature [K]
Sea Level Pressure [hPa]
Date
04-21 00
04-21 06
04-21 12
04-21 18
04-22 00
04-22 06
04-22 12
04-22 18
04-23 00
Observed
Observed Gusts
MYJ

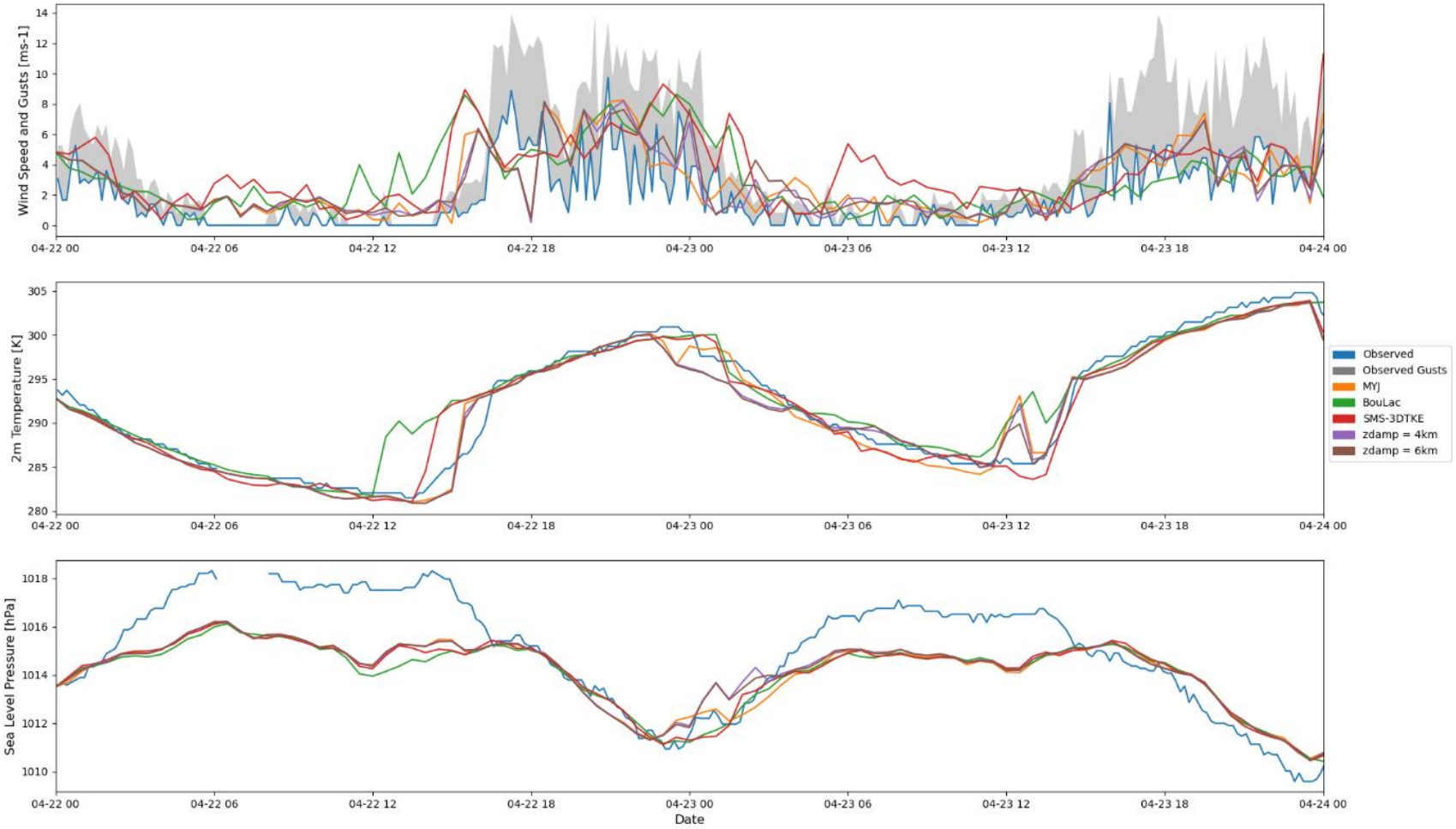
Wind Speed and Gusts [ms-1]
2m Temperature [K]
Sea Level Pressure [hPa]
Date
04-22 00
04-22 06
04-22 12
04-22 18
04-23 00
04-23 06
04-23 12
04-23 18
04-24 00
Observed
Observed Gusts
MYJ
BouLac
SMS-3DTKE
zdamp = 4km
zdamp = 6km

Figures D10-D18. WRF Model comparisons to weather station AU239.

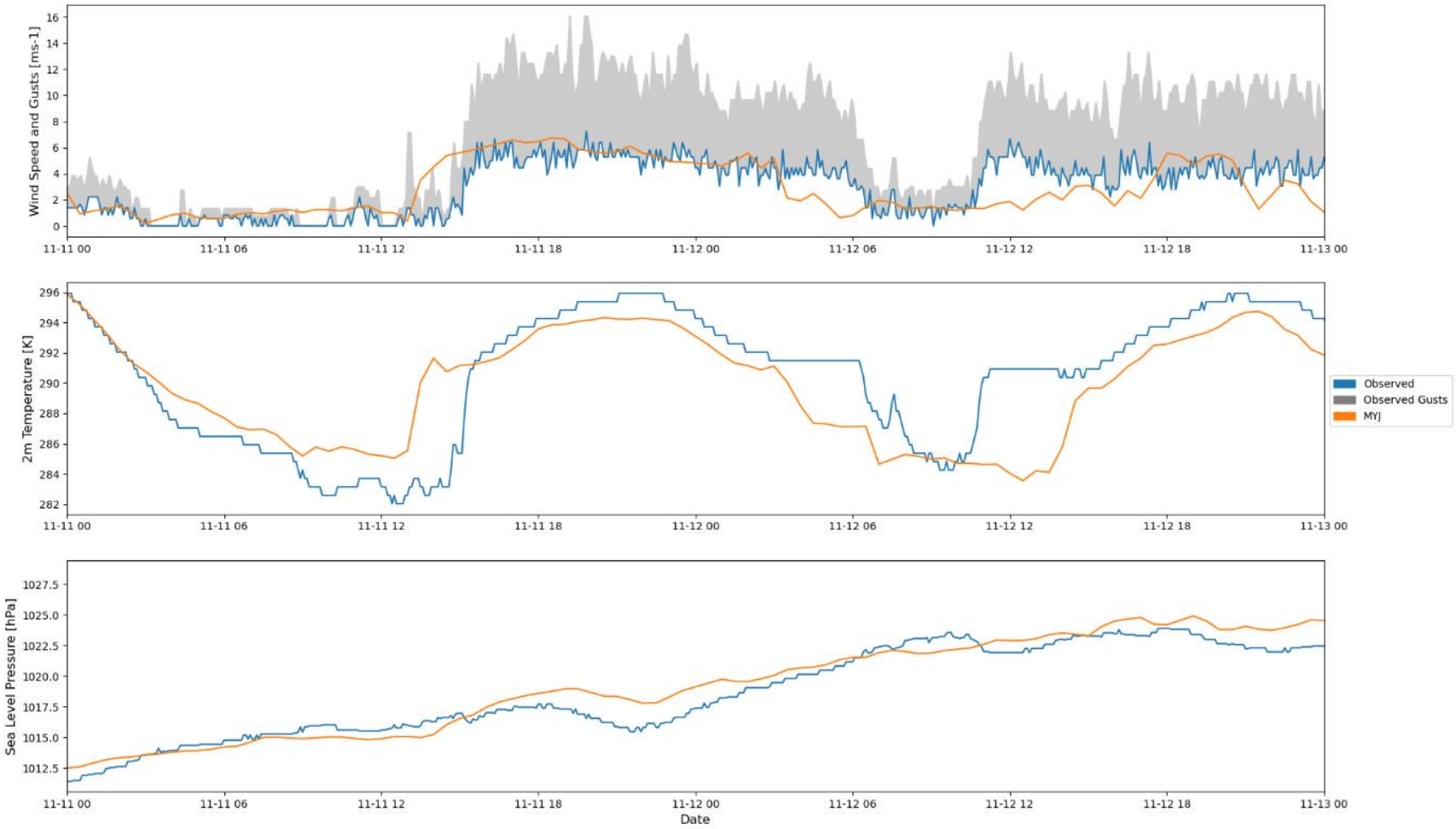

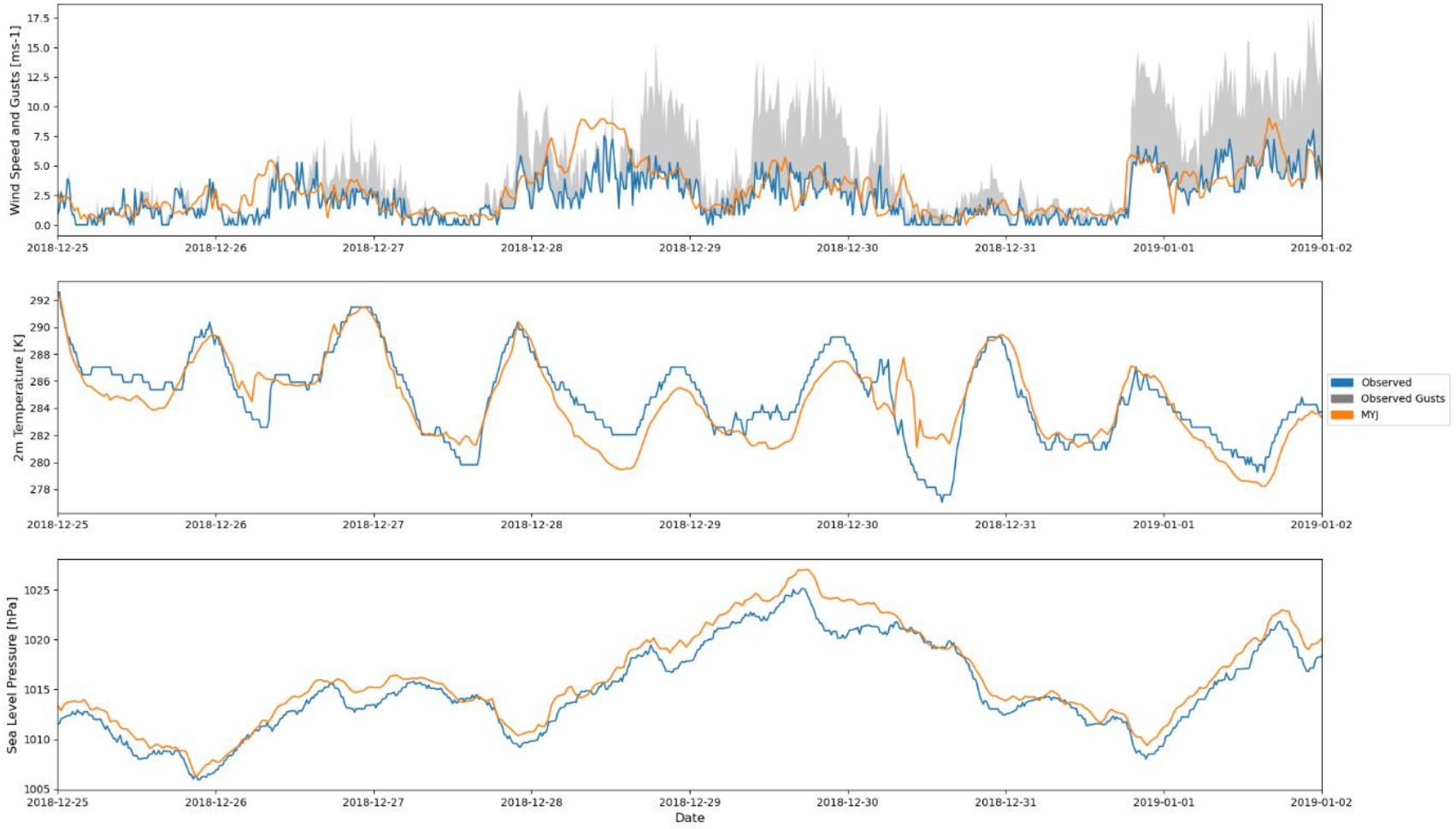
Wind Speed and Gusts [ms-1]
17.5
15.0
12.5
10.0
7.5
5.0
2.5
0.0
2m Temperature [K]
292
290
288
286
284
282
280
278
Sea Level Pressure [hPa]
1025
1020
1015
1010
1005
2018-12-25
2018-12-26
2018-12-27
2018-12-28
2018-12-29
2018-12-30
2018-12-31
2019-01-01
2019-01-02
Date
Observed
Observed Gusts
MYJ

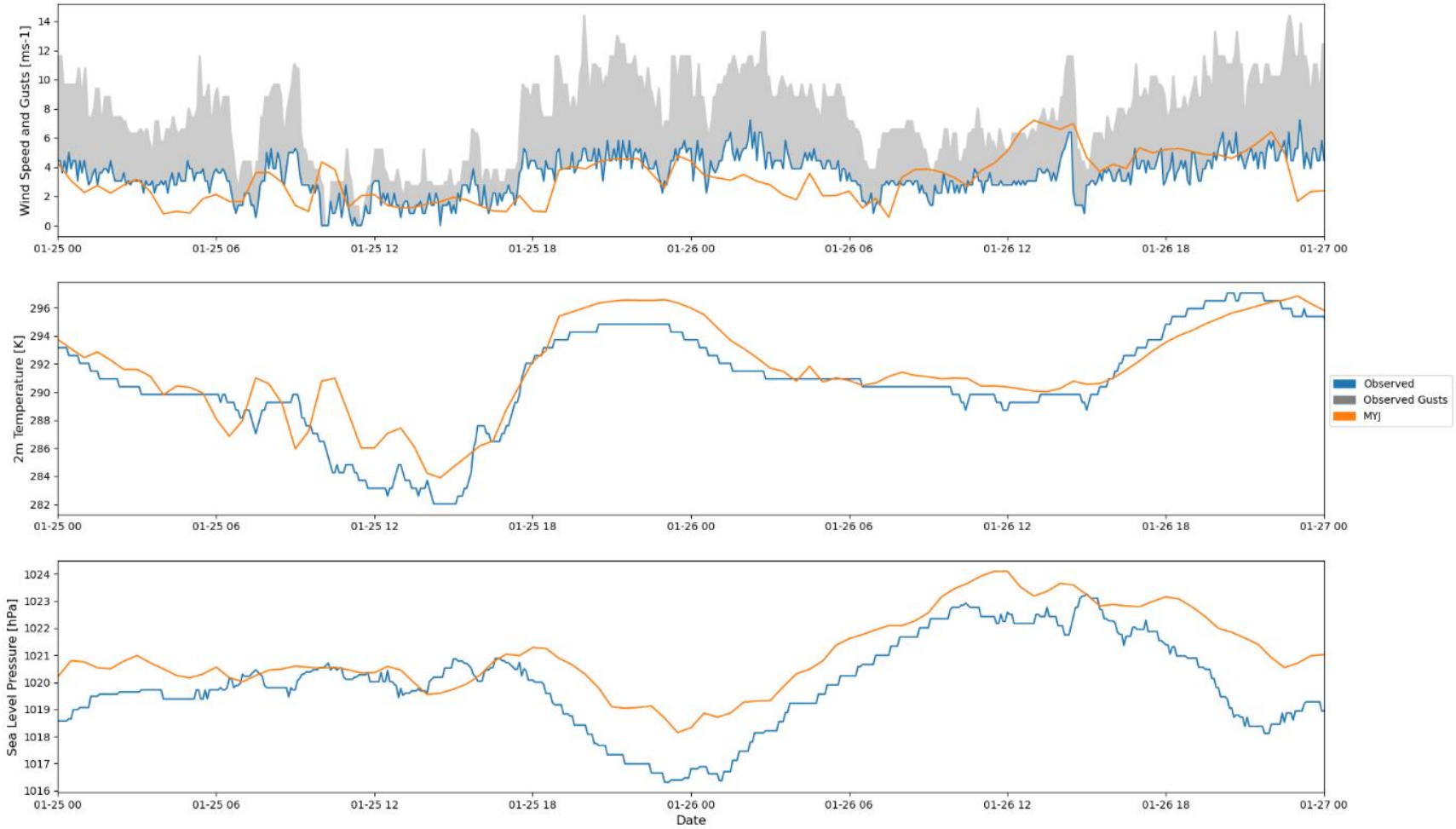
Wind Speed and Gusts [ms-1]
2m Temperature [K]
Sea Level Pressure [hPa]
Date
01-25 00
01-25 06
01-25 12
01-25 18
01-26 00
01-26 06
01-26 12
01-26 18
01-27 00
Observed
Observed Gusts
MYJ

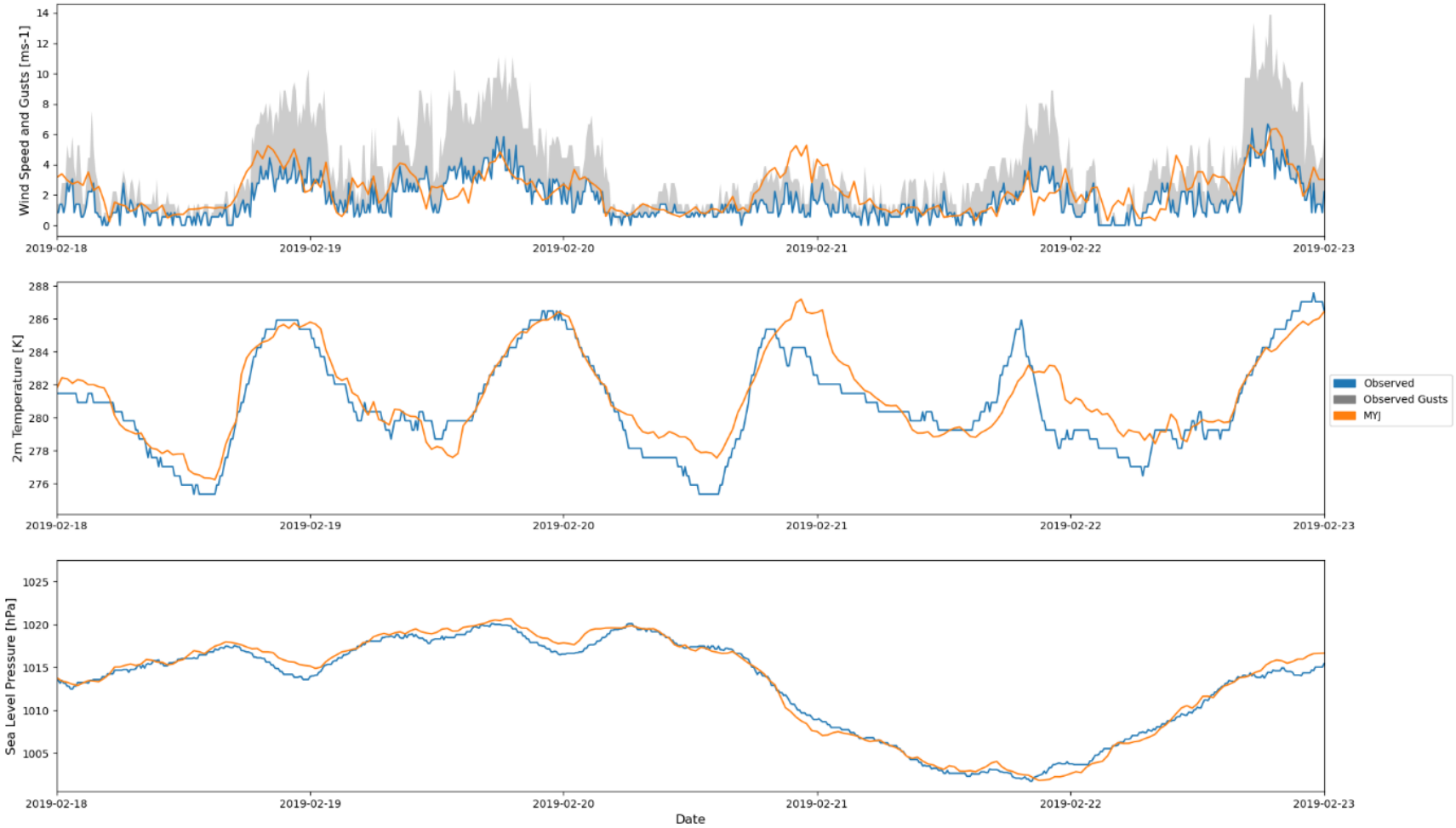
Wind Speed and Gusts [ms-1]
2m Temperature [K]
Sea Level Pressure [hPa]
Date
2019-02-18
2019-02-19
2019-02-20
2019-02-21
2019-02-22
2019-02-23
Observed
Observed Gusts
MYJ

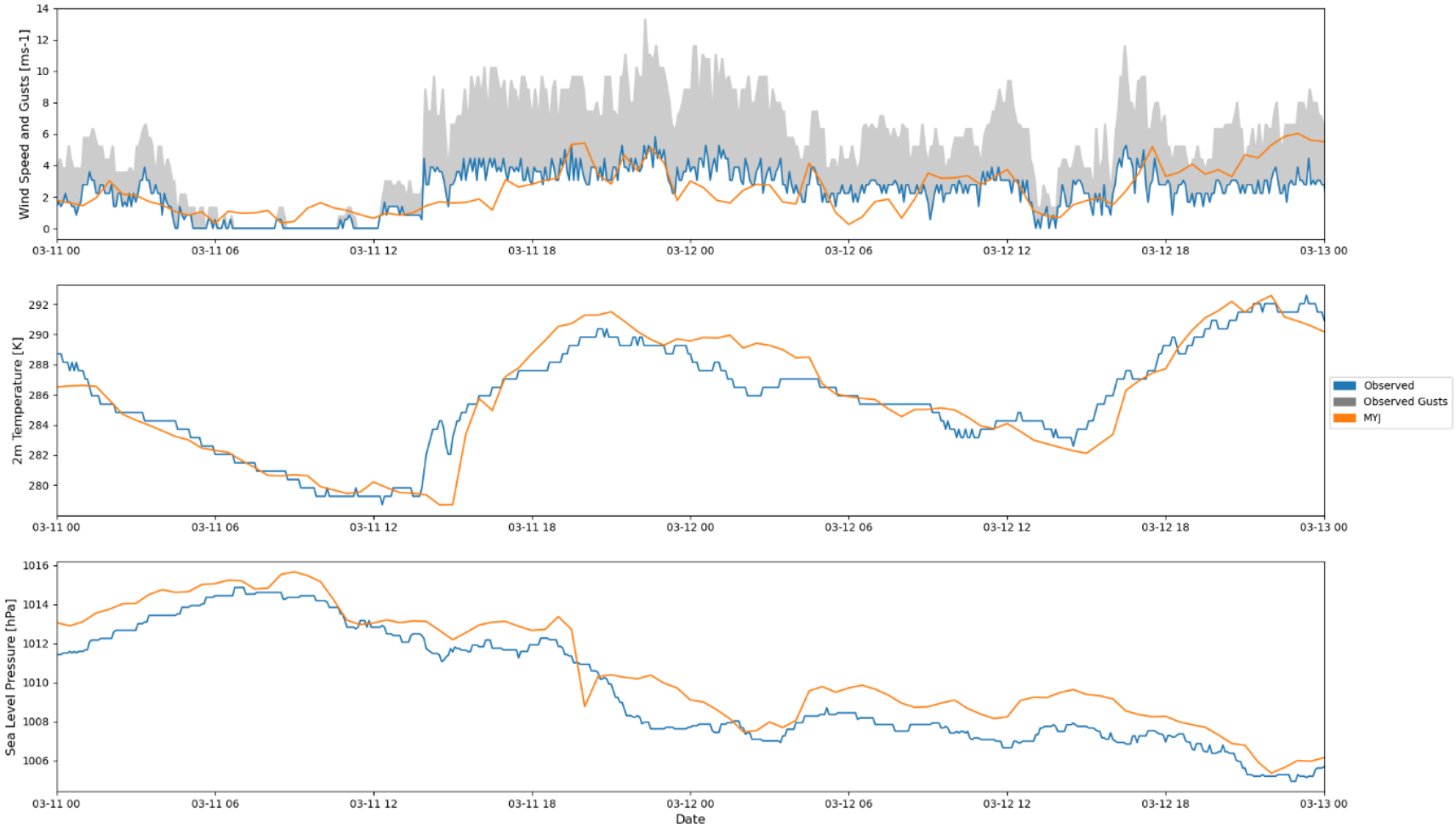
Wind Speed and Gusts [ms-1]
2m Temperature [K]
Sea Level Pressure [hPa]
Date
03-11 00
03-11 06
03-11 12
03-11 18
03-12 00
03-12 06
03-12 12
03-12 18
03-13 00
Observed
Observed Gusts
MYJ

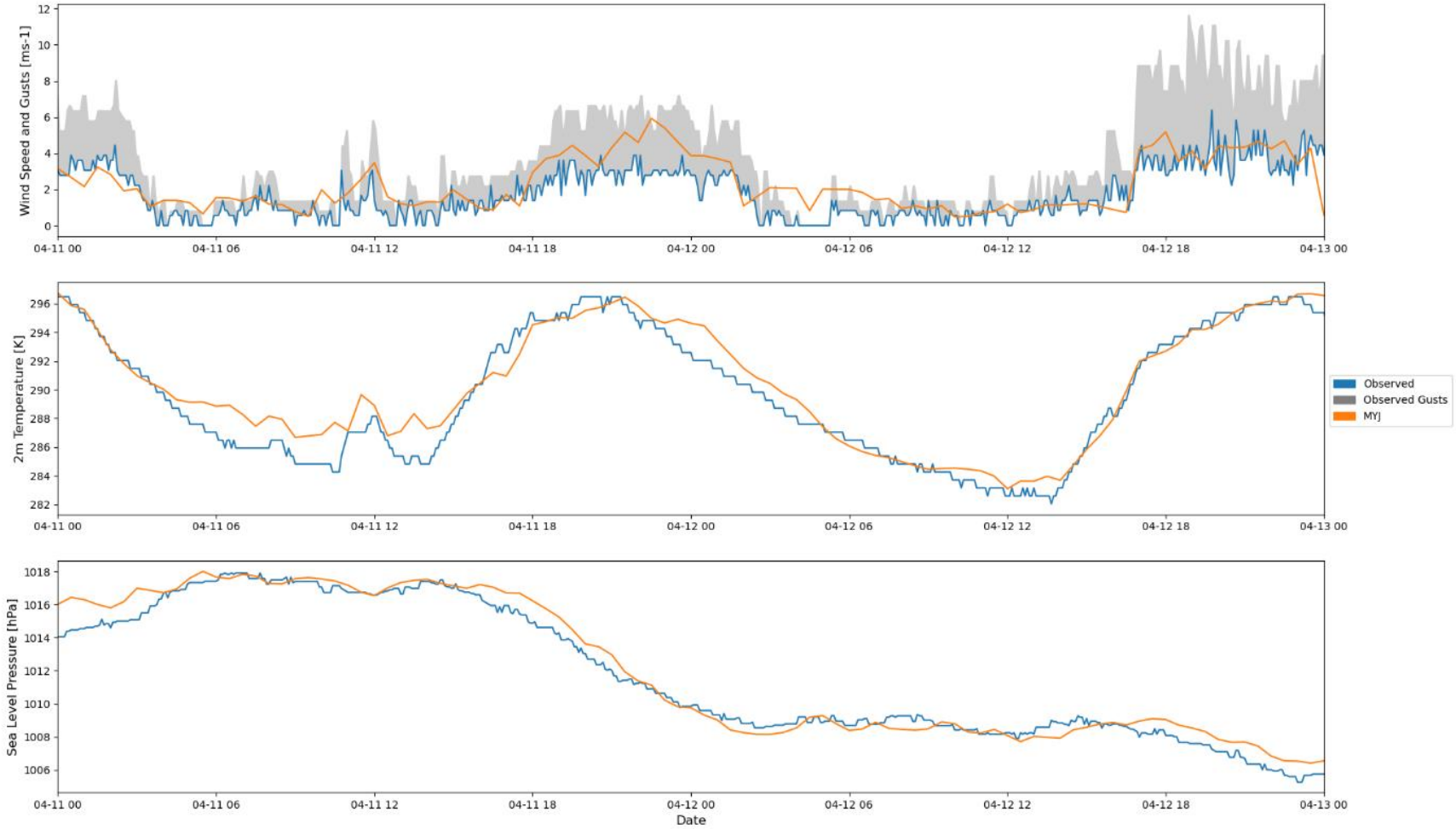
Wind Speed and Gusts [ms-1]
2m Temperature [K]
Sea Level Pressure [hPa]
Date
04-11 00
04-11 06
04-11 12
04-11 18
04-12 00
04-12 06
04-12 12
04-12 18
04-13 00
Observed
Observed Gusts
MYJ

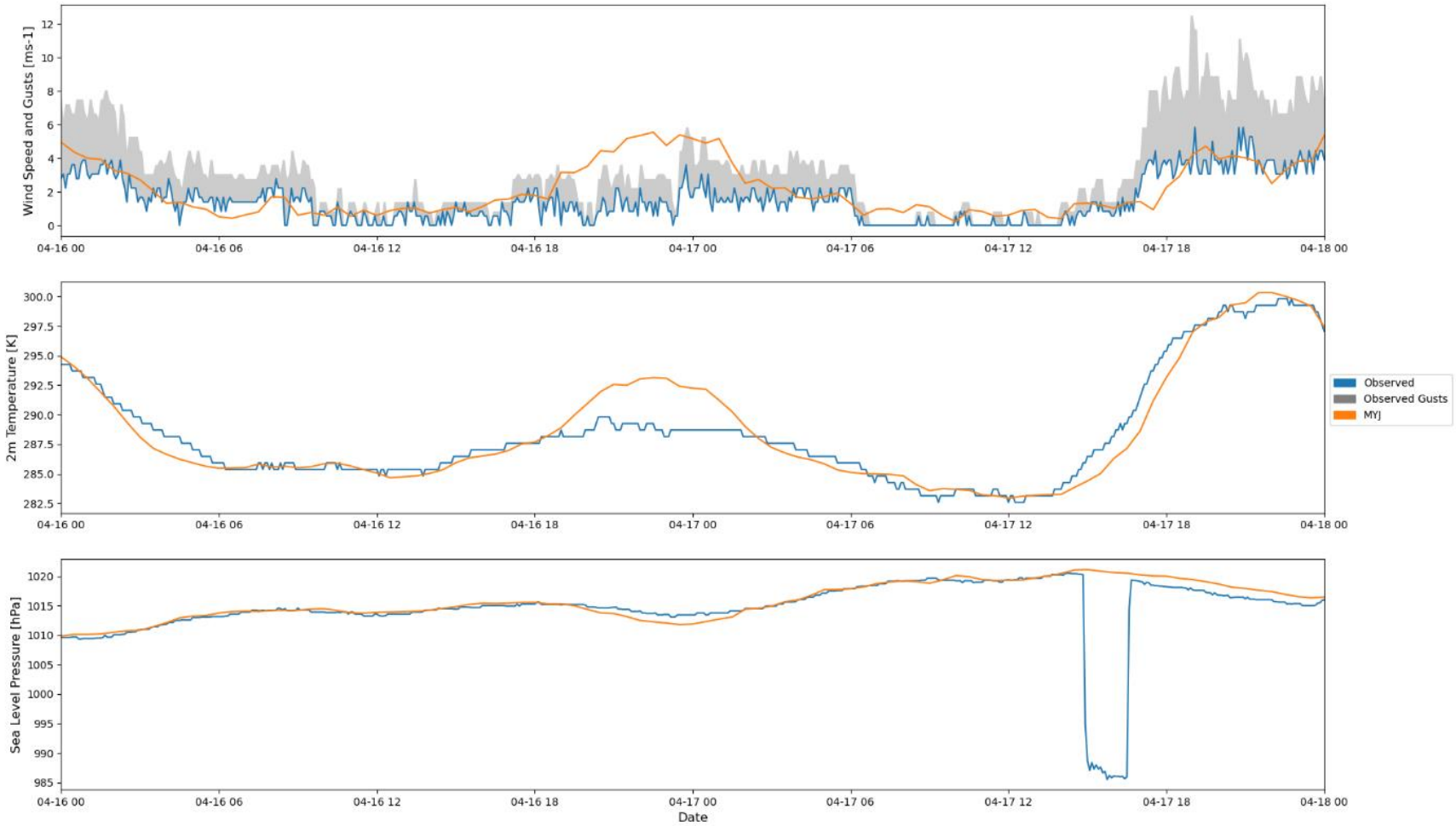
Wind Speed and Gusts [ms-1]
2m Temperature [K]
Sea Level Pressure [hPa]
Date
04-16 00
04-16 06
04-16 12
04-16 18
04-17 00
04-17 06
04-17 12
04-17 18
04-18 00
Observed
Observed Gusts
MYJ

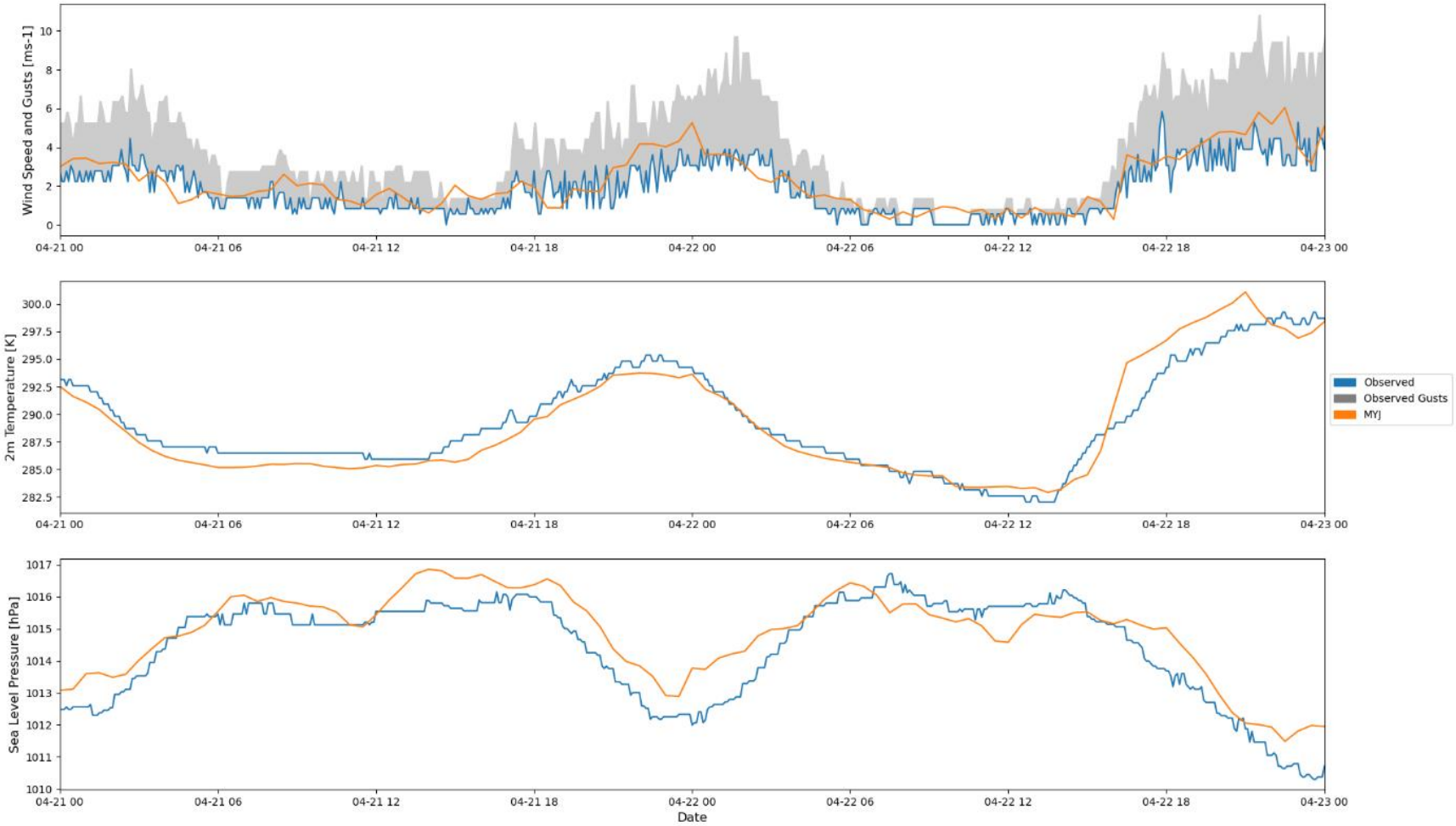
Wind Speed and Gusts [ms-1]
2m Temperature [K]
Sea Level Pressure [hPa]
Date
04-21 00
04-21 06
04-21 12
04-21 18
04-22 00
04-22 06
04-22 12
04-22 18
04-23 00
Observed
Observed Gusts
MYJ

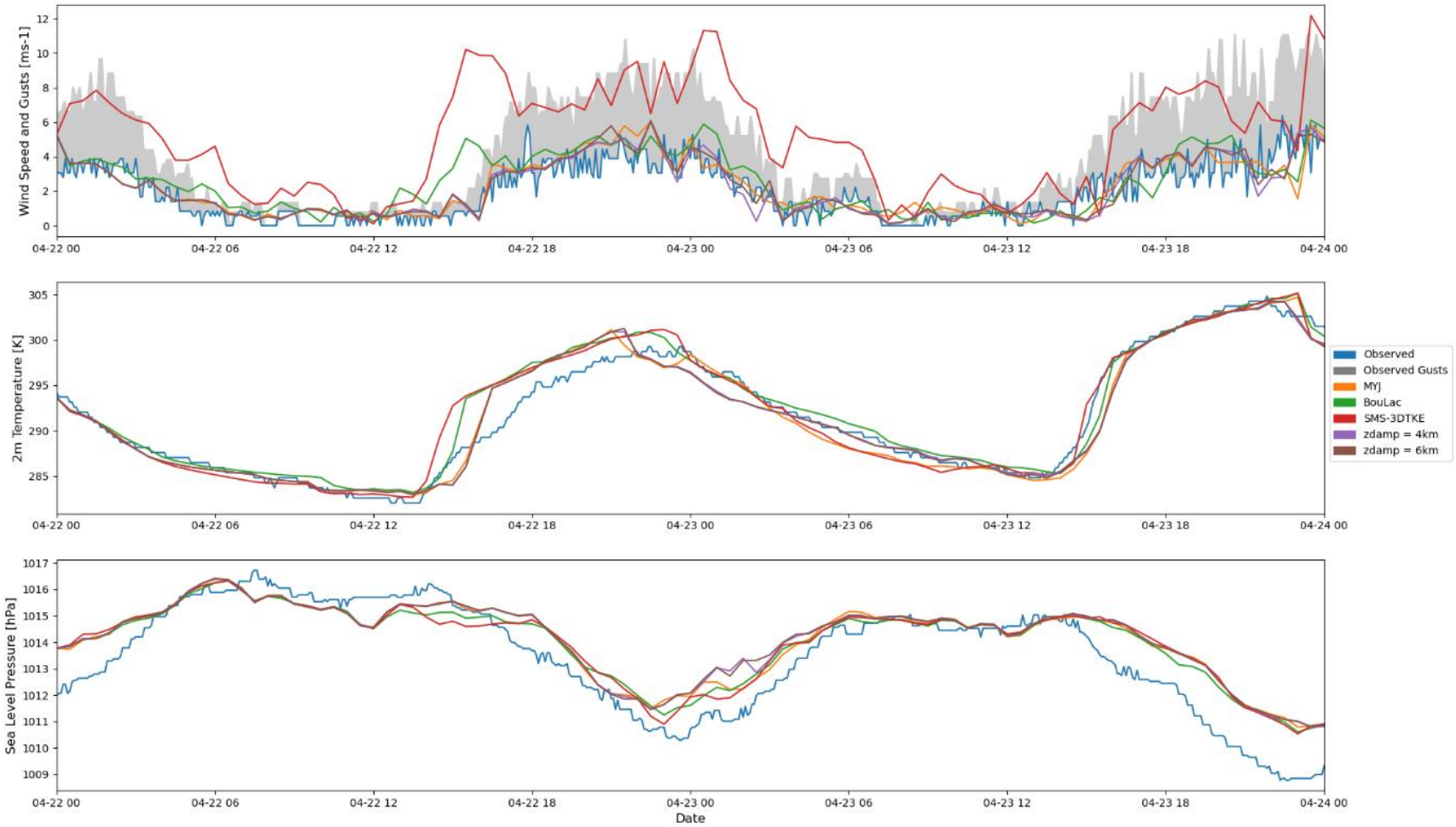
Wind Speed and Gusts [ms-1]
2m Temperature [K]
Sea Level Pressure [hPa]
Date
04-22 00
04-22 06
04-22 12
04-22 18
04-23 00
04-23 06
04-23 12
04-23 18
04-24 00
Observed
Observed Gusts
MYJ
BouLac
SMS-3DTKE
zdamp = 4km
zdamp = 6km

Figures D19-D27. WRF Model comparisons to weather station F1895.

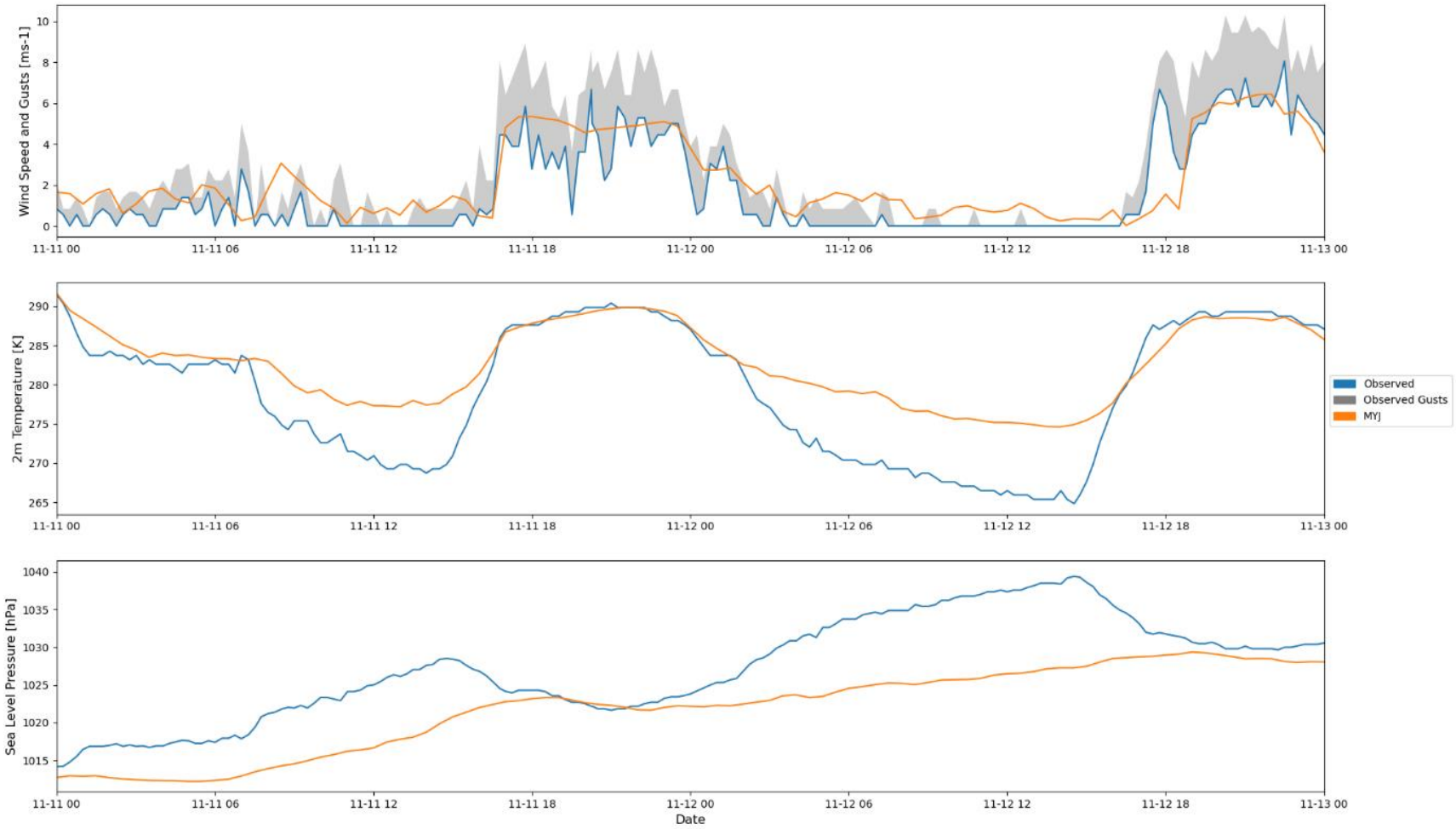

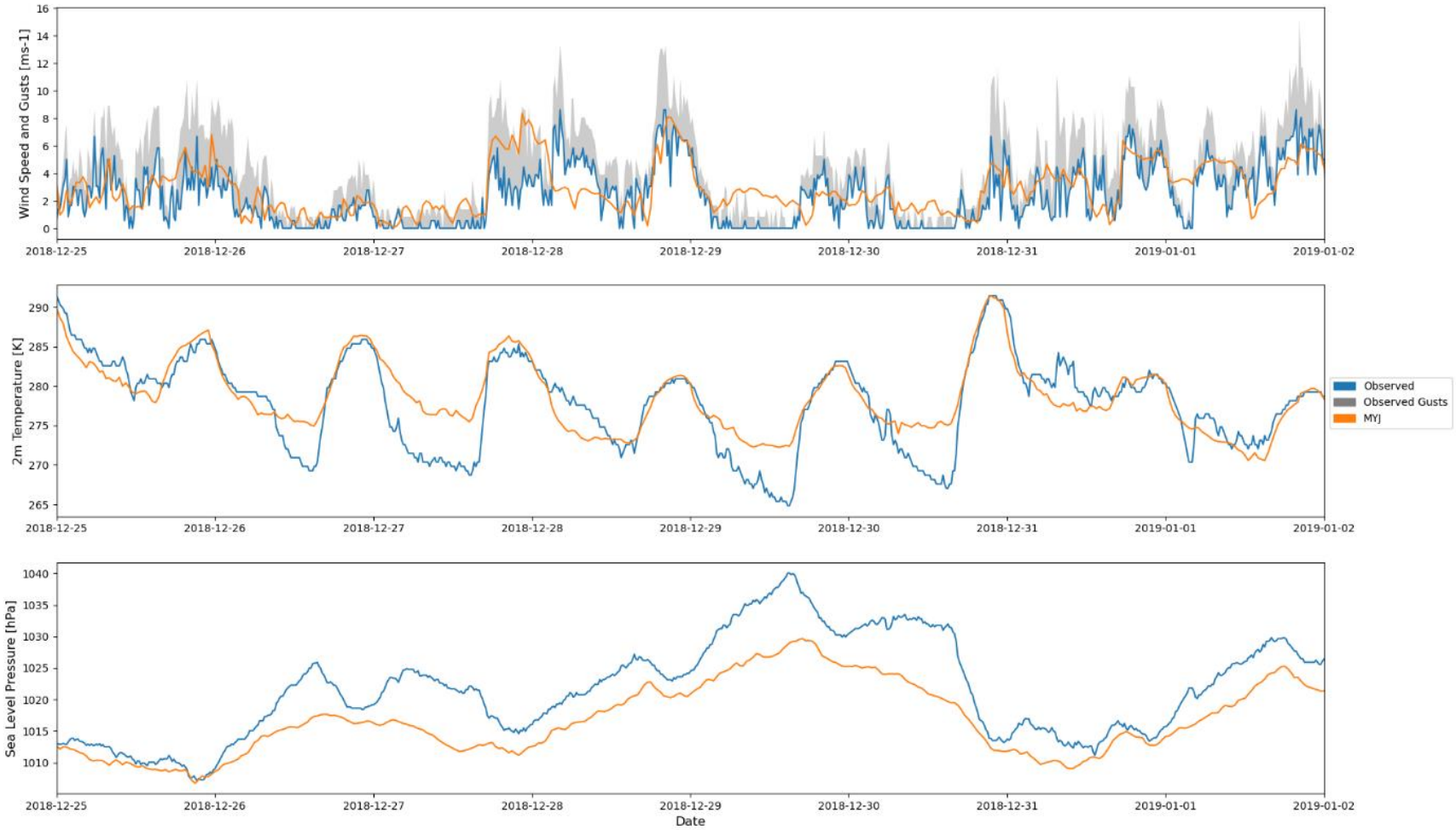
Wind Speed and Gusts [ms-1]
2m Temperature [K]
Sea Level Pressure [hPa]
Date
2018-12-25
2018-12-26
2018-12-27
2018-12-28
2018-12-29
2018-12-30
2018-12-31
2019-01-01
2019-01-02
Observed
Observed Gusts
MYJ

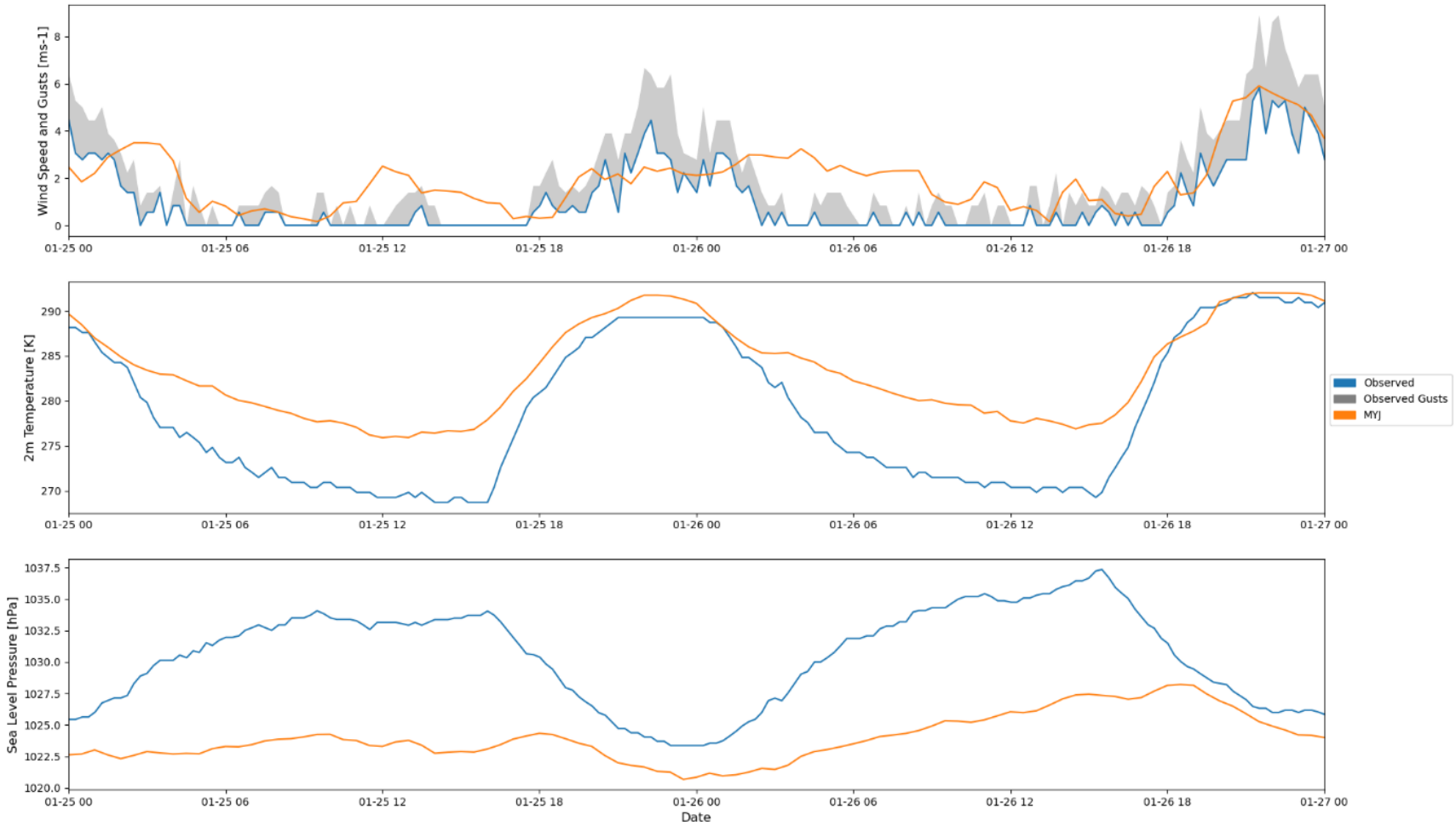
Wind Speed and Gusts [ms-1]
2m Temperature [K]
Sea Level Pressure [hPa]
Date
01-25 00
01-25 06
01-25 12
01-25 18
01-26 00
01-26 06
01-26 12
01-26 18
01-27 00
Observed
Observed Gusts
MYJ

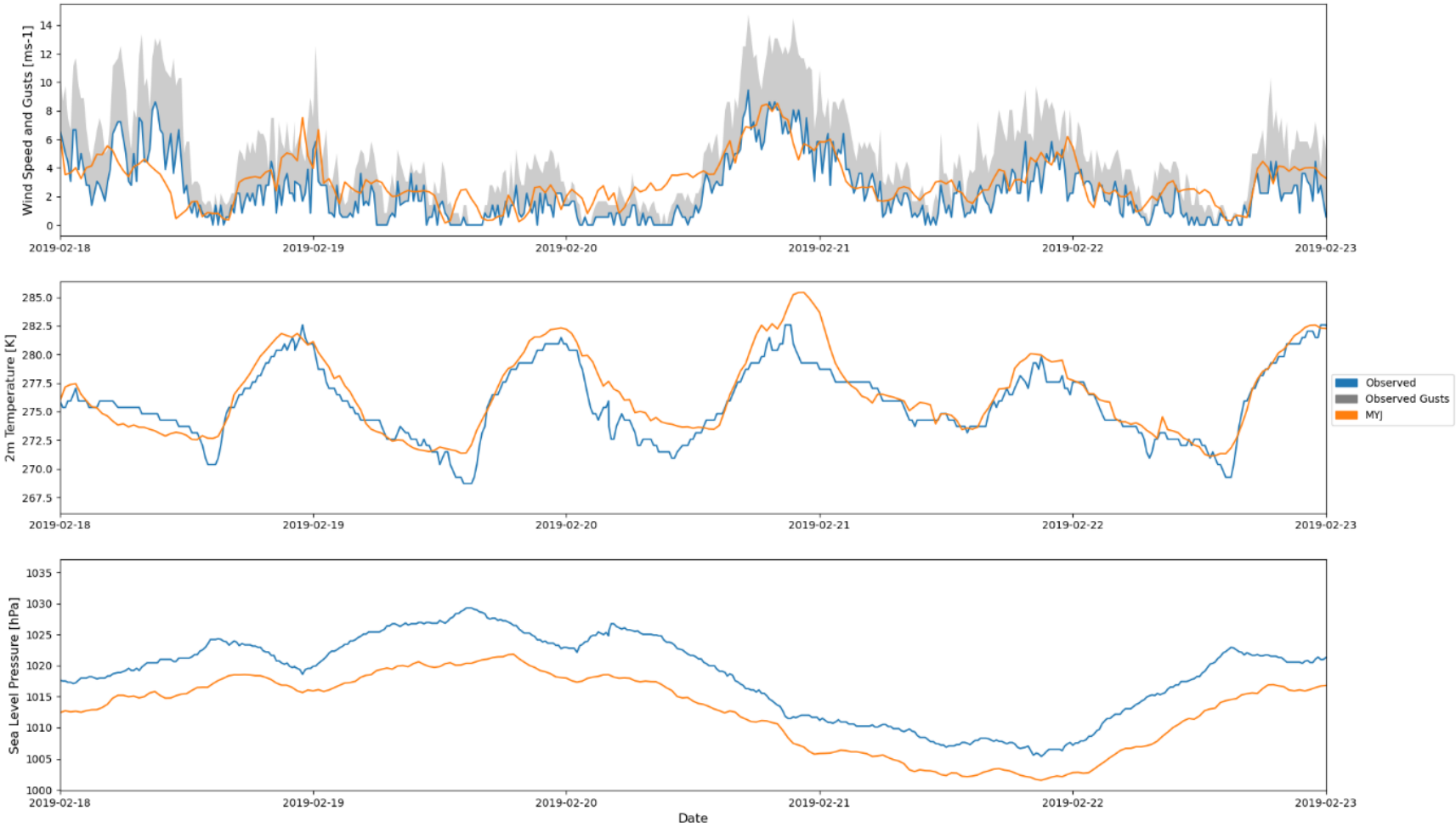
Wind Speed and Gusts [ms-1]
2m Temperature [K]
Sea Level Pressure [hPa]
Date
2019-02-18
2019-02-19
2019-02-20
2019-02-21
2019-02-22
2019-02-23
Observed
Observed Gusts
MYJ

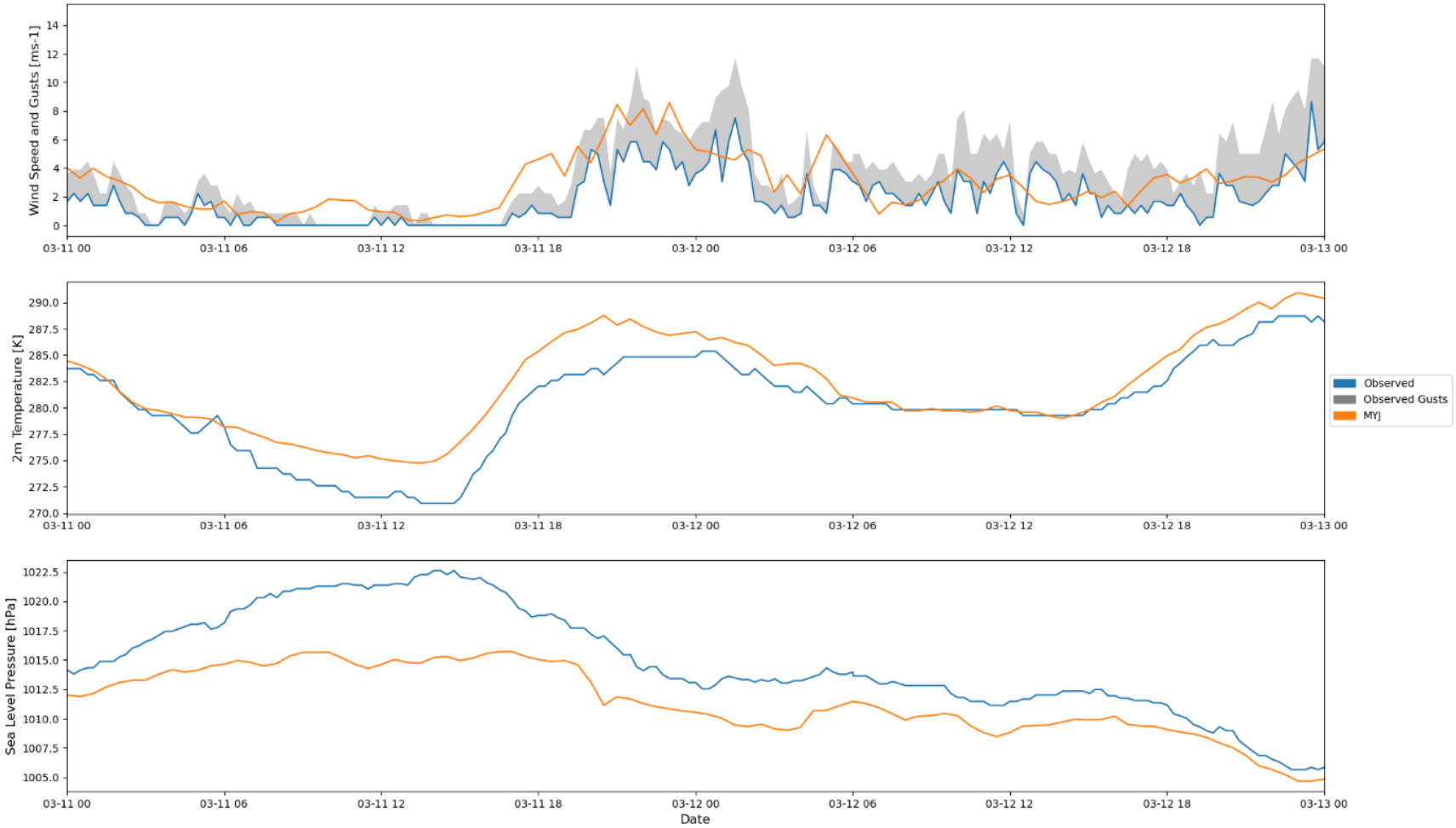
Wind Speed and Gusts [ms-1]
2m Temperature [K]
Sea Level Pressure [hPa]
Date
03-11 00
03-11 06
03-11 12
03-11 18
03-12 00
03-12 06
03-12 12
03-12 18
03-13 00
Observed
Observed Gusts
MYJ

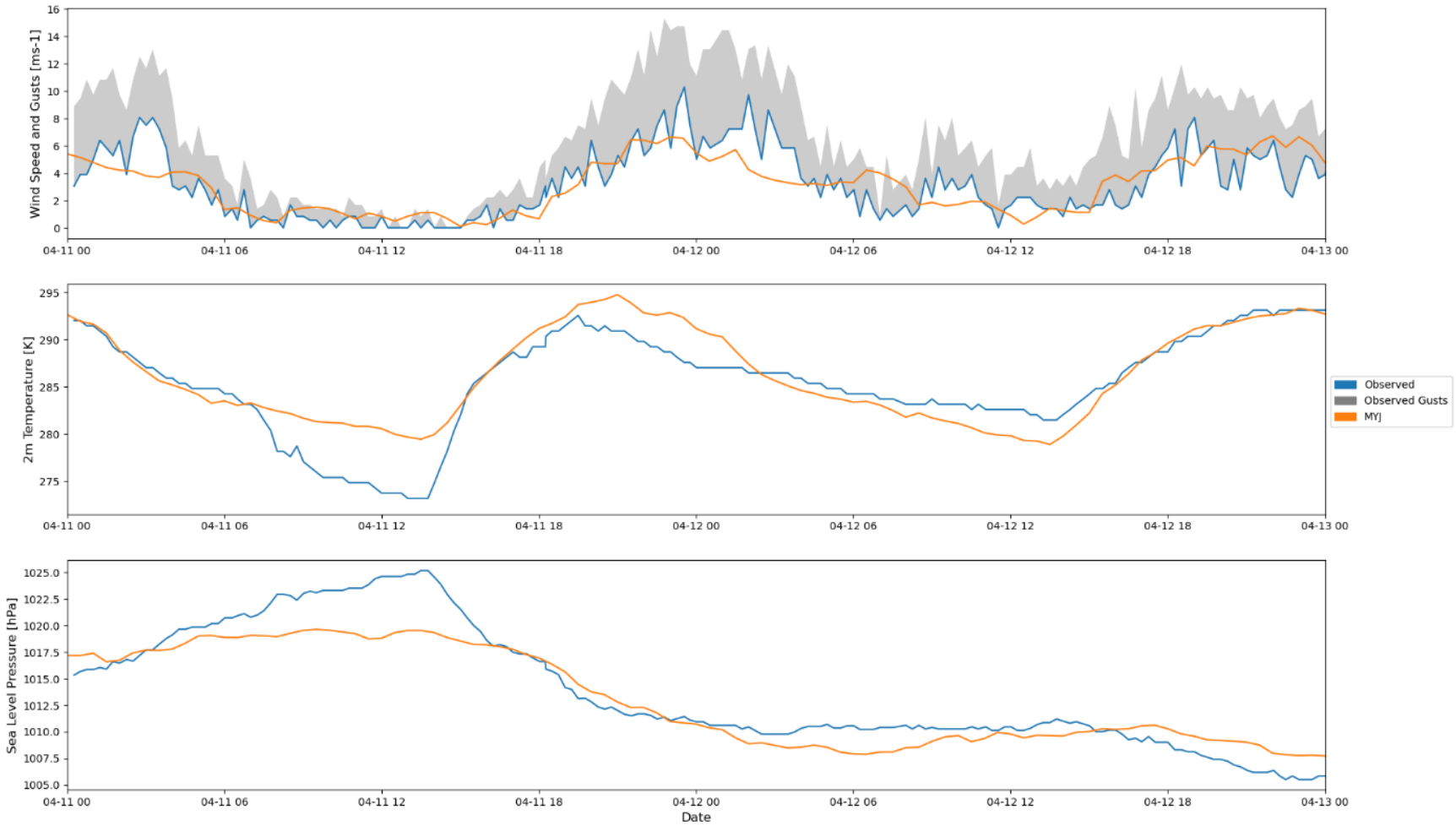
Wind Speed and Gusts [ms-1]
2m Temperature [K]
Sea Level Pressure [hPa]
Date
04-11 00
04-11 06
04-11 12
04-11 18
04-12 00
04-12 06
04-12 12
04-12 18
04-13 00
Observed
Observed Gusts
MYJ

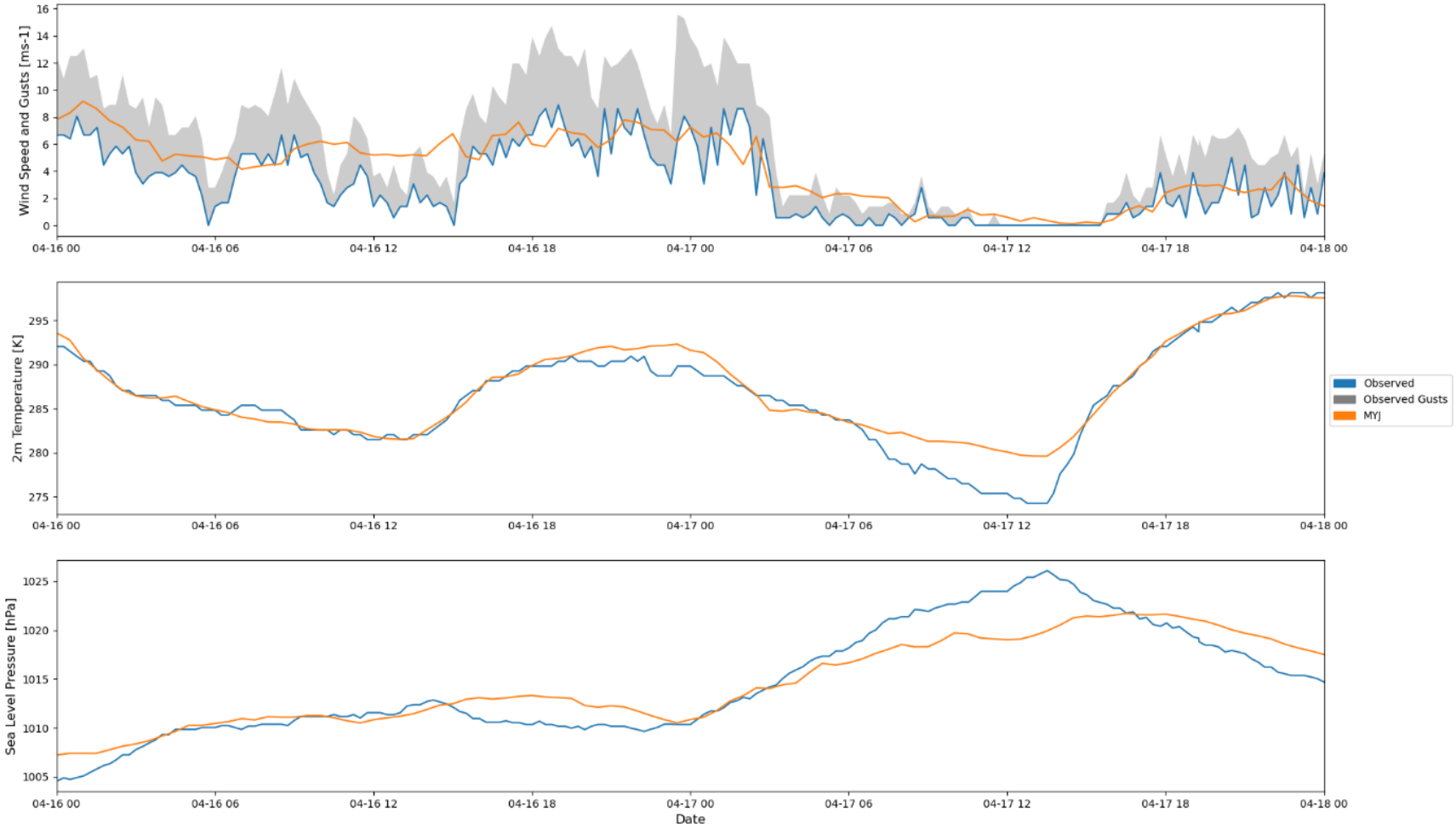
Wind Speed and Gusts [ms-1]
2m Temperature [K]
Sea Level Pressure [hPa]
Date
04-16 00
04-16 06
04-16 12
04-16 18
04-17 00
04-17 06
04-17 12
04-17 18
04-18 00
Observed
Observed Gusts
MYJ

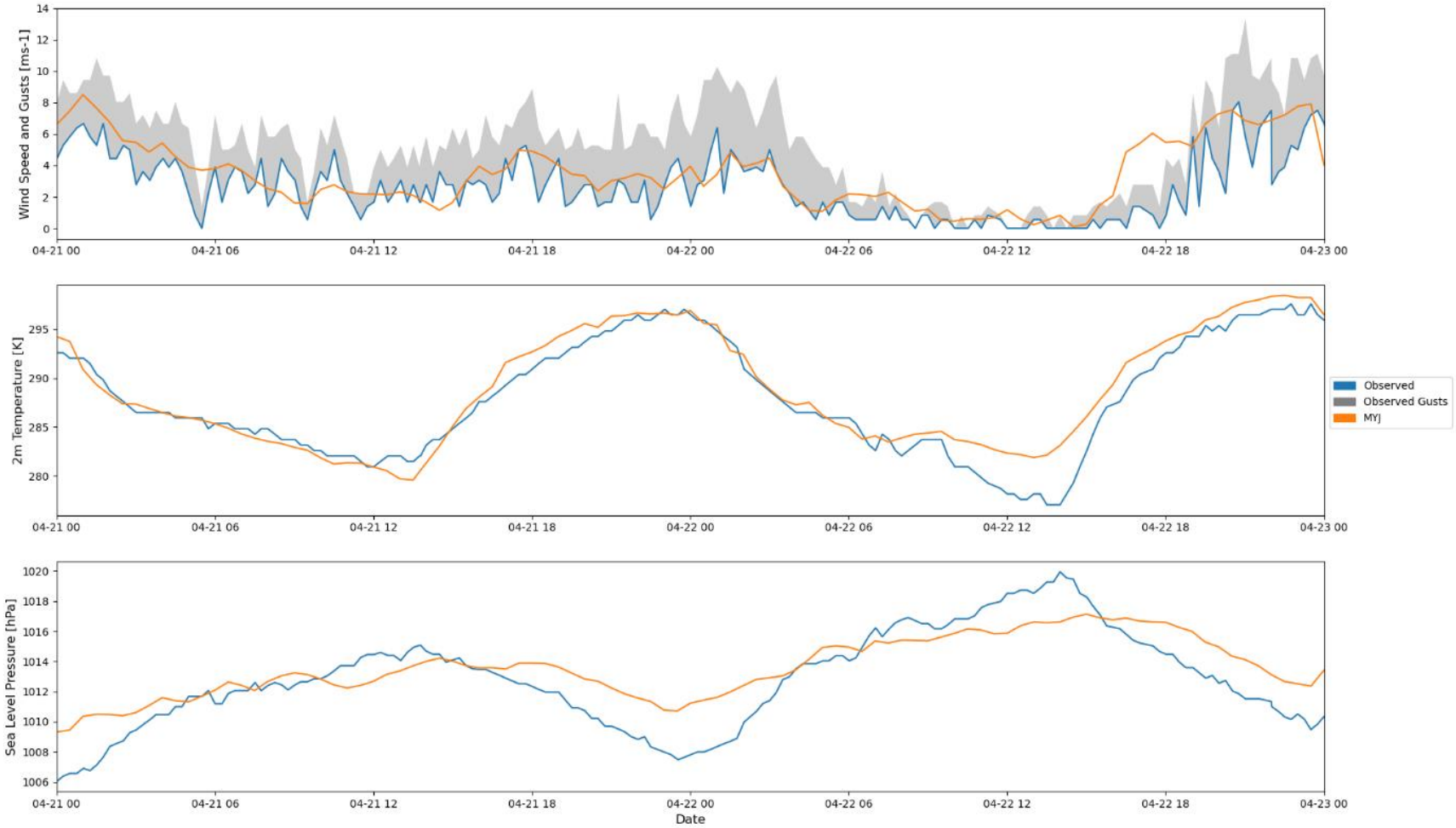
Wind Speed and Gusts [ms-1]
2m Temperature [K]
Sea Level Pressure [hPa]
Date
04-21 00
04-21 06
04-21 12
04-21 18
04-22 00
04-22 06
04-22 12
04-22 18
04-23 00
Observed
Observed Gusts
MYJ

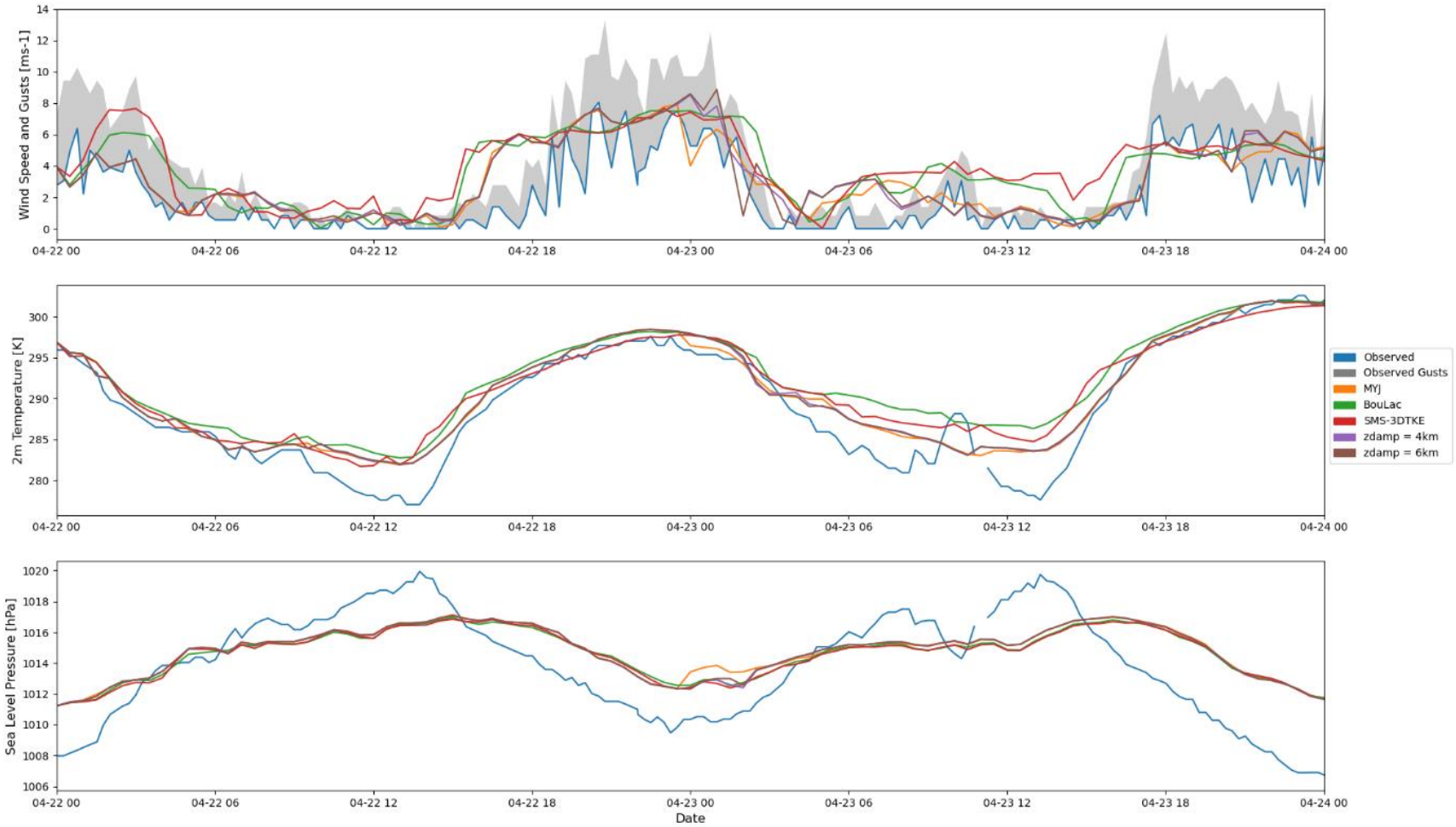
Wind Speed and Gusts [ms-1]
2m Temperature [K]
Sea Level Pressure [hPa]
Date
04-22 00
04-22 06
04-22 12
04-22 18
04-23 00
04-23 06
04-23 12
04-23 18
04-24 00
Observed
Observed Gusts
MYJ
BouLac
SMS-3DTKE
zdamp = 4km
zdamp = 6km

Appendix E – Skew-T Plots

Figures E1-E26. Skew-T diagrams for Day 1 (a) and Day 2 (b) at the specified UTC time at P577 upwind of the San Bernardino Mountains.

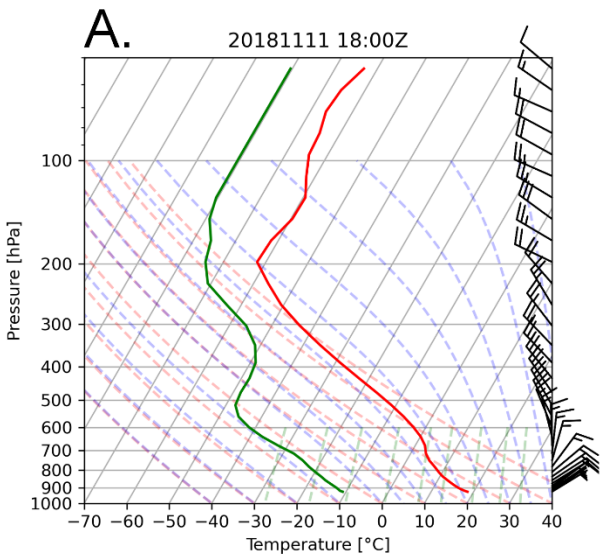

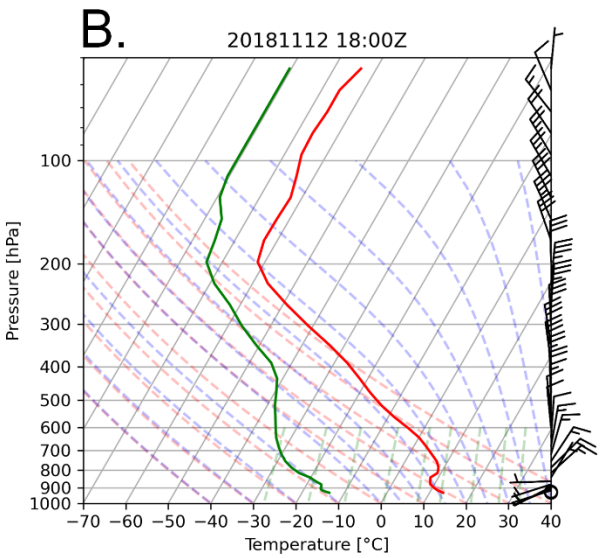

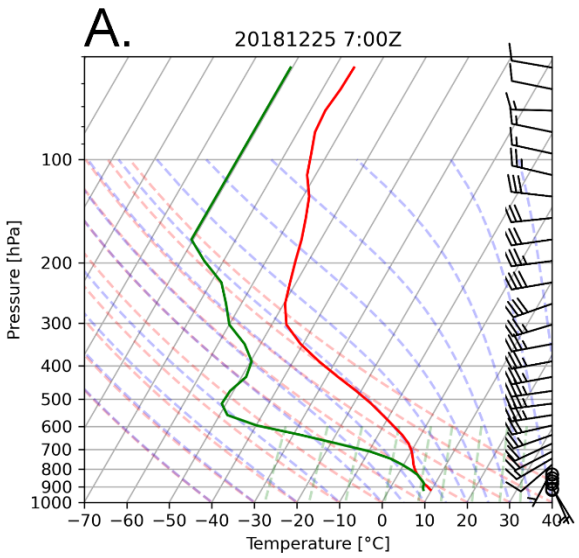

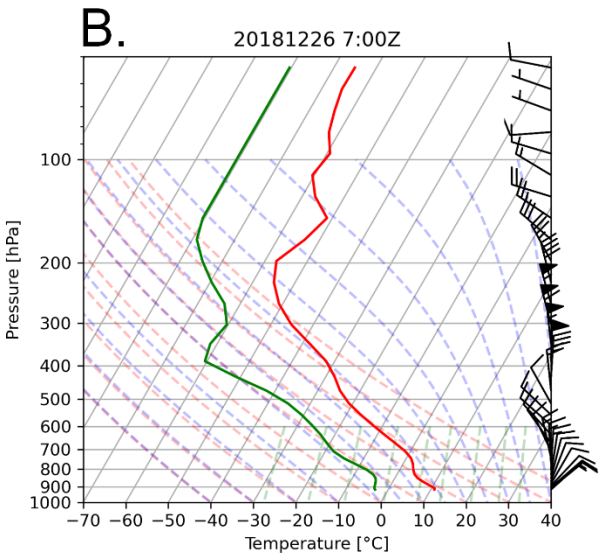

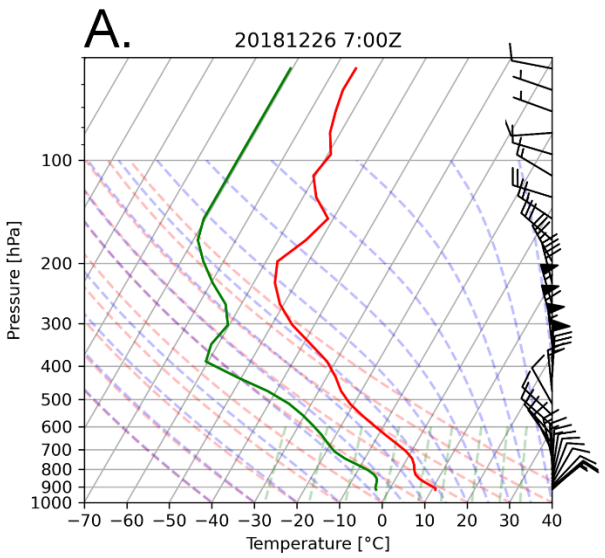
A.
20181226 7:00Z
Pressure [hPa]
100
200
300
400
500
600
700
800
900
1000
−70 −60 −50 −40 −30 −20 −10 0 10 20 30 40
Temperature [°C]

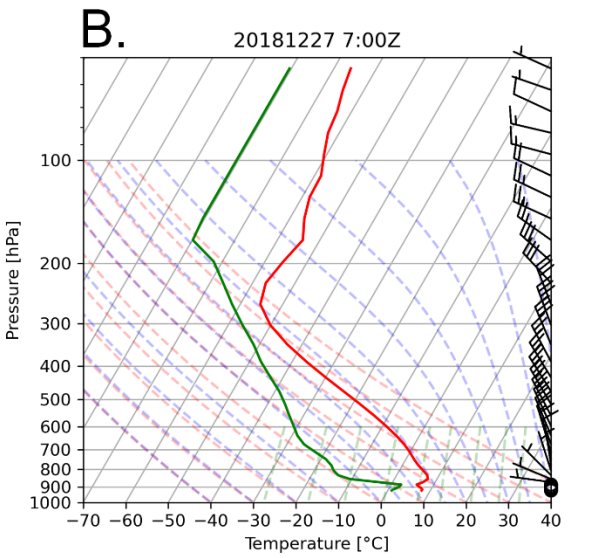
B.
20181227 7:00Z
Pressure [hPa]
100
200
300
400
500
600
700
800
900
1000
−70 −60 −50 −40 −30 −20 −10 0 10 20 30 40
Temperature [°C]

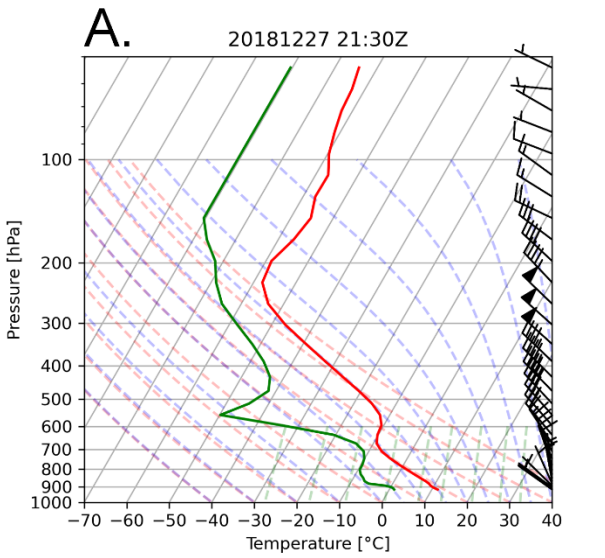
A.
20181227 21:30Z
Pressure [hPa]
100
200
300
400
500
600
700
800
900
1000
−70 −60 −50 −40 −30 −20 −10 0 10 20 30 40
Temperature [°C]

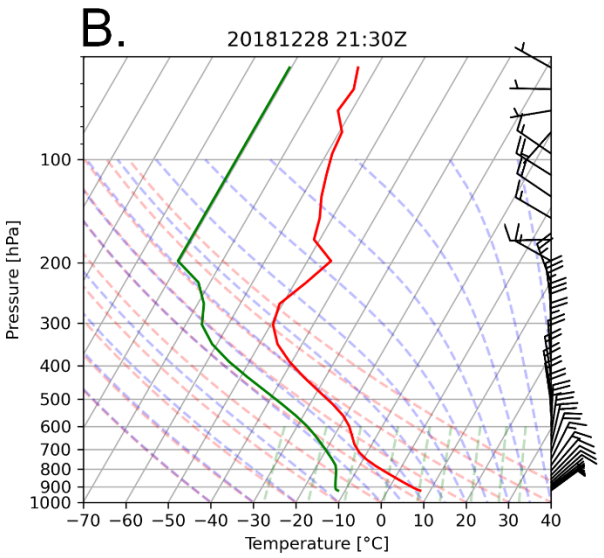
B.
20181228 21:30Z
Pressure [hPa]
100
200
300
400
500
600
700
800
900
1000
−70 −60 −50 −40 −30 −20 −10 0 10 20 30 40
Temperature [°C]

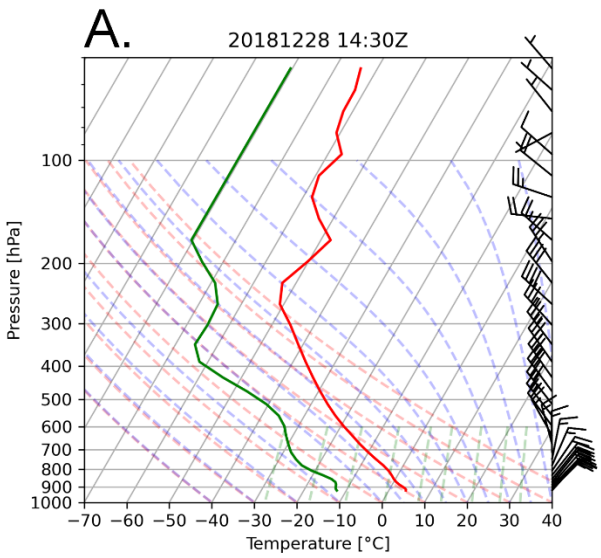
A.
20181228 14:30Z
Pressure [hPa]
100
200
300
400
500
600
700
800
900
1000
−70 −60 −50 −40 −30 −20 −10 0 10 20 30 40
Temperature [°C]

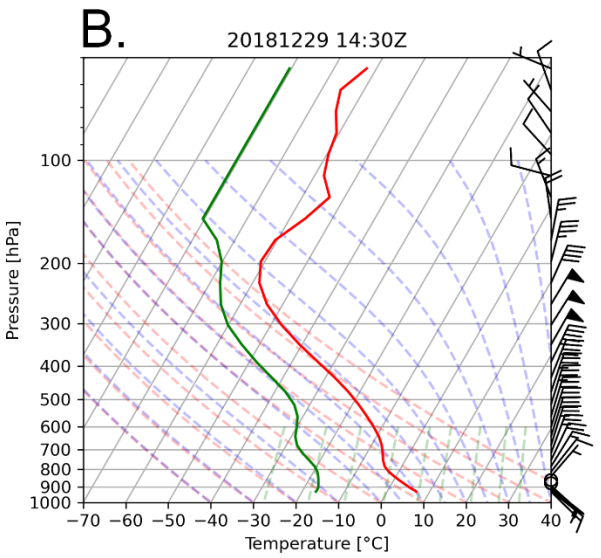
B.
20181229 14:30Z
Pressure [hPa]
100
200
300
400
500
600
700
800
900
1000
−70 −60 −50 −40 −30 −20 −10 0 10 20 30 40
Temperature [°C]

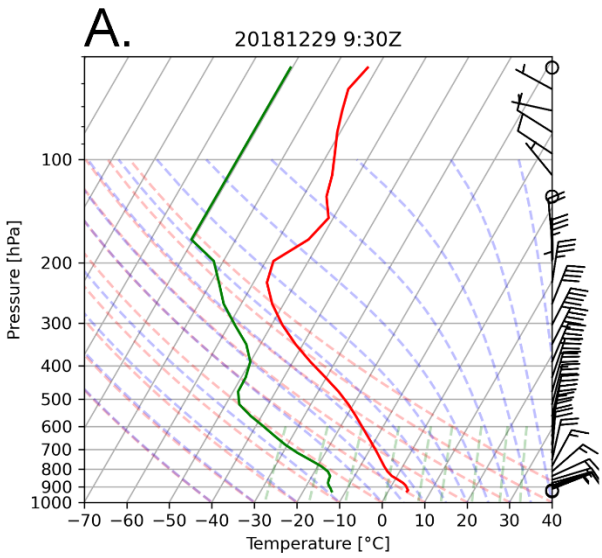
A.
20181229 9:30Z
Pressure [hPa]
100
200
300
400
500
600
700
800
900
1000
−70 −60 −50 −40 −30 −20 −10 0 10 20 30 40
Temperature [°C]

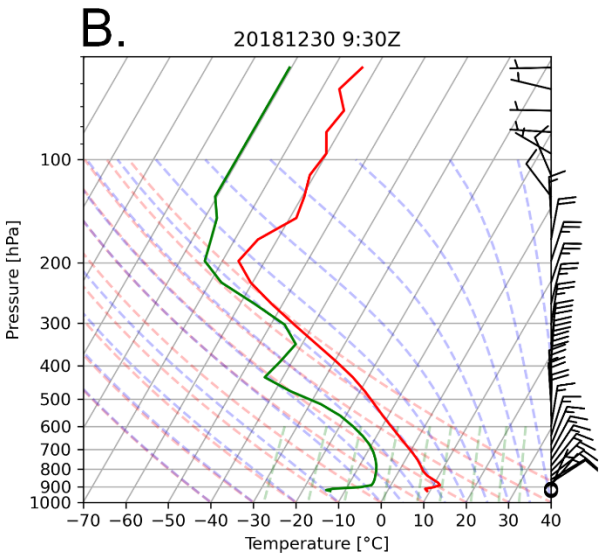
B.
20181230 9:30Z
Pressure [hPa]
100
200
300
400
500
600
700
800
900
1000
−70 −60 −50 −40 −30 −20 −10 0 10 20 30 40
Temperature [°C]

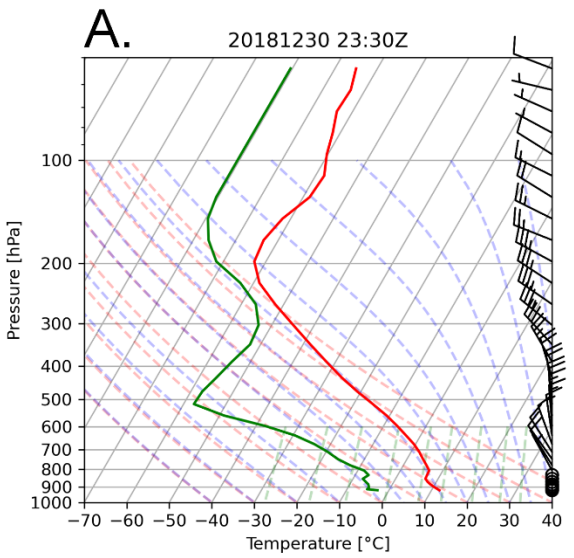
A.
20181230 23:30Z
Pressure [hPa]
100
200
300
400
500
600
700
800
900
1000
−70 −60 −50 −40 −30 −20 −10 0 10 20 30 40
Temperature [°C]

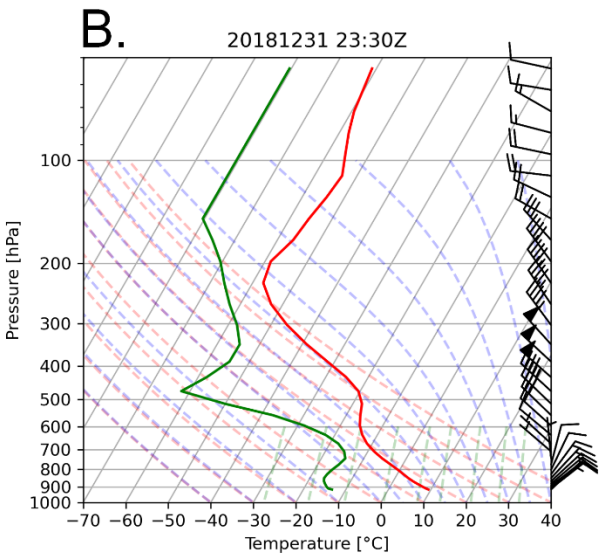
B.
20181231 23:30Z
Pressure [hPa]
100
200
300
400
500
600
700
800
900
1000
−70 −60 −50 −40 −30 −20 −10 0 10 20 30 40
Temperature [°C]

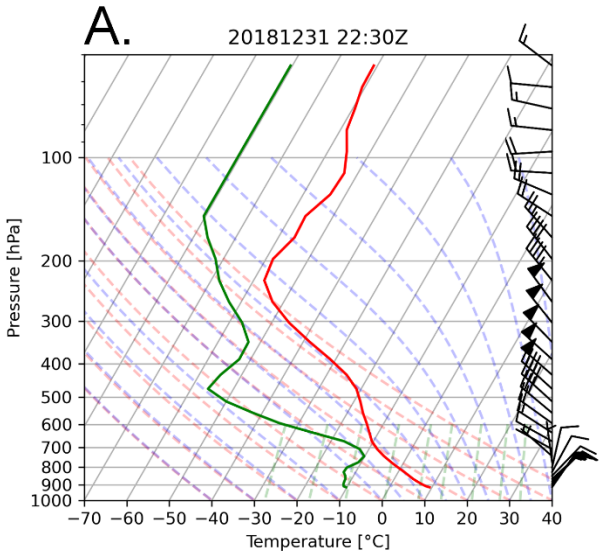
A.
20181231 22:30Z
Pressure [hPa]
100
200
300
400
500
600
700
800
900
1000
−70 −60 −50 −40 −30 −20 −10 0 10 20 30 40
Temperature [°C]

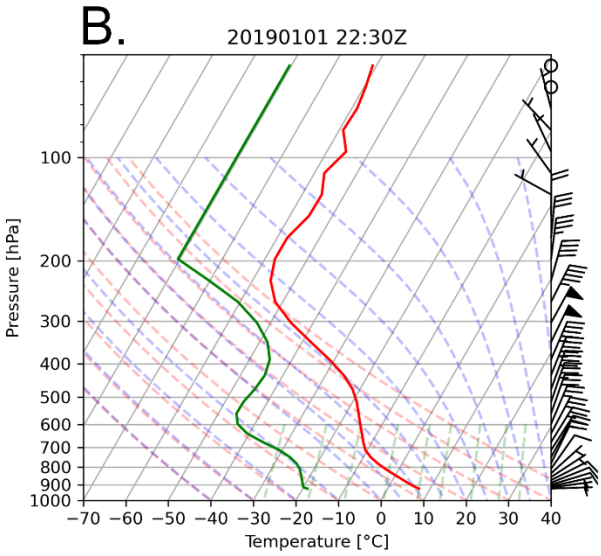
B.
20190101 22:30Z
Pressure [hPa]
100
200
300
400
500
600
700
800
900
1000
−70 −60 −50 −40 −30 −20 −10 0 10 20 30 40
Temperature [°C]

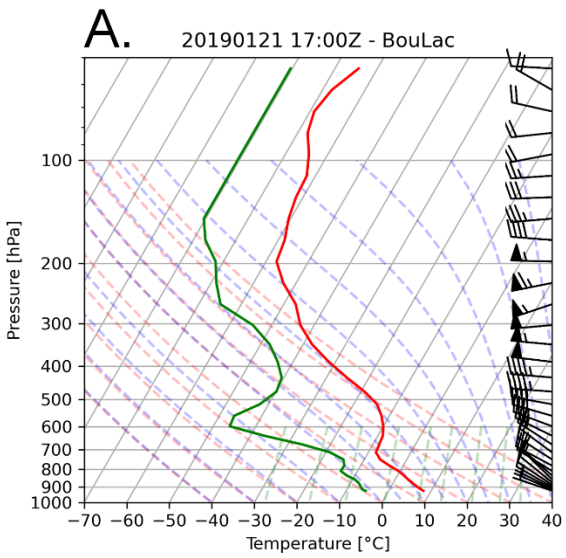
A.
20190121 17:00Z - BouLac
Pressure [hPa]
100
200
300
400
500
600
700
800
900
1000
−70 −60 −50 −40 −30 −20 −10 0 10 20 30 40
Temperature [°C]

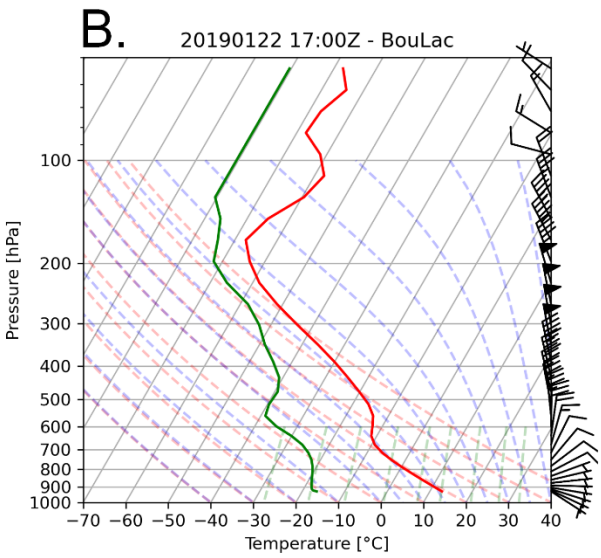
B.
20190122 17:00Z - BouLac
Pressure [hPa]
100
200
300
400
500
600
700
800
900
1000
−70 −60 −50 −40 −30 −20 −10 0 10 20 30 40
Temperature [°C]

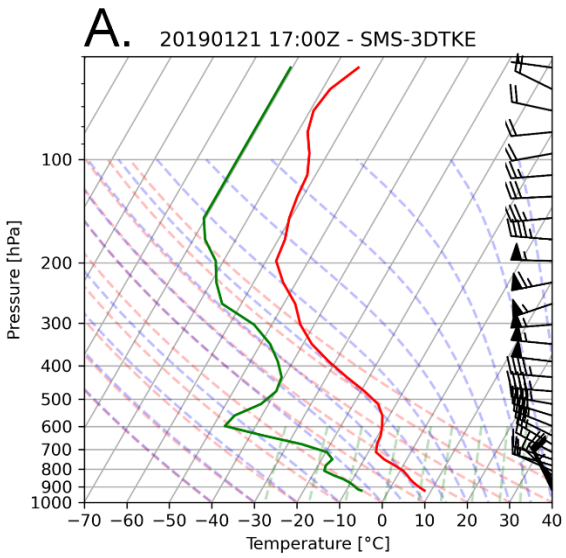
A.
20190121 17:00Z - SMS-3DTKE
Pressure [hPa]
100
200
300
400
500
600
700
800
900
1000
−70 −60 −50 −40 −30 −20 −10 0 10 20 30 40
Temperature [°C]

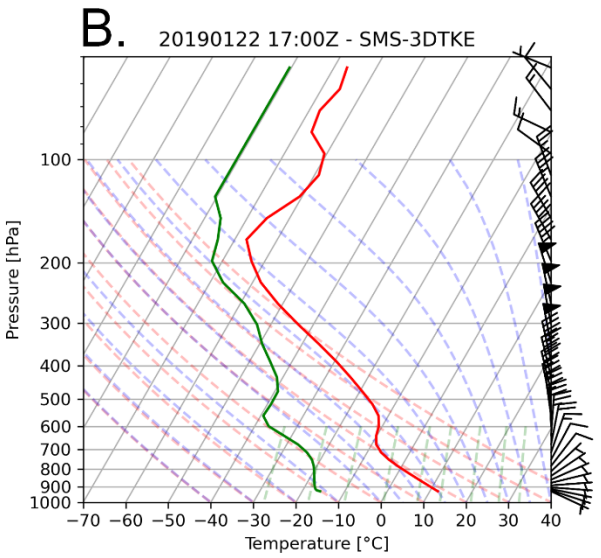
B.
20190122 17:00Z - SMS-3DTKE
Pressure [hPa]
100
200
300
400
500
600
700
800
900
1000
−70 −60 −50 −40 −30 −20 −10 0 10 20 30 40
Temperature [°C]

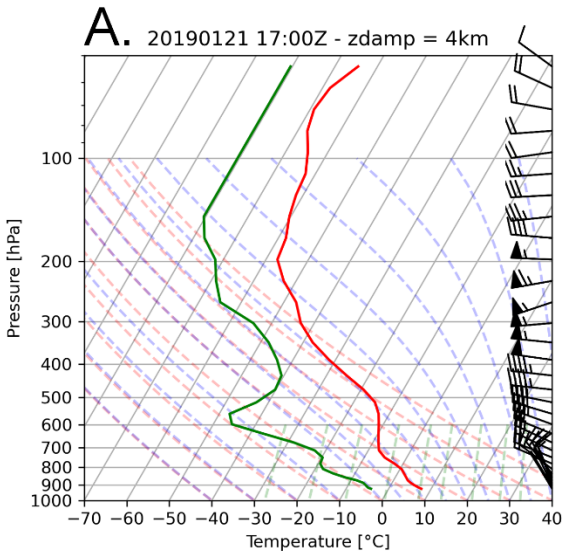
A.
20190121 17:00Z - zdamp = 4km
Pressure [hPa]
100
200
300
400
500
600
700
800
900
1000
−70 −60 −50 −40 −30 −20 −10 0 10 20 30 40
Temperature [°C]

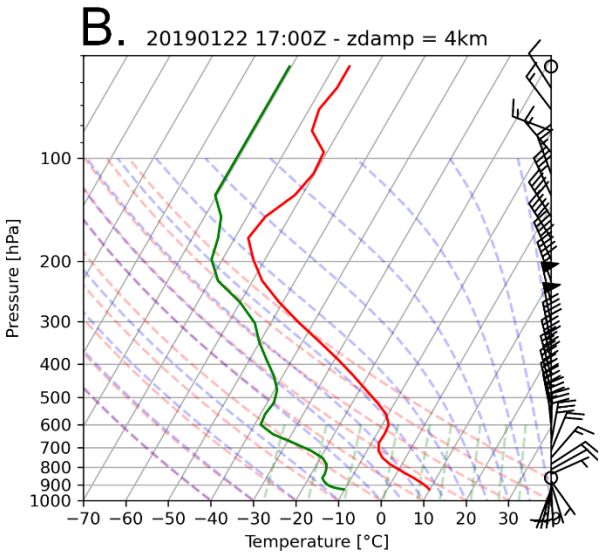
B.
20190122 17:00Z - zdamp = 4km
Pressure [hPa]
100
200
300
400
500
600
700
800
900
1000
−70 −60 −50 −40 −30 −20 −10 0 10 20 30
Temperature [°C]

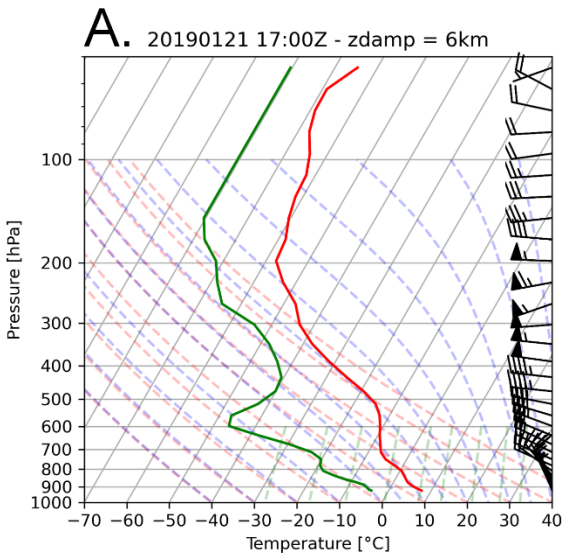
A.
20190121 17:00Z - zdamp = 6km
Pressure [hPa]
100
200
300
400
500
600
700
800
900
1000
−70 −60 −50 −40 −30 −20 −10 0 10 20 30 40
Temperature [°C]

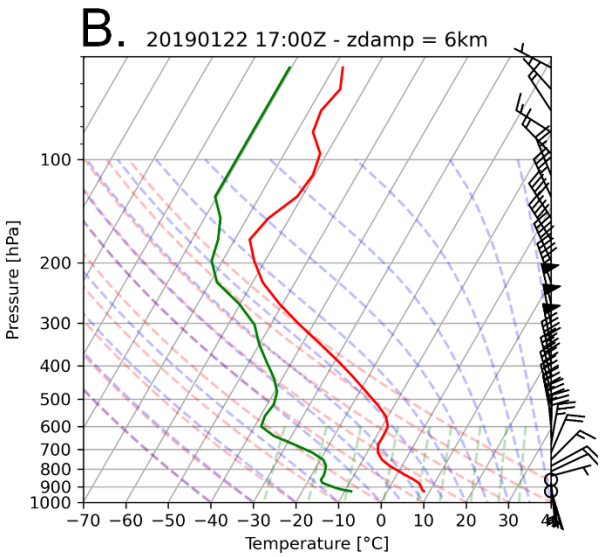
B.
20190122 17:00Z - zdamp = 6km
Pressure [hPa]
100
200
300
400
500
600
700
800
900
1000
−70 −60 −50 −40 −30 −20 −10 0 10 20 30
Temperature [°C]

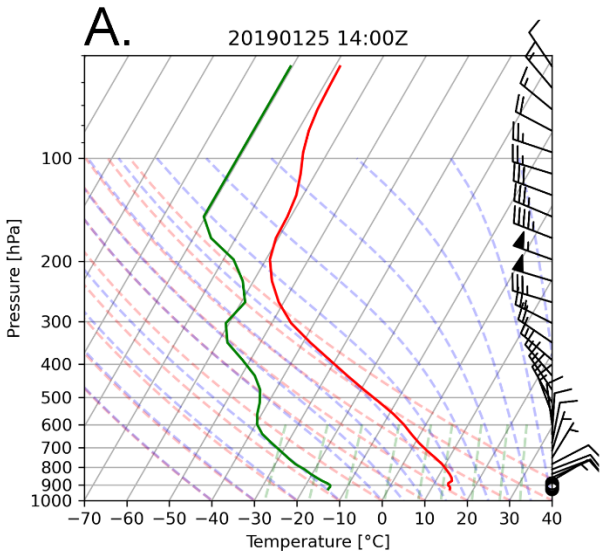
A.
20190125 14:00Z
Pressure [hPa]
100
200
300
400
500
600
700
800
900
1000
−70 −60 −50 −40 −30 −20 −10 0 10 20 30 40
Temperature [°C]

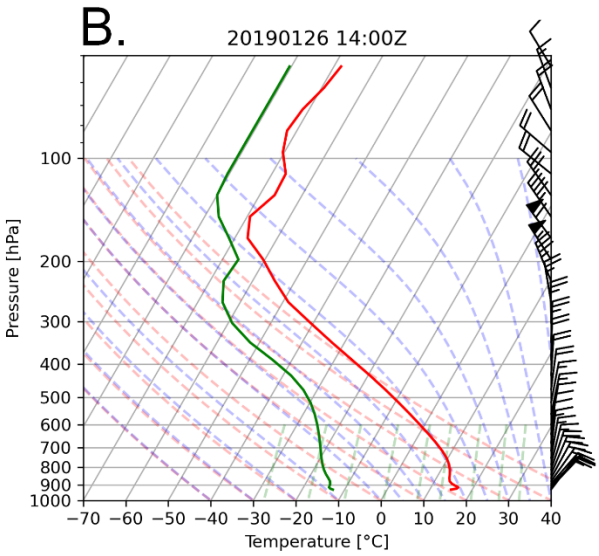
B.
20190126 14:00Z
Pressure [hPa]
100
200
300
400
500
600
700
800
900
1000
−70 −60 −50 −40 −30 −20 −10 0 10 20 30 40
Temperature [°C]

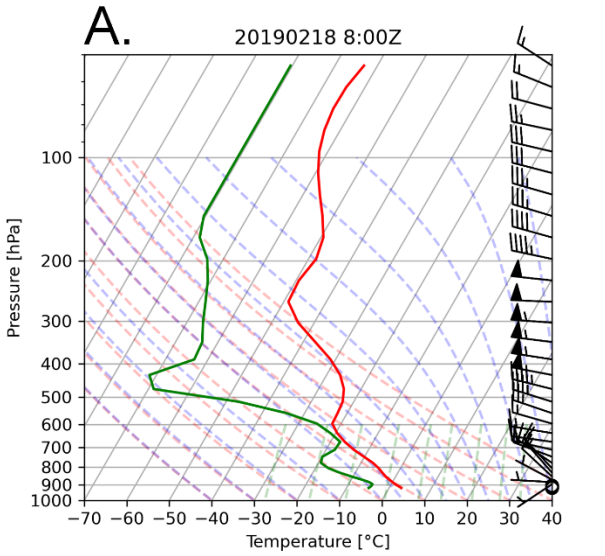
A.
20190218 8:00Z
Pressure [hPa]
100
200
300
400
500
600
700
800
900
1000
−70 −60 −50 −40 −30 −20 −10 0 10 20 30 40
Temperature [°C]

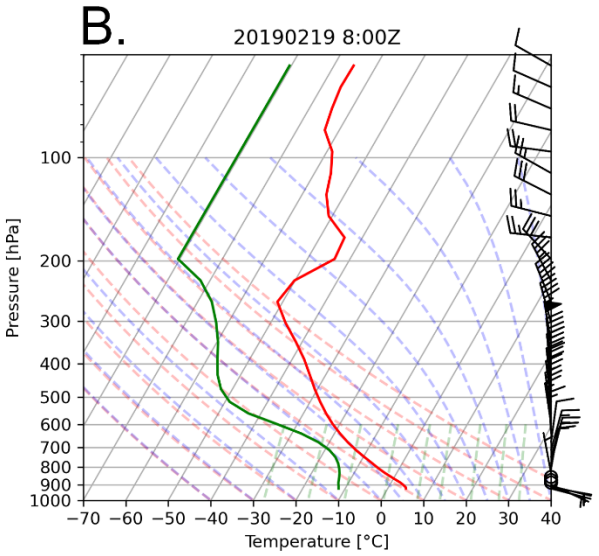
B.
20190219 8:00Z
Pressure [hPa]
100
200
300
400
500
600
700
800
900
1000
−70 −60 −50 −40 −30 −20 −10 0 10 20 30 40
Temperature [°C]

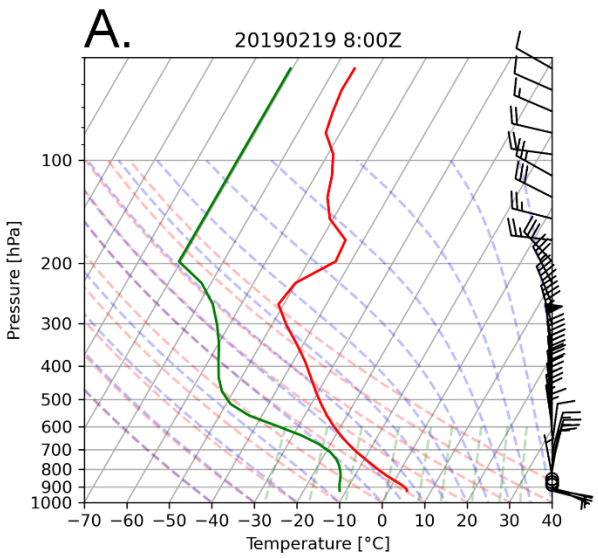
A.
20190219 8:00Z
Pressure [hPa]
100
200
300
400
500
600
700
800
900
1000
−70 −60 −50 −40 −30 −20 −10 0 10 20 30 40
Temperature [°C]

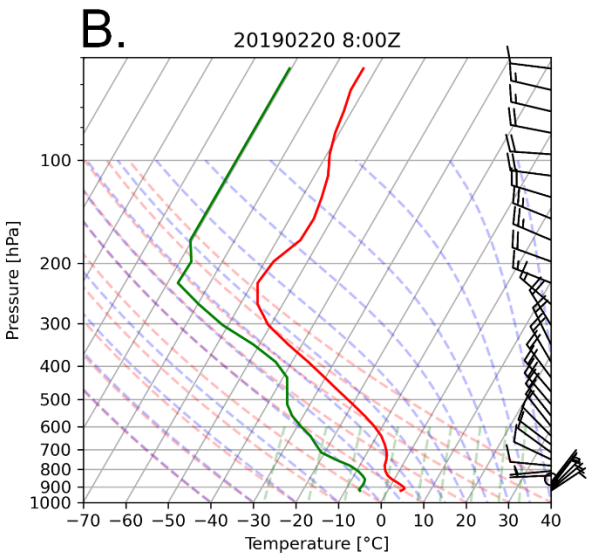
B.
20190220 8:00Z
Pressure [hPa]
100
200
300
400
500
600
700
800
900
1000
−70 −60 −50 −40 −30 −20 −10 0 10 20 30 40
Temperature [°C]

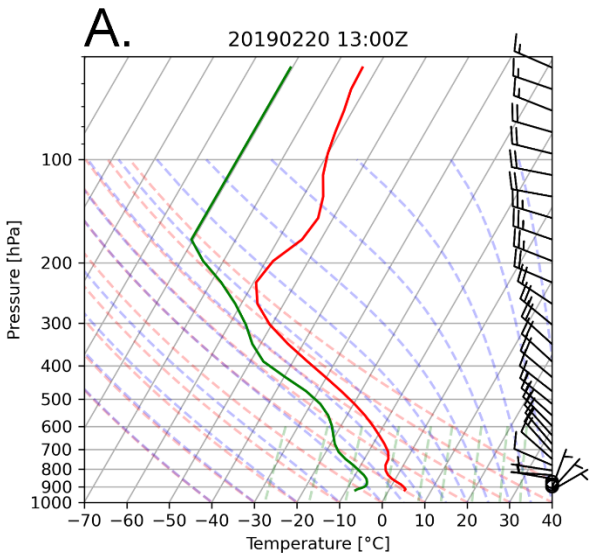
A.
20190220 13:00Z
Pressure [hPa]
100
200
300
400
500
600
700
800
900
1000
−70 −60 −50 −40 −30 −20 −10 0 10 20 30 40
Temperature [°C]

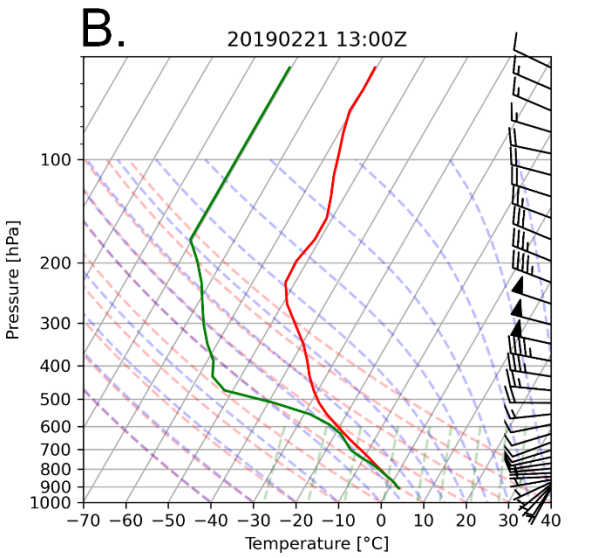
B.
20190221 13:00Z
Pressure [hPa]
100
200
300
400
500
600
700
800
900
1000
−70 −60 −50 −40 −30 −20 −10 0 10 20 30 40
Temperature [°C]

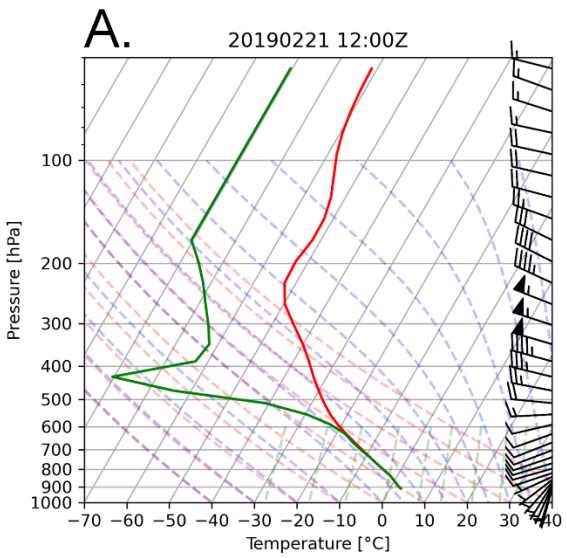
A.
20190221 12:00Z
Pressure [hPa]
100
200
300
400
500
600
700
800
900
1000
−70 −60 −50 −40 −30 −20 −10 0 10 20 30 40
Temperature [°C]

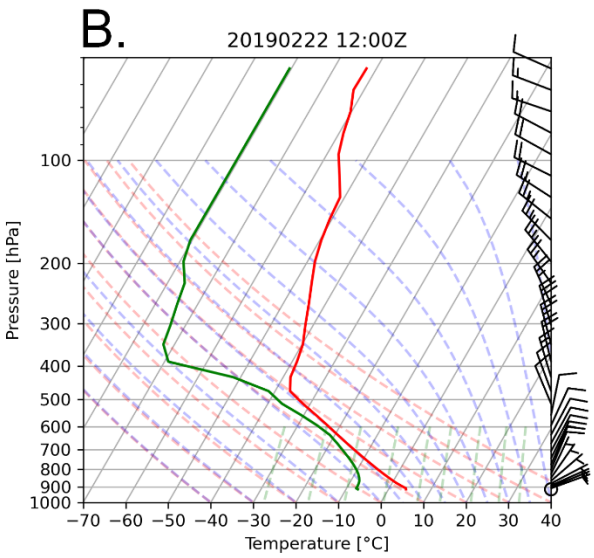
B.
20190222 12:00Z
Pressure [hPa]
100
200
300
400
500
600
700
800
900
1000
−70 −60 −50 −40 −30 −20 −10 0 10 20 30 40
Temperature [°C]

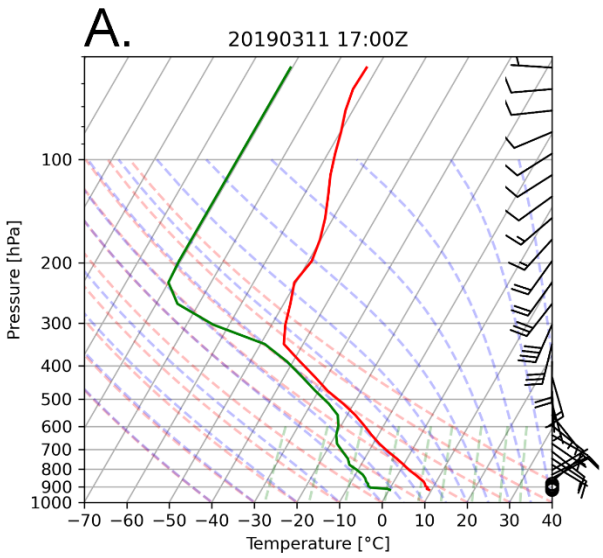
A.
20190311 17:00Z
Pressure [hPa]
100
200
300
400
500
600
700
800
900
1000
−70 −60 −50 −40 −30 −20 −10 0 10 20 30 40
Temperature [°C]

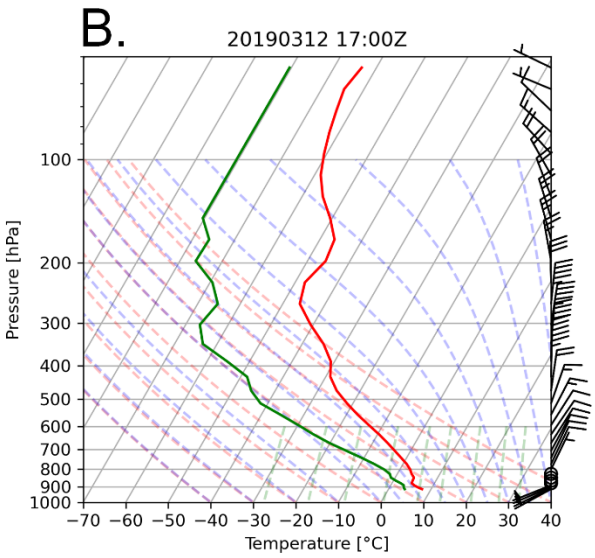
B.
20190312 17:00Z
Pressure [hPa]
100
200
300
400
500
600
700
800
900
1000
−70 −60 −50 −40 −30 −20 −10 0 10 20 30 40
Temperature [°C]

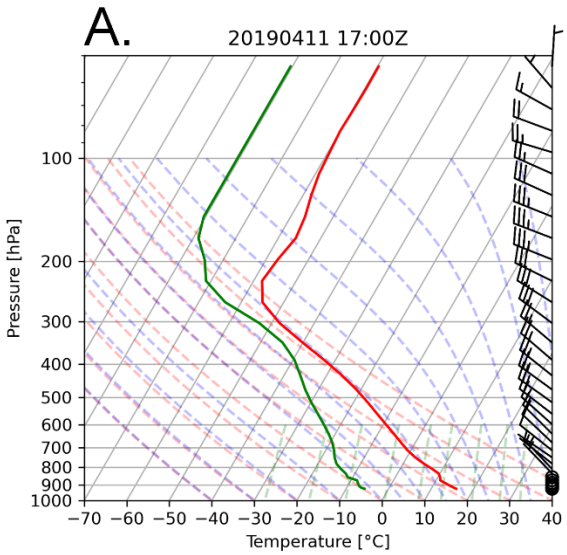
A.
20190411 17:00Z
Pressure [hPa]
100
200
300
400
500
600
700
800
900
1000
−70 −60 −50 −40 −30 −20 −10 0 10 20 30 40
Temperature [°C]

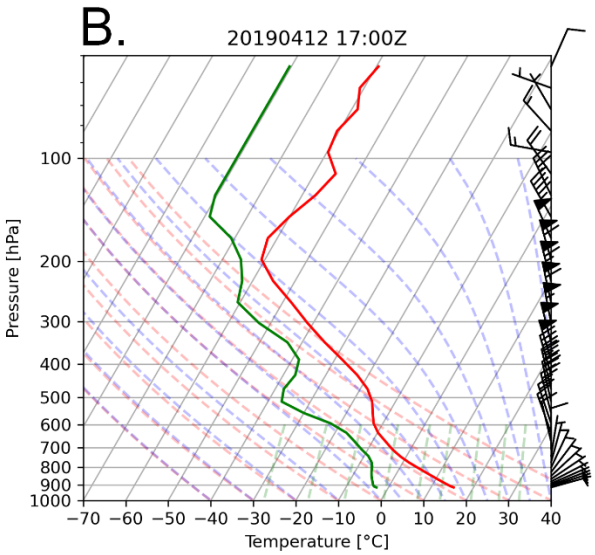
B.
20190412 17:00Z
Pressure [hPa]
100
200
300
400
500
600
700
800
900
1000
−70 −60 −50 −40 −30 −20 −10 0 10 20 30 40
Temperature [°C]

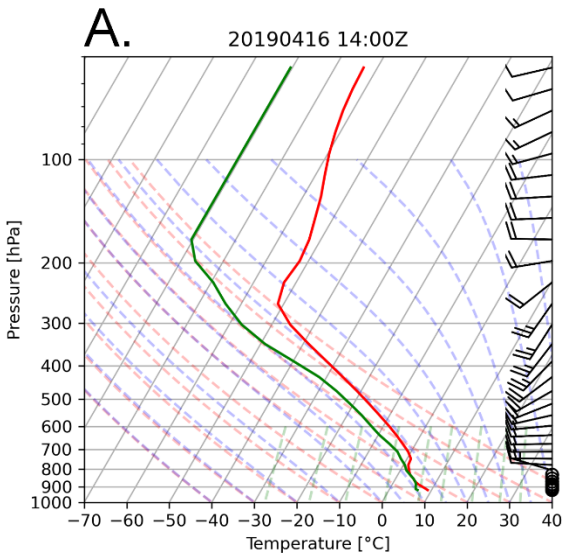
A.
20190416 14:00Z
Pressure [hPa]
100
200
300
400
500
600
700
800
900
1000
−70 −60 −50 −40 −30 −20 −10 0 10 20 30 40
Temperature [°C]

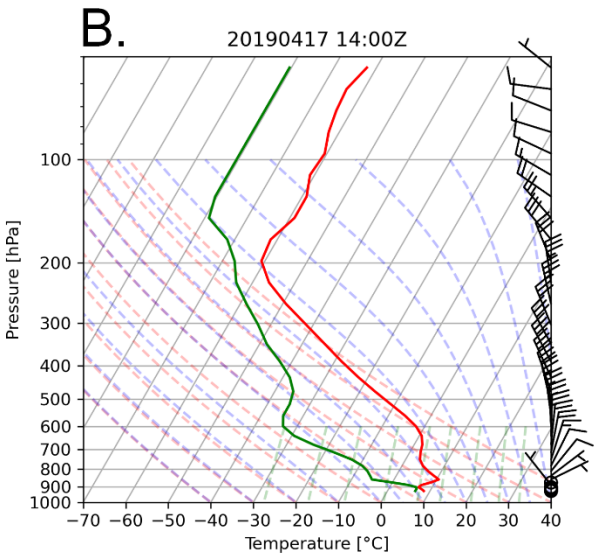
B.
20190417 14:00Z
Pressure [hPa]
100
200
300
400
500
600
700
800
900
1000
−70 −60 −50 −40 −30 −20 −10 0 10 20 30 40
Temperature [°C]

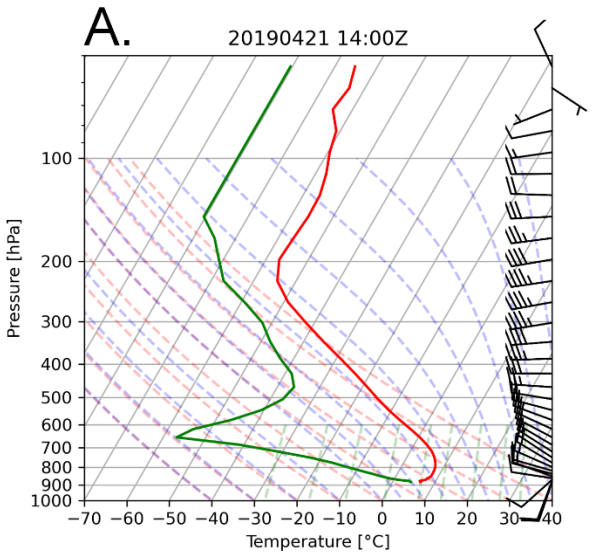
A.
20190421 14:00Z
Pressure [hPa]
100
200
300
400
500
600
700
800
900
1000
−70 −60 −50 −40 −30 −20 −10 0 10 20 30 40
Temperature [°C]

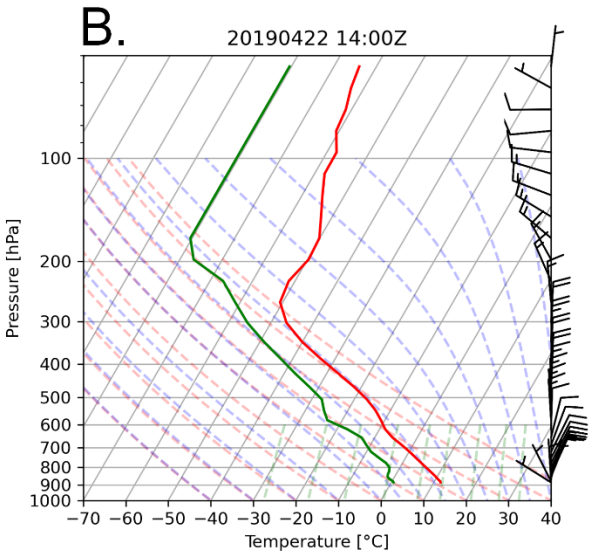
B.
20190422 14:00Z
Pressure [hPa]
100
200
300
400
500
600
700
800
900
1000
−70 −60 −50 −40 −30 −20 −10 0 10 20 30 40
Temperature [°C]

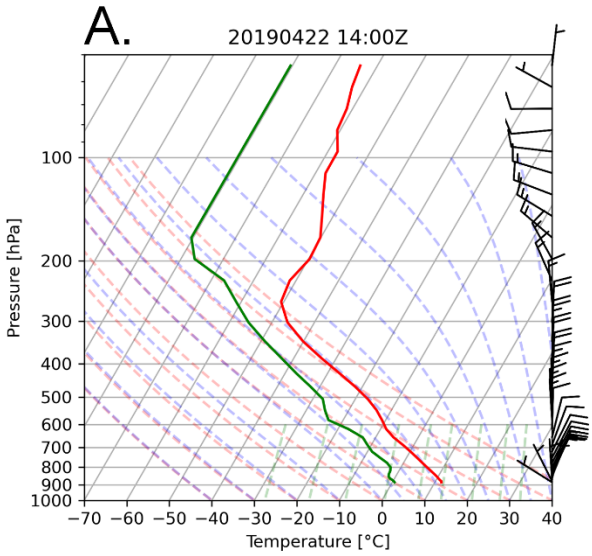
A.
20190422 14:00Z
Pressure [hPa]
100
200
300
400
500
600
700
800
900
1000
−70 −60 −50 −40 −30 −20 −10 0 10 20 30 40
Temperature [°C]

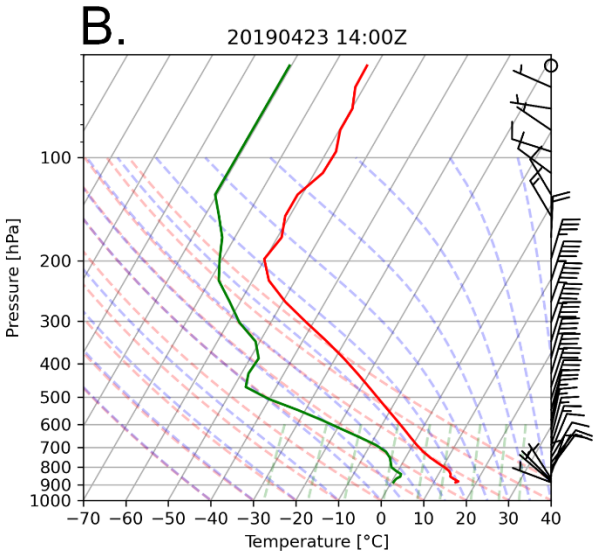
B.
20190423 14:00Z
Pressure [hPa]
100
200
300
400
500
600
700
800
900
1000
−70 −60 −50 −40 −30 −20 −10 0 10 20 30 40
Temperature [°C]

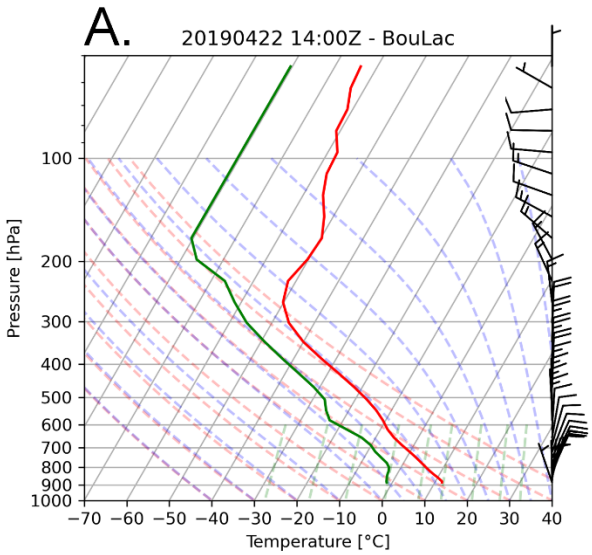
A.
20190422 14:00Z - BouLac
Pressure [hPa]
100
200
300
400
500
600
700
800
900
1000
−70 −60 −50 −40 −30 −20 −10 0 10 20 30 40
Temperature [°C]

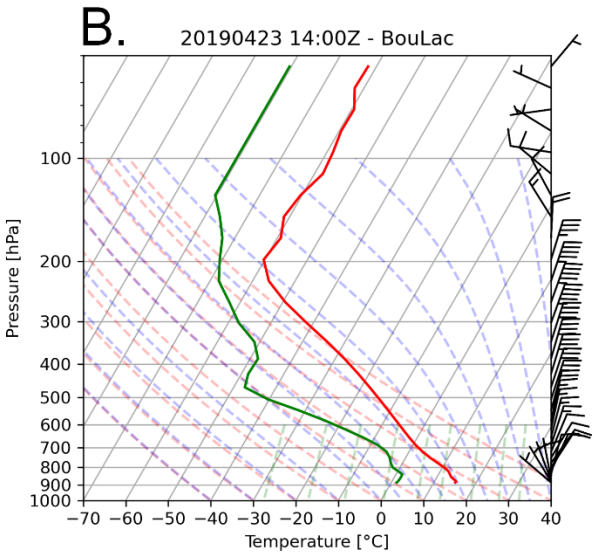
B.
20190423 14:00Z - BouLac
Pressure [hPa]
100
200
300
400
500
600
700
800
900
1000
−70 −60 −50 −40 −30 −20 −10 0 10 20 30 40
Temperature [°C]

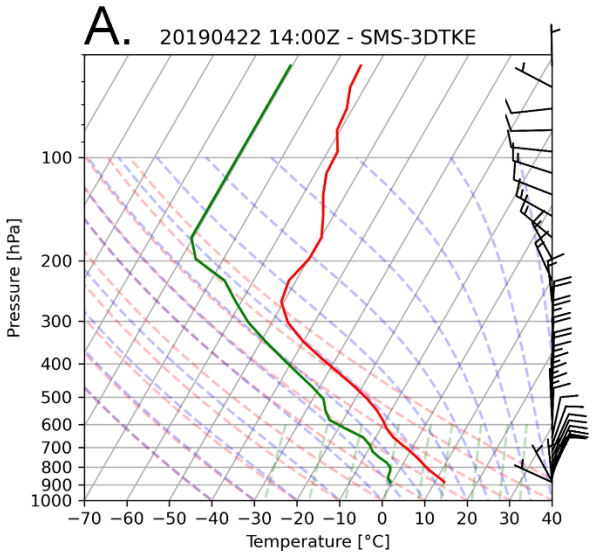
A.
20190422 14:00Z - SMS-3DTKE
Pressure [hPa]
100
200
300
400
500
600
700
800
900
1000
−70 −60 −50 −40 −30 −20 −10 0 10 20 30 40
Temperature [°C]

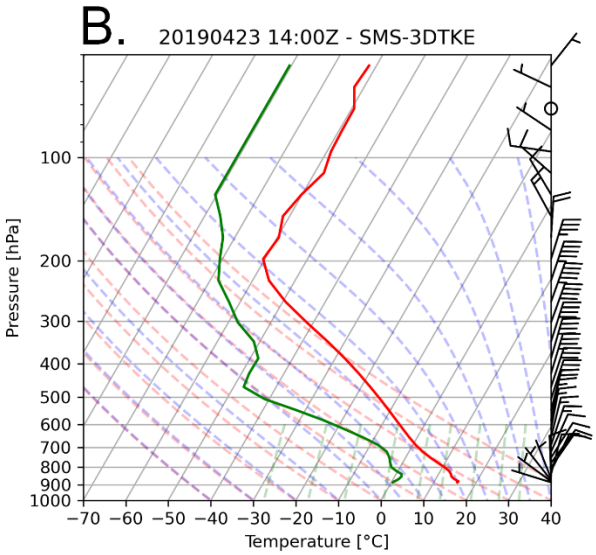
B.
20190423 14:00Z - SMS-3DTKE
Pressure [hPa]
100
200
300
400
500
600
700
800
900
1000
−70 −60 −50 −40 −30 −20 −10 0 10 20 30 40
Temperature [°C]

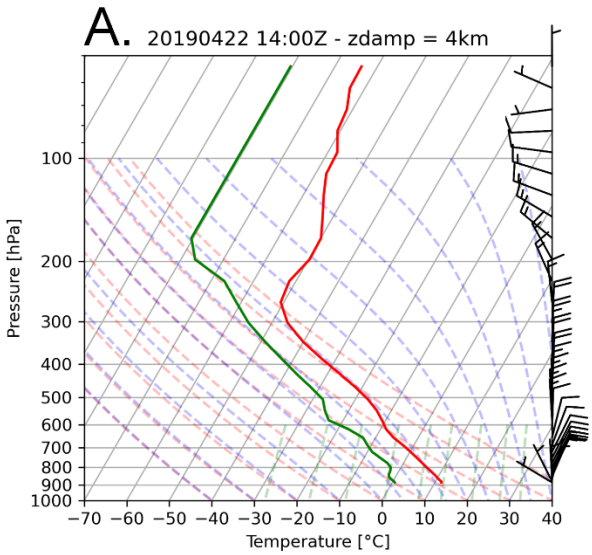
A.
20190422 14:00Z - zdamp = 4km
Pressure [hPa]
100
200
300
400
500
600
700
800
900
1000
−70 −60 −50 −40 −30 −20 −10 0 10 20 30 40
Temperature [°C]

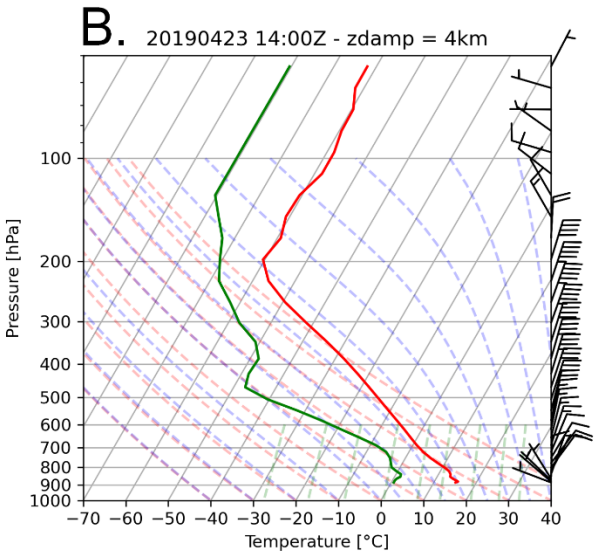
B.
20190423 14:00Z - zdamp = 4km
Pressure [hPa]
100
200
300
400
500
600
700
800
900
1000
−70 −60 −50 −40 −30 −20 −10 0 10 20 30 40
Temperature [°C]

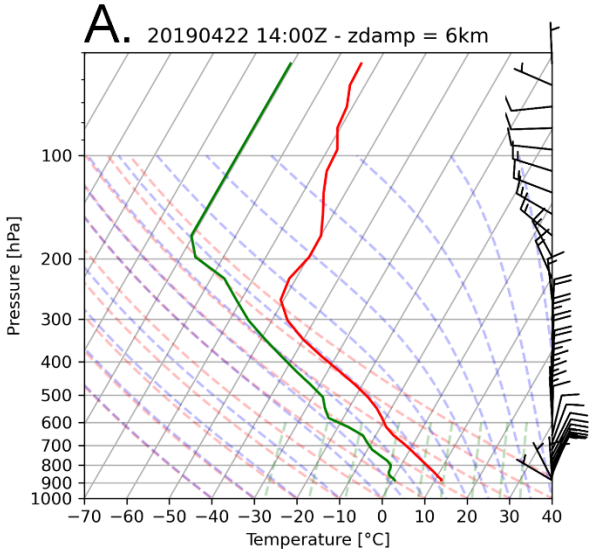
A.
20190422 14:00Z - zdamp = 6km
Pressure [hPa]
100
200
300
400
500
600
700
800
900
1000
−70 −60 −50 −40 −30 −20 −10 0 10 20 30 40
Temperature [°C]

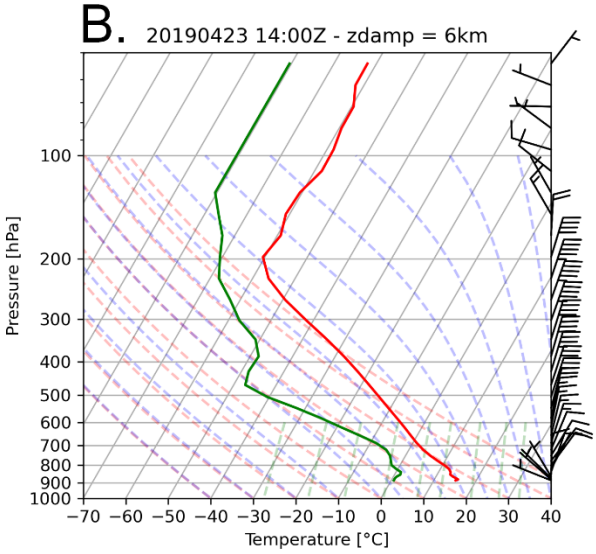
B.
20190423 14:00Z - zdamp = 6km
Pressure [hPa]
100
200
300
400
500
600
700
800
900
1000
−70 −60 −50 −40 −30 −20 −10 0 10 20 30 40
Temperature [°C]

Appendix F – Refractivity Plots

Figures F1-F11. Refractivities for each specified day pair up to 9 km (a, c) and 20 km (b, d), or up to 20 km (a-e) for 21-22 January and 22-23 April 2019 from the ray tracer beginning at P612.

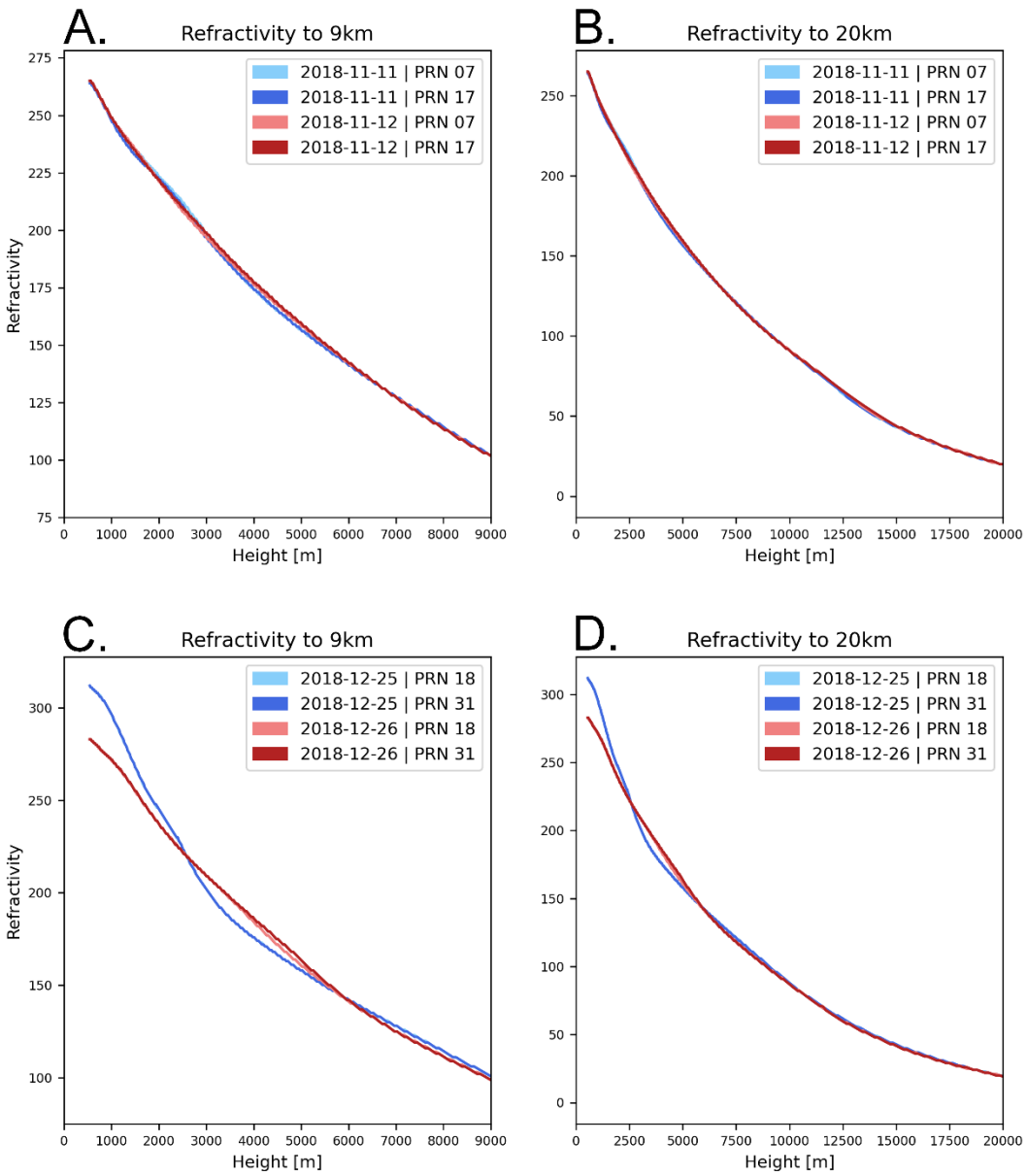

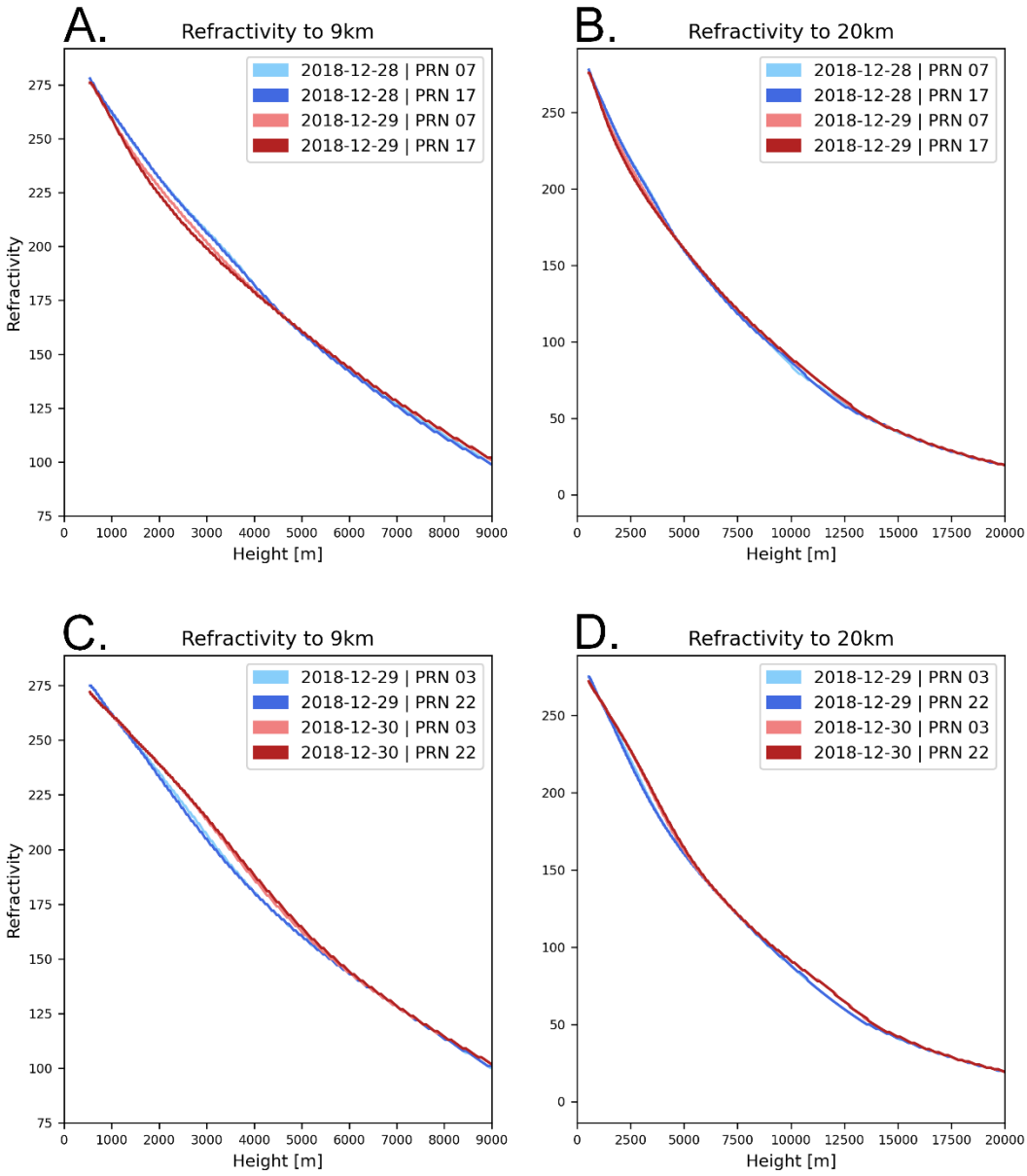
A.
Refractivity to 9km
2018-12-28 | PRN 07
2018-12-28 | PRN 17
2018-12-29 | PRN 07
2018-12-29 | PRN 17
Refractivity
Height [m]
B.
Refractivity to 20km
2018-12-28 | PRN 07
2018-12-28 | PRN 17
2018-12-29 | PRN 07
2018-12-29 | PRN 17
Height [m]
C.
Refractivity to 9km
2018-12-29 | PRN 03
2018-12-29 | PRN 22
2018-12-30 | PRN 03
2018-12-30 | PRN 22
Refractivity
Height [m]
D.
Refractivity to 20km
2018-12-29 | PRN 03
2018-12-29 | PRN 22
2018-12-30 | PRN 03
2018-12-30 | PRN 22
Height [m]

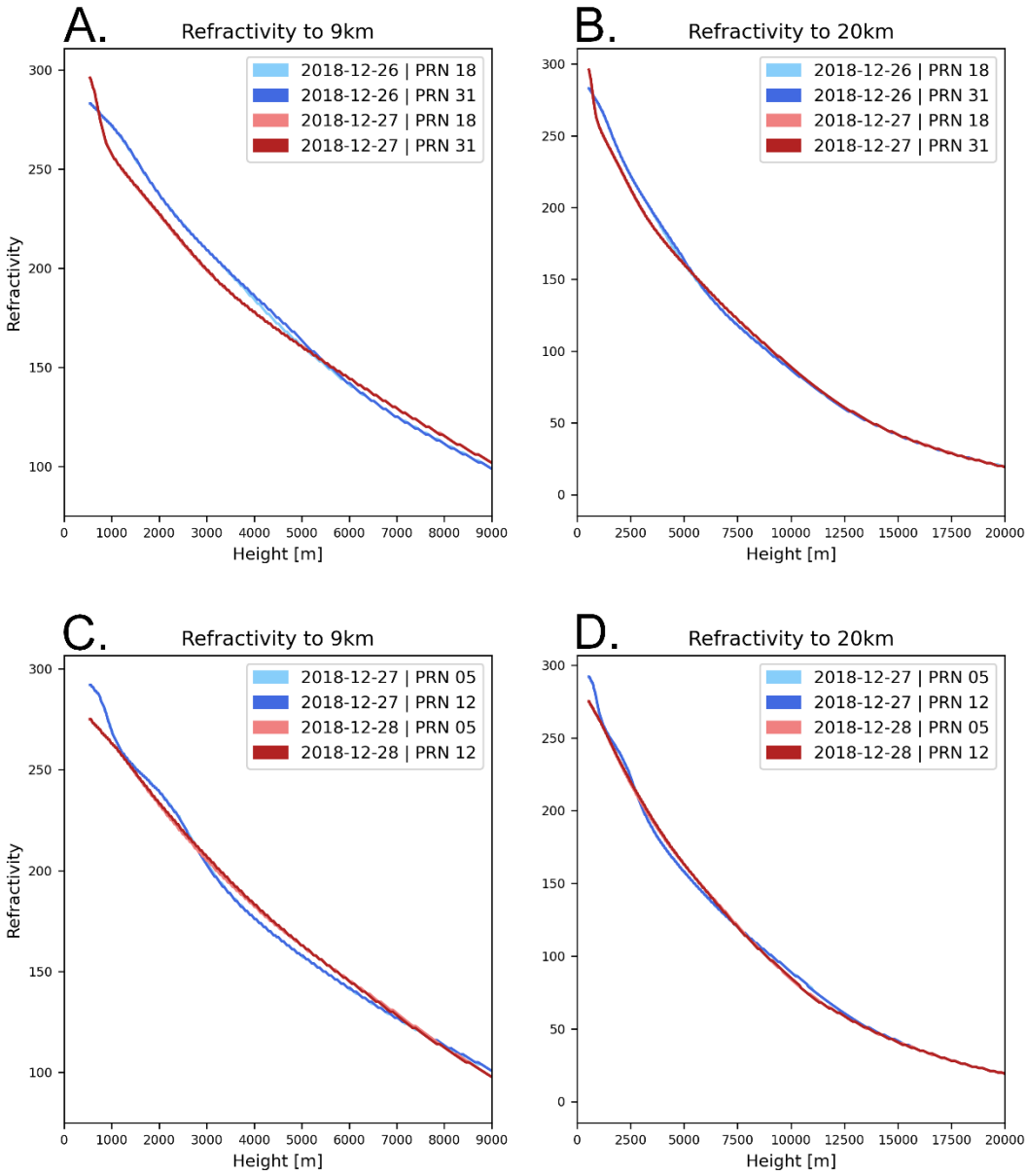
A.
Refractivity to 9km
2018-12-26 | PRN 18
2018-12-26 | PRN 31
2018-12-27 | PRN 18
2018-12-27 | PRN 31
Refractivity
Height [m]
B.
Refractivity to 20km
2018-12-26 | PRN 18
2018-12-26 | PRN 31
2018-12-27 | PRN 18
2018-12-27 | PRN 31
Height [m]
C.
Refractivity to 9km
2018-12-27 | PRN 05
2018-12-27 | PRN 12
2018-12-28 | PRN 05
2018-12-28 | PRN 12
Refractivity
Height [m]
D.
Refractivity to 20km
2018-12-27 | PRN 05
2018-12-27 | PRN 12
2018-12-28 | PRN 05
2018-12-28 | PRN 12
Height [m]

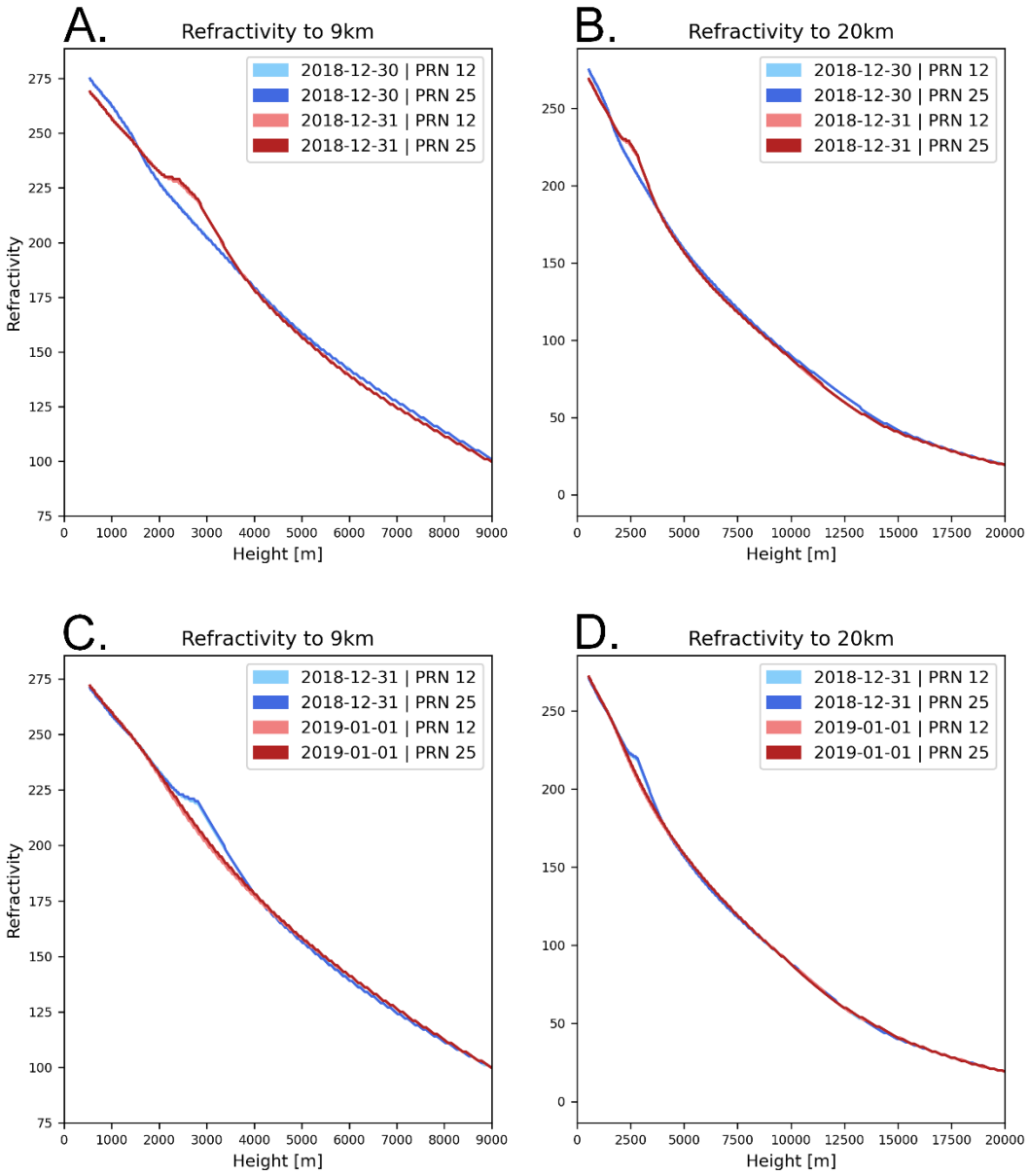
A.
Refractivity to 9km
2018-12-30 | PRN 12
2018-12-30 | PRN 25
2018-12-31 | PRN 12
2018-12-31 | PRN 25
Refractivity
Height [m]
B.
Refractivity to 20km
2018-12-30 | PRN 12
2018-12-30 | PRN 25
2018-12-31 | PRN 12
2018-12-31 | PRN 25
Height [m]
C.
Refractivity to 9km
2018-12-31 | PRN 12
2018-12-31 | PRN 25
2019-01-01 | PRN 12
2019-01-01 | PRN 25
Refractivity
Height [m]
D.
Refractivity to 20km
2018-12-31 | PRN 12
2018-12-31 | PRN 25
2019-01-01 | PRN 12
2019-01-01 | PRN 25
Height [m]

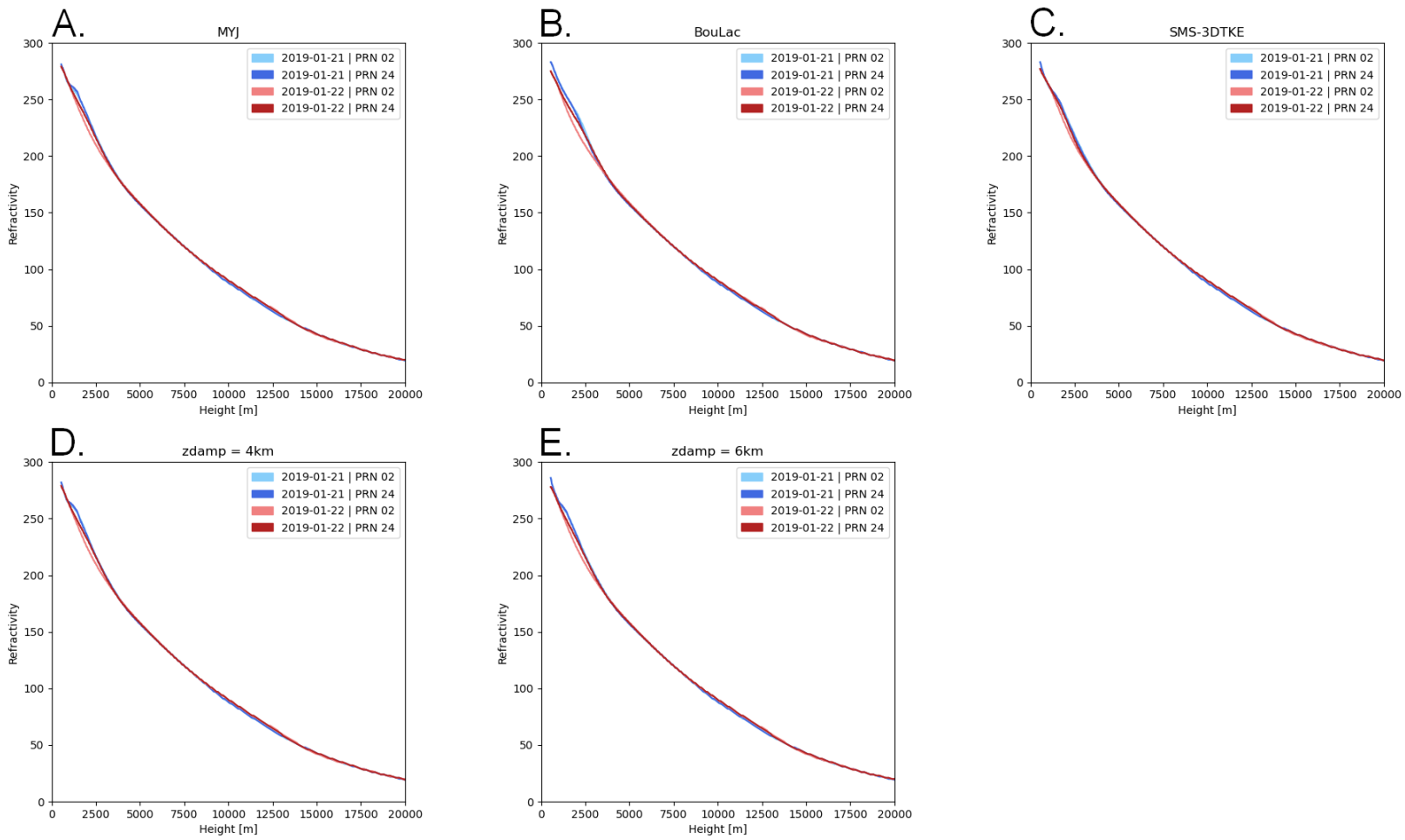
A.
MYJ
B.
BouLac
C.
SMS-3DTKE
D.
zdamp = 4km
E.
zdamp = 6km
2019-01-21 | PRN 02
2019-01-21 | PRN 24
2019-01-22 | PRN 02
2019-01-22 | PRN 24
Refractivity
Height [m]
0
50
100
150
200
250
300
0
2500
5000
7500
10000
12500
15000
17500
20000

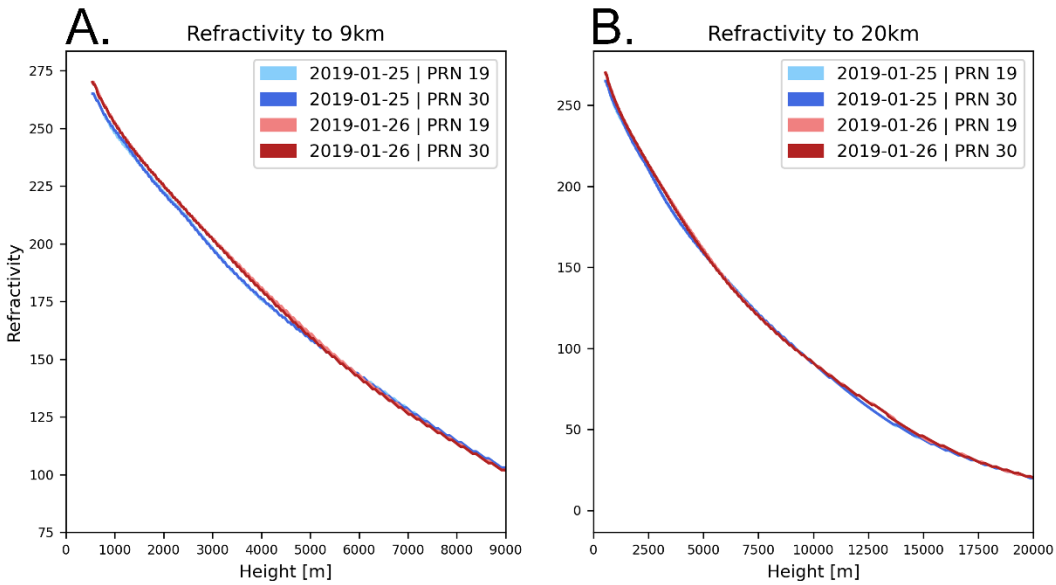
A.
Refractivity to 9km
2019-01-25 | PRN 19
2019-01-25 | PRN 30
2019-01-26 | PRN 19
2019-01-26 | PRN 30
Refractivity
Height [m]
B.
Refractivity to 20km
2019-01-25 | PRN 19
2019-01-25 | PRN 30
2019-01-26 | PRN 19
2019-01-26 | PRN 30
Height [m]

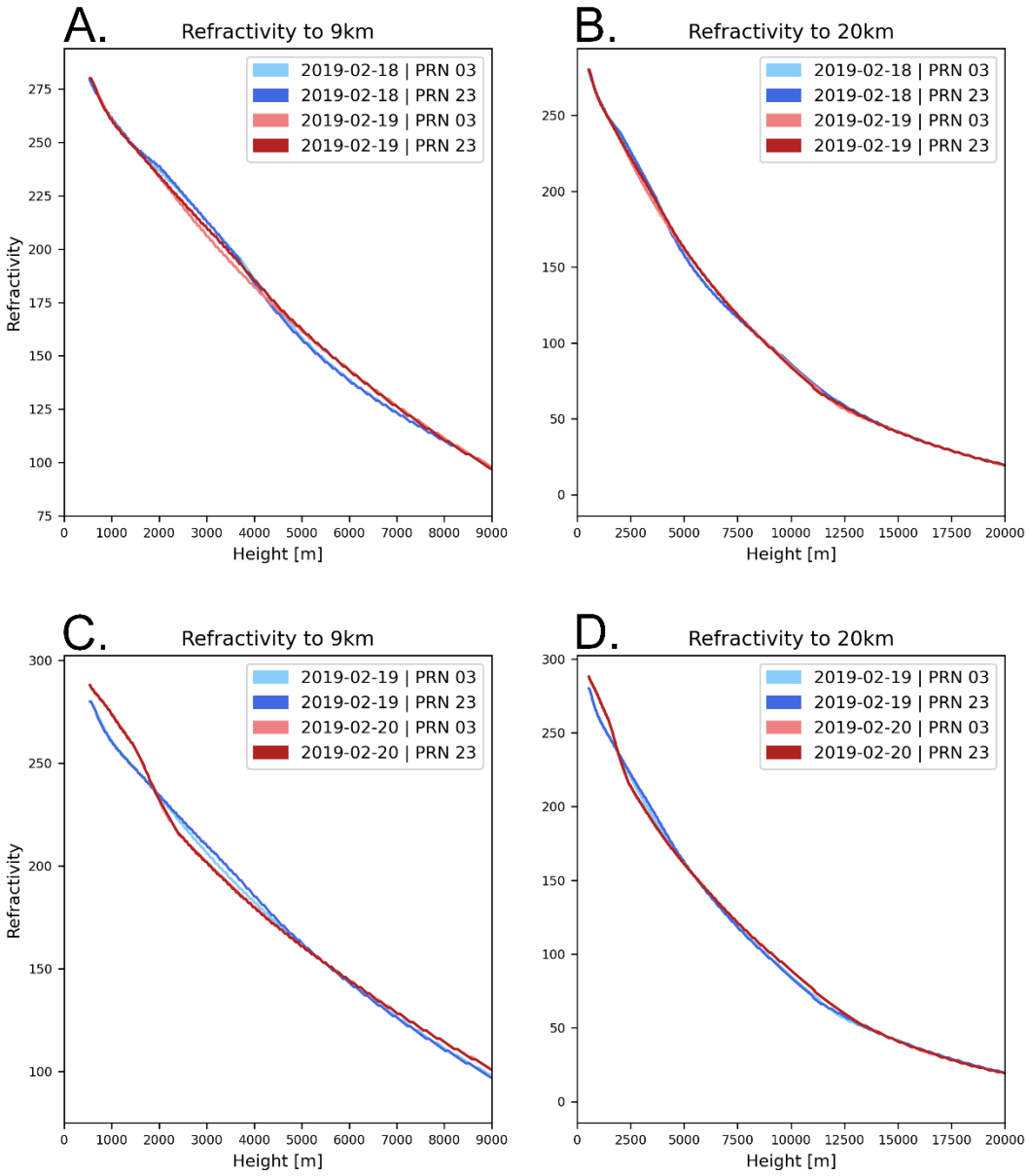
A.
Refractivity to 9km
2019-02-18 | PRN 03
2019-02-18 | PRN 23
2019-02-19 | PRN 03
2019-02-19 | PRN 23
Refractivity
Height [m]
B.
Refractivity to 20km
2019-02-18 | PRN 03
2019-02-18 | PRN 23
2019-02-19 | PRN 03
2019-02-19 | PRN 23
Height [m]
C.
Refractivity to 9km
2019-02-19 | PRN 03
2019-02-19 | PRN 23
2019-02-20 | PRN 03
2019-02-20 | PRN 23
Refractivity
Height [m]
D.
Refractivity to 20km
2019-02-19 | PRN 03
2019-02-19 | PRN 23
2019-02-20 | PRN 03
2019-02-20 | PRN 23
Height [m]

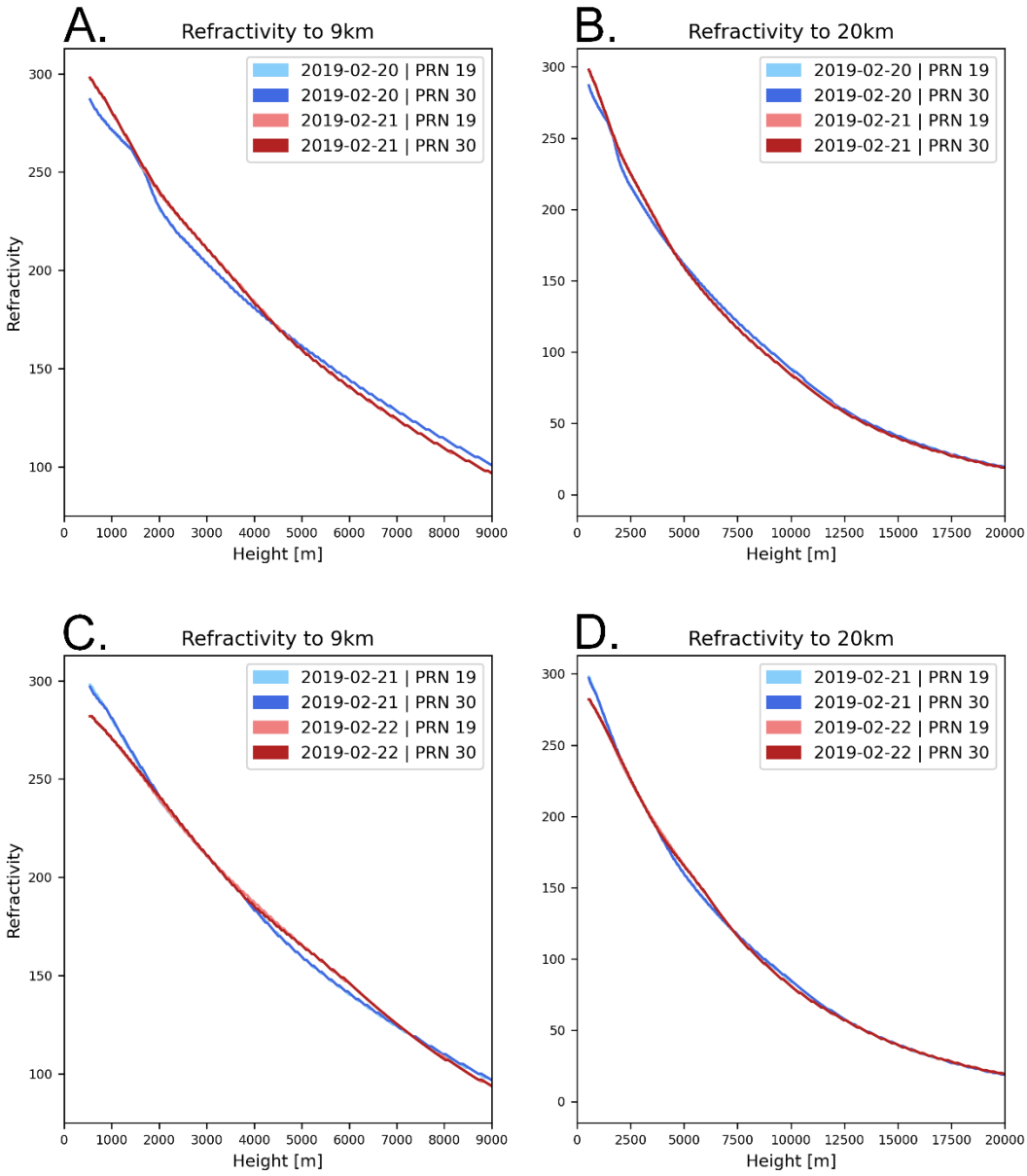
A.
Refractivity to 9km
2019-02-20 | PRN 19
2019-02-20 | PRN 30
2019-02-21 | PRN 19
2019-02-21 | PRN 30
Refractivity
Height [m]
B.
Refractivity to 20km
2019-02-20 | PRN 19
2019-02-20 | PRN 30
2019-02-21 | PRN 19
2019-02-21 | PRN 30
Height [m]
C.
Refractivity to 9km
2019-02-21 | PRN 19
2019-02-21 | PRN 30
2019-02-22 | PRN 19
2019-02-22 | PRN 30
Refractivity
Height [m]
D.
Refractivity to 20km
2019-02-21 | PRN 19
2019-02-21 | PRN 30
2019-02-22 | PRN 19
2019-02-22 | PRN 30
Height [m]

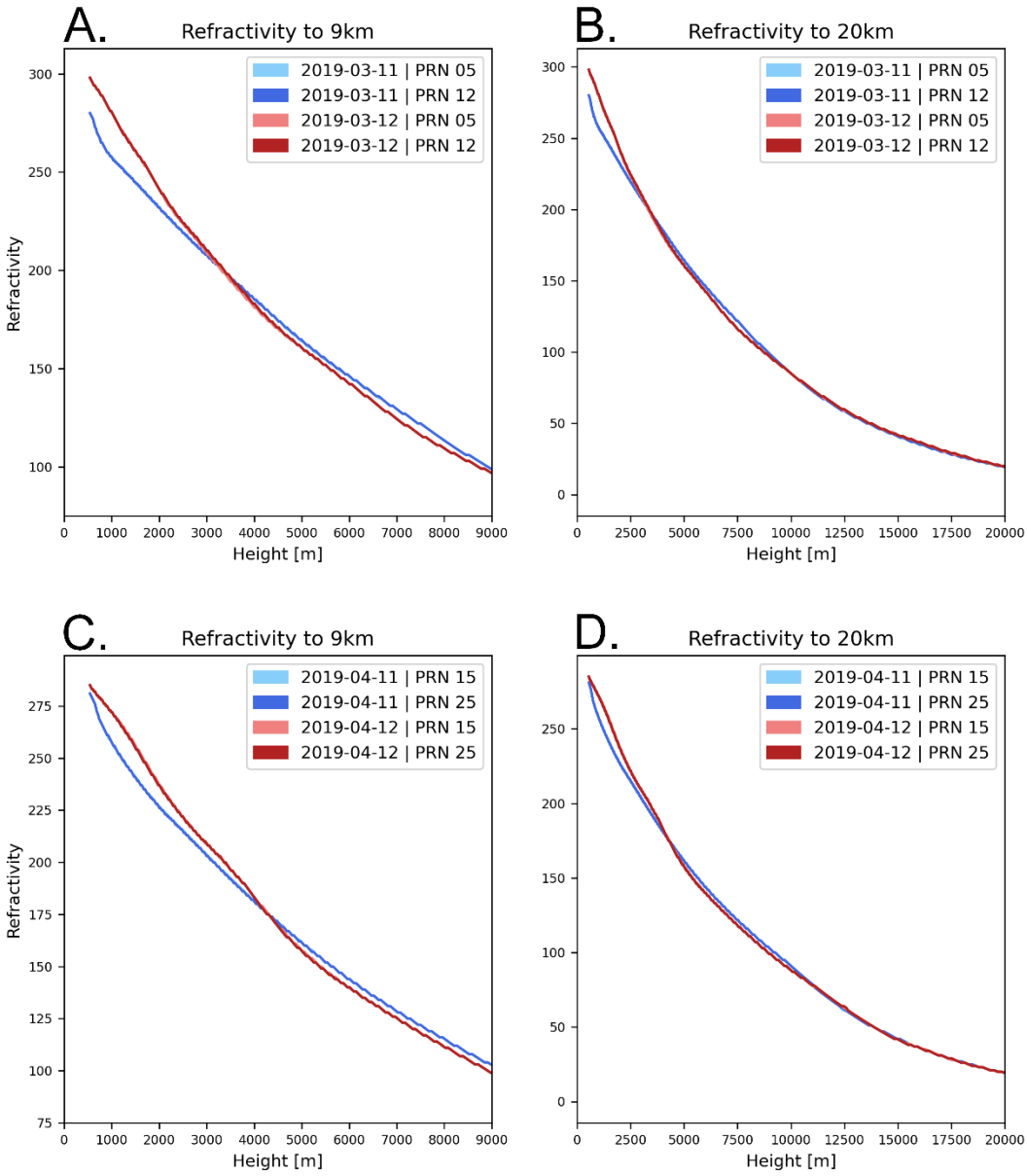
A.
Refractivity to 9km
2019-03-11 | PRN 05
2019-03-11 | PRN 12
2019-03-12 | PRN 05
2019-03-12 | PRN 12
Refractivity
Height [m]
B.
Refractivity to 20km
2019-03-11 | PRN 05
2019-03-11 | PRN 12
2019-03-12 | PRN 05
2019-03-12 | PRN 12
Height [m]
C.
Refractivity to 9km
2019-04-11 | PRN 15
2019-04-11 | PRN 25
2019-04-12 | PRN 15
2019-04-12 | PRN 25
Refractivity
Height [m]
D.
Refractivity to 20km
2019-04-11 | PRN 15
2019-04-11 | PRN 25
2019-04-12 | PRN 15
2019-04-12 | PRN 25
Height [m]

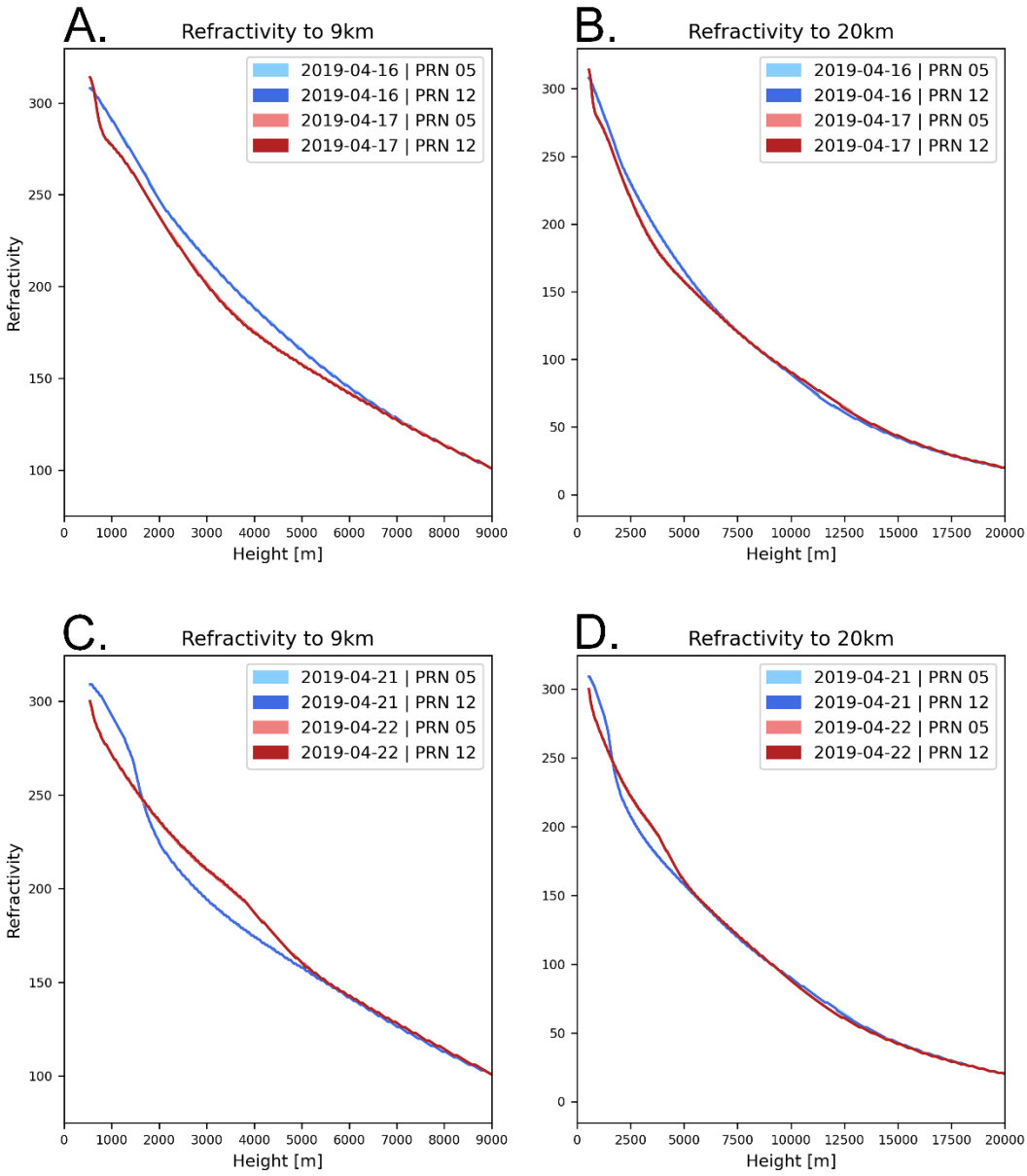
A.
Refractivity to 9km
2019-04-16 | PRN 05
2019-04-16 | PRN 12
2019-04-17 | PRN 05
2019-04-17 | PRN 12
Refractivity
Height [m]
B.
Refractivity to 20km
2019-04-16 | PRN 05
2019-04-16 | PRN 12
2019-04-17 | PRN 05
2019-04-17 | PRN 12
Height [m]
C.
Refractivity to 9km
2019-04-21 | PRN 05
2019-04-21 | PRN 12
2019-04-22 | PRN 05
2019-04-22 | PRN 12
Refractivity
Height [m]
D.
Refractivity to 20km
2019-04-21 | PRN 05
2019-04-21 | PRN 12
2019-04-22 | PRN 05
2019-04-22 | PRN 12
Height [m]

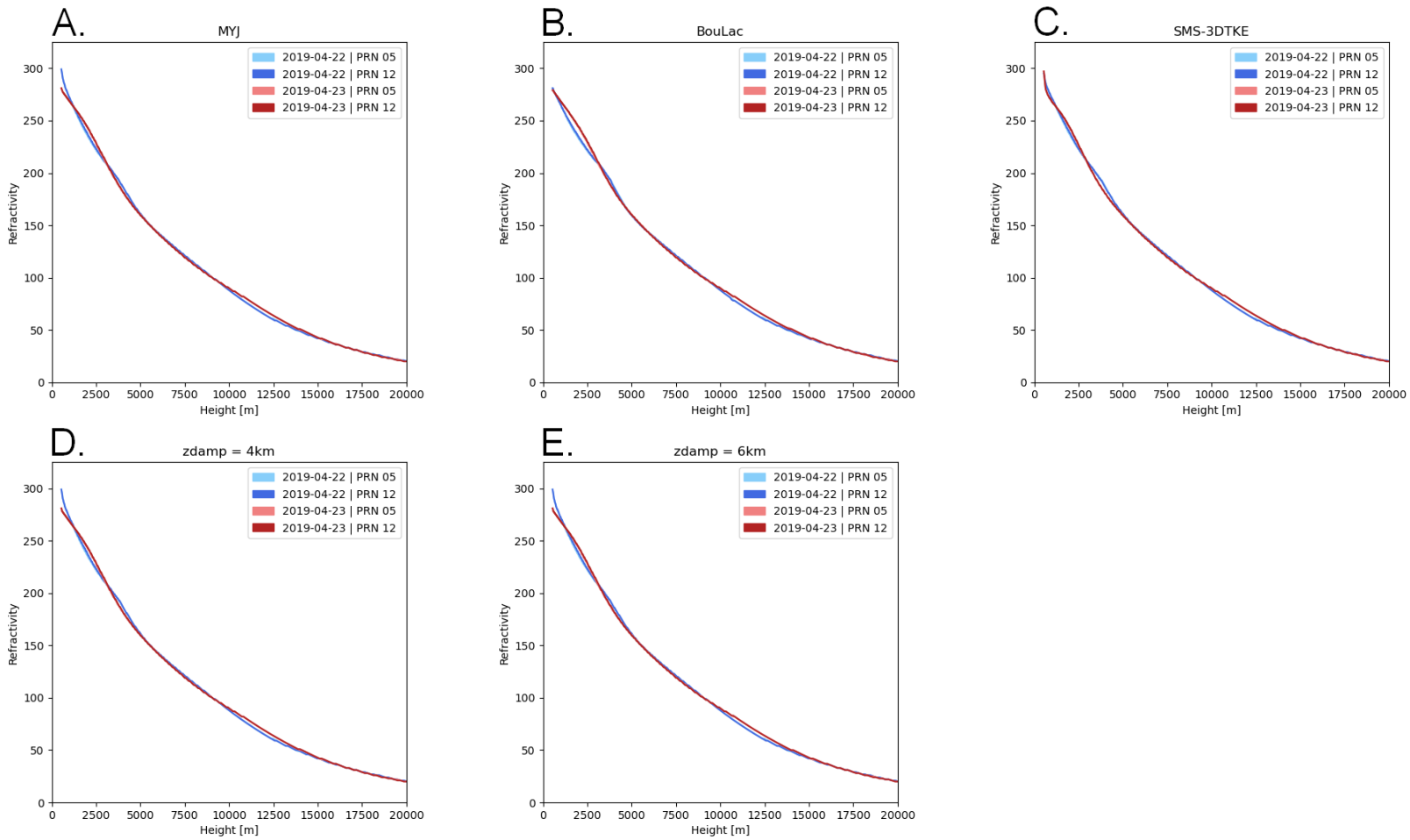
A.
MYJ
B.
BouLac
C.
SMS-3DTKE
D.
zdamp = 4km
E.
zdamp = 6km
2019-04-22 | PRN 05
2019-04-22 | PRN 12
2019-04-23 | PRN 05
2019-04-23 | PRN 12
Refractivity
Height [m]
0
50
100
150
200
250
300
0
2500
5000
7500
10000
12500
15000
17500
20000

Appendix G – Delay Difference Plots

Figures G1-G6. Difference of delay estimate for the specified day pair (a-d or a-e) from the ray tracer beginning at P612.

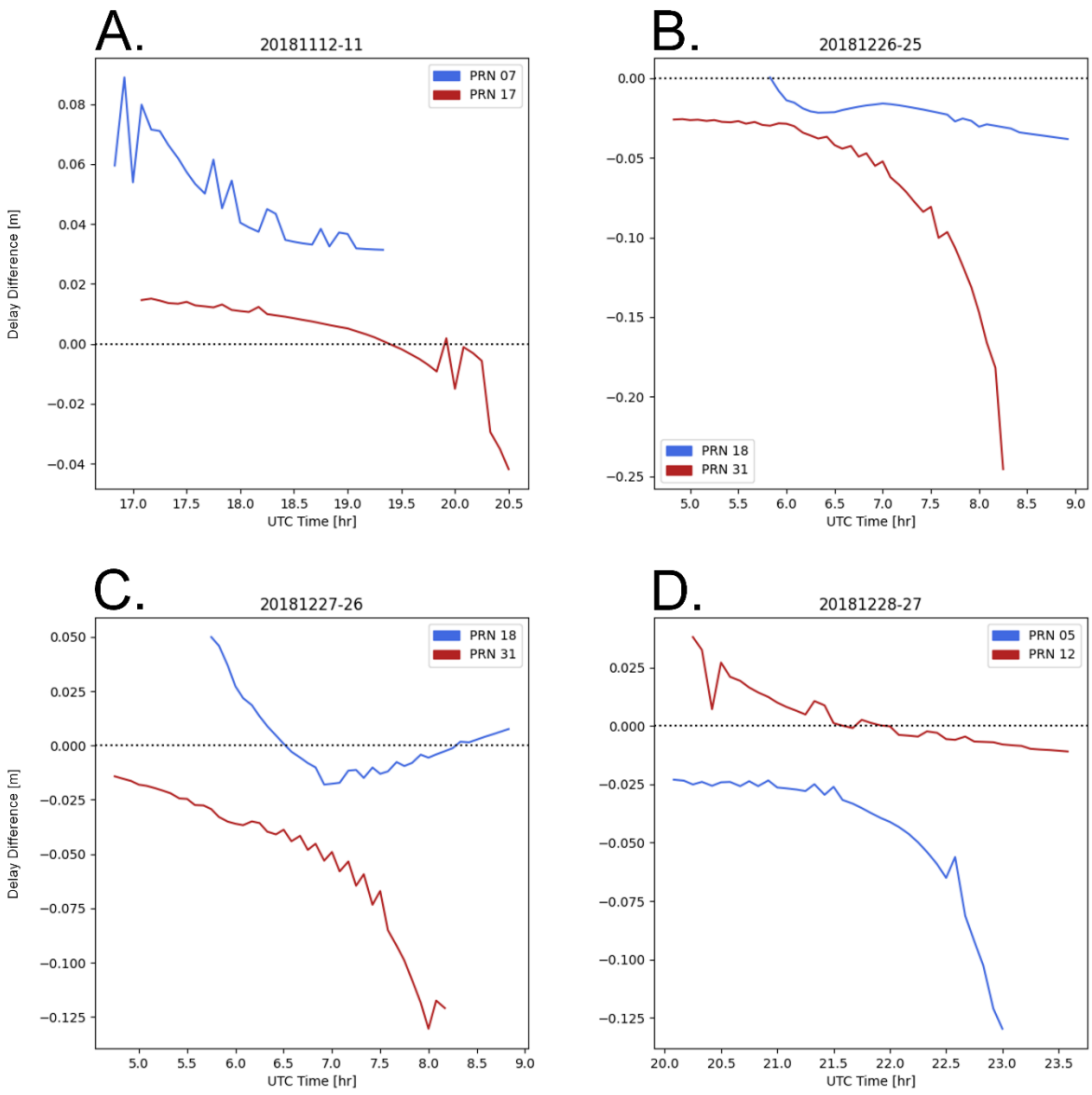

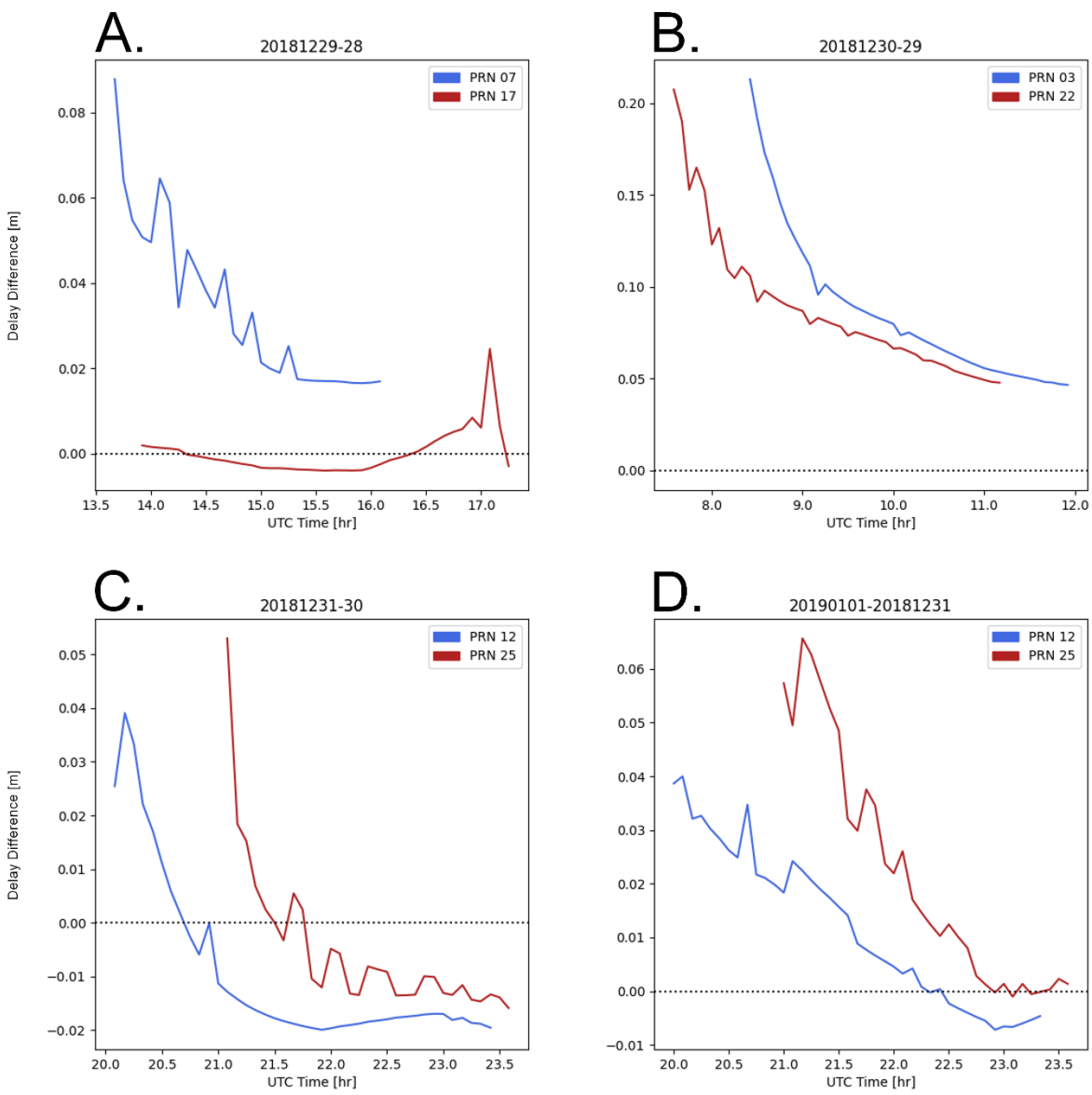
A.
20181229-28
PRN 07
PRN 17
Delay Difference [m]
UTC Time [hr]
B.
20181230-29
PRN 03
PRN 22
UTC Time [hr]
C.
20181231-30
PRN 12
PRN 25
Delay Difference [m]
UTC Time [hr]
D.
20190101-20181231
PRN 12
PRN 25
UTC Time [hr]

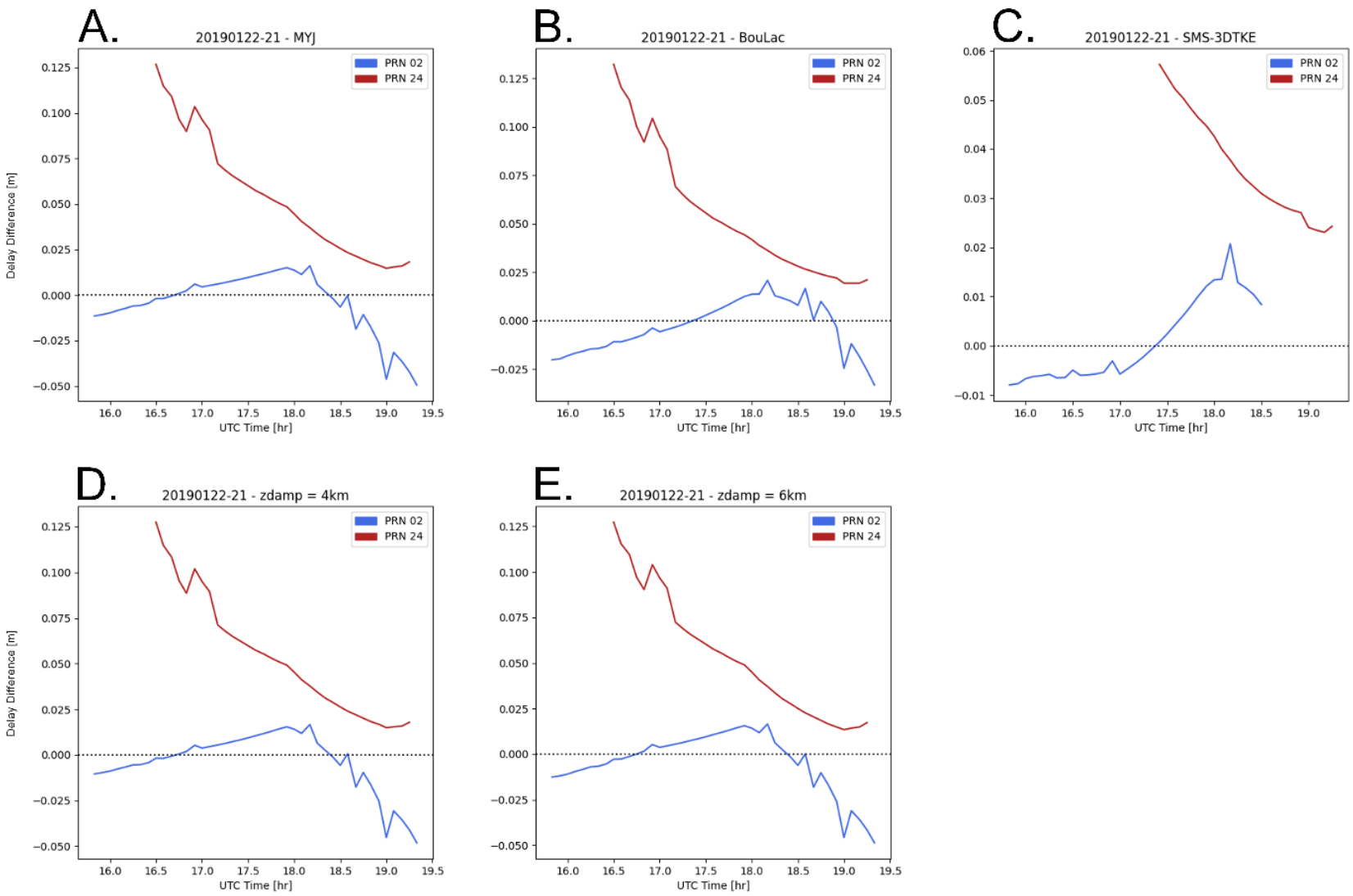
A.
20190122-21 - MYJ
B.
20190122-21 - BouLac
C.
20190122-21 - SMS-3DTKE
D.
20190122-21 - zdamp = 4km
E.
20190122-21 - zdamp = 6km
PRN 02
PRN 24
Delay Difference [m]
UTC Time [hr]

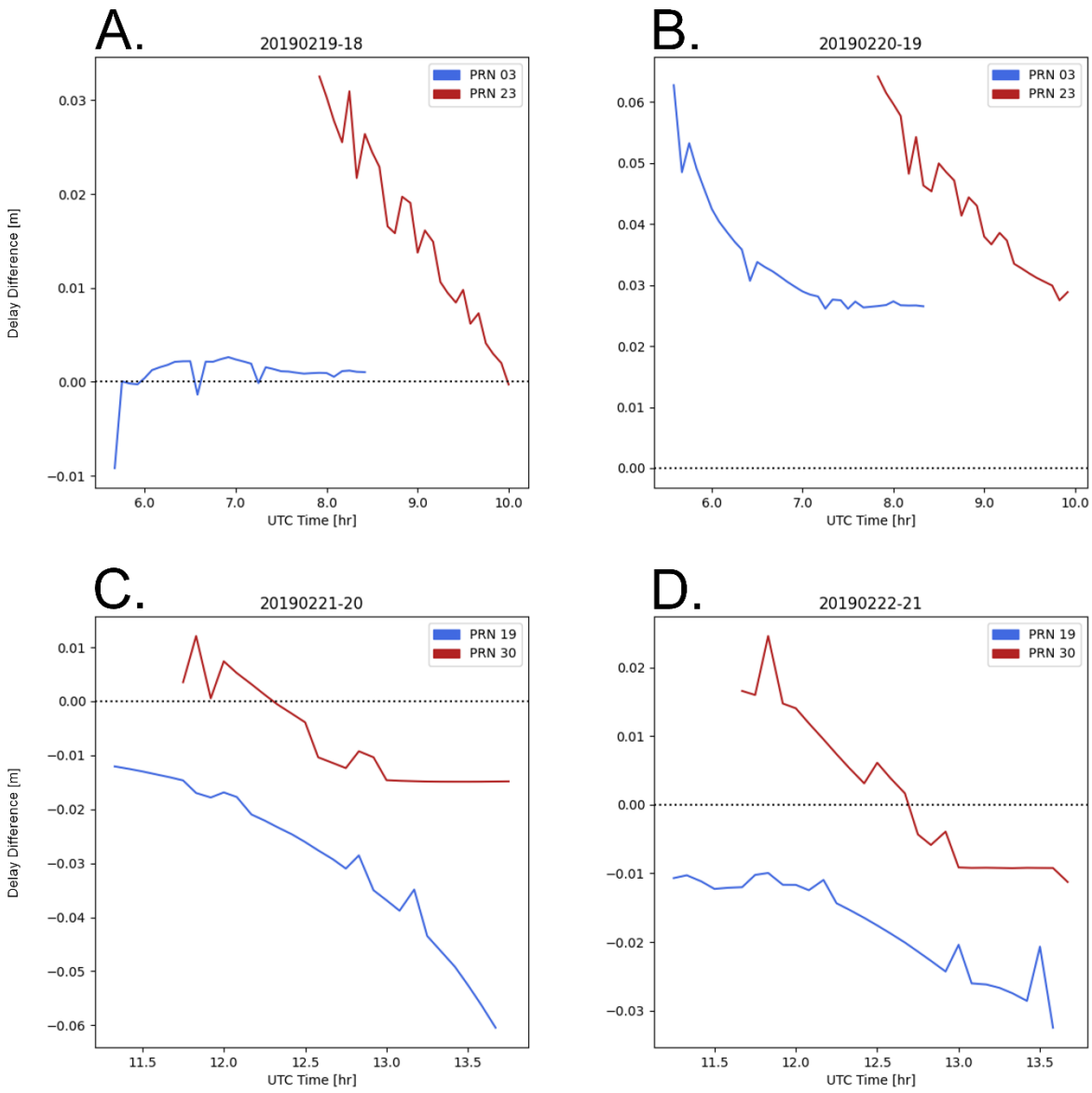
A.
20190219-18
PRN 03
PRN 23
Delay Difference [m]
UTC Time [hr]
B.
20190220-19
PRN 03
PRN 23
UTC Time [hr]
C.
20190221-20
PRN 19
PRN 30
Delay Difference [m]
UTC Time [hr]
D.
20190222-21
PRN 19
PRN 30
UTC Time [hr]

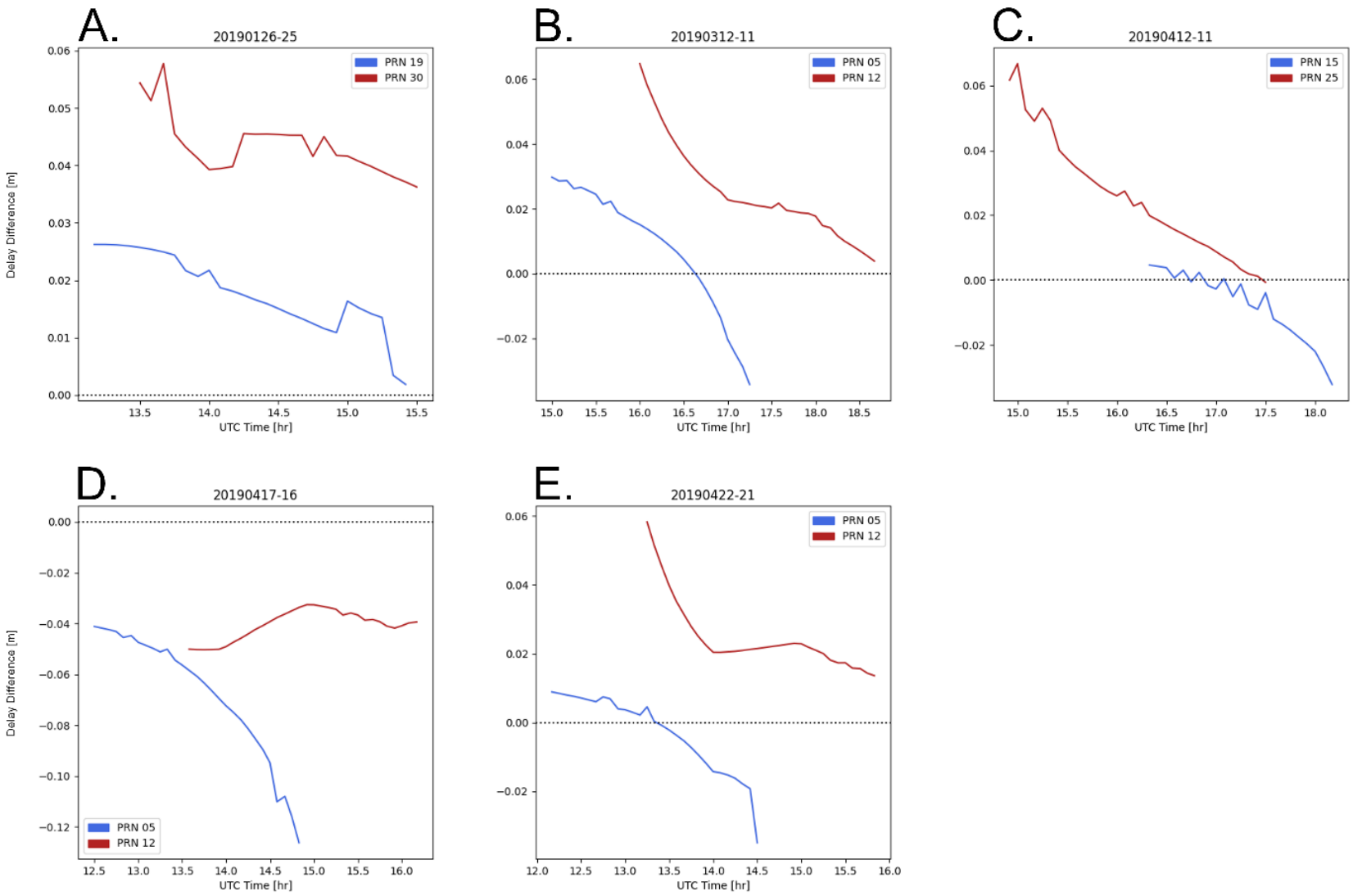
A.
20190126-25
PRN 19
PRN 30
Delay Difference [m]
UTC Time [hr]
B.
20190312-11
PRN 05
PRN 12
UTC Time [hr]
C.
20190412-11
PRN 15
PRN 25
UTC Time [hr]
D.
20190417-16
PRN 05
PRN 12
Delay Difference [m]
UTC Time [hr]
E.
20190422-21
PRN 05
PRN 12
UTC Time [hr]

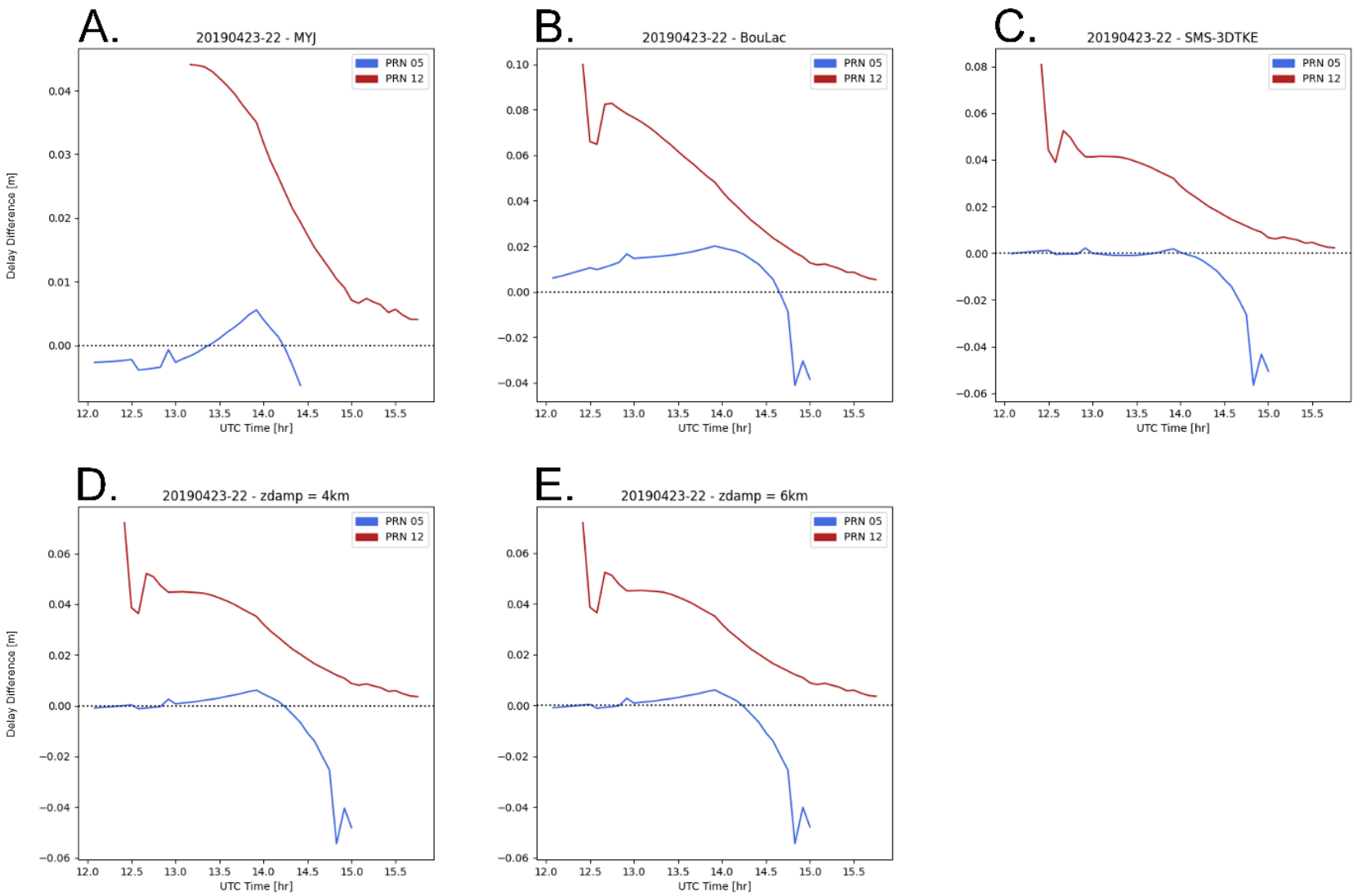
A.
20190423-22 - MYJ
B.
20190423-22 - BouLac
C.
20190423-22 - SMS-3DTKE
D.
20190423-22 - zdamp = 4km
E.
20190423-22 - zdamp = 6km
PRN 05
PRN 12
Delay Difference [m]
UTC Time [hr]

Figures G7-G10. Difference of delay estimate between MYJ and the specified scheme for the specified day pair (a-d) from the ray tracer beginning at P612.

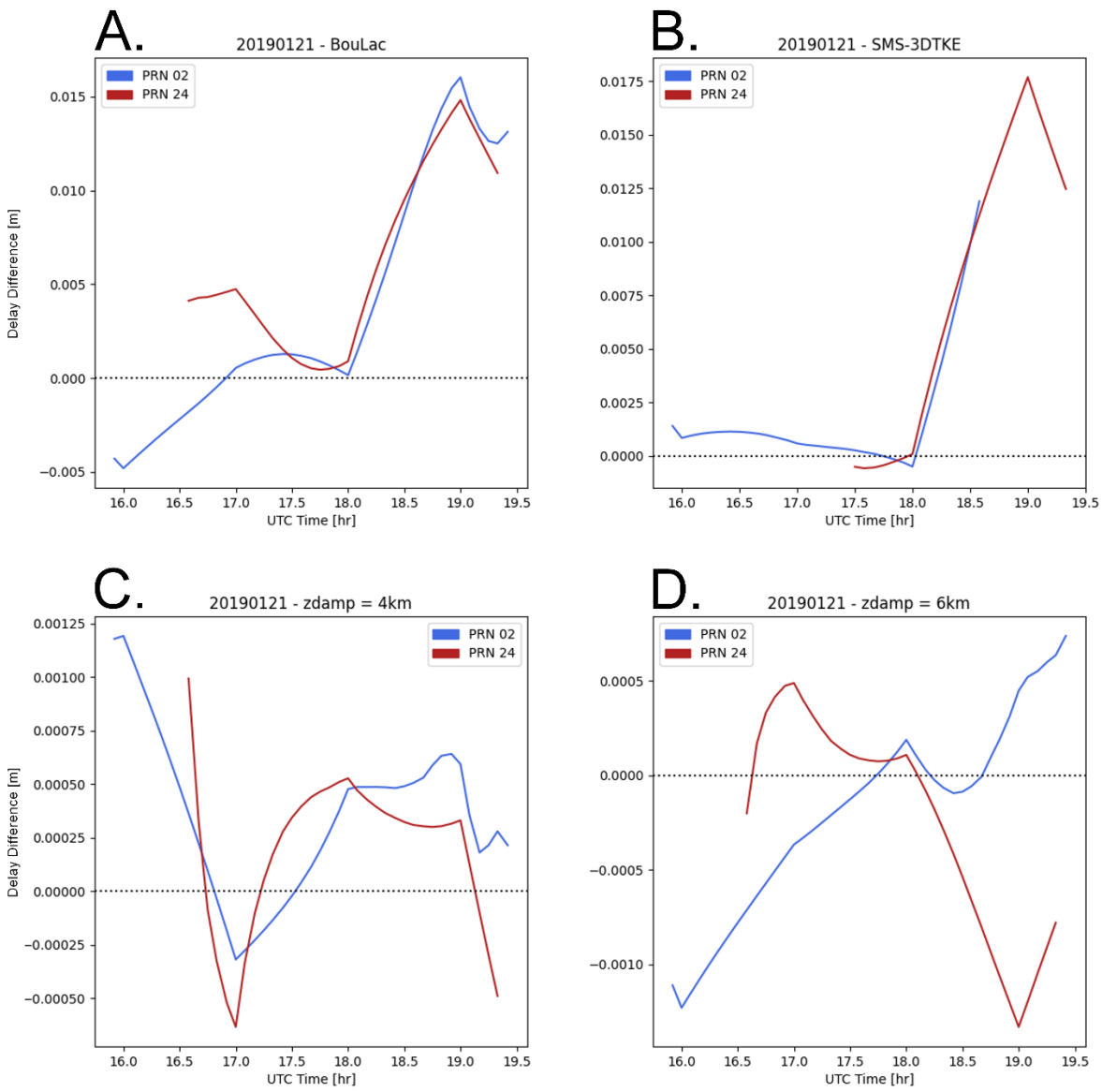

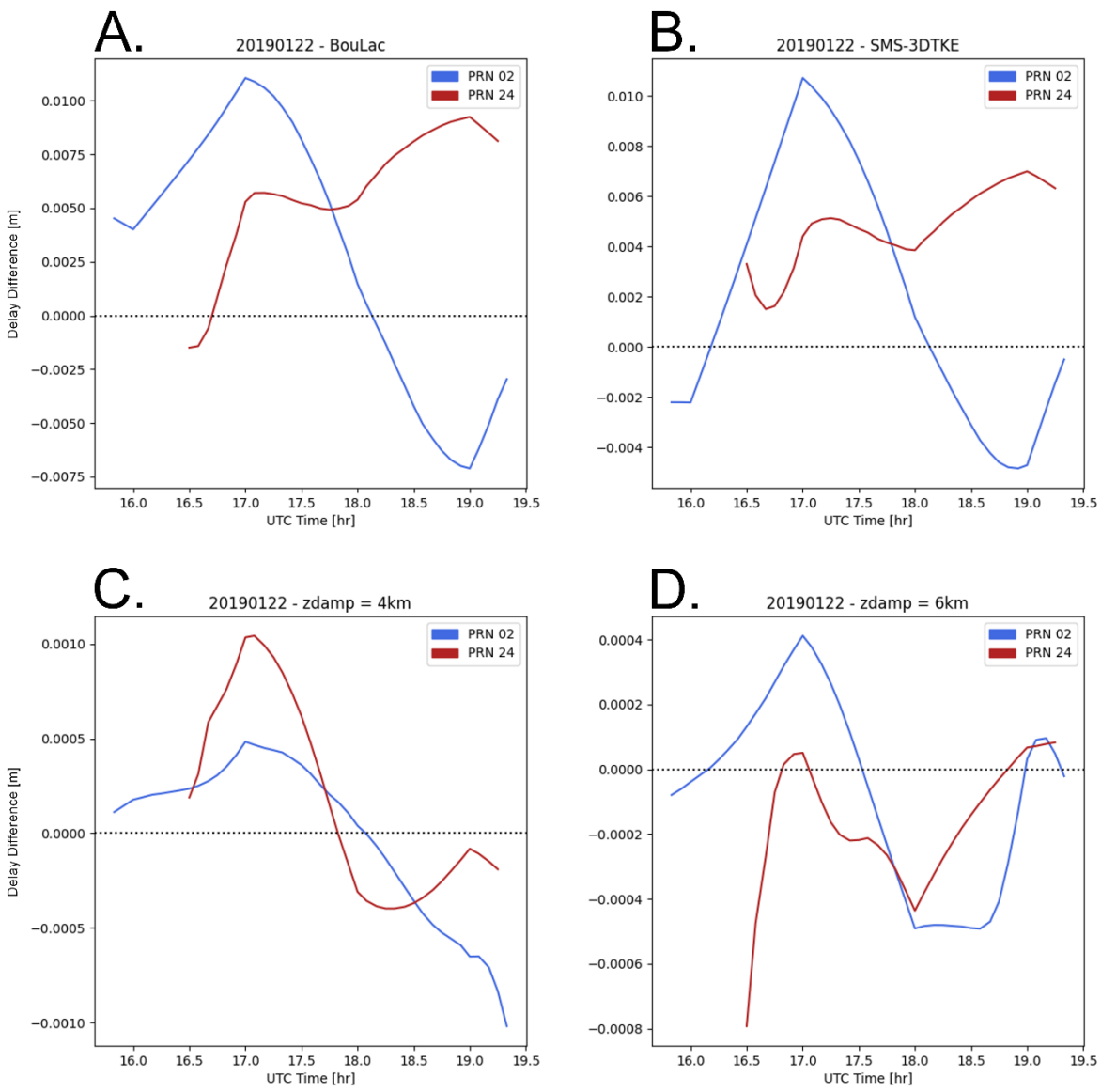
A.
20190122 - BouLac
PRN 02
PRN 24
Delay Difference [m]
UTC Time [hr]
B.
20190122 - SMS-3DTKE
PRN 02
PRN 24
UTC Time [hr]
C.
20190122 - zdamp = 4km
PRN 02
PRN 24
Delay Difference [m]
UTC Time [hr]
D.
20190122 - zdamp = 6km
PRN 02
PRN 24
UTC Time [hr]

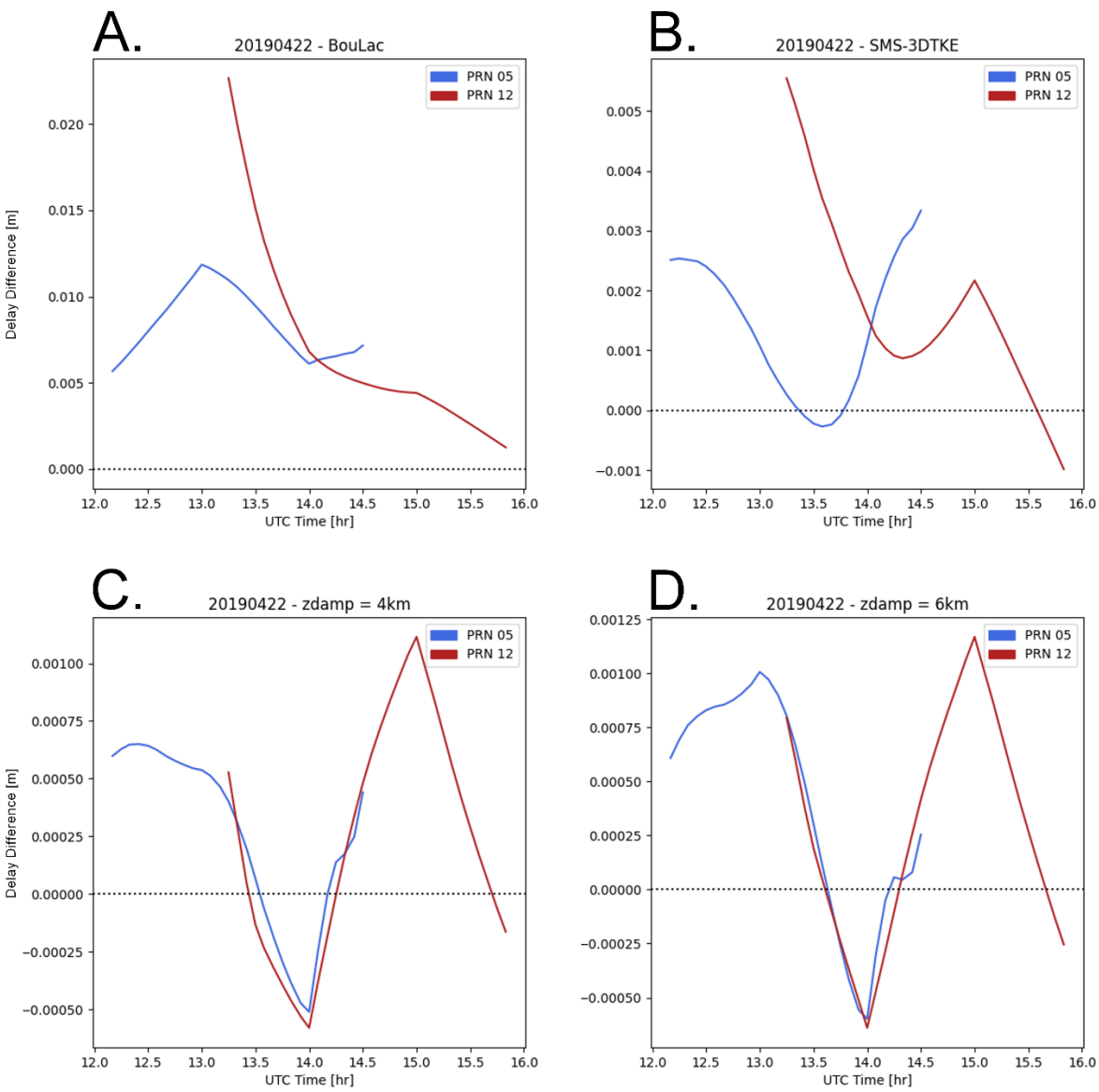
A.
20190422 - BouLac
PRN 05
PRN 12
Delay Difference [m]
UTC Time [hr]
B.
20190422 - SMS-3DTKE
PRN 05
PRN 12
UTC Time [hr]
C.
20190422 - zdamp = 4km
PRN 05
PRN 12
Delay Difference [m]
UTC Time [hr]
D.
20190422 - zdamp = 6km
PRN 05
PRN 12
UTC Time [hr]

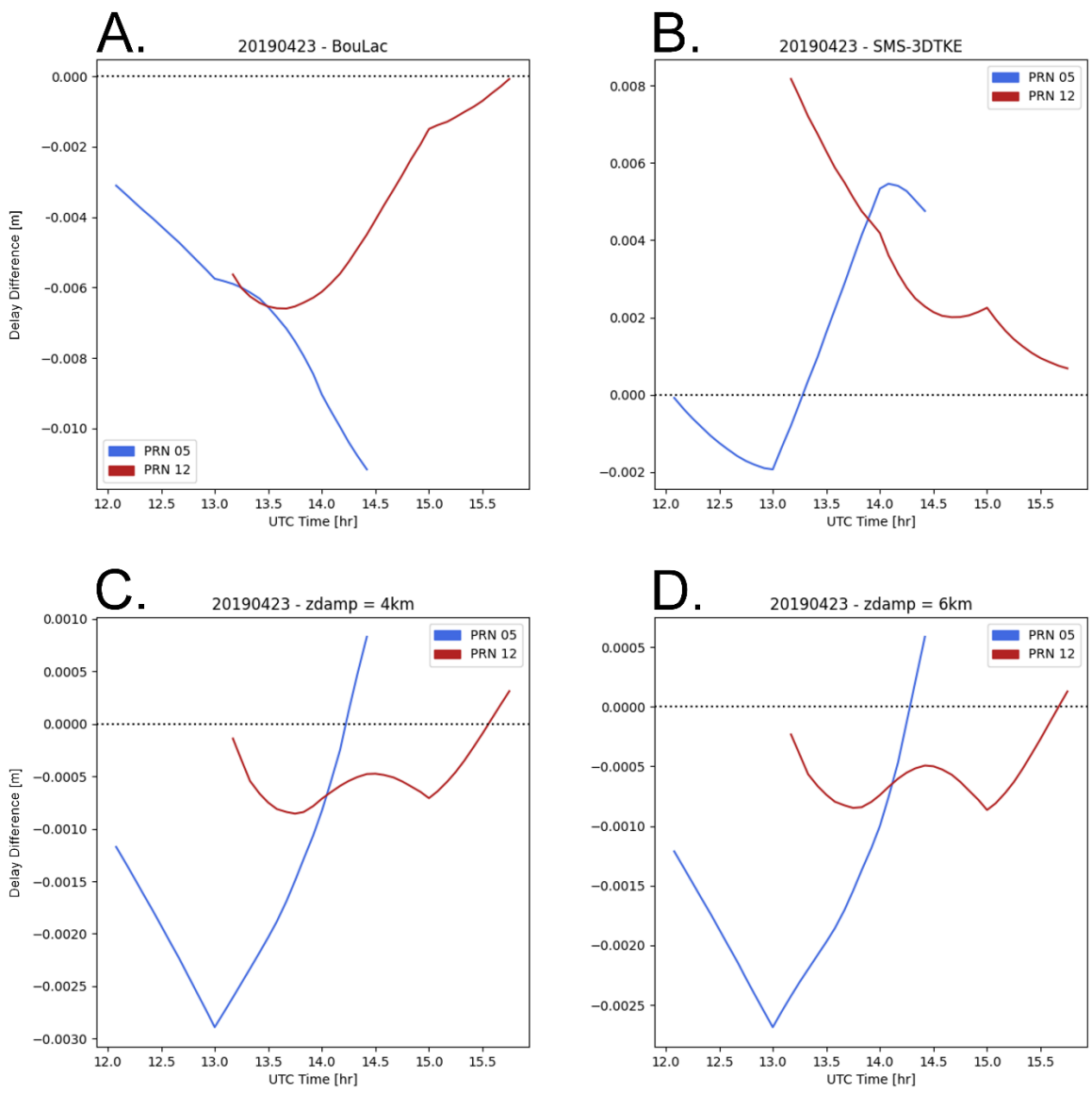
A.
20190423 - BouLac
Delay Difference [m]
UTC Time [hr]
PRN 05
PRN 12
B.
20190423 - SMS-3DTKE
UTC Time [hr]
PRN 05
PRN 12
C.
20190423 - zdamp = 4km
Delay Difference [m]
UTC Time [hr]
PRN 05
PRN 12
D.
20190423 - zdamp = 6km
UTC Time [hr]
PRN 05
PRN 12